KfK 3769
August 1986

Post Test Investigation of the Bundle Test ESBU-1

On Temperature Escalation in PWR Fuel Rod Simulator Bundles due to the Zircaloy/Steam Reaction

S. Hagen, H. Kapulla, H. Malauschek,
K. P. Wallenfels, B. J. Buescher
Hauptabteilung Ingenieurtechnik
Projekt Nukleare Sicherheit

Kernforschungszentrum Karlsruhe

KERNFORSCHUNGSZENTRUM KARLSRUHE
Hauptabteilung Ingenieurtechnik
Projekt Nukleare Sicherheit

KfK 3769

Post Test Investigation of the Bundle Test ESBU-1.

On Temperature Escalation in PWR Fuel Rod Simulator Bundles due to the Zircaloy/Steam Reaction

S. Hagen, H. Kapulla, H. Malauschek, K.P. Wallenfels
B.J. Buescher[+])

[+]) USNRC Delegate to Kernforschungszentrum Karlsruhe
from EG&G, Idaho Falls, Idaho

KERNFORSCHUNGSZENTRUM KARLSRUHE GMBH, KARLSRUHE

Als Manuskript vervielfältigt
Für diesen Bericht behalten wir uns alle Rechte vor

Kernforschungszentrum Karlsruhe GmbH
Postfach 3640, 7500 Karlsruhe 1

ISSN 0303-4003

Summary

This KfK report describes the post test investigation of bundle experiment ESBU-1. ESBU-1 was the first of two bundle tests on the temperature escalation of zircaloy clad fuel rods. The investigation of the temperature escalation is part of the program of out-of-pile experiments performed within the frame work of the PNS - Severe Fuel Damage program.

The bundle was composed of a 3x3 fuel rod array of our fuel rod simulators (control tungsten heater, UO_2-ring pellet and zircaloy cladding). The length was 0.4 meter. After the test the bundle was embedded in epoxy and cut by a diamant saw. The cross sections are investigated by metallographic, SEM and EMP examinations.

The results of these examinations are in good agreement with the seperate effects tests investigation of the PNS SFD-Program and inpile experiments of the Power Burst Facility.

The investigations show that liquid zircaloy dissolves UO_2 by taking away the oxygen from the oxide. Depending on the overall oxygen content the (U,Zr,O)-melt forms at refreezing

a) three phases (low oxygen content): metallic α-Zry(U), a uranium-rich metallic (U,Zr)alloy, and a $(U,Zr)O_2$ mixed oxide, or
b) two phases (high oxigen content): α-Zr(O) and the $(U,Zr)O_2$ mixed oxide.
c) In melt regions where the local oxidation was very severe, such as in steam contact, only the $(U,Zr)O_2$ mixed oxide is formed already at test temperature. Also ZrO_2 formed during the initial time of the test is dissolved by the melt.

Temperatureskalation in DWR Brennstabbündeln infolge der Zircaloy/Dampf-Reaktion: Nachuntersuchung des Bündels ESBU-1.

Kurzfassung

Dieser KfK-Bericht beschreibt die metallographische Nachuntersuchung des Bündelversuchs ESBU-1. ESBU-1 war der erste von zwei Bündelversuchen für die Untersuchung der Temperatureskalation von zirkaloy-umhüllten Brennelementstäben. Die Untersuchung des Eskalationsverhaltens gehört zum Programm der out-of-pile-Experimente (CORA), die im Rahmen der Severe Fuel Damage Untersuchungen des PNS durchgeführt werden.

Das Bündel war in einer 3x3 Anordnung aus den üblichen Brennstabsimulatoren aufgebaut (zentraler W-Heizer, UO_2-Ringpellets und Zircaloy-Hüllrohre). Die Länge betrug 40 cm. Nach dem Versuch wurde das Bündel in Epoxidharz eingebettet und mit einer Diamantsäge geschnitten. Die Schnitte wurden mit dem Metallmikroskop, dem Rasterelektronenmikroskop und der Mikrosonde untersucht.

Die Ergebnisse dieser Untersuchungen sind in guter Übereinstimmung mit Einzeleffekt-Untersuchungen im Rahmen des PNS SFD-Programms und der in-pile-Untersuchungen in der Power Burst Facility.

Die Untersuchungen zeigen, daß flüssiges Zircaloy UO_2 durch Sauerstoffentzug auflöst. In Abhängigkeit vom Sauerstoffgehalt bildet die U,ZrO-Schmelze beim Erstarren

a) drei Phasen (bei geringem Sauerstoffgehalt): metallische Zry(O)-, eine uranreiche metallische (U,Zr)-Legierung und ein $(Zr,U)O_2$-Mischoxid oder
b) zwei Phasen (bei höherer Sauerstoffkonzentration): α-Zr(O) und $(U,Zr)O_2$;
c) bei starker Oxidation, d.h. in direktem Kontakt zum Dampf wird nur das Mischoxid gebildet. Auch das am Anfang des Tests gebildete ZrO_2 der Hülle wird durch die Schmelze angegriffen.

Contents

		Page
1.	Introduction	1
2.	Experiment facility	2
3.	Test conduct	2
4.	Posttest appearance (Fig. 3-11)	3
5.	Post test sectioning (Fig. 13-20)	4
6.	Microstructural examination of the damaged test bundle (Fig. 21-93)	7
6.1	Overview	7
6.2	Discussion of figures 20 to 68	9
6.3	Interaction between liquid zircaloy and UO_2 and the phases present in the frozen melt	15
6.4	Dissolution of oxidized cladding by the melt	17
6.5	Oxidation of the melt	18
7.	Acknowledgement	20
8.	References	20
9.	List of Figures	21

1. Introduction

Within the Project Nuclear Safety (PNS) at the Kernforschungszentrum Karlsruhe (KfK), a comprehensive program /1/ for the investigation of Severe Fuel Damage (SFD) is being performed. As part of the overall program, out-of-pile experiments (CORA Program /2/) are being conducted at the Hauptabteilung Ingenieurtechnik (IT). The tests provide information on the mechanisms causing damage to PWR fuel rods for temperatures up to 2200 °C. The experiments are designed to give information on the integral behaviour of the processes, which are investigated in detail and under well defined conditions in the separate effect tests /3,4/ of the SFD--program. The out-of-pile experiments are also used for the assessment of the SFD computer codes which calculate the integral behaviour of the fuel rods under Severe Fuel Damage conditions. In addition, these experiments directly complement integral in-pile bundle tests being conducted at PBF, ACRR, NRU and PHEBUS.

Earlier experiments have shown that the behaviour of fuel rods at high temperatures is strongly dependent on the degree of cladding oxidation. Highly oxidized rods are very brittle and can fragment during operation or during quenching, whereas relatively unoxidized cladding melts, dissolves UO_2, and runs down the rod. The extent of oxidation depends, in part, on the temperature rise rate, which in turn is influenced by the exothermic oxidation process. If the heat of reaction is not removed fast enough, the exponential increase of the reaction with temperature can give rise to a rapid temperature escalation. Therefore, oxidation-induced temperature escalation plays an important role in determining fuel behaviour. To investigate the temperature escalation and the processes leading to a turnaround of the escalation, a series of single rod and bundle experiments with fuel rod simulators are being performed.

The results of single rod tests are given in the KfK-reports 3507, 3557 and 3567 /5,6,7/. The bundle tests ESBU-1 and ESBU-2 are described in the KfK-reports 3508 and 3509 /8,9/. This paper reports on the posttest investigation of the ESBU-1 bundle test.

2. Experiment facility

The testing is performed in the NIELS facility located in the Hauptabteilung Ingenieurtechnik at KfK. Figure 1 shows side and top cross sections of the 3x3 bundle made with PWR fuel rod simulators. The simulators conform as nearly as possible to German PWR dimensions and pitch, using zircaloy cladding of 10.75 mm outer and 9.29 mm inner diameter, UO_2 ring pellets of 9.2 mm outer and 6.1 mm inner diameter, and a tungsten heater element 6.0 mm in diameter. The overall length of the simulators is 400 mm.

To simulate the exothermic reaction energy of neighbouring rods a zircaloy shroud is installed around the 3x3 bundle. To reduce radial heat losses, the shroud is wrapped in a fiber ceramic insulation (6 mm) as shown in the inset photograph in Figure 1. Steam is inlet to the bottom of the bundle at 16 locations so that the flow is evenly distributed across the bundle cross section. Temperatures are measured by two-color pyrometers and NiCrNi thermocouples with Inconel sheaths. Additional detailed information is given in the test results report /8/.

3. Test conduct

The time dependent power input is shown in Figure 2. At the beginning of the test, the argon pressure is 770 Torr. An inlet steam flow of about 1 g/s to the bundle is begun at a time of approximately 41 minutes into the test. The steam flow is then held constant through the high temperature transient until a time of 66 minutes.

As seen in Figure 2 the surface temperature of the central rod increases at a rate of about 2 °C/s until about 1700 °C is reached. After reaching this temperature, the influence of zircaloy oxidation increases the heatup rate to about 6 °C/s, the temperature escalates to a peak of 2250 °C and then falls rapidly. On the outer rods and the shroud, the initial temperature peaking occurs somewhat later and is much lower in temperature. At 60 minutes into the test all three temperatures show a minimum. During the transient the electric power increases continuously up

to 60 minutes, from 60 to 64 minutes the voltage and the resulting electric power is constant and finally, at 64 minutes, the power is shut off and the experiment terminated.

4. Posttest appearance (Fig. 3-11)

The appearance of the test assembly following the test with the insulation and shroud still in place is shown in Figure 3. The insulation and shroud were intact following the test. However, both were severely embrittled, as seen during the removal of the insulation from the shroud. The insulation, originally a flexible mat, broke into many pieces. Even though removal of the insulation was done carefully, pieces of the shroud broke off as is seen in Figure 4. The shroud was severely oxidized over the center region of the bundle and broke away in several places revealing the fuel rod simulators.

Figures 5 and 6 show the fuel rod simulators after removal of the shroud. The cladding from all nine rods has melted over the center portion of the bundle, liquefied some of the UO_2 fuel and formed a molten mixture which flowed down the rods. The molten mixture has frozen in a solid mass near the bottom of the bundle which substantially blocks the coolant flow channels. The upper end of the bundle contains intact but oxidized zircaloy cladding. In the middle region, only a thin layer of UO_2 and some fragments of pellets stuck to the tungsten rod can be seen. Figure 6 shows the lower part of the bundle after removal of the shroud from above and below the blockage. In this figure one can see metallic looking zircaloy near the steam inlet changing to oxidized zircaloy near the blocked region.

Figures 7 and 8 show the detail of the lower bundle region as seen from below. Oxide spalling is evident as are refrozen drops of liquefied material. The frozen melt shows poor wetting of the solid surface as indicated by the large wetting angles and small contact areas. Melt viscosity, oxygen content, and the relatively cold fuel rod simulators probably influenced the behaviour in this region.

The appearance of the blocked region from above is shown in Figures 9 through 11. The frozen melt has a smooth surface and has wet what is remaining of the simulators rather well (small wetting angle and large contact surface). This is clear evidence of an interaction of the melt with the oxidized fuel rod simulators. The composition of the melt and these interactions are the primary subject of the posttest examination. A large amount of powdery rubble, not shown in these photographs, was found on top of the blockage.

From the post test appearance of the bundle and shroud, the following conclusions are reached regarding the behaviour of the test bundle and shroud during the high temperature transient. During the initial heatup to high temperature, a layer of ZrO_2 formed on the outer cladding wall after the introduction of steam into the test chamber. Once the melting point of zircaloy was reached, the inner region of the cladding, which had not yet been oxidized started to melt. The molten zircaloy in contact with the fuel pellets took up oxygen from the UO_2 and started to dissolve the pellets. The ZrO_2 layer that had formed was apparently to thin to retain the molten material and the molten material broke free and flowed down towards the lower part of the bundle sweeping the oxide layer along with it. The molten core material then froze in the lower cooler part of the bundle in a series of layers.

The smooth upper surface of the blocked region (Fig. 11) with loose powder lying on top of the blockage indicates that the powder must have fallen down onto the melt after it was frozen and that the fragmentation of the upper part of the bundle happened during cooldown.

5. Posttest sectioning (Fig. 13-20)

The bundle was encapsulated in epoxy after the test and cut into sections as shown in Figure 13. Figure 14 shows a summary of the six bundle cross sections made in the blocked region. Figures 15 through 19 are enlargements of the cross sections starting above the blockage at 129 mm elevation and going below the blocked region to 15 mm elevation.

Note that the photographs at 15 mm (Figure 19) and at 119 mm, and 129 mm (Figure 15) are left-right reversed with respect to the other photographs because they were taken from the bottom rather than top of the sections. The photographs at 119 and 116 mm (Figures 15 and 16) are of the bottom and top surfaces, respectively, of adjacent cross sections and are separated only by the 3 mm saw kerf.

The right hand photgraph in Figure 15 shows the cross section at 119 mm, corresponding to the bottom of section 2. The cross section is less than 10 mm below the upper surface of the refrozen melt. The white circular areas are the tungsten heaters, surrounded by black UO_2 ring pellets. The outer radius of the UO_2 ring pellets have been reduced to about 4.2 mm from 4.6 mm, indicating dissolution of UO_2 by liquid zircaloy. The cladding has essentially disappeared and only faint rings at the original cladding boundaries can be recognized for some rods. A large coherent lump of frozen melt has filled the space between pellets and shroud.

The frozen material consists of molten zircaloy from the high temperature region of the bundle containing UO_2 from dissolved fuel pellets. When the melting temperature of zircaloy was reached, the inner unoxidized cladding melted and ran into the gap between the cladding and the UO_2 pellets. The molten zircaloy ran down, further dissolving UO_2. The first droplets froze in the lower part of the blocked region. Melt running down later froze on top of the melt which had run down and frozen earlier. The appearance of the cross section at 119 mm indicates that at that elevation the melt froze at the same time.

The hole in upper left part of the cross section at 119 mm is the only channel left open for steam flow. The dark seam around this channel is melt oxidized by steam, which forms a $(U, Zr)O_2$ mixed oxide. Similar oxidation of the melt is seen in Figures 16 and 17 (116-86 mm).

With decreasing elevation the hole size increases and oxidized cladding forms part of the boundary of the channel. At the 106 mm elevation a second hole is seen in the lower part of the cross section. A comparison to the 116 mm cross section shows that no steam flow was possible there.

Stagnant steam or perhaps a hydrogen bubble may have been responsible for the second hole. Consequently there was no steam flow through this hole and only minor oxidation is evident.

The first evidence of oxidized cladding appears at 106 mm, and this becomes more evident at lower elevations. Above 106 mm the oxidized cladding appears to have been completely dissolved by the melt. Below 106 mm the cladding attack decreases with decreasing elevation and temperature.

The cross sections shown in Figure 17 provide evidence that the interaction history was not necessarily the same in different regions of the same cross section. In the channel between the four rods on the upper left the low contact angle betwen the melt and the cladding outer surface shows that there was no appreciable interaction here between the melt and the oxidized cladding.

This is in contrast to what is seen in the channel between the four rods in the lower right hand quadrant. Here the contact angle between the melt and the cladding surface is high and it is evident that the melt has interacted with the cladding. The structure of the different cross sections indicates that droplets of varying lengths have frozen at different times in the channels between the rods. The droplets may have also been at different temperatures. When the droplets arrived and froze later in a particular position, the time available for cladding oxidation was longer and the melt time available for interaction was shorter.

The center rod at 96 mm (Figure 17) illustrates four distinct cladding regions, beginning clockwise from the lower right: (a) strong cladding/melt interaction such that the two are visually indistinguishable, (b) weaker cladding/melt interaction, with the interface still visible, (c) oxidized cladding/melt contact with very little interaction, and (d) severely oxidized cladding with no melt contact.

Figure 18 at 76 mm shows severe oxidation of all nine rods. From the oxidation visible along the edges of the melt, one concludes that most of the oxidation occurred after the melt ran down and refroze. Figure 18 at 66 mm and Figure 19 at 51 mm show successively less oxidation until, in Figure 19 at 15 mm, almost no oxidation is visible. Since the steam flow was obviously ample, the temperatures in this region must have been much lower.

6. Microstructural Examination of the Damaged Test Bundle (Fig. 21-93)

6.1 Overview:

Figures 20 through 93 show photographs of the microstructures obtained with a metallurgical microscope or in some cases a microprobe. The results of the point analysis by the microprobe are included.

The figures can be separated into the following groups: Figures 20 to 68 are a systematic series of pictures taken from the location where the cladding is in contact with UO_2 or relocated melt. Eight subgroups are given for the cross sections at the different elevations above the lower end of the bundle.

Figures	21-26:	119 mm
"	27-31:	116 mm
"	32-37:	106 mm
"	38-50:	96 mm
"	51-62:	86 mm
"	63-65:	76 mm
"	66-67:	66 mm
"	68:	51, 15, 7 mm

Figure 20 gives an overview of the positions of the micrographs at the different elevations. Also, in each of the figures from 21 to 68, there is a small picture of the respective cross section included and the positions presented in each figure are marked.

The cross sections were photographed with normal camera while the micrographs were made using a metallographic microscope and the micrographs are left-right reversed in relation to the photographs showing the whole cross sections.

Figures 69-71 and 72-76 show enlarged representations of areas with oxidized cladding from the cross sections at 106 mm and 86 mm respectively. These pictures illustrate the attack of the melt on initially oxidized cladding.

Figure 77 demonstrates the interaction between molten Zry and UO_2 at different areas from the elevations 119 mm and 106 mm.

Figures 81 through 88 show the results of the microprobe analyses made of various locations on cross section 4 (106 mm elevation). Figure 78 shows a SEM-picture of the interface between UO_2 and Zircaloy at 106 mm. The point analysis of the three phases found are given. This figure is representative of the interaction between UO_2 and liquid zircaloy.

The distribution of the three phases at different elevations are given in Figures 79 and 80.

Figures 82 and 83 show the results of the analysis of the three phases in cross section 4. The SEM pictures with the point analysis results of material oxidized in stagment and flowing steam are given in Figures 84 to 86. Figure 87 shows a SEM photograph with the point analysis results of an area, where previously oxidized cladding was covered with melt (see also Figure 69 area A). Finally a summary of the point analysis results is given in Figure 88.

Figure 89 to 93 show the variation in microstructure of the refrozen melt with elevation. In these figures a series of micrographs are shown which were taken at the same cross sectional position of the array at different elevations. The elevations range from 15 mm to 116 mm above the lower end of the cladding and the micrographs were taken at magnifications ranging from 50 x to 500 x.

6.2 Discussion of figures 20 to 68

The micrographs from elevation 119 mm are given in figures 21 to 26. Position 1 gives the region of the former shroud in contact with the melt. This region is shown in the upper half of Figures 21 and 22. The outside of the shroud corresponds in Figure 21 to the upper part of the pictures and in Figure 22 to the left side of the picture. The pictures show that a relatively small oxide layer has formed on the outside surfaces of the shroud. Inside this oxide layer we can recognize two main phases, the bright α-zircaloy matrix and the grey inclusions. The inclusions consist of $(U,Zr)O_2$. The presence of mixed uranium zirconium oxide in the frozen melt shows that most of the shroud must have been molten at high temperature.

The two lower photographs in Figure 21 are from location 2, the area in the neighbourhood of the UO_2 pellet of rod 7. The UO_2 is the dark region in the picture in the lower part of the left side (50x magnification). The UO_2 is not visible in the picture on the right side. The frozen melt also contains the two phases here, the white matrix of -zircaloy and the frozen mixed oxide which is present as grey inclusions. The dark areas correspond to positions where material has broken away from the cross sections. The refrozen melt in the neighbourhood of the fuel pellet can also be seen at the positions 3, 4, 5, 6 and 7, given in figures 23, 24 and the upper half of 25. The position of the UO_2 in these figures is always at the lower end of the photographs.

Position 8 and 9 in figures 25 and 26 show the frozen melt in direct contact with the steam channel. In these pictures the steam channel is in the direction of the lower end of the photographs. The micrographs show that the region next to the steam channel is completely oxidized. This region corresponds to the dark ring which is seen in the overview picture.

The micrographs of the cross section at 116 mm are given in figures 27 to 31. As one can see in figure 13 the cross section at 119 mm is the surface above the saw cut and the cross section at 116 mm is the surface below the saw cut. This means that the overview pictures from the cross section 119 mm are left-right reversed to the overview pictures of the cross section at 116 mm.

This is also seen in the position of the steam channel. Consequently the positions marked on cross section 116 mm are on the other side of the bundle compared to the positions on the cross secitons at 119 mm elevation.

Location 1 is the region containing the former shroud. On this side of the bundle much less oxidation is found than on the other side 3 mm higher. The frozen melt in areas 2, 3, 4, 5 and 6 is shown in figures 27 to 29.

The attack of the melt on the UO_2 pellet can be clearly seen in locations 4, 5 and 6 which show the melt UO_2 pellet interfaces at higher magnification. One cann see how little particles are broken away from the pellet to be dissolved into the melt. This process is discussed in more detail in a following section.

Figure 30 shows two micrographs taken from location 7. At this location and elevation, the UO_2 ring pellet is missing. The test rod here was not heated and extended only part way up the bundle to allow temperature measurements of the central rod with the two color pyrometer. The test rod contained a part length tungsten rod to position the test rod. During the high temperature transient, the cladding melted and filled the gap at this elevation between the cladding and the tungsten rod. The piece of tungsten fell out of the section during cutting and the hole left by the tungsten rod is filled with epoxy.

As a consequence of this location 7 shows a cross section of the refrozen melt consisting of zircaloy matrix and refrozen melt.

Area 8 gives the region of the melt directly next to the steam channel. Here one can see that the melt is completely oxidized. This region corresponds to the dark ring in the overview picture. This layer was probably already solidified during the test at high temperature.

The micrographs of cross section 4 at 106 mm elevation are given in Figures 32 to 37. This cross section corresponds to the upper surface of segment 4 and it is equivalant to the cross section from 119 mm elevation. The shroud is located at position a in these cross sections. Due to the fact that the melt had not covered the inner surface of the shroud at this elevation we find much more oxidation of the zircaloy than is observed in the cross section 30 mm higher.

In Figure 32, location 1 shows the region of former cladding which was not covered by melt. The outer highly oxidized surface of the cladding is seen in the upper part of the picture. Location 2 shows the opposite side of the test rod. Here the cladding is completely covered with melt and has been completely dissolved. Section 2 shown on Figure 32 is the region where the UO_2 and melt are in contact.

The micrographs taken of locations 3 b and c in Figures 32, 34 and 35 respectively show areas of previously oxidized cladding which were not completely dissolved by the melt at the end of the test. One can see here how the zirconium is attacked by the melt through cracks in the oxide layer. This attack of the melt on the oxidized zircaloy is discussed in a later chapter. Figures 69 to 71 show enlarged views of the same regions.

Location 4 shows a region of the cladding which was in direct contact with the steam channel. The cladding is completely oxidized at this position. The oxidation process was much stronger here than in location 1. The fuel rod at location 1 had only access to stagnant steam at this elevation. Area d shows the melt in direct contact to the steam channel. In this picture the steam channel is on the right side and one recognizes the oxidized melt by its much darker appearance.

The micrographs of cross section 5 at 69 mm elevation are given in Figures 38 to 50. Locations 1, 10 and 11 in Figure 38 show oxidized cladding in direct contact with steam which has been nearly completely oxidized. In Figure 39 locations 2, 3, 4 and 5 show regions of former cladding which are covered by melt.

The melt between locations 2 and 3 appears to have run down much earlier than the melt between location 4 and 5 for much less zirconium oxide is found in areas 2 and 3. In Figure 40 locations 6, 7, 8 and 9 show cladding which has had direct access to the steam channel. In comparison to the oxidized cladding in Figure 38 which reacted under the conditions of stagnant steam, a quite different oxide structure is found. In Figure 40 typical large grains of zirconium oxide are found. Location a, c and d in Figures 41, 43 and 44 respectively show regions of oxidized cladding on the same rods which are covered by melt. Here one can clearly see the reaction of the melt with the zirconium oxide as well as the sharp boundary line between the outside surface of the oxidized cladding and the region of the melt. In all the micrographs one can see a high concentration of oxide phases. This appears as a seam around the former boundary of the cladding. Location b in Figure 42, location e in Figure 45 and location f in Figure 46 shows the melt next to the fuel rod and in direct contact with the steam channel. Here the melt adjacent to the UO_2 pellets is in direct contact with the steam and is completely oxidized. In Figure 42 on the right side of the lower picture one can see the UO_2 pellet. On the lower side of the picture, one sees completely oxidized melt which is in direct contact with the steam channel. And in the upper photograph a mixture of -zircaloy and oxidized inclusions is seen. In Figure 45, the UO_2 pellet is again seen on the right side, but in this picture the completely oxidized melt is at the top. In Figure 46, the UO_2 pellet once again is on the right side, but the fully oxidized region appears in the lower part of the picture. In Figure 47 position g shows a region of former cladding in direct contact with the steam. The cladding is nearly completely oxidized. Position h on Figure 48 gives the melt in direct contact to the steam. One can see here how the oxidation forms a layer on the surfce of the melt. Positions i and k in Figures 49 and 50 show the oxidized shroud.

The micrographs of the cross section from the 86 mm elevation are given in Figures 51 to 62. In Figure 51 positions 10 and 11 show the oxidation of the cladding which had access to stagnant steam without being covered by the melt. We find more oxidation in positions 10 and 11 than in position 1. This may be due to the fact that the rods at position 10 and 11 were in contact with more melt from the upper region at this elevations and extra heating of these rods may have occurred at this elevation.

In Figure 52 positions 2, 3, 4 and 5 are given. At these locations, oxidized cladding was covered by the melt, running down from the upper part of the bundle. One can recognize in all of the pictures that the oxide is attacked by the melt. The thickness of the different oxide layers show that the oxidation behaviour clearly depends on the arrival time of the melt from the upper part of the bundle. If one compares positions 2 and 3 which are adjacent locations on neighbouring rods one finds nearly the same oxide layer thickness although the oxide layer in position 3 is a little bit thicker than in area 2. This is expected as position 3 is located on a side rod sitting between two corner rods and this rod should run a little higher in temperature than a corner rod. If one compares positions 3 and 4 which are on opposite sides of the same rod but otherwise equivalent, a marked difference is seen in the thickness of the oxide layer. This means the melt between the positions 2 and 3 must have come down much earlier than the melt between the positions 4 and 5 and thus in locations 2 and 3 the cladding had a shorter time for oxidation. The thinner oxide layers of area 2 and 3 which were in contact for a longer time with the melt are also more strongly attacked by the melt.

In Figure 53, positions 6, 7, 8 and 9 show areas of cladding which were not covered by melt. In these areas the cladding was in direct contact with the steam channel and is fully oxidized. In these pictures, the cladding surface exposed to the flowing steam is at the top and the UO_2 is located in the lower section.

A detailed view showing the oxidation of the shroud is given in Figures 54 and 62. Here, the oxide layer on the inside of the shroud is much thicker than the oxide layer on the outside of the shroud. This is because the inside of the shroud had better access to the steam.

Positions b and c on Figures 55 and 56 compare the location on the same fuel rod in which the first location remains uncoverd during the test and the second location is covered by the melt from the upper part of the bundle. Figure 56 shows that a strong attack of the oxidized cladding by the melt has occurred. The outer surface of the oxidized cladding is also clearly defined. Position d on Figure 57 shows a region of oxidized cladding which is strongly attacked by the surrounding melt.

In this micrograph the cladding is on the left side of the figure and the UO_2 is seen on the right side.

Positions e and f in Figure 58 show positions in which the melt over the cladding is in direct contact with the steam channel. Here one can see a region in which the previously oxidized zirconium is attacked by the melt and also a region in which the material over the UO_2 is completely oxidized. For position e the completely oxidized melt is located on the right side of the picture. In position f the completely oxidized region is on the left side of the picture. In both cases the UO_2 is seen in the lower end of the picture.

Figure 59 shows position g and h on the central rod. Here one can see that at position g much less attack on the zirconium oxide has occurred than at position h. In location h the oxidized cladding has completely disappeared. This means that the melt in this region must have moved down much earlier than in the region corresponding to position g.

In location l shown in Figure 61 the oxide layer has completely disappeared. For the regions i, k and m in Figures 60 and 61, the melt is in direct contact to the steam channel and the melt covering the UO_2 in contact with the steam is nearly completely oxidized. In the region where the melt had no direct access to the steam, the ZrO_2 layer has disappeared. The fully oxidized region is shown on the right side of the picture for position i and m and for position k on the left side of the picture.

The micrographs of the cross section at 76 mm are shown in Figures 63 to 65. Position 1 shows the oxidation of the cladding with no melt present. Region 5 on Figure 65 shows the thickness of the oxide layer on the central rod. The oxide layer here is nearly three times larger than at position 1 on the outer rod. Area 3 in Figure 64 shows the region of the former cladding on the central rod which was covered by melt. One can recognize here that the oxide layer has disappeared completely. Region 4 in Figure 64 shows the transition from the covered to uncovered region. The uncovered region is on the left and the covered is on the right. Once again no oxidized cladding is left in the covered region. The upper left

hand side of the pictures shows the oxidized melt. Areas 7,8 and 9 in Figure 65 show the thickness of the oxide layer of three outer fuel rods.

The oxide layers in these rods can be compared to the thickness of the oxide layer on the central rod in location 5 shown on the same figure. As these four rods lie next to the same sub-channel, the availability of steam should be the same for all four. Consequently the difference in oxide thicknesses is due to the difference in the temperature of the central fuel rod.

The micrographs of cross section 8 at 66 mm are given in Figures 66 and 67. The thicknesses of the oxide layer around the upper right sub-channel are shown in position 2,4, 5 and 6. As expected, the oxide layer of the central fuel rod simulator is the thickest. If one compares the oxide layers at the two equivalent positions 4 and 6, the oxide layer, at location 6 is much thicker. This means this fuel rod must have been somewhat higher in temperature. A thicker oxide layer was found on this fuel rod simulator 10 mm higher at 76 mm in Figure 65.

Finally Figure 68 shows cross sections from 51, 15 and 7 mm elevations. One recognizes here that at 51 mm only a thin oxide layer has formed. At the two other elevations the temperature was too low for the formation of an oxide layer.

6.3 Interaction between liquid zircaloy and UO_2 and the phases present in the frozen melt

Under high temperature conditions, UO_2 is not stable in contact with zircaloy. Zircaloy reduces UO_2 to form oxygen stabilized α-Zr(O) and metallic uranium. The process of UO_2 dissolution has been investigated in detail in separate effect tests by P. Hofmann /3/. Dissolution of the UO_2 by molten zircaloy occurred in test ESBU-1 and the dissolution process is shown in figures 77 and 78. In these figures the molten zircaloy is seen pentrating into cracks at the UO_2 surface. The UO_2 is reduced by the molten zircaloy and forms metallic uranium along the grain boundaries of

the UO_2. When this occurs, UO_2 particles are separated from the solid UO_2 pellet and are dissolved into the melt forming a (U,Zr,O) mixture. As the oxygen concentration increases, the high temperature melt becomes a liquid/solid mixture consisting of molten (U,Zr,O) and $(U,Zr)O_2$ particles. During cooling the melt decomposes into α-Zr(O) and a uranium-rich (U,Zr) alloy.

Figure 78 shows the UO_2 pellet on the right side. On the left side of the region where there was formerly cladding, frozen melt is seen. At the boundary of the pellet small areas which are darker than the UO_2 are visible. The point analysis (1) of one of these areas shows that it is mainly metallic uranium. The oxygen values have the tendency to be to high, due to oxygen contamination of the surface. The matrix (2) of the refrozen melt consists of α-Zry. In this matrix we also find two additional phases, a uranium rich (U,Zr) alloy in (3) and uranium zirconium oxide $(U,Zr)O_2$ in (4).

Along the pellet edge one can see particles which have just separated from the pellet. Figure 77 shows this process, the formation of small UO_2 particles, for different rods at two different elevations.
The distribution of the three different phases in the refrozen melt is shown in Figures 79 to 83. Figure 79 shows the position in the frozen melt where SEM-micrographs were made at three different elevations. The micrographs and the analysis of the phases are given in Figure 80. Once again the matrix is formed of -Zr. The black phase is the uranium rich (U,Zr) alloy and the grey phase is $(U,Zr)O_2$ mixed oxide. At the higher elevations the melt was at high temperature for a longer time and larger inclusions could form. Figures 82 and 83 show SEM-micrographs of the frozen melt at six different positions from cross section 4 at 106 mm elevation. The same three phases are found once again. The "white" α-Zry matrix, the uranium rich (U,Zr) alloy and the $(U,Zr)O_2$ mixed oxide. The uranium rich alloy is only a minor component at this location.

In Figure 88, the results of the point analysis are represented in a (U, Zr,O) diagramm. One sees that the oxides lie in the neighbourhood of the line connecting UO_2 and ZrO_2. The zircaloy rich phase is found in the neighbourhood of the α-Zr(O). The uranium rich alloy has an unexpectedly high oxygen content. It appears that for this phase the measurement was influenced strongly by oxygen contamination of the surface.

6.4 Dissolution of oxidized cladding by the melt

During the initial escalation to high temperature, the cladding in the high temperature zone reacted with the inlet steam forming a thick layer of ZrO_2. Figures 69 to 76 and figure 87 show the interaction of the ZrO2 with the UO_2-Zircaloy melt. In Figure 69, fragments of oxidized cladding pieces from the four rods labeled A,B, C and D can be seen. These pieces were oxidized during the initial heating and then covered by the molten zircaloy-fuel mixture. Enlarged photographs of these pieces are shown in Figures 70 to 71. The photographs in Figures 70 to 71 were made with the microscope and are left right reversed to the cross section shown in Figure 69 which was made with a normal camera. Figure 87 shows a SEM picture of a region of rod A where a microprobe analysis was made and the positions are marked in this picture by black dots. These are numbered from 1 to 11 starting in the frozen melt close to the UO_2 pellet. The results of the microprobe analysis are shown in the bargraphs. In the region of the of the oxidized cladding fragments, analyses were made at three points (St7, St8 and St9). The middle white layer of ZrO_2 (St8) is sandwiched on both sides by α-Zry (St7 and St9). It is assumed that the whole region had oxidized to ZrO_{2-x} during the initial phase of the test. When the melt came into contact with the ZrO_2 cladding fragments, reduction of the ZrO_2 back to α-Zr(O) occurred. The reduction started on the inner and outer surfaces of the oxidized cladding and progressed toward the middle. The analyses made at points St4, St5 and St6 show the formation of three layers of $(U,Zr)O_2$ mixed oxide next to the α-Zr(O) layer, St7. These three layers were formed of $(Zr,U)O_2$ with a varying ratio of zircaloy to uranium. These layers appear to have precipitated from the melt when the uptake of oxygen increased their melting point. The composition of the melt appears to have changed with time. The minimum value of uranium in the middle layer may be explained by the change of the melt composition due to vertical movement.

The melt in this region which was molten at test temperature, contains two recognizable phases after cooldown: The α-Zry-matrix (St1, St3 and St11) and the $(Zr,U)O_2$ inclusions (St2, St10).

In the enlarged view of the ZrO_2 remnants from rods A, B, C, D in Figures 70 and 71 one can see the attack of the melt on the oxide. These figures clearly show the penetration of the oxide along the cracks. In the light microscope pictures here, the oxide appears darker than the metallic phase.

The attack of the melt on the ZrO_2 can also be clearly seen from the comparison of different locations on the same rods. These locations were selected as they had the same oxidation history, until one of the regions was covered with melt. This is seen in the cross section at 86 mm elevation. The overview of this cross section is given in figure 72. The comparison of 4 rods at this elevation is found in figures 73 to 76. This comparison clearly demonstrates the attack of the melt on the ZrO_2 at the macroscopic scale.

6.5 Oxidation of the melt

Figures 84 to 86 show the SEM pictures from oxidized regions under different conditions. In fig. 84 region 1 from fig. 81 is investigated. This cavity was blocked from above and only stagnant steam was available, which left primarily hydrogen after reaction with the zircaloy. If we start from the right side of Figure 84, the outer layer consists of ZrO_2 (St2) with some α-Zry incursions (St1).

On the inner side of this ZrO_2 layer a three fold layered structure of $(Zr,U)O_2$ (St2, 3, 4, 5) has precipitated. This layer solidified at the test temperature. The next layer, a mixture of α-Zry (St6) and $(U,Zr)O_2$ (St7) formed during cooldown. The final layer next to the UO_2-pellet is formed of α-Zry and ZrO_2.

Figure 85 shows the oxidation of melt which is separated from the steam flow by an oxide layer which formed during the initial heatup. Figure 85 is the enlargement of area A in Figure 81. On the right side of the figure we find the ZrO_2-layer (St1), which formed during the initial heatup. After reaching the melting point of zircaloy the inner part of the

cladding melted and started to dissolve the UO_2 forming a (Zr,U,O) melt. The oxygen diffusing through the ZrO_2 skin increased the oxygen content in the region close to the oxide layer leading to the precipitation of a $(Zr,U)O_2$ layer (St2 and St3) at the test temperature. The layer appears to be homogenous, but the concentration of uranium changes with location.

Between the homogenous layer and the UO_2 pellet we find a region with a fine structured appearance. The analysis of the region (St4 and St5) gives nearly the same oxygen concentration as in the homogenous layer, but the zirconium-concentration is increased and the uranium concentration decreased. It is assumed that this layer froze during cooldown.

In Figure 86, a SEM picture of a region between two rods is given where the melt was in direct contact with the steam. The mark (St5) in figure 81 should be somewhat higher. The right side of Figure 86 corresponds to the dark seam at the surface of the steam channels. Analysis points St4 to 8 show that this is a fully oxidized region. This layer appears to have formed at high temperatures during the test. One can recognize a fine structure within this oxide layer. Due to the bright and dark appearance of the components one may assume that a separation of the $(Zr,U)O_2$ into ZrO and UO_2 has taken place. From the phase diagramm of the U,Zr,O system this is expected to occur at equilibrium conditions.

With increasing distance from the steam channel the degree of oxidation decreases. In the region of the positions St1, St2, St3 we find two phases after cooldown: α-Zry with a small U-concentration and $(Zr,U)O_2$. As was discussed early at greater distances from a steam source an additional third phase is found, uranium rich metallic U,Zr-alloy.

7. Acknowledgement

The authors would particularly like to thank Mr. Brand for the picture taking, Mr. Seibert for the preparation of the microscopic pictures and Mrs. Ivanitsch for her careful typing of the manuscript.

8. References

1. A. Fiege, Severe Fuel Damage Investigations of KfK/PNS, KfK 3431B, 1983

2. S. Hagen et.al., CORA-Programm, KfK 3677, 1986

3. P. Hofman et.al., UO_2/Zircaloy-4 Chemical Interactions and Reaction Kinetics, KfK 3552, 1983

4. S. Leistikow, G. Schanz, Zircaloy-4 Oxidation Results 600-1600 °C, OECD-NEA-CSNI/IAEA Specialists Meeting on Water Reactor Fuel Safety, Riso National Laboratory (Denmark), 16-20 May, 1983

5. S. Hagen et.al., Temperature Escalation in PWR Fuel Rod Simulators due to the Zircaloy/Steam Reaction: Tests ESSI 1-3, Test Results Report, KfK 3507, 1983

6. S. Hagen et.al. Temperature Escalation in PWR Fuel Rod Simulators due to the Zircaloy/Steam Reaction: Tests ESSI 4-11, Test Results Report, KfK 3557, 1985

7. S. Hagen, Out-of-pile Experiments on the High Temperature Behaviour of Zry-4 Clad Fuel Rods, KfK 3567, 1983

8. S. Hagen et.al., Temperature Escalation in PWR Fuel Rod Bundles due to the Zircaloy/Steam Reaction: Bundle Test ESBU 1, Test Results Report, KfK 3508, 1983

9. S. Hagen et.al., Temperature Escalation in PWR Fuel Rod Bundles due to the Zircaloy/Steam Reaction: Bundle Test ESBU 2A, Test Results Report, KfK 3509, 1984

9. List of Figures

Fig. 1: ESBU-1 axial and radial cross sections and the locations of the two-color pyrometers.

Fig. 2: Temperatures on the central rod (Z). Side rod (N) and shroud (S) 145 mm from the upper end of cladding compared to the electric power input for ESBU-1.

Fig. 2A: Temperatures on the central rod at 50 mm from the lower end (LO) and 25 mm (UPB and UPD) and 145 mm (MI) from the upper end: ESBU-1.

Fig. 3: Bundle ESBU-1 with insulation after the test.

Fig. 4: Four orientations of the ESBU-1 shroud after removal of the insulation.

Fig. 5: 3x3 bundle of ESBU-1 ater removal of the upper part of the shroud.

Fig. 6: Lower region of ESBU-1 after removal of the shroud.

Fig. 7: Appearance of the blocked region of ESBU-1 as seen from below.

Fig. 8: Details of oxide spalling and refrozuen melt of ESBU-1 below blocked region.

Fig. 9: Appearance of the blocked region of ESBU-1 as seen from above.

Fig. 10: Details of blocked region of ESBU-1 showing the refrozen melt from above.

Fig. 11: Enlargement of the blocked region of ESBU-1 illustrating the wetting behaviour of the melt.

Fig. 13: Schematic diagram showing axial elevations of the ESBU-1 cross sections.

Fig. 14: Bundle cross section summary. The following figures give detail.

Fig. 15: Cross sections of ESBU-1 at 129 and 119 mm above the bottom of the bundle.

Fig. 16: Cross sections of ESBU-1 at 116 and 106 mm above the bottom of the bundle.

Fig. 17: Cross sections of ESBU-1 at 96 and 86 mm above the bottom of the bundle.

Fig. 18: Cross sections of ESBU-1 at 76 and 66 mm above the bottom of the bundle.

Fig. 19: Cross sections of ESBU-1 at 51 and 15 mm above the bottom of the bundle.

Fig. 20: Positions of micrographs given in figures 21-67.

Fig. 21: Details of the cross section at 119 mm.

Fig. 22: Details of the cross section at 119 mm.

Fig. 23: Details of the cross section at 119 mm.

Fig. 24: Details of the cross section at 119 mm.

Fig. 25: Details of the cross section at 119 mm.

Fig. 26: Details of the cross section at 119 mm.

Fig. 27: Details of the cross section at 116 mm.

Fig. 28: Details of the cross section at 116 mm.

Fig. 29: Details of the cross section at 116 mm.

Fig. 30: Details of the cross section at 116 mm.

Fig. 31: Details of the cross section at 116 mm.

Fig. 32: Details of the cross section at 106 mm.

Fig. 33: Details of the cross section at 106 mm.

Fig. 34: Details of the cross section at 106 mm.

Fig. 35: Details of the cross section at 106 mm.

Fig. 36: Details of the cross section at 106 mm.

Fig. 37: Details fo the cross section at 106 mm.

Fig. 38: Details of the cross section at 96 mm.

Fig. 39: Details of the cross section at 96 mm.

Fig. 40: Details of the cross section at 96 mm.

Fig. 41: Details of the cross section at 96 mm.

Fig. 42: Details of the cross section at 96 mm.

Fig. 43: Details of the cross section at 96 mm.

Fig. 44: Details of the cross section at 96 mm.

Fig. 45: Details of the cross section at 96 mm.

Fig. 46: Details of the cross section at 96 mm.

Fig. 47: Details of the cross section at 96 mm.

Fig. 48: Details of the cross section at 96 mm.

Fig. 49: Details of the cross section at 96 mm.

Fig. 50: Details of the cross section at 96 mm.

Fig. 51: Details of the cross section at 86 mm.

Fig. 52: Details of the cross section at 86 mm.

Fig. 53: Details of the cross section at 86 mm.

Fig. 54: Details of the cross section at 86 mm.

Fig. 55: Details of the cross section at 86 mm.

Fig. 56: Details of the cross section at 86 mm.

Fig. 57: Details of the cross section at 86 mm.

Fig. 58: Details of the cross section at 86 mm.

Fig. 59: Details of the cross section at 86 mm.

Fig. 60: Details of the cross section at 86 mm.

Fig. 61: Details of the cross section at 86 mm.

Fig. 62: Details of the cross section at 86 mm.

Fig. 63: Details of the cross section at 76 mm.

Fig. 64: Details of the cross section at 76 mm.

Fig. 65: Details of the cross section at 76 mm.

Fig. 66: Details of the cross section at 66 mm.

Fig. 67: Details of the cross section at 66 mm.

Fig. 68: Details of cross sections at 51, 15 and 7 mm at the positions shown.

Fig. 69: Positions of enlarged views of the cross section at 106 mm given in the following figures, ESBU-1.

Fig. 70: Enlarged view of former cladding region A of the cross section at 106 mm above the bottom of the bundle (ESBU-1).

Fig. 70a: Details of former cladding region A in the cross section at 106 mm elevation (ESBU-1).

Fig. 71: Enlarged views of former cladding regions B, C, D of the cross section at 106 mm above the bottom of the bundle (ESBU-1).

Fig. 72: Positions of enlarged views of the cross section at 86 mm for the comparison of surface regions covered and uncovered with melt (ESBU-1).

Fig. 73: Comparison of oxidized parts of cladding from same rod. Melt covered regions (A) and uncovered regions (G) shown from cross section at 86 mm ESBU-1.

Fig. 74: Comparison of oxidized parts of cladding from same rod. Melt covered regions (B) and uncovered regions (E) shown from cross section at 86 mm, ESBU-1.

Fig. 75: Comparison of oxidized parts of cladding from same rod. Melt covered regions (C) and uncovered regions (F) shown from cross section at 86 mm, ESBU-1.

Fig. 76: Comparison of oxidized parts of cladding from same rod. Melt covered regions (D) and uncovered regions (H) shown from cross section at 86 mm, ESBU-1.

Fig. 77: Dissolution of UO_2 by molten zry for different positions of cross sections 2 (119 mm) and 3 (109 mm). (ESBU-1).

Fig. 78: Microprobe results of the phases in the refrozen melt at position 2 in the cross section at 106 mm, uncorrected O-values (ESBU-1).

Fig. 79: Positions of the microprobe analysis of the 3 phases in the refrozen melt for Fig. 80.

Fig. 80: Microprobe analysis of the 3 phases in the refrozen melt for the elevations 3 (116 mm), 9 (51 mm) and 11 (7 mm above the bottom) at the position given in Fig. 79.

Fig. 81: Locations of microprobe investigations from cross section 4 (106 mm) of ESBU-1).

Fig. 82: Microprobe analysis of the 3 phases in the refrozen melt.

Fig. 83: Microprobe analysis of the 3 phases in the refrozen melt.

Fig. 84: Oxidation in stagnant steam.

Fig. 85: Oxidation of cladding in continuous steam flow.

Fig. 86: Oxidation of melt in direct contact with steam.

Fig. 87: Microprobe analysis of remaining oxidized cladding in contact with refrozen melt.

Fig. 88: Summary of compositions found by microprobe measurements at cross section 4 (106 mm) of ESBU-1.

Fig. 89: Position of microsope pictures in the following Fig. 90-93.

Fig. 90: Structure of the refrozen melt for different elevations at the position given in Fig. 89 with a magnification 50x (ESBU-1).

Fig. 91: Structure of the refrozen melt for different elevations at the position given in Fig. 89 with a magnificaiton 100x (ESBU-1).

Fig. 92: Structure of the refrozen melt for different elevations at the position given ing Fig. 89 with a magnification 200x (ESBU-1).

Fig. 93: Structure of the refrozen melt for different elevations at the position given in Fig. 89 with a magnification 500x (ESBU-1).

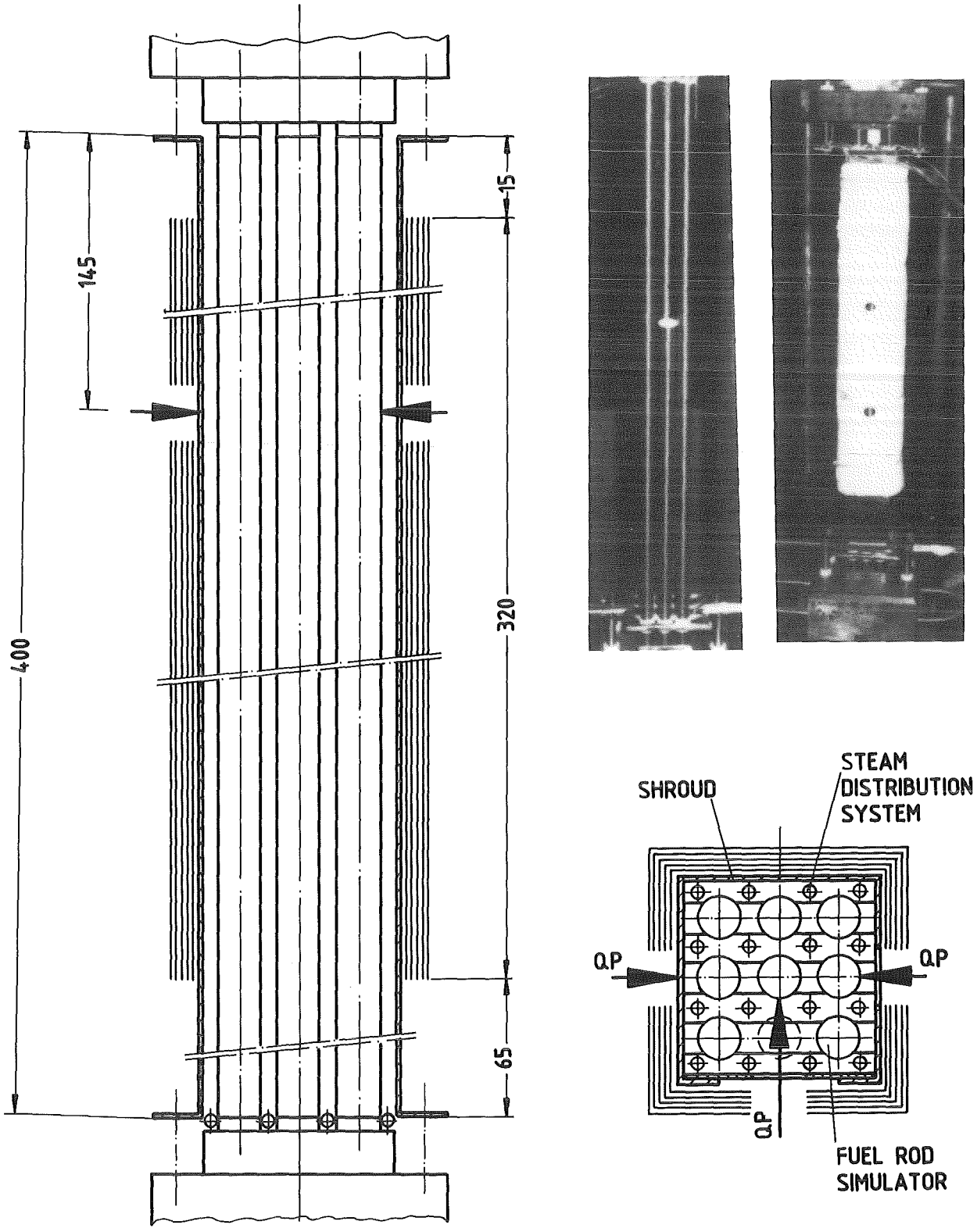

FIGURE 1: ESBU-1 AXIAL AND RADIAL CROSS SECTIONS AND THE LOCATIONS OF THE TWO-COLOR PYROMETERS

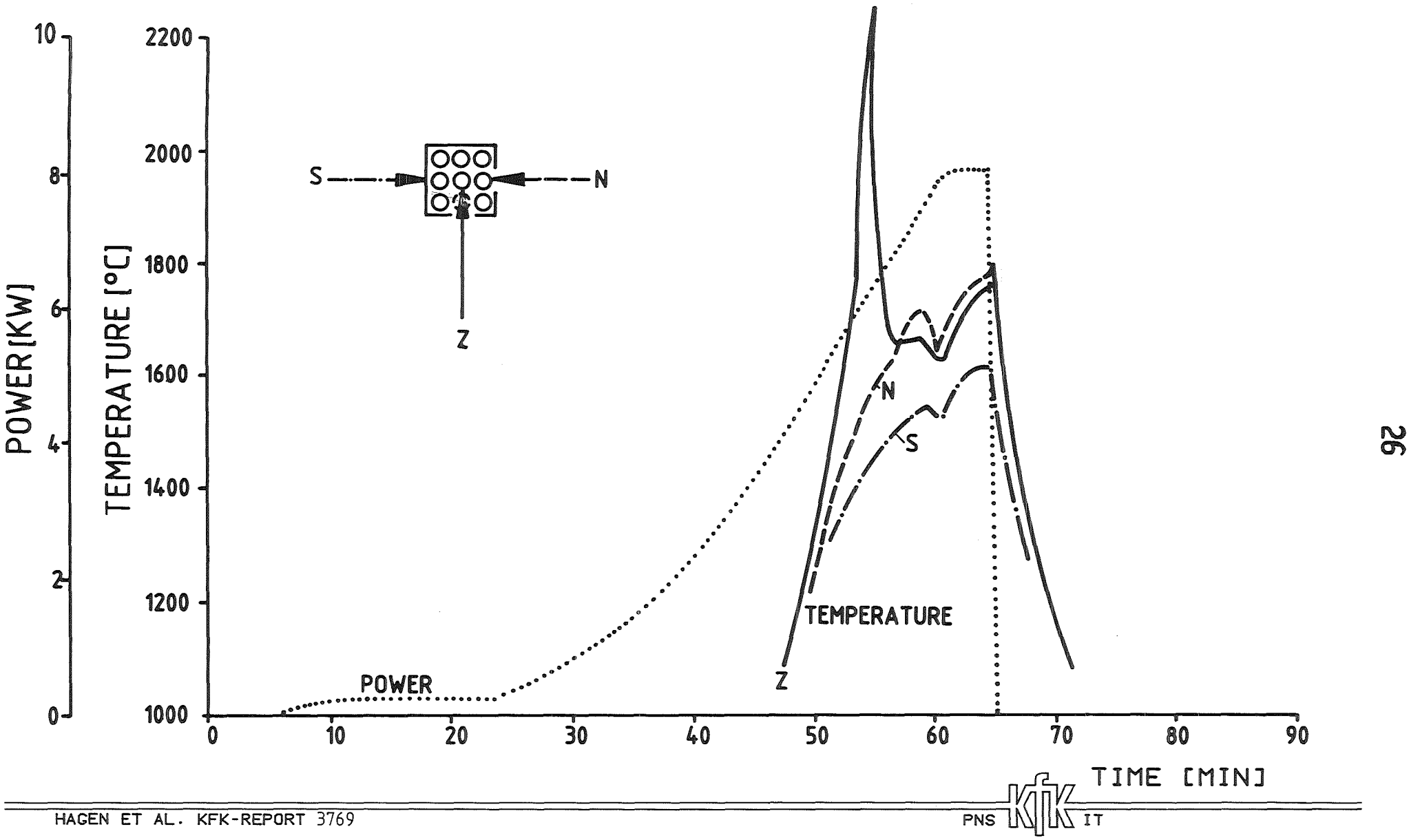

FIG.2 : TEMPERATURES ON THE CENTRAL ROD (Z), SIDE ROD (N) AND SHROUD (S) 145 MM FROM THE UPPER END OF CLADDING COMPARED TO THE ELECTRIC POWER INPUT FOR ESBU-1

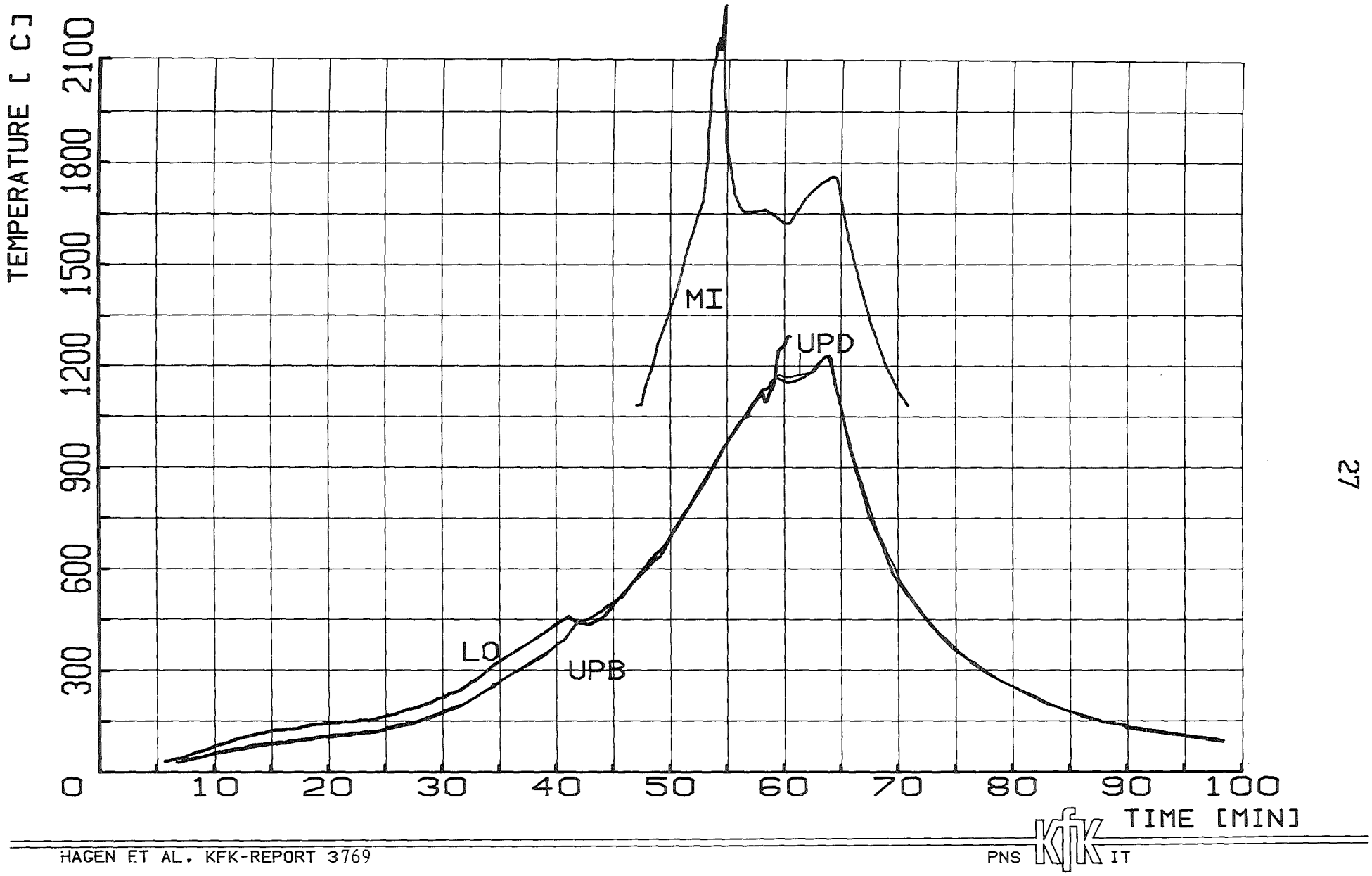

FIG. 2A: TEMPERATURES ON THE CENTRAL ROD AT 50 MM FROM THE LOWER END (LO). AND 25 MM (UPB AND UPD) AND 145 MM (MI) FROM THE UPPER END : ESBU-1

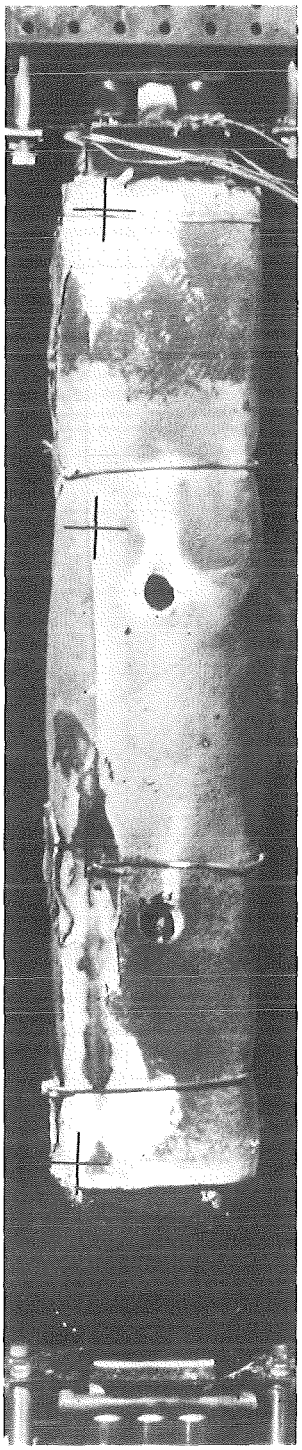

FIGURE 3: BUNDLE ESBU-1 WITH INSULATION AFTER THE TEST

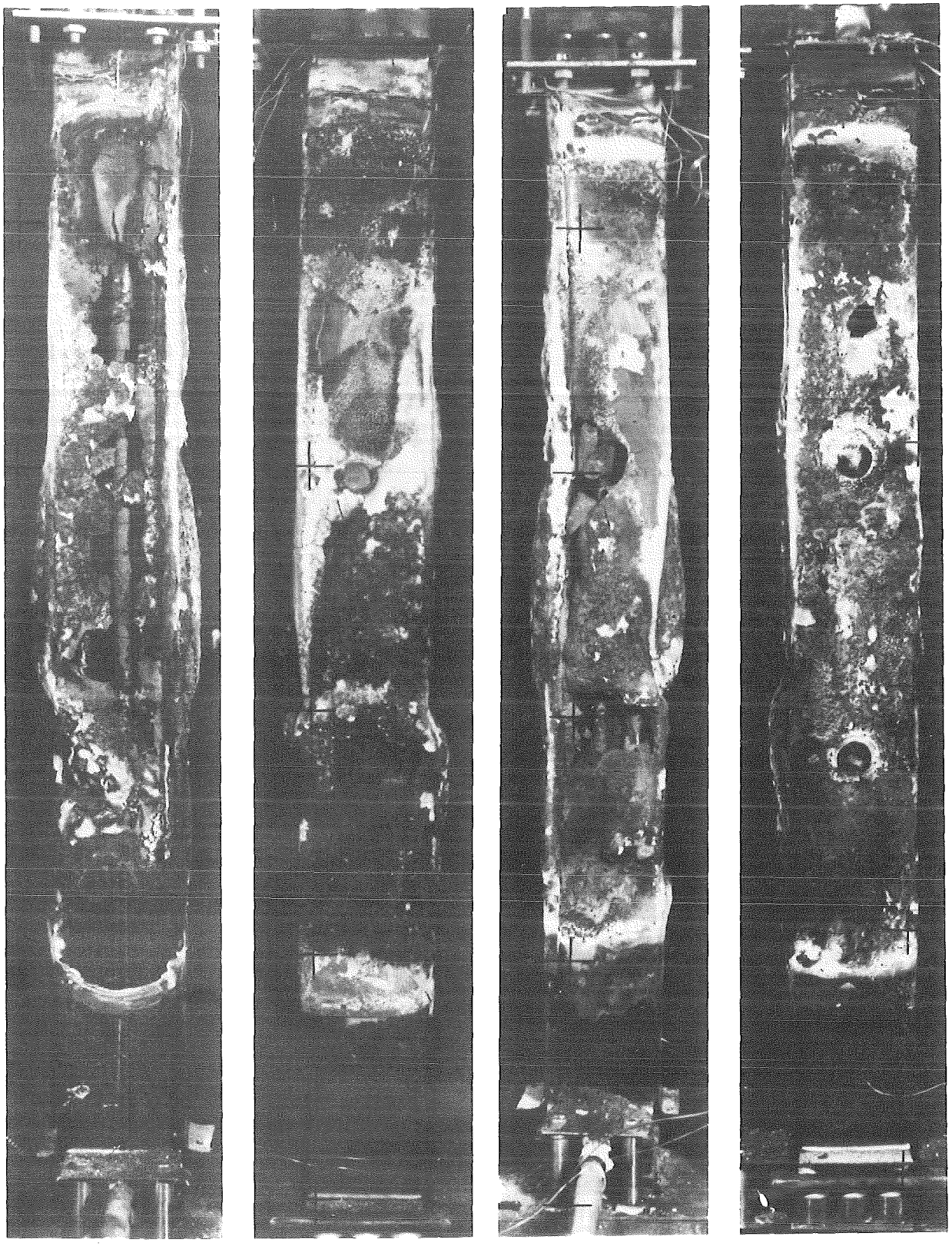

FIGURE 4: FOUR ORIENTATIONS OF THE ESBU-1 SHROUD AFTER REMOVAL OF THE INSULATION

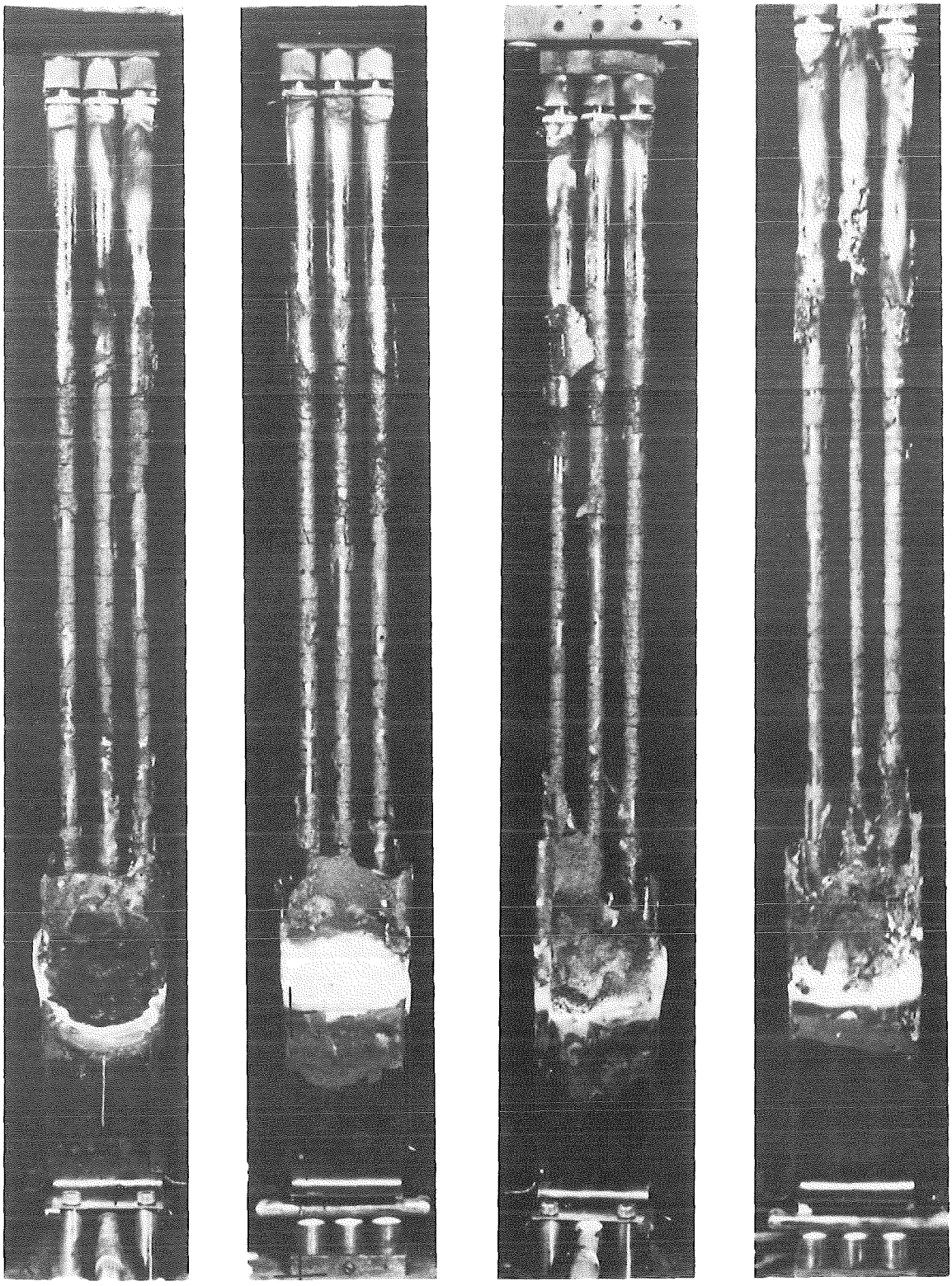

FIGURE 5: 3x3 BUNDLE OF ESBU-1 AFTER REMOVAL OF THE UPPER PART OF THE SHROUD

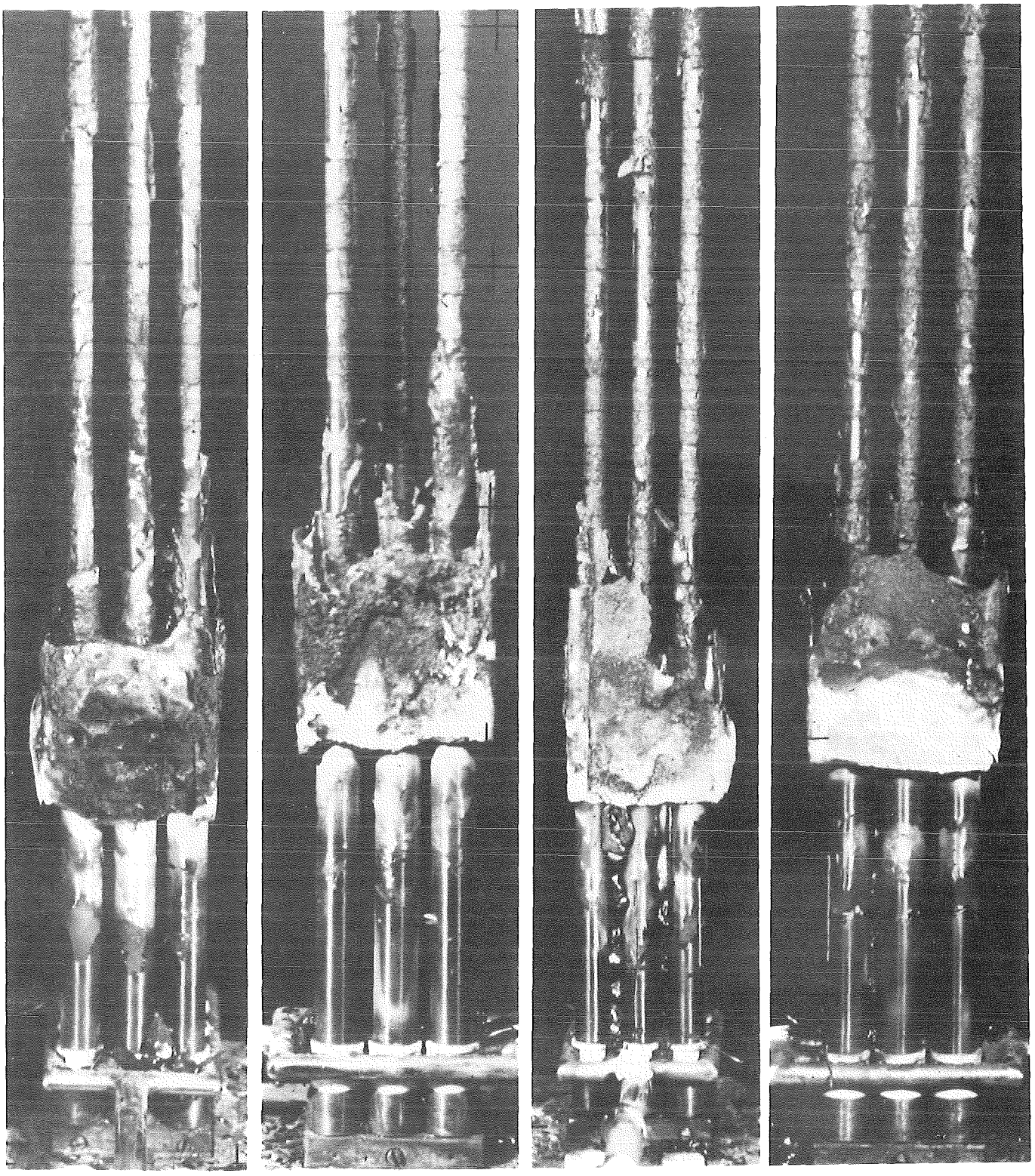

FIGURE 6: LOWER REGION OF ESBU-1 AFTER REMOVAL OF THE SHROUD

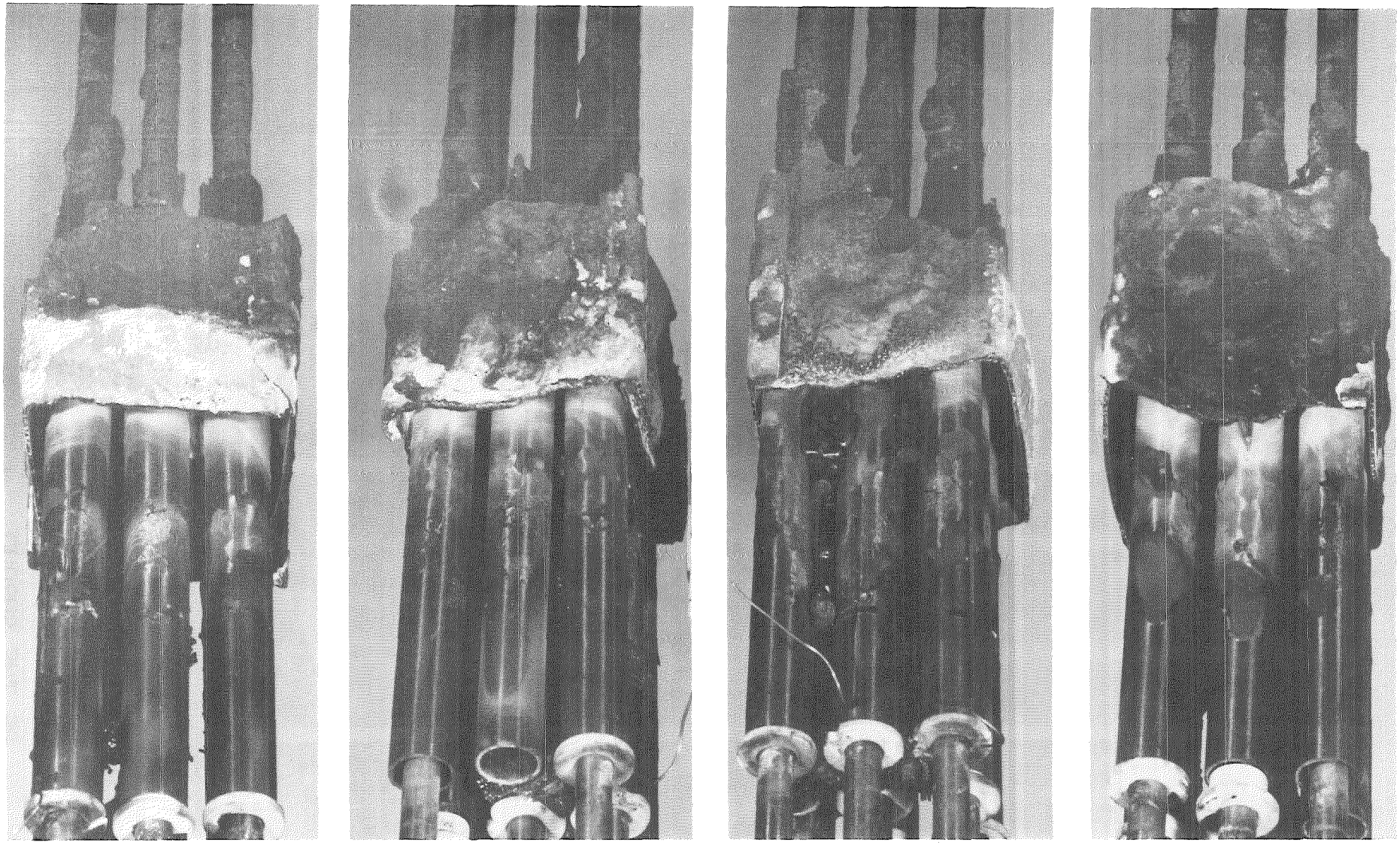

FIGURE 7: APPEARANCE OF THE BLOCKED REGION OF ESBU-1 AS SEEN FROM BELOW

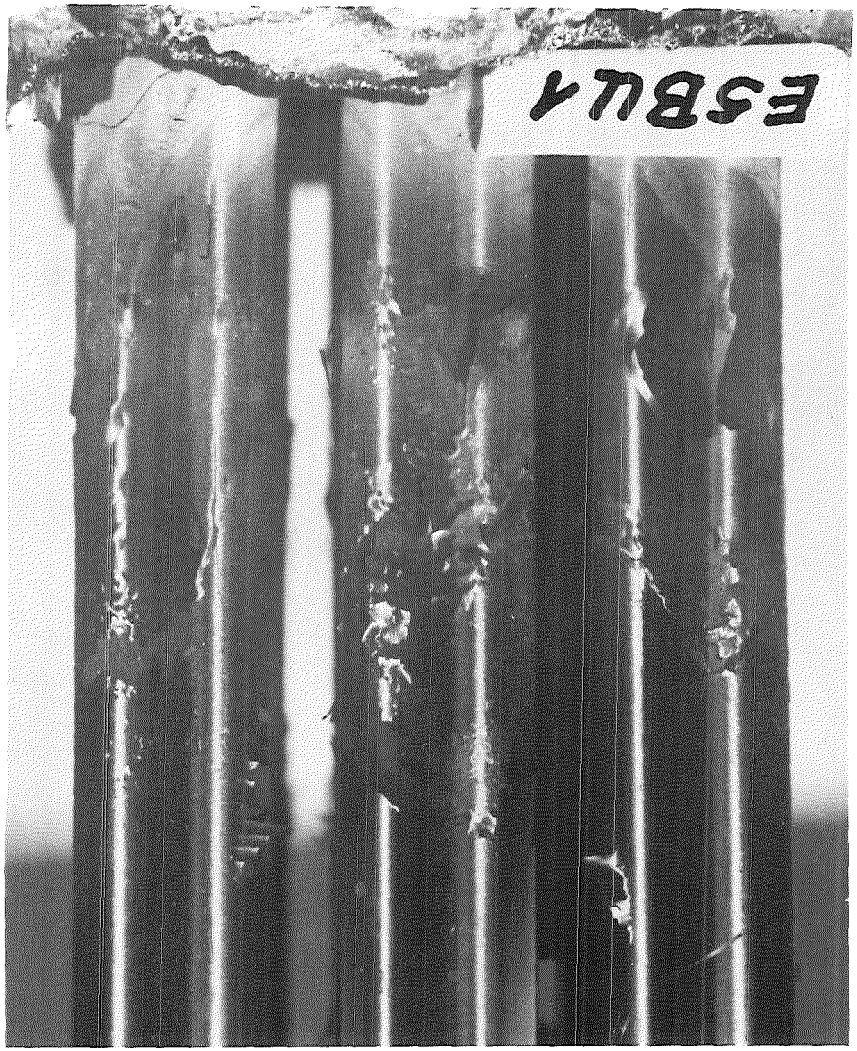

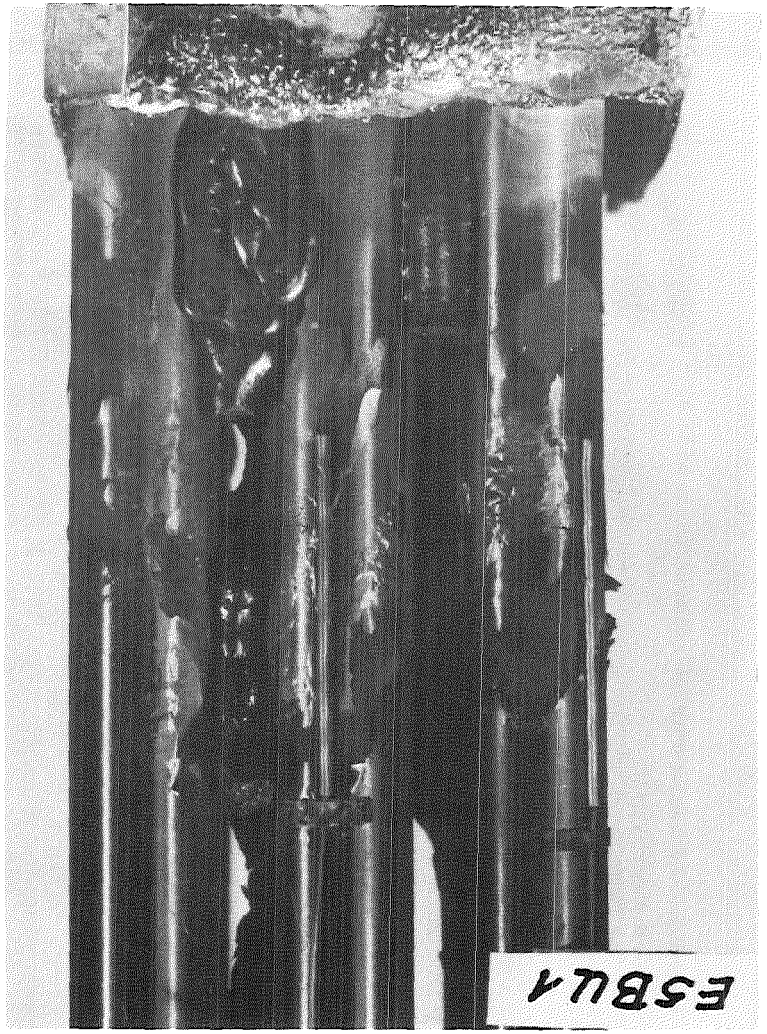

FIGURE 8: DETAILS OF OXIDE SPALLING AND REFROZEN MELT OF ESBU-1 BELOW BLOCKED REGION

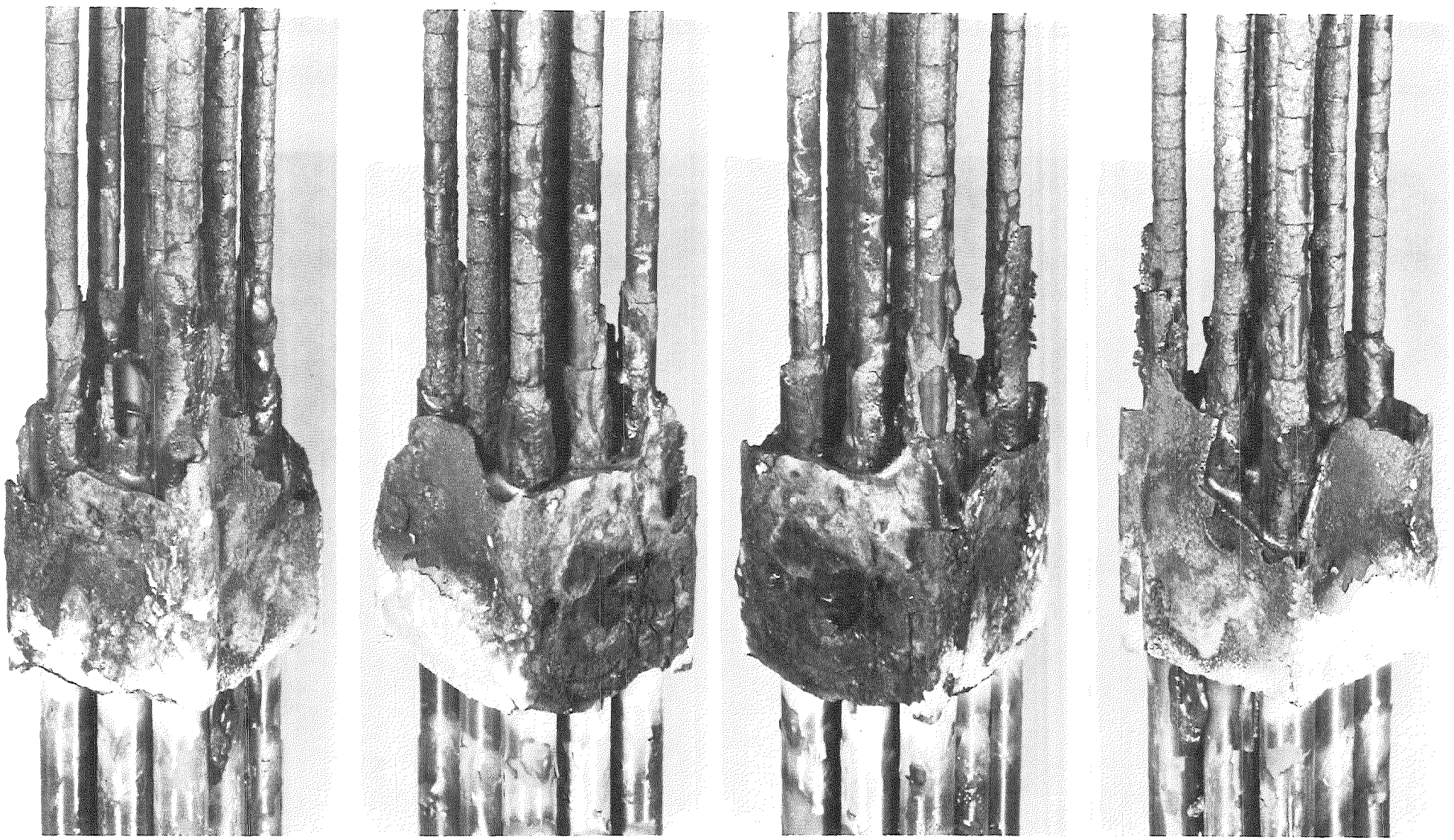

FIGURE 9: APPEARANCE OF THE BLOCKED REGION OF ESBU-1 AS SEEN FROM ABOVE

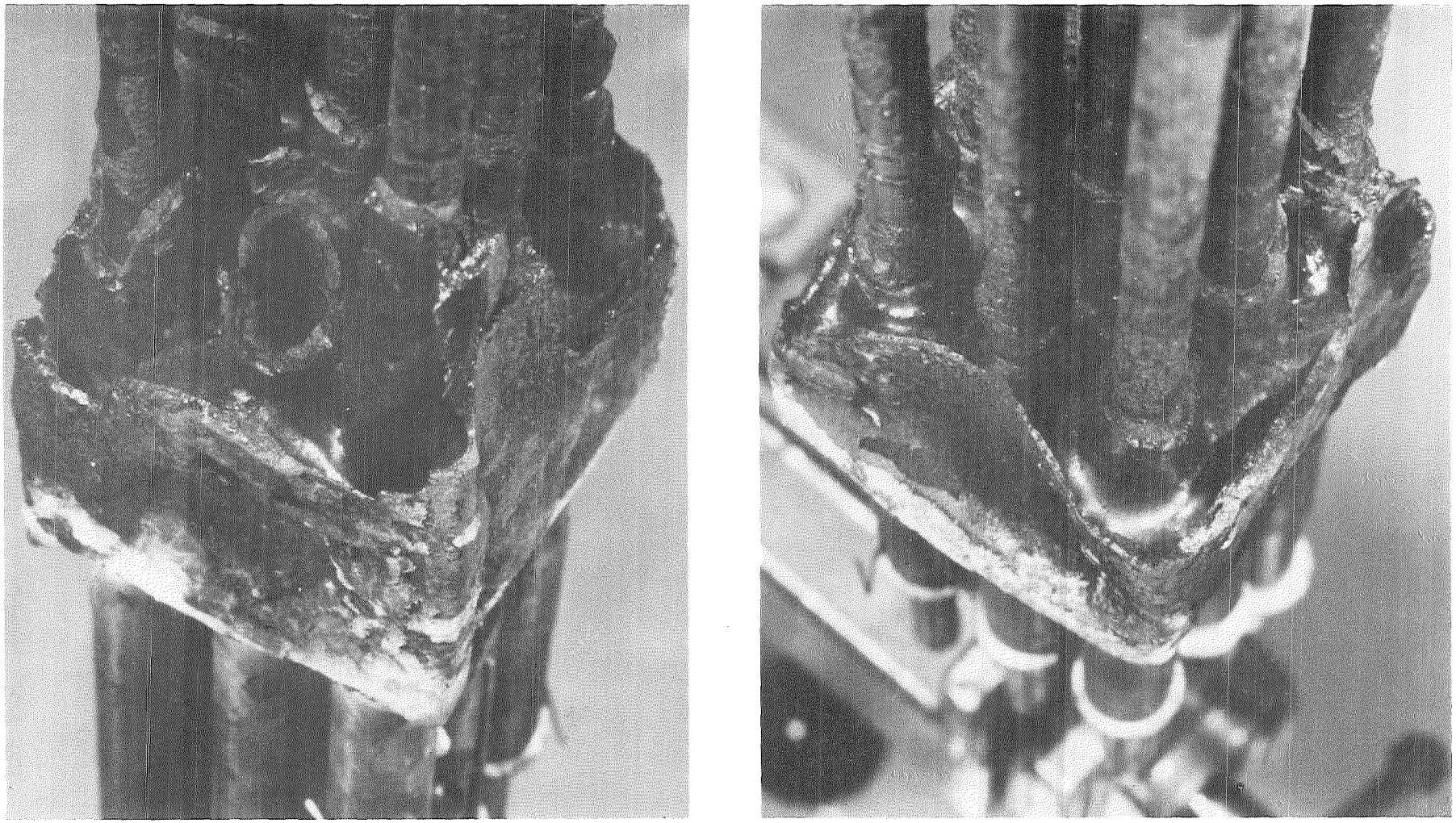

FIGURE 10: DETAILS OF BLOCKED REGION OF ESBU-1 SHOWING THE REFROZEN MELT FROM ABOVE

FIGURE 11: ENLARGEMENT OF THE BLOCKED REGION OF ESBU-1 ILLUSTRATING THE WETTING BEHAVIOR OF THE MELT

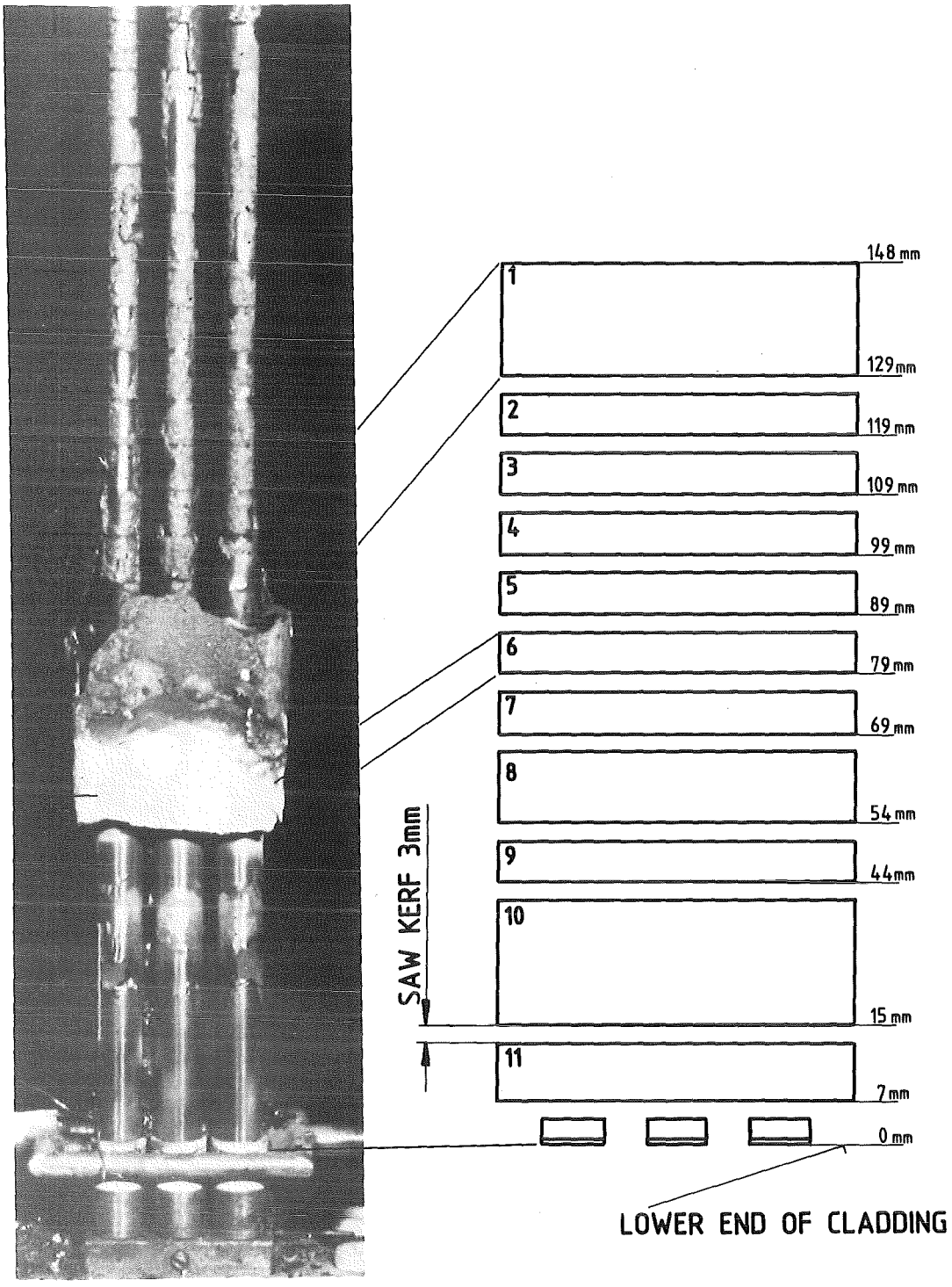

FIGURE 13: SCHEMATIC DIAGRAM SHOWING AXIAL ELEVATIONS OF THE ESBU-1 CROSS SECTIONS.

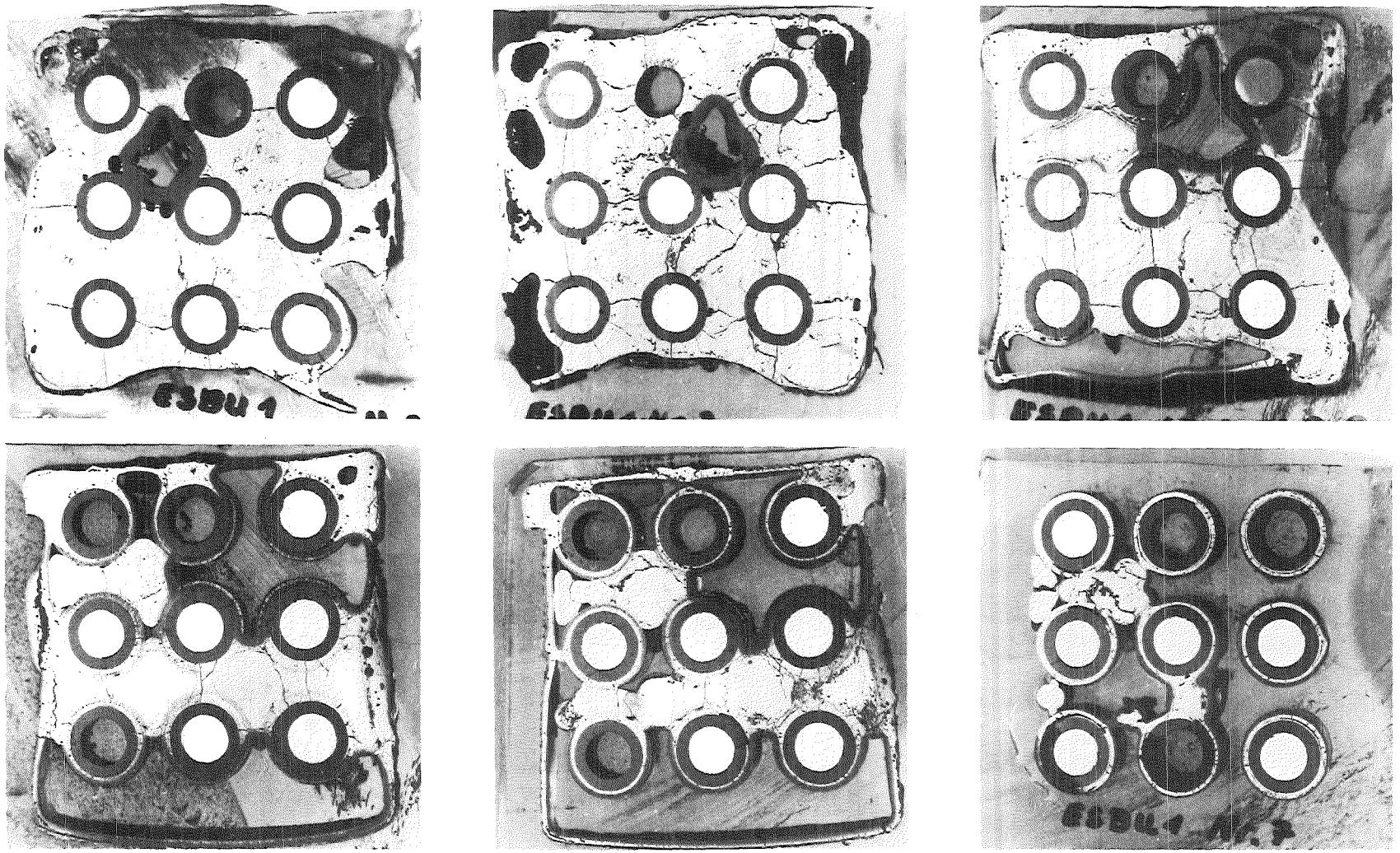

FIGURE 14: BUNDLE CROSS SECTION SUMMARY. THE FOLLOWING FIGURES GIVE DETAIL

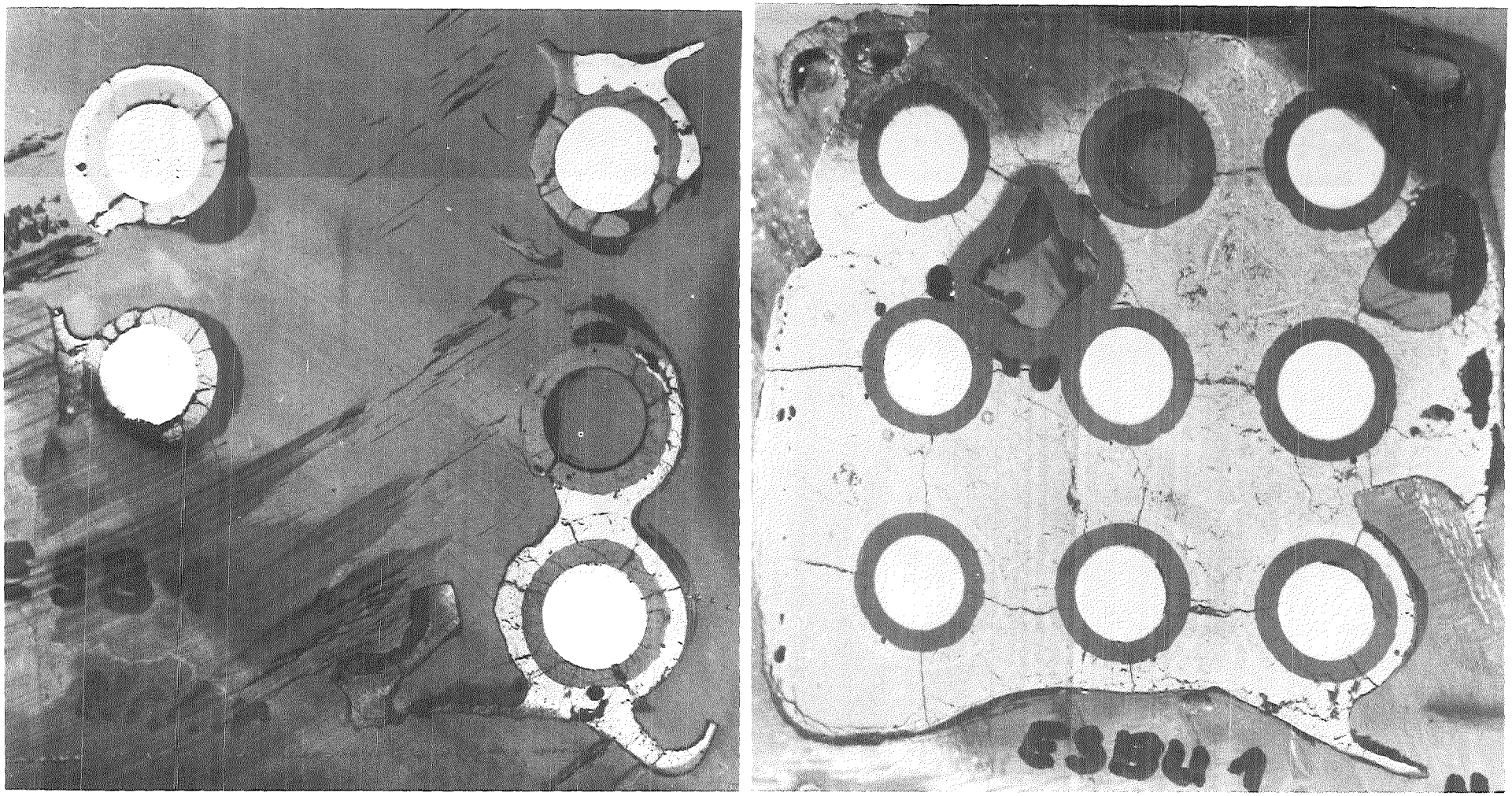

FIGURE 15: CROSS SECTIONS OF ESBU-1 AT 129 AND 119 MM ABOVE THE BOTTOM OF THE BUNDLE

116 mm

106 mm

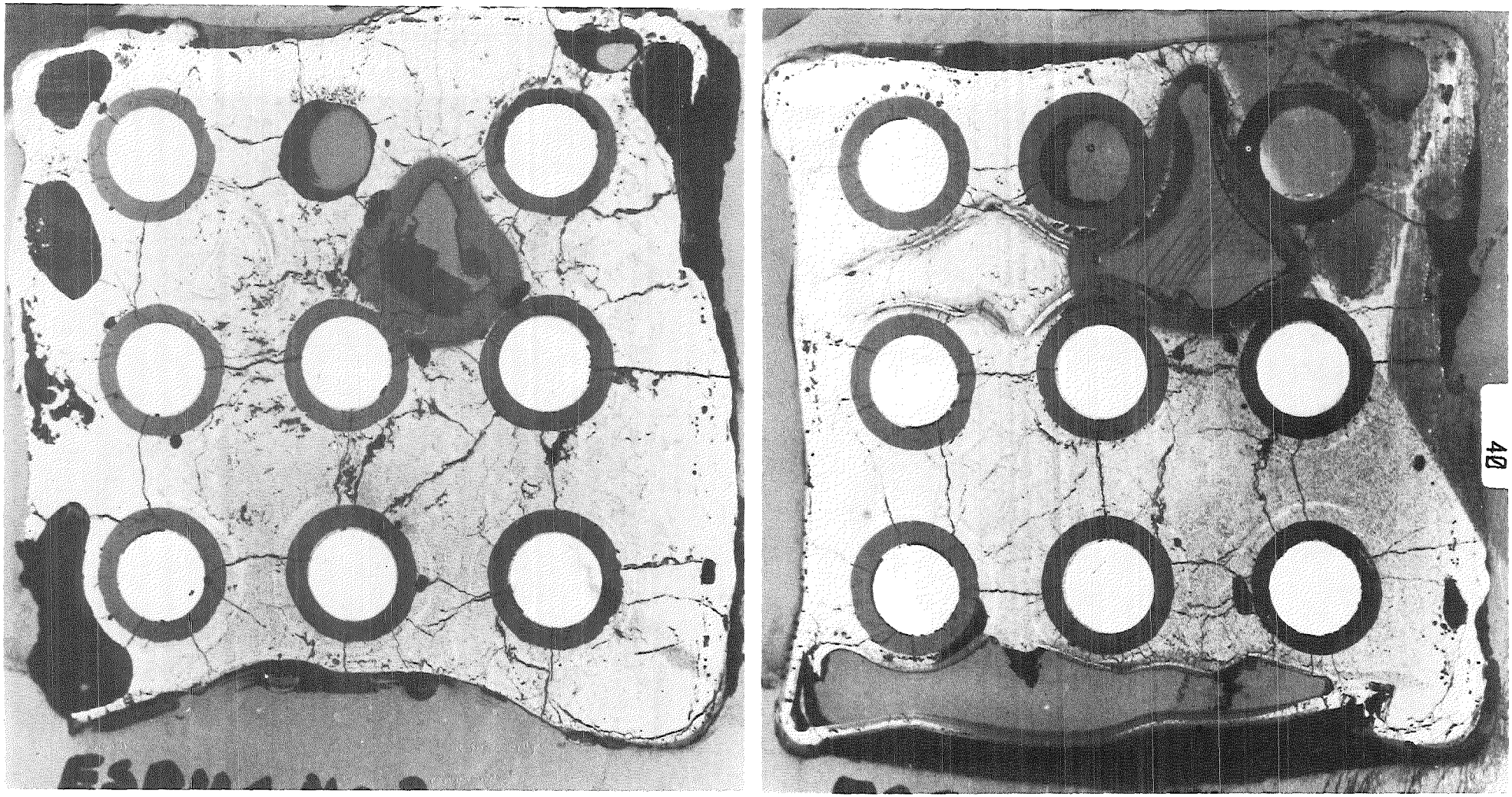

FIGURE 16: CROSS SECTIONS OF ESBU-1 AT 116 AND 106 MM ABOVE THE BOTTOM OF THE BUNDLE

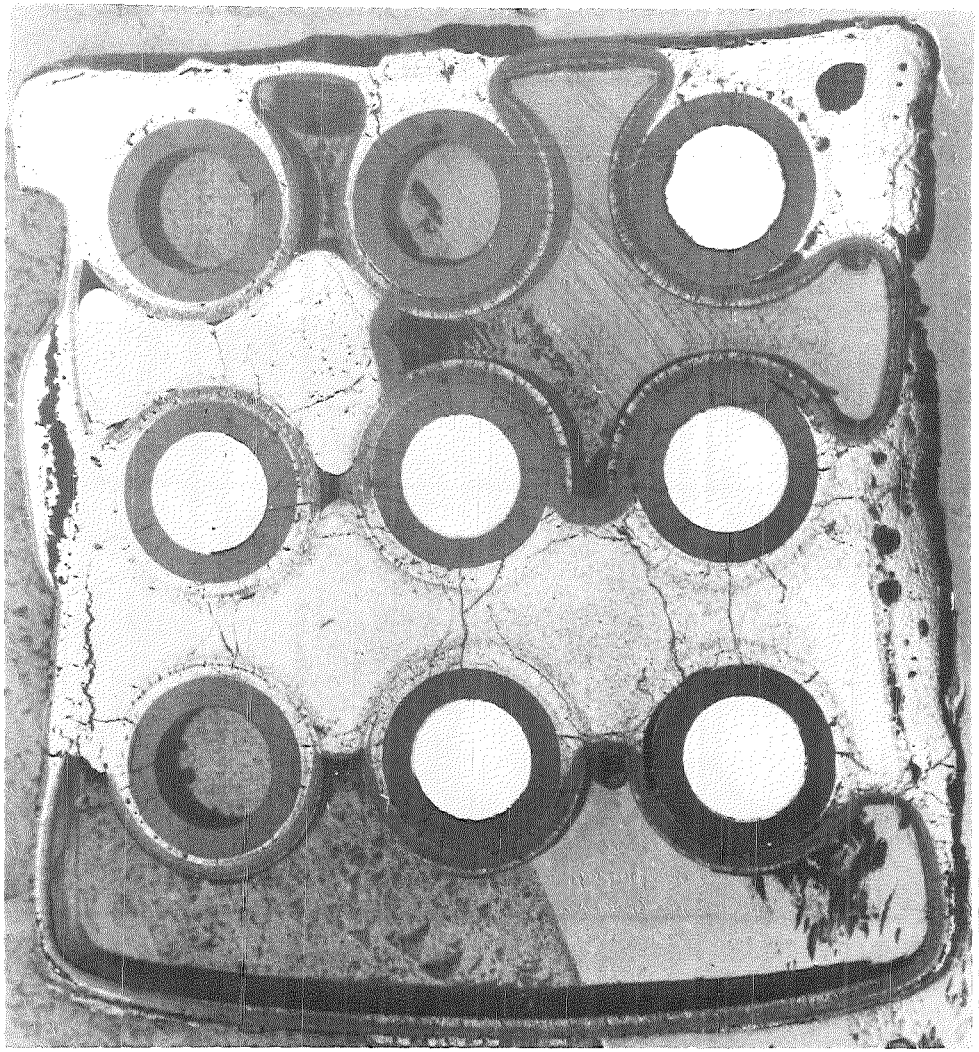

96 mm

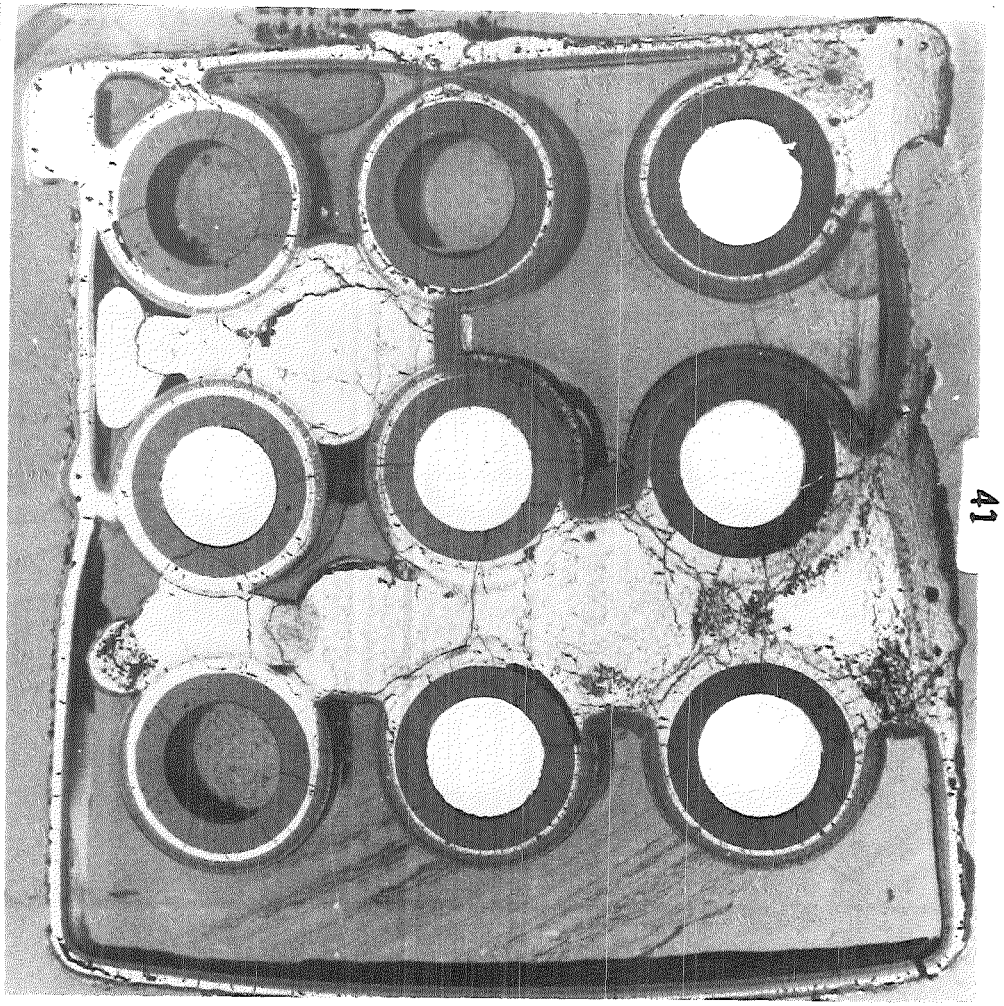

86 mm

FIGURE 17: CROSS SECTIONS OF ESBU-1 AT 96 AND 86 MM ABOVE THE BOTTOM OF THE BUNDLE

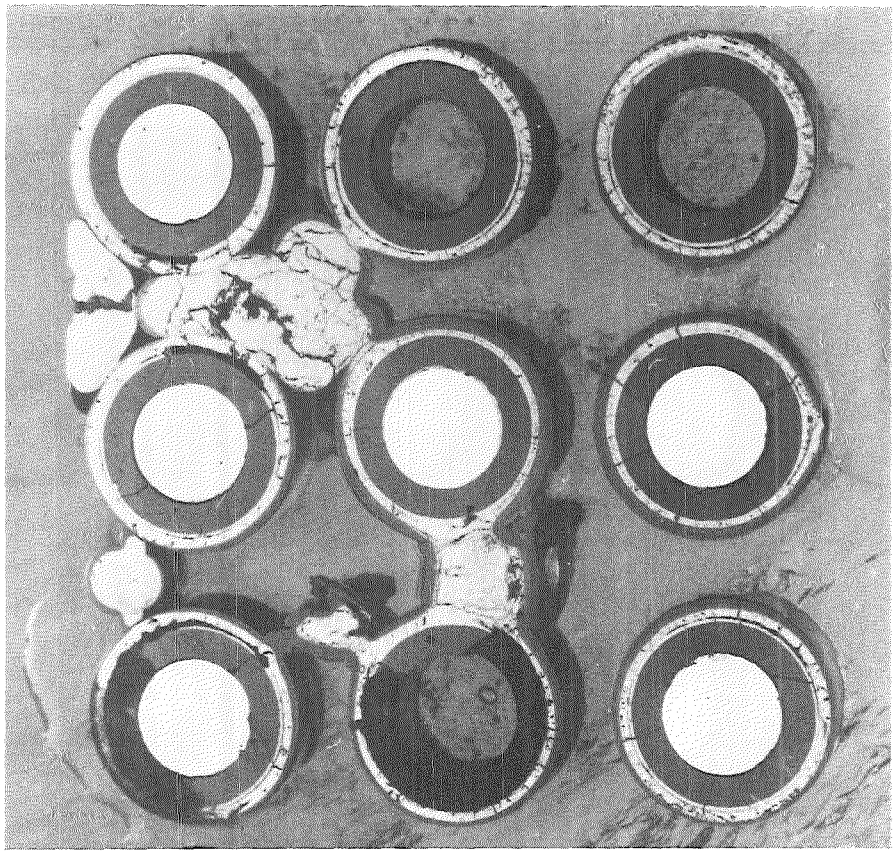

76 mm

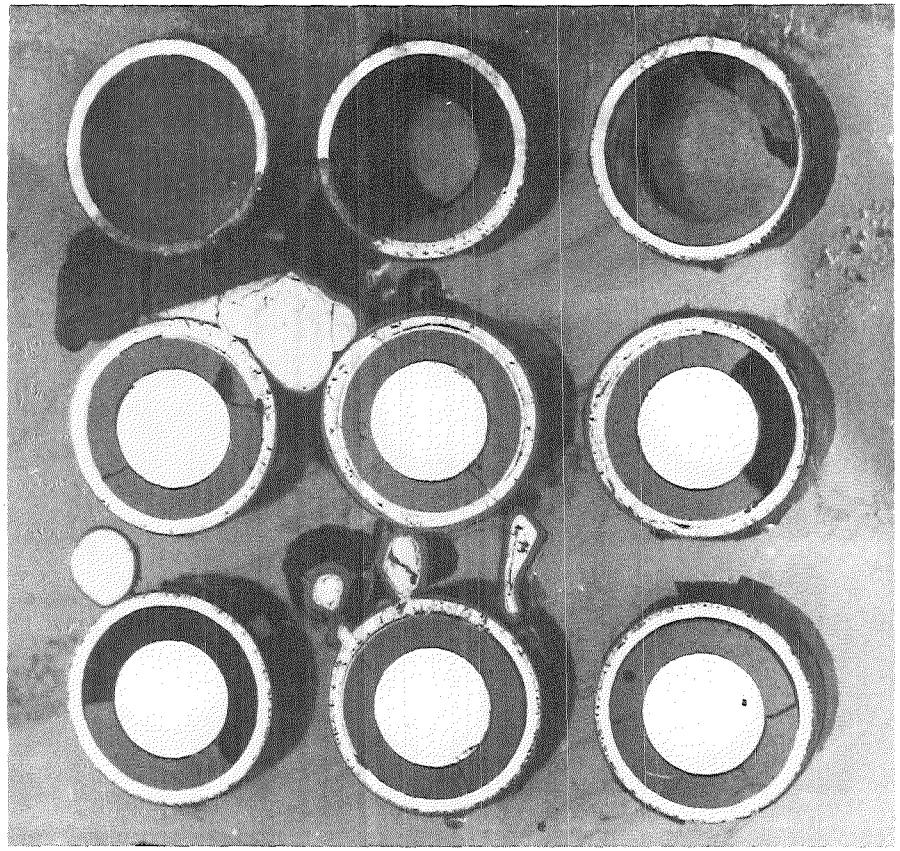

66 mm

FIGURE 18: CROSS SECTIONS OF ESBU-1 AT 76 AND 66 MM ABOVE THE BOTTOM OF THE BUNDLE

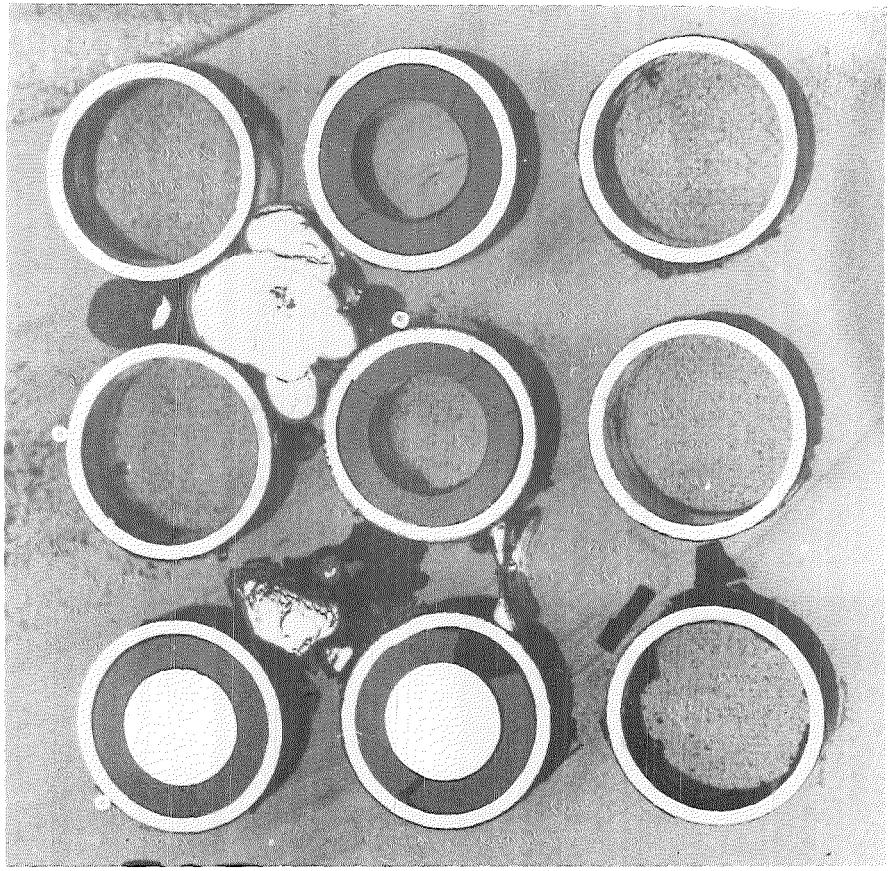

51 mm

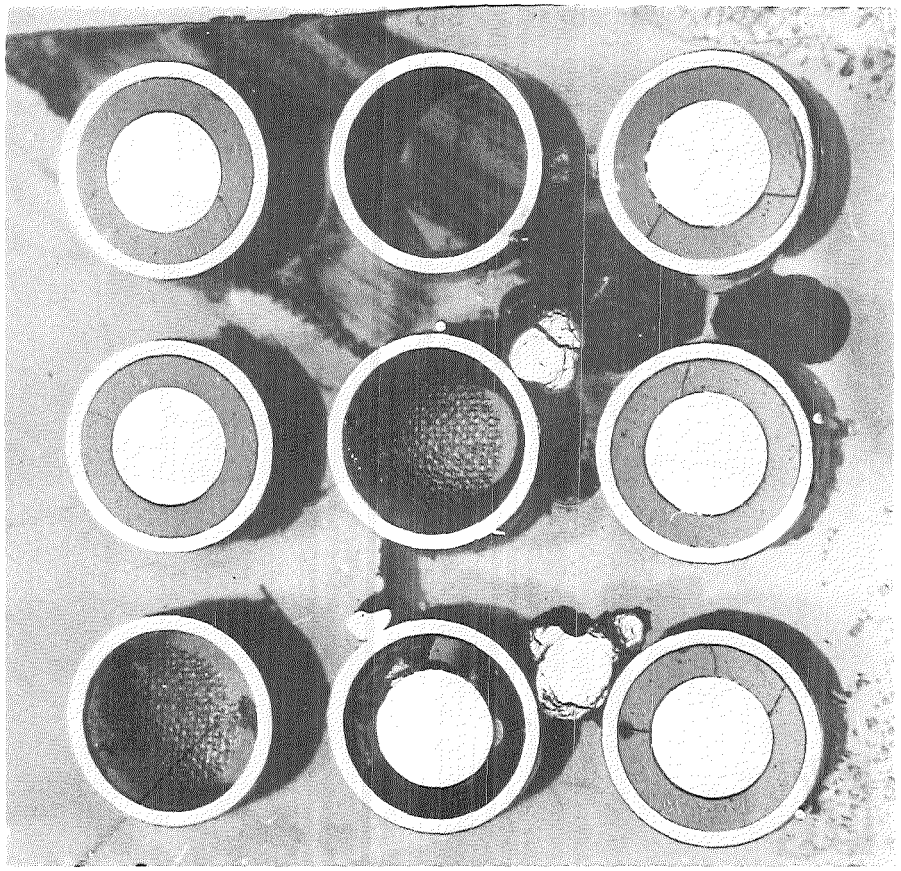

15 mm

FIGURE 19: CROSS SECTIONS OF ESBU-1 AT 51 AND 15 MM ABOVE THE BOTTOM OF THE BUNDLE

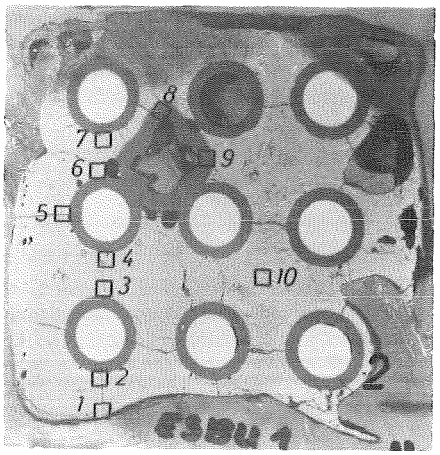

Fig.20 Positions of micro graphs given in figures 21-67.

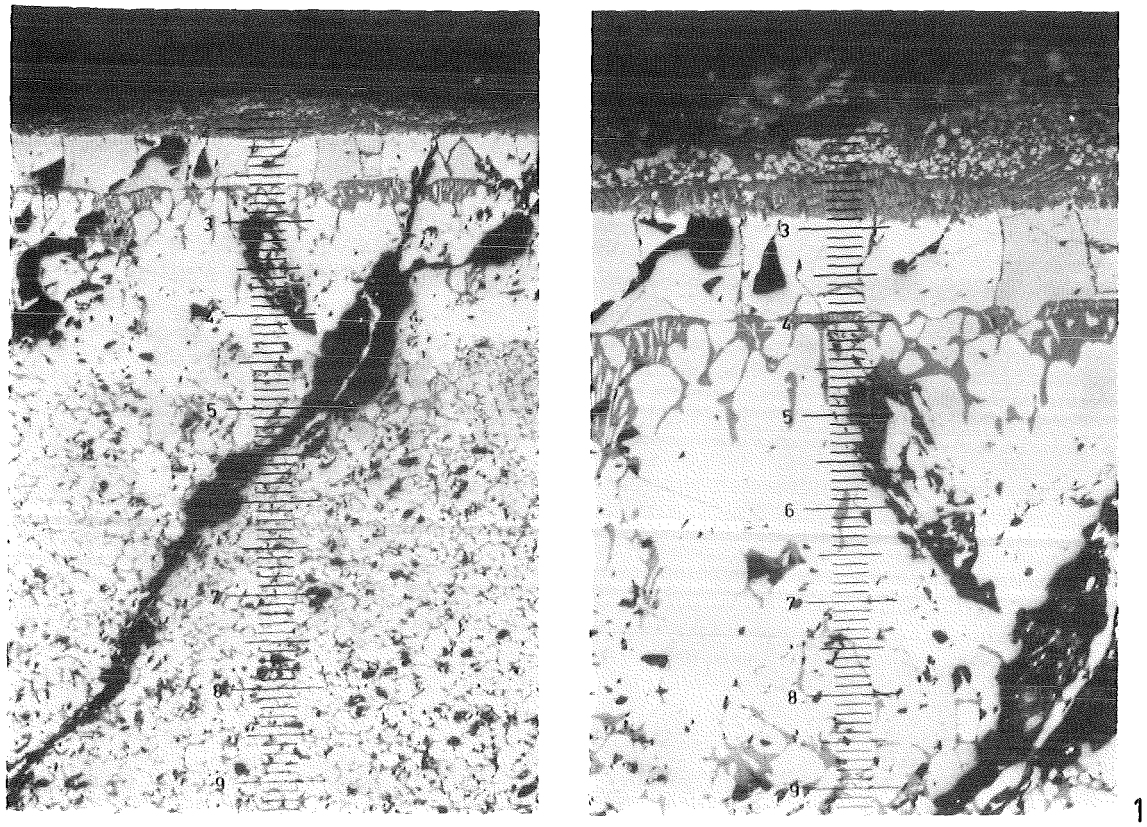

1

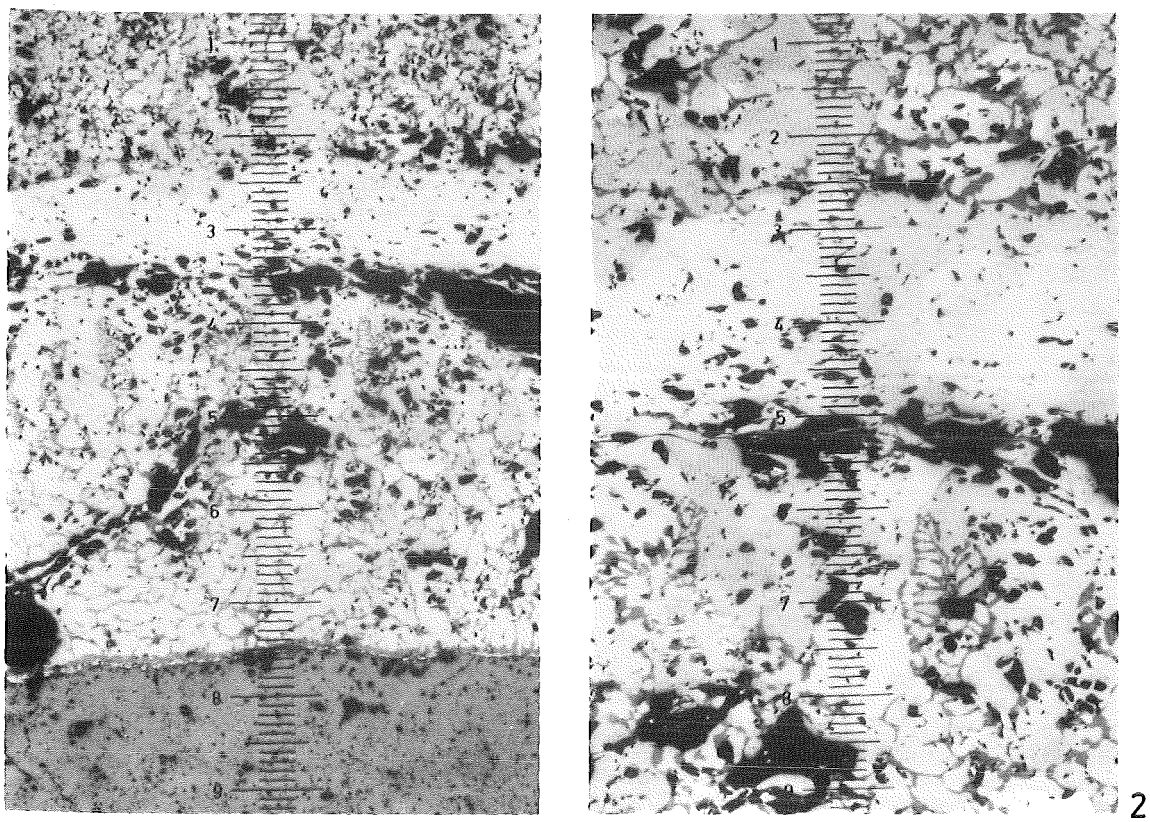

2

50 x

100 x

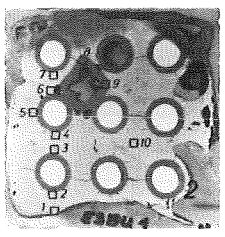

FIG. 21 DETAILS OF THE CROSS SECTION AT 119 MM AT POS. SHOWN IN THE OVERVIEW FIG. 20 (ESBU-1)

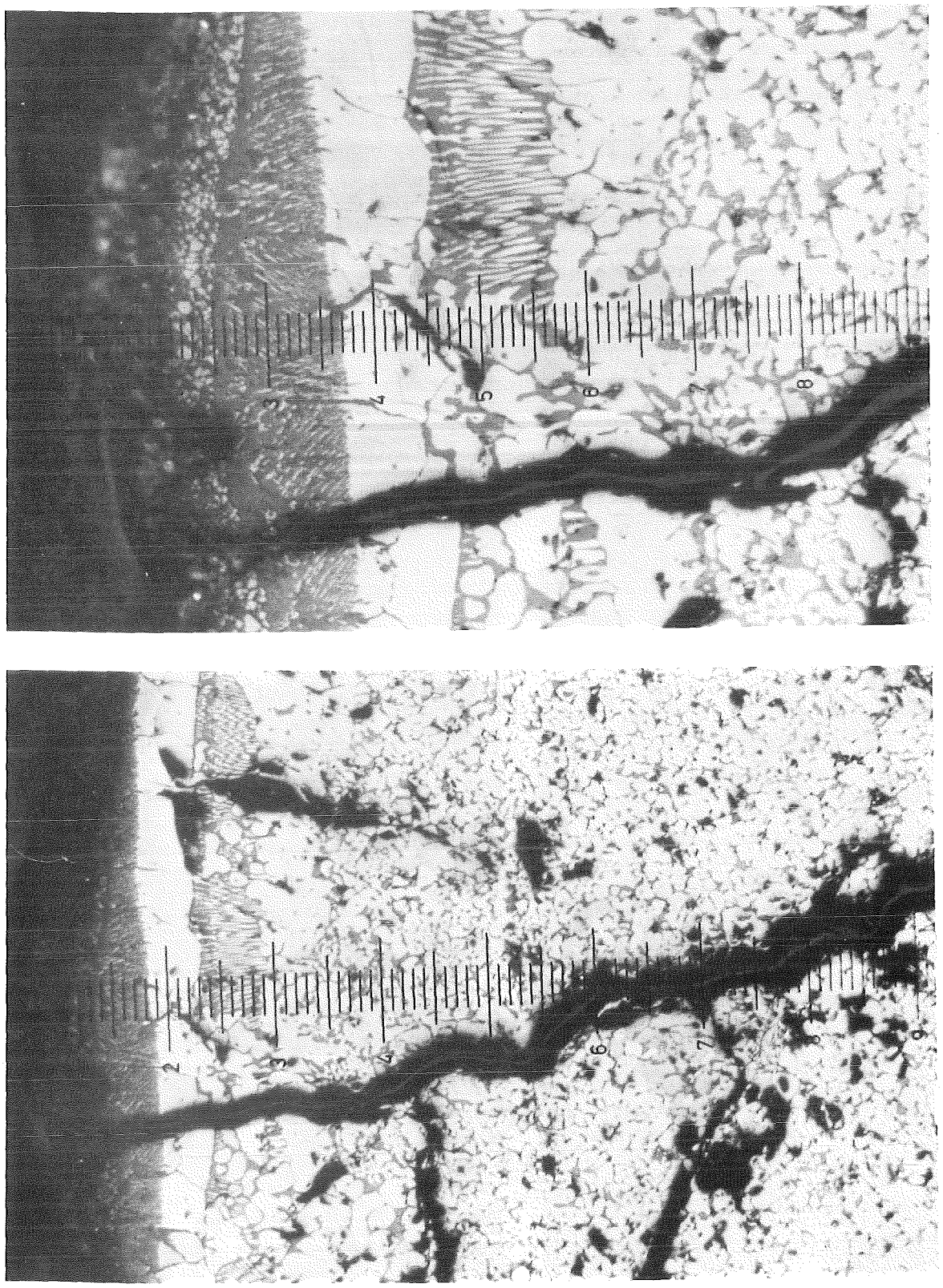

Position 1

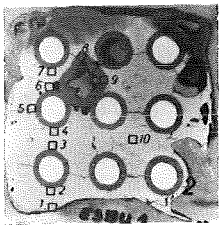

FIG.22 DETAILS OF THE CROSS SECTION AT 119 MM AT POS. SHOWN IN THE OVERVIEW FIG.20 (ESBU-1)

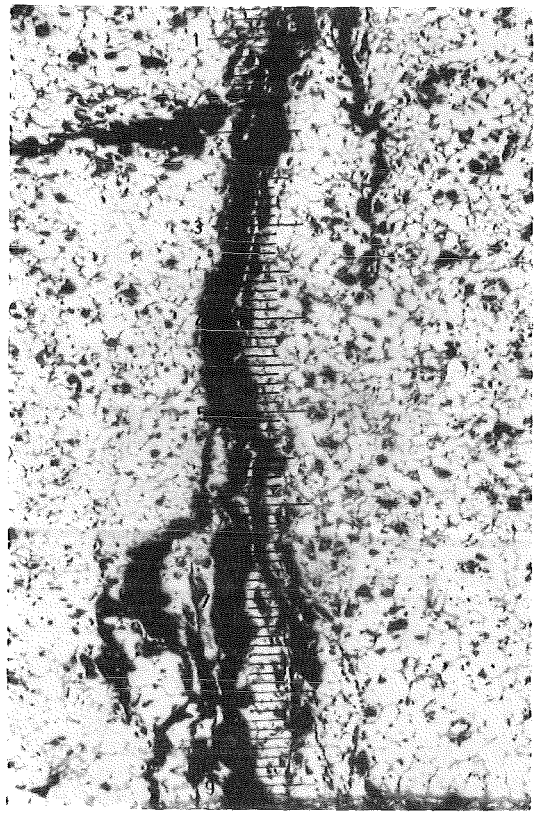

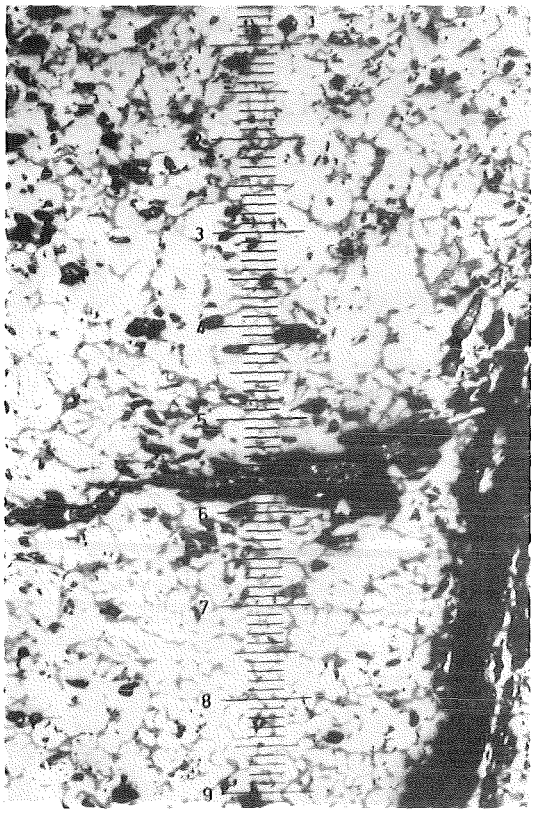

3

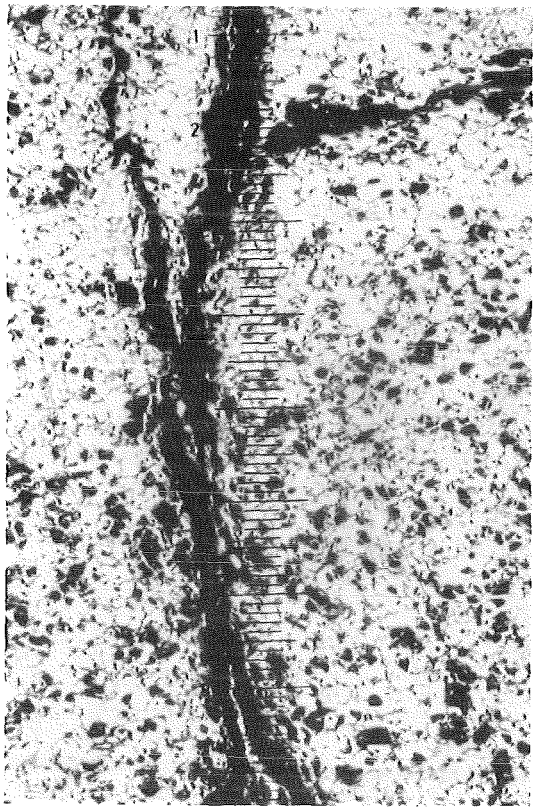

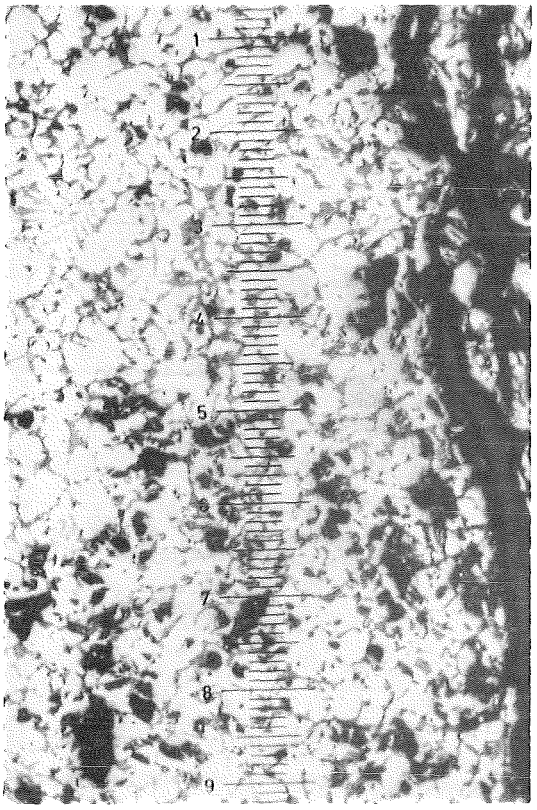

4

50x

100x

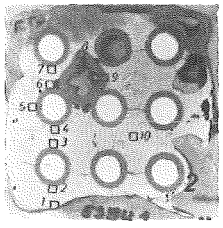

FIG.23 DETAILS OF THE CROSS SECTION AT 119 MM AT POS. SHOWN IN THE OVERVIEW FIG.20 (ESBU-1)

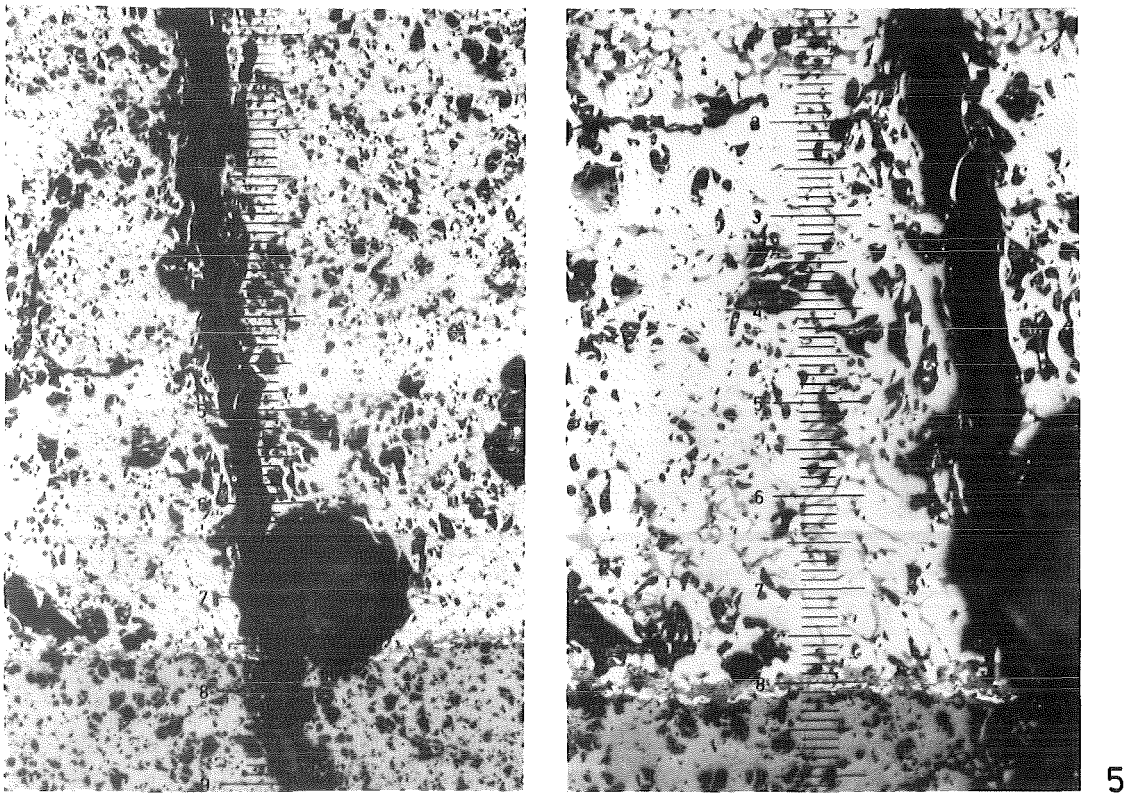

5

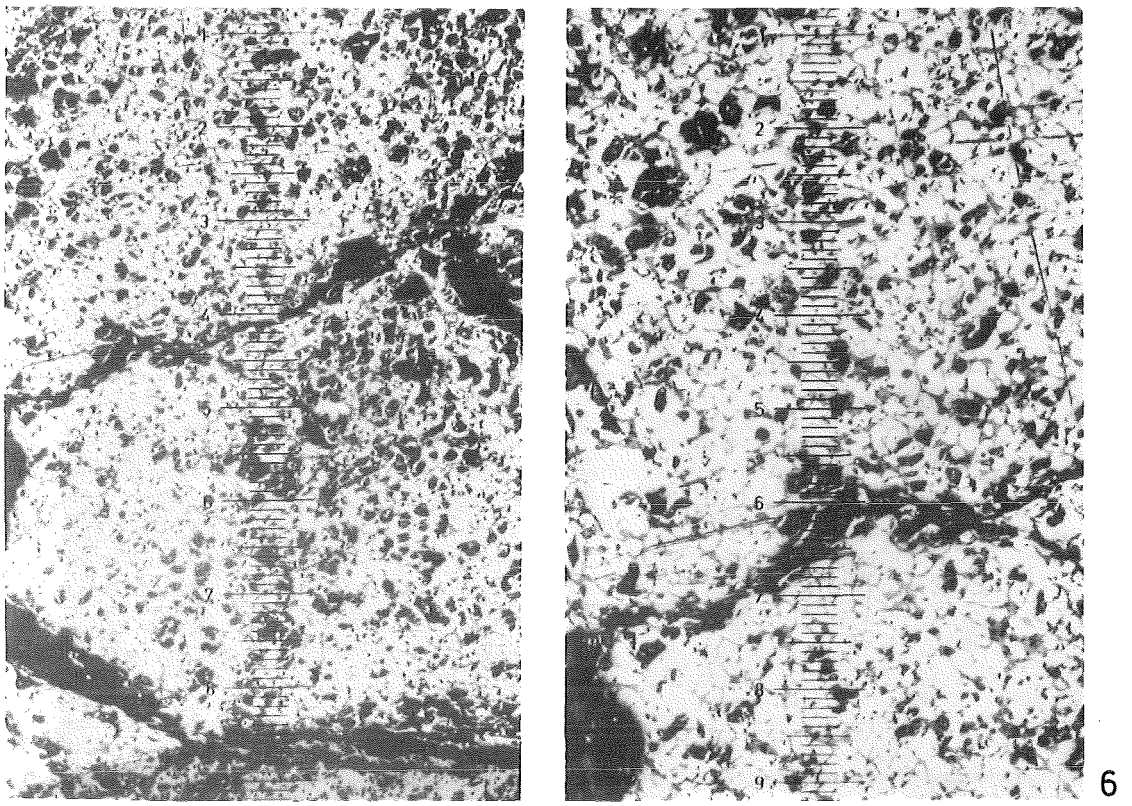

6

50 x

100 x

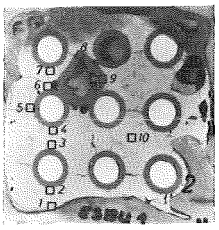

FIG. 24 DETAILS OF THE CROSS SECTION AT 119 MM AT POS. SHOWN IN THE OVERVIEW FIG. 20 (ESBU-1)

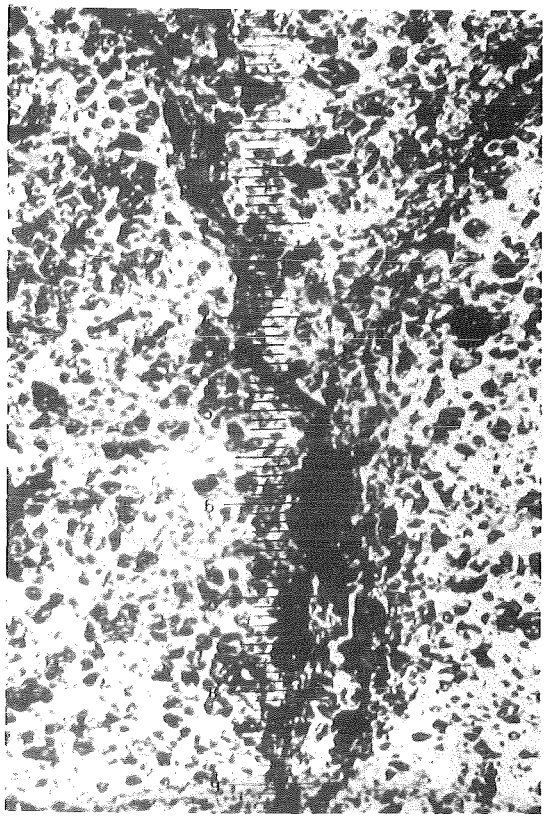

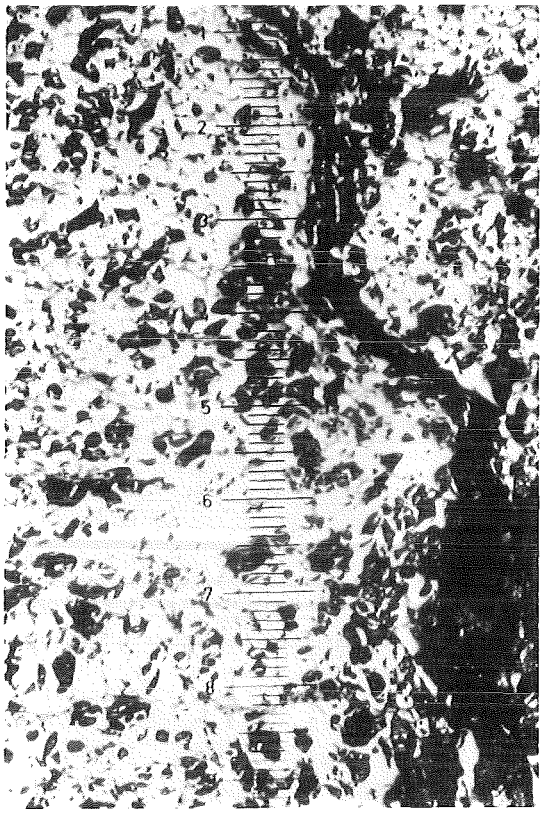

7

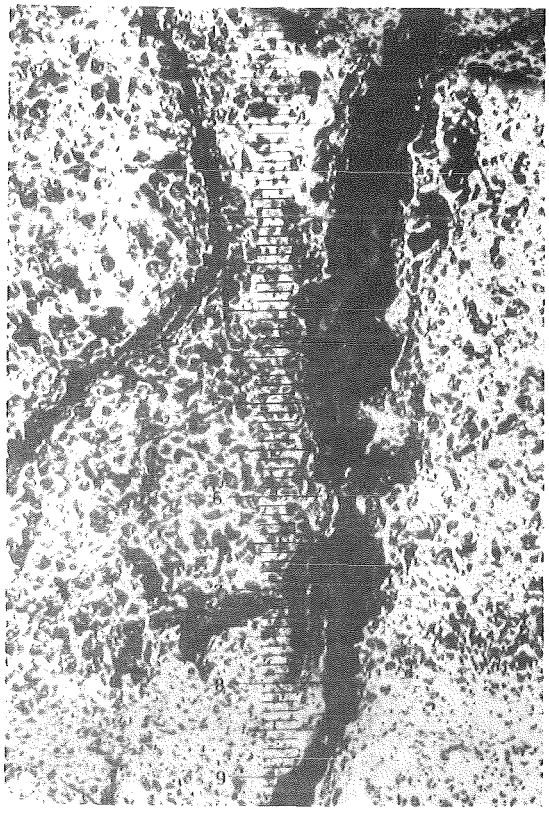

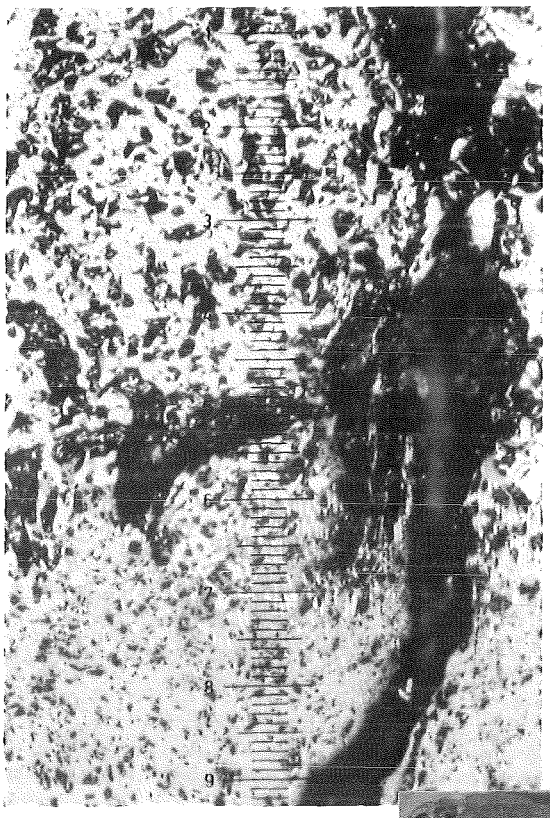

8

50 x

100 x

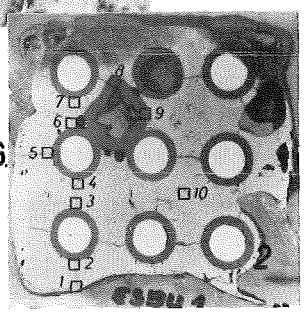

FIG. 25 DETAILS OF THE CROSS SECTION AT 119 MM AT POS. SHOWN IN THE OVERVIEW FIG. 20 (ESBU-1)

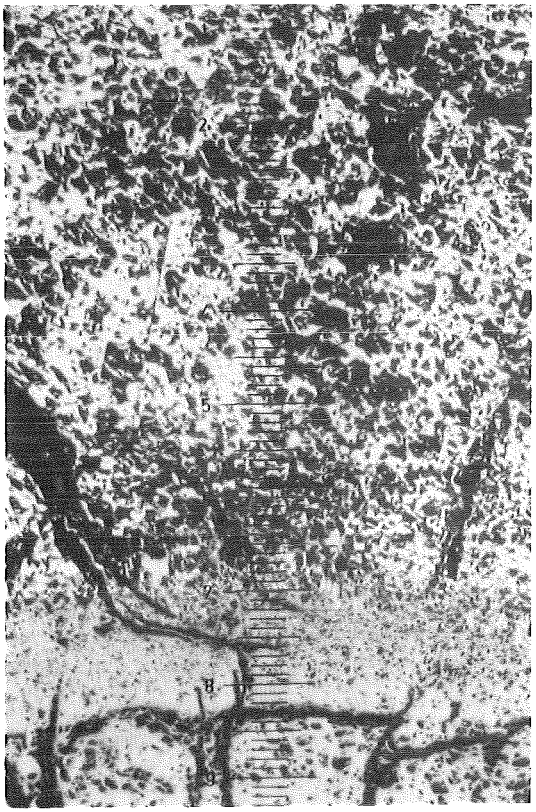

50x

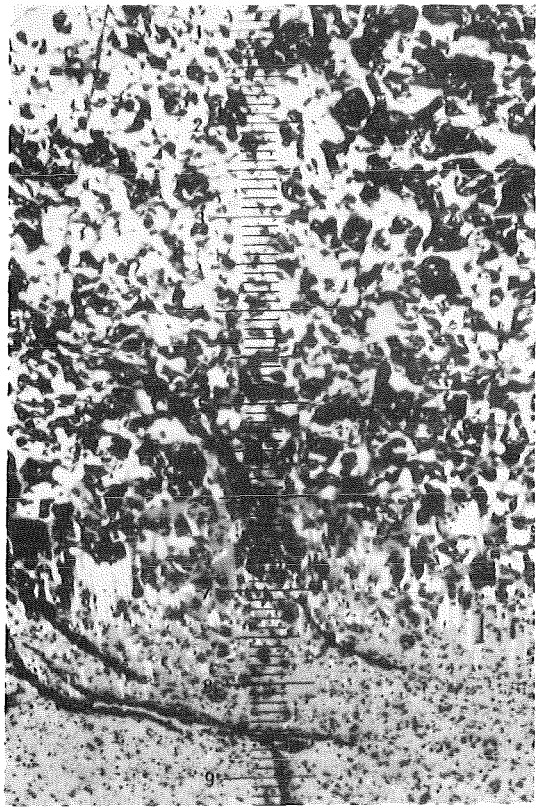

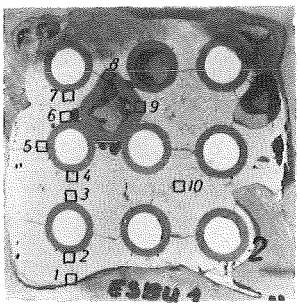

100 x

FIG. 26 DETAILS OF THE CROSS SECTION AT 119 MM AT POSITIONS SHOWN IN THE OVERVIEW FIG. 20 (ESBU-1)

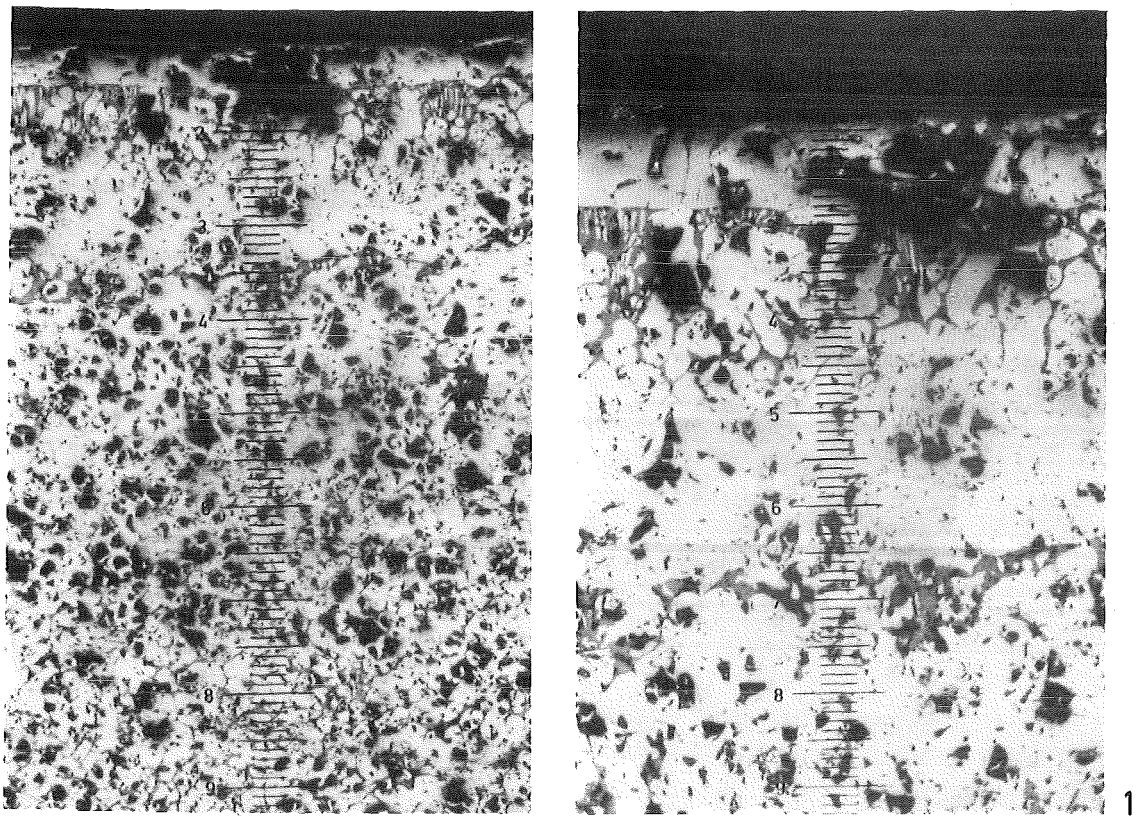

1

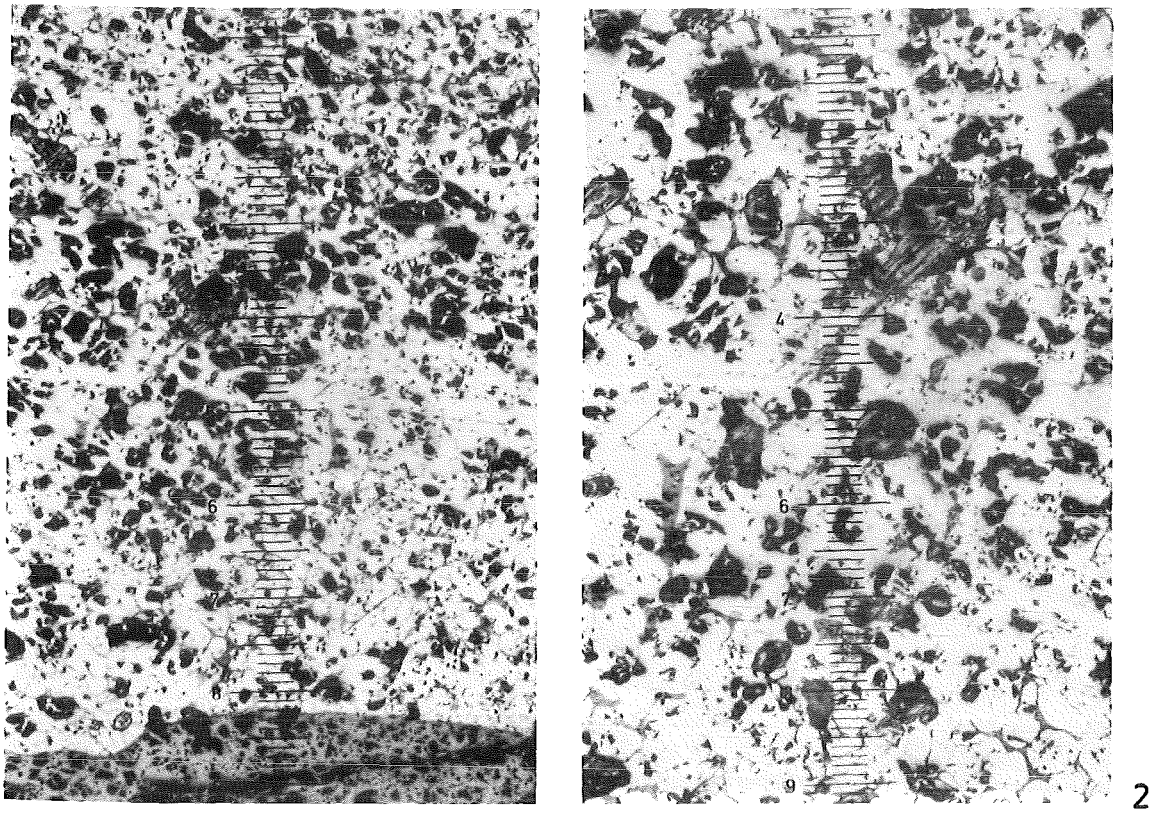

2

50x

100x

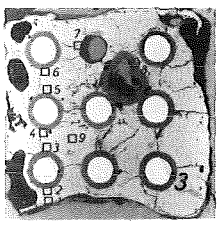

FIG. 27 DETAILS OF THE CROSS SECTION AT 116 MM AT POS. SHOWN IN THE OVERVIEW FIG. 20 (ESBU-1)

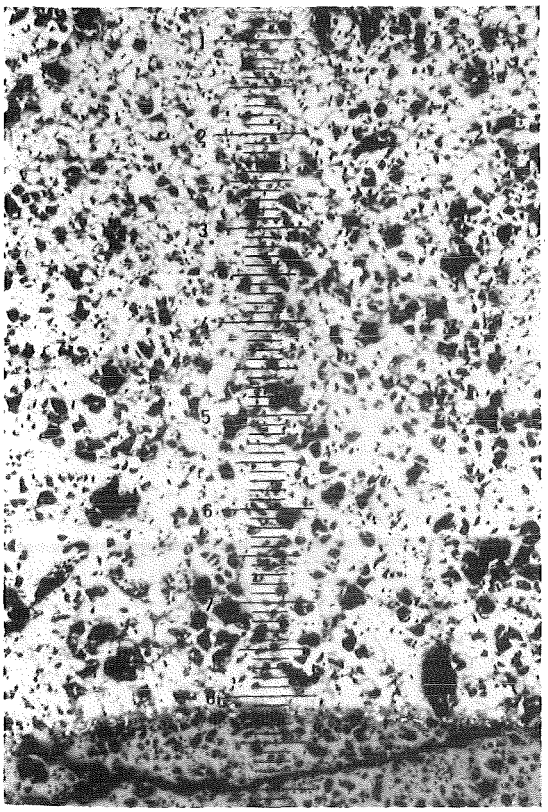

50x

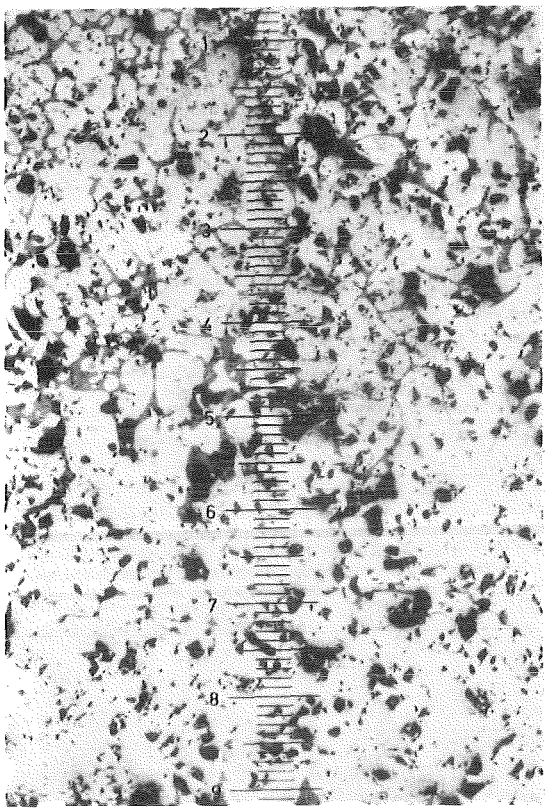

3

100x

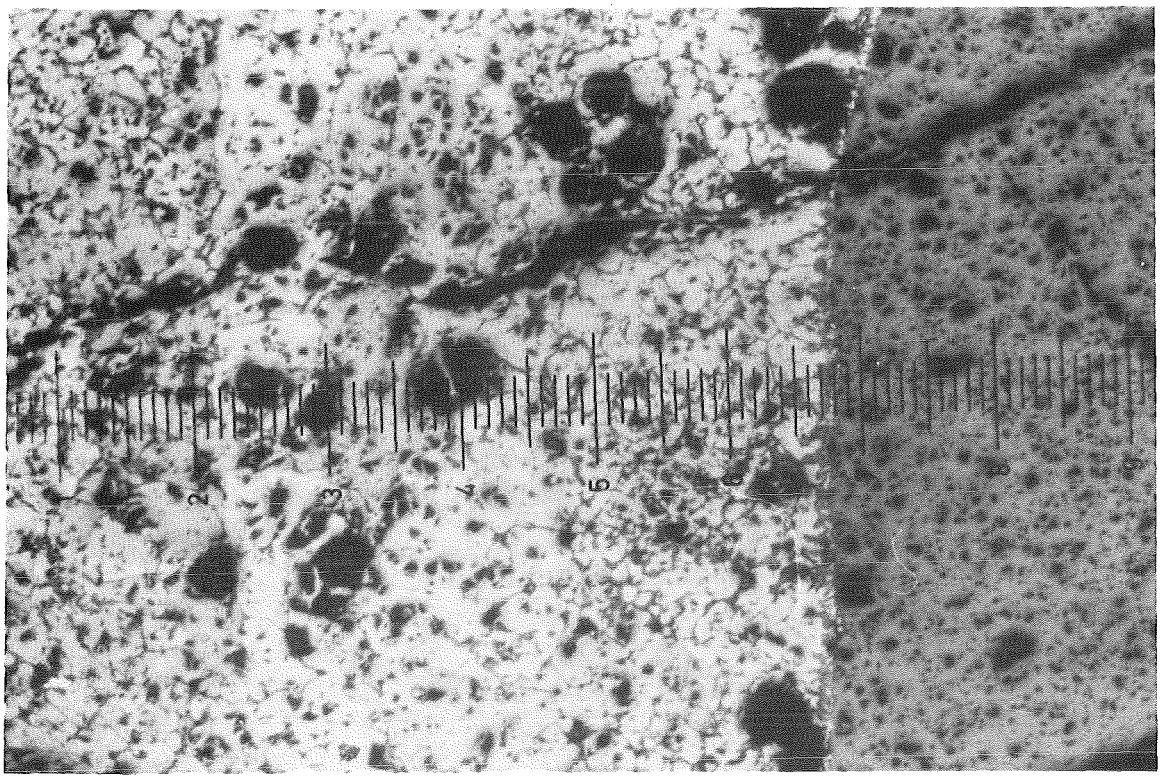

4

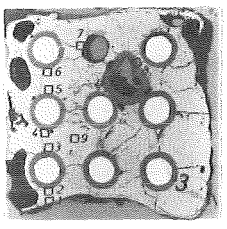

FIG. 28 DETAILS OF THE CROSS SECTION AT 116 MM AT POS. SHOWN IN THE OVERVIEW FIG. 20 (ESBU-1)

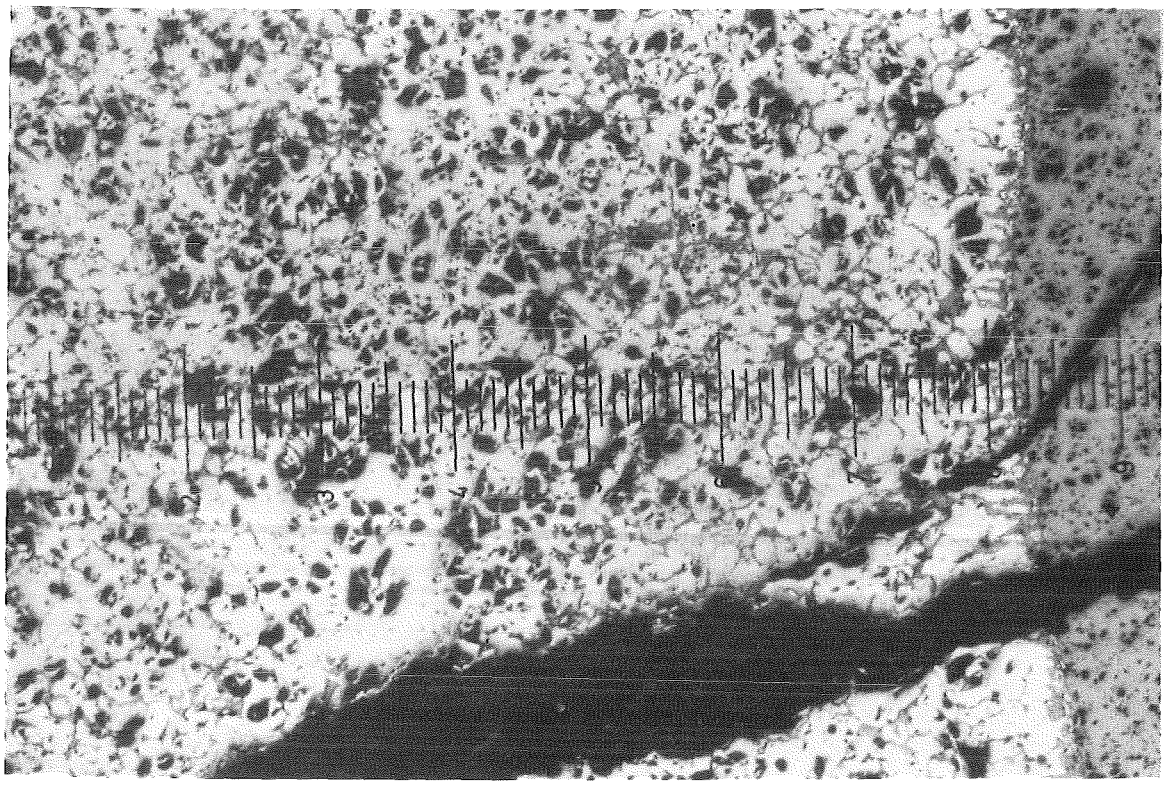

6

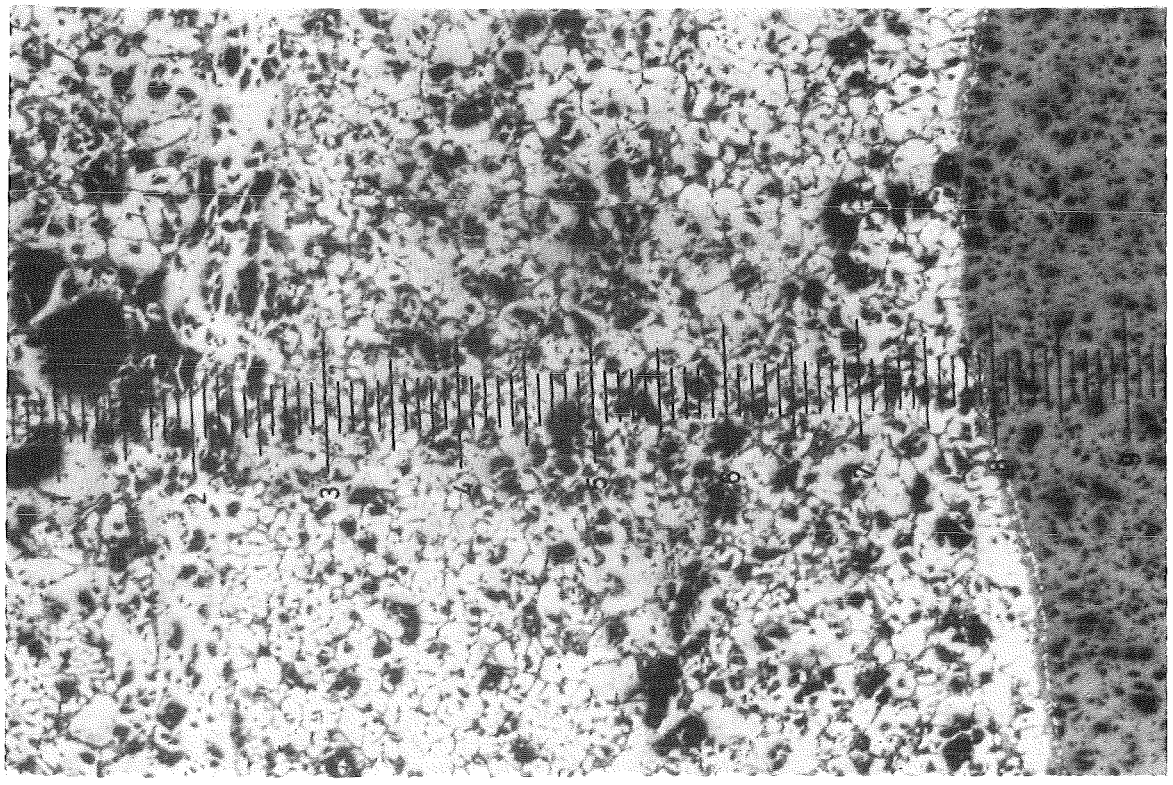

5

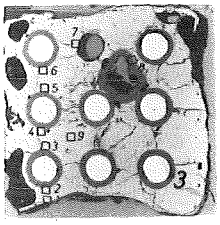

FIG.29 DETAILS OF THE CROSS SECTION AT 116 MM AT POS. SHOWN IN THE OVERVIEW FIG.20 (ESBU-1)

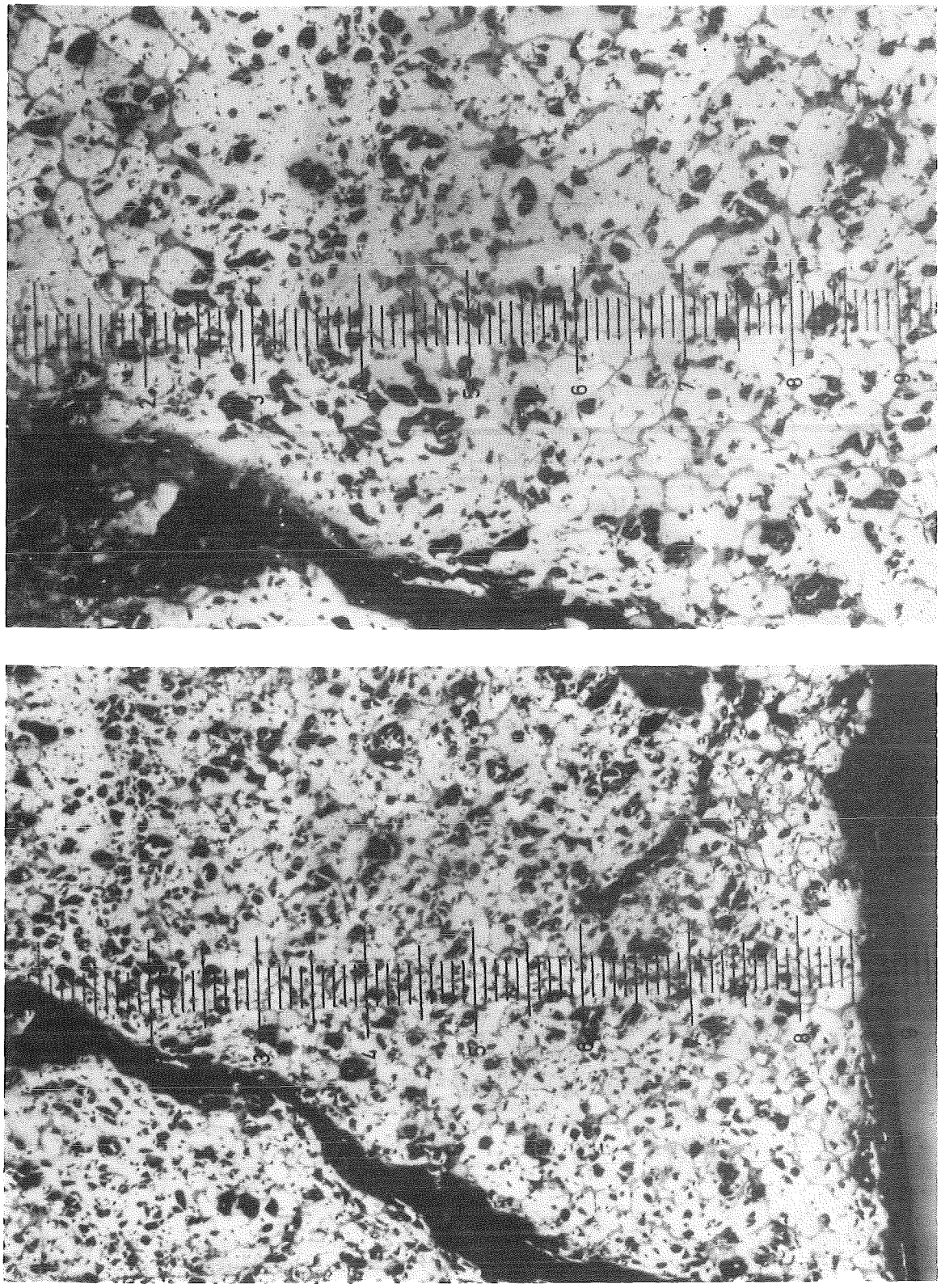

Position 7

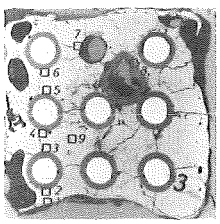

FIG. 30 DETAILS OF THE CROSS SECTION AT 116 MM AT POS. SHOWN IN THE OVERVIEW FIG. 20 (ESBU-1)

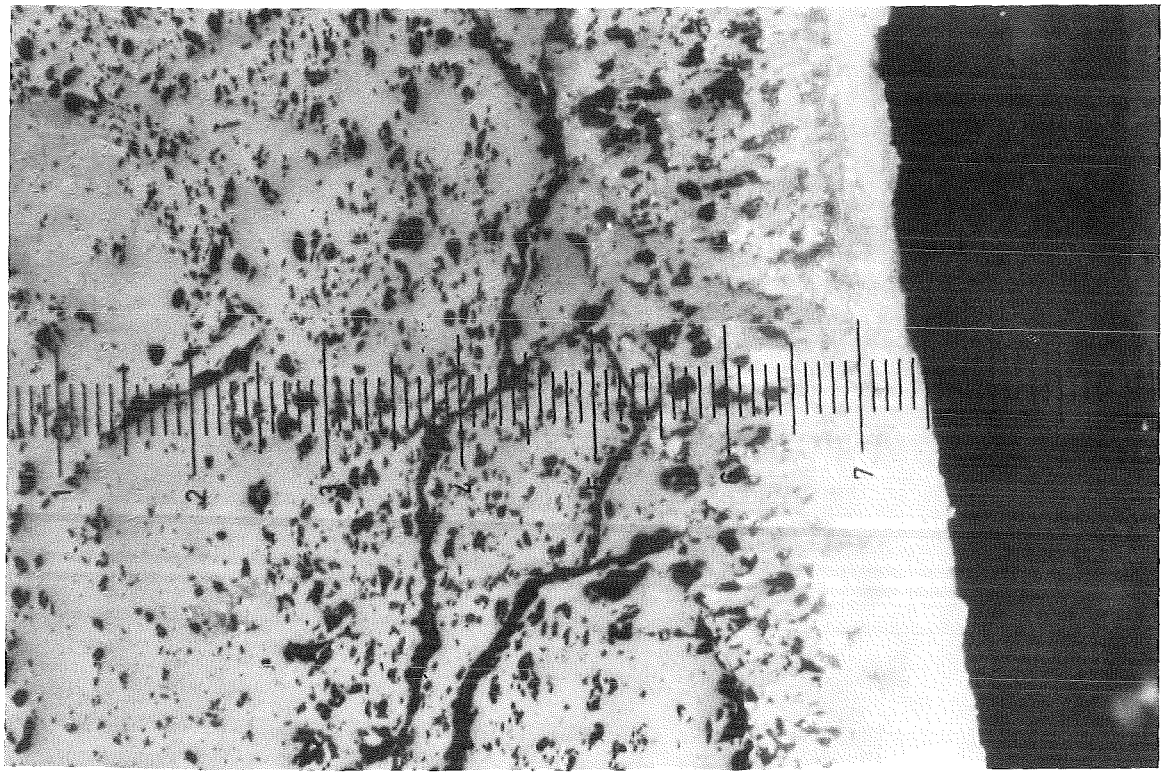

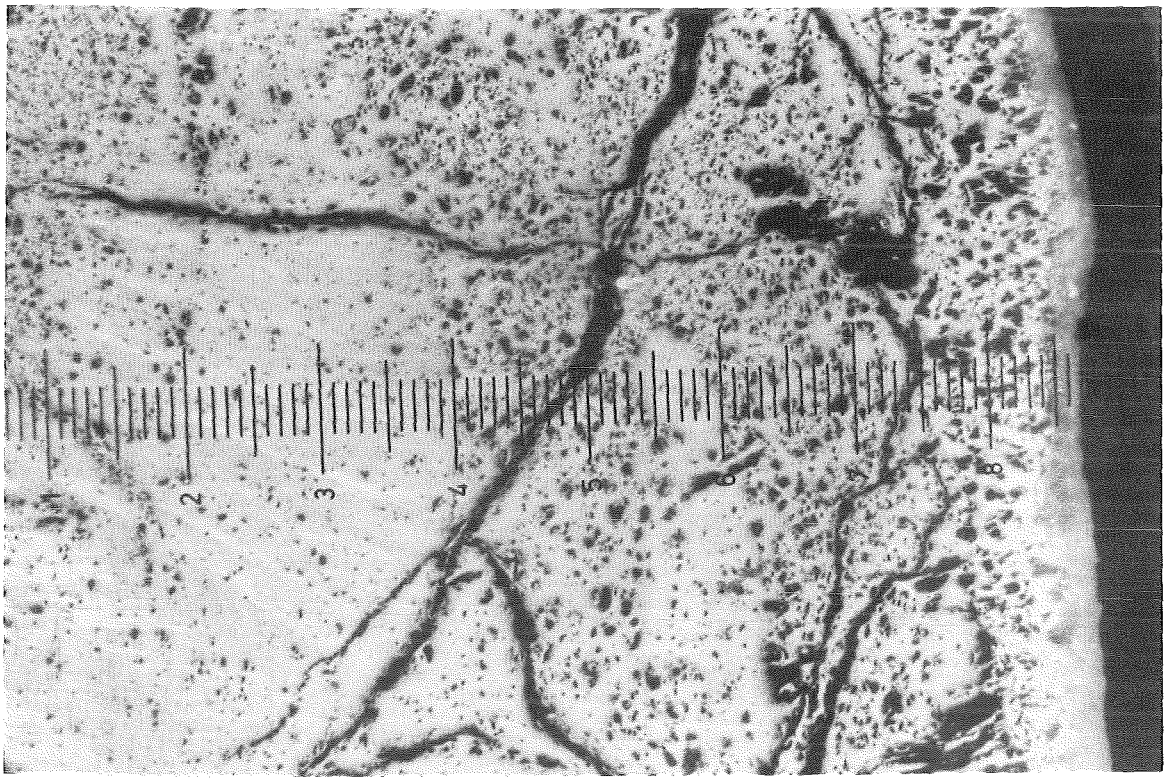

Position 8

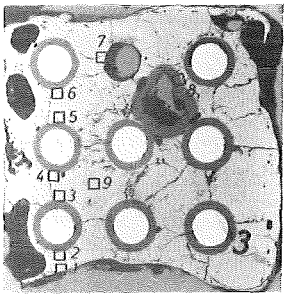

FIG. 31 DETAILS OF THE CROSS SECTION AT 116 MM AT POS. 8 SHOWN IN THE OVERVIEW FIG. 20 (ESBU-1)

1

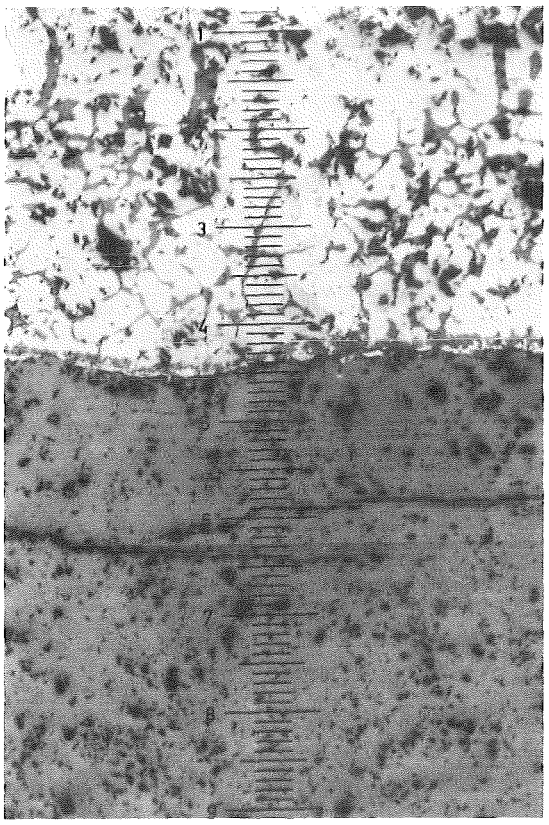

2

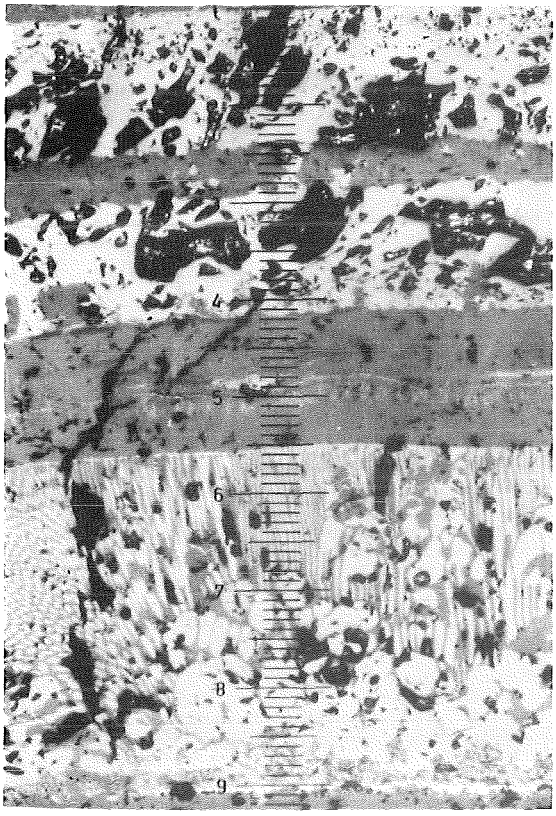

3

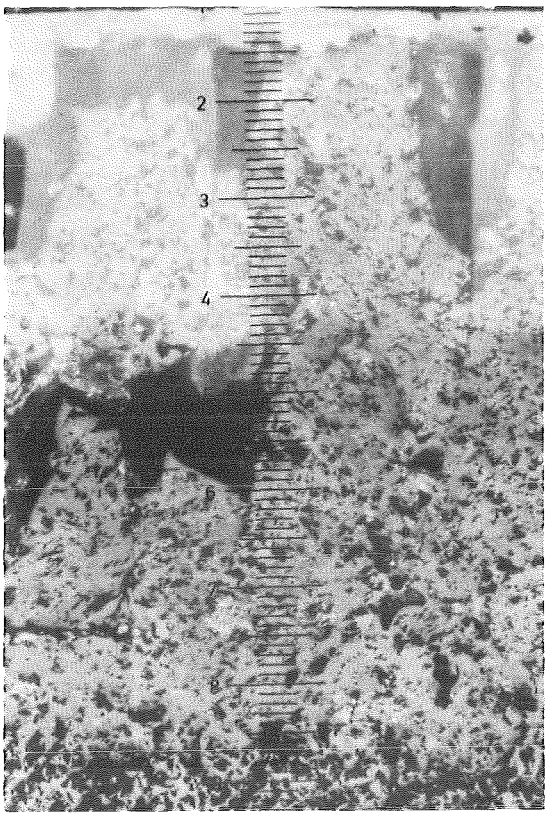

4

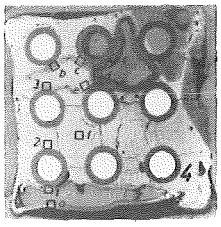

FIG. 32 DETAILS OF THE CROSS SECTION AT 106 MM AT POS. SHOWN IN THE OVERVIEW FIG. 20 (ESBU-1)

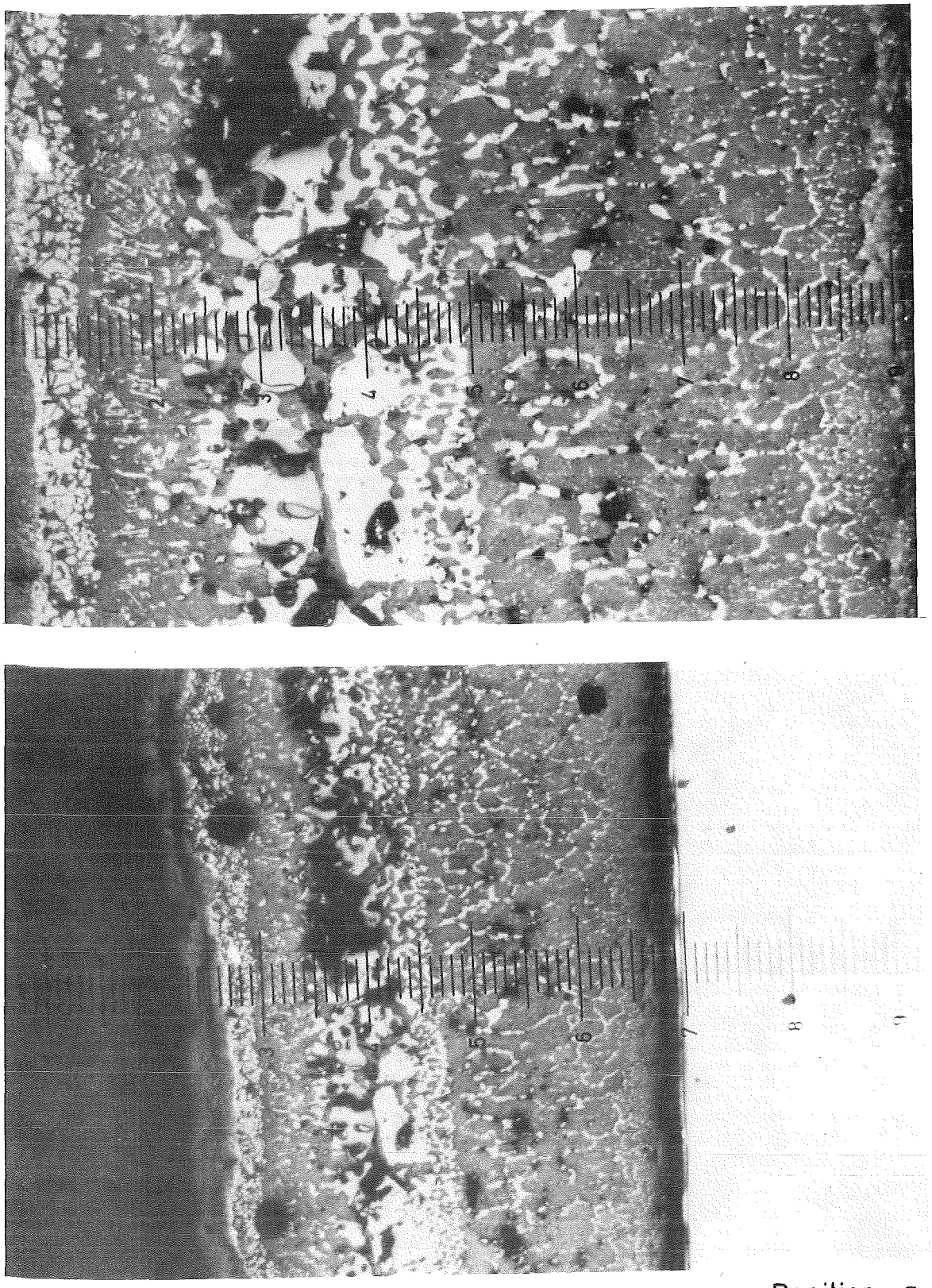

Position a

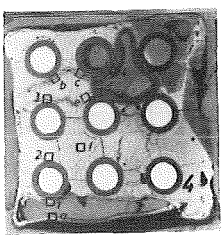

FIG. 33 DETAILS OF THE CROSS SECTION AT 106 MM AT POS. SHOWN IN THE OVERVIEW FIG. 20 (ESBU-1)

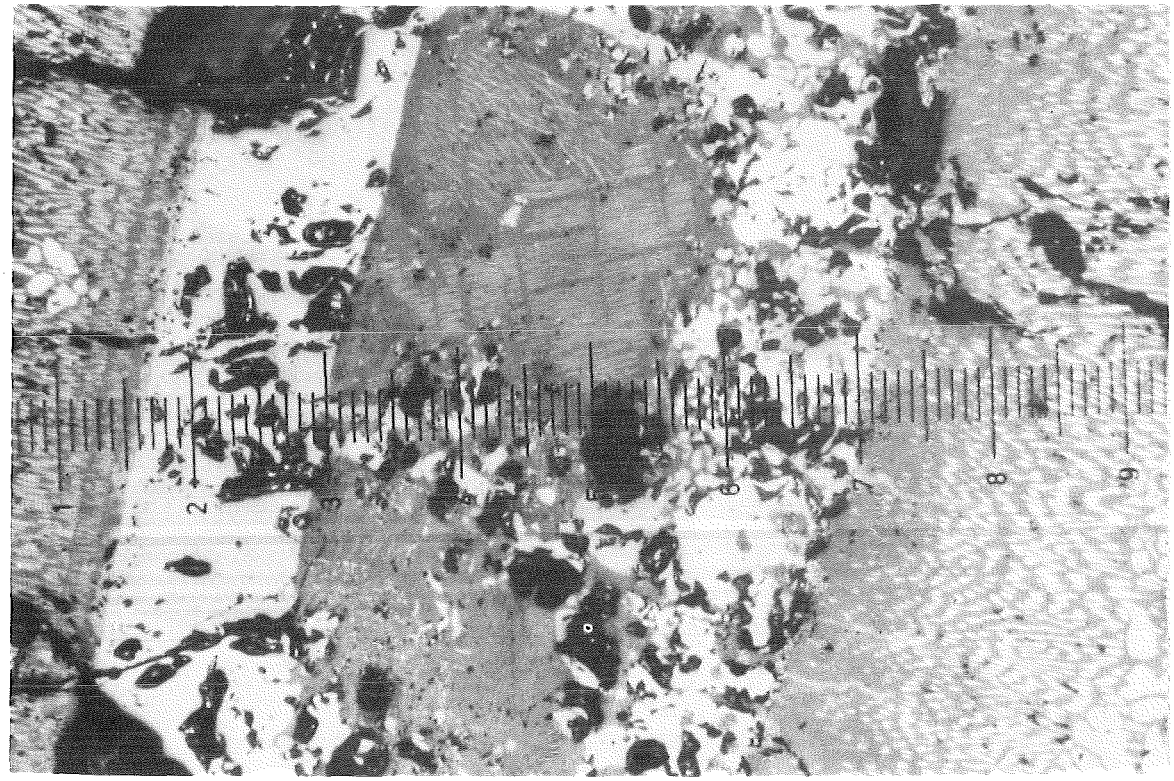

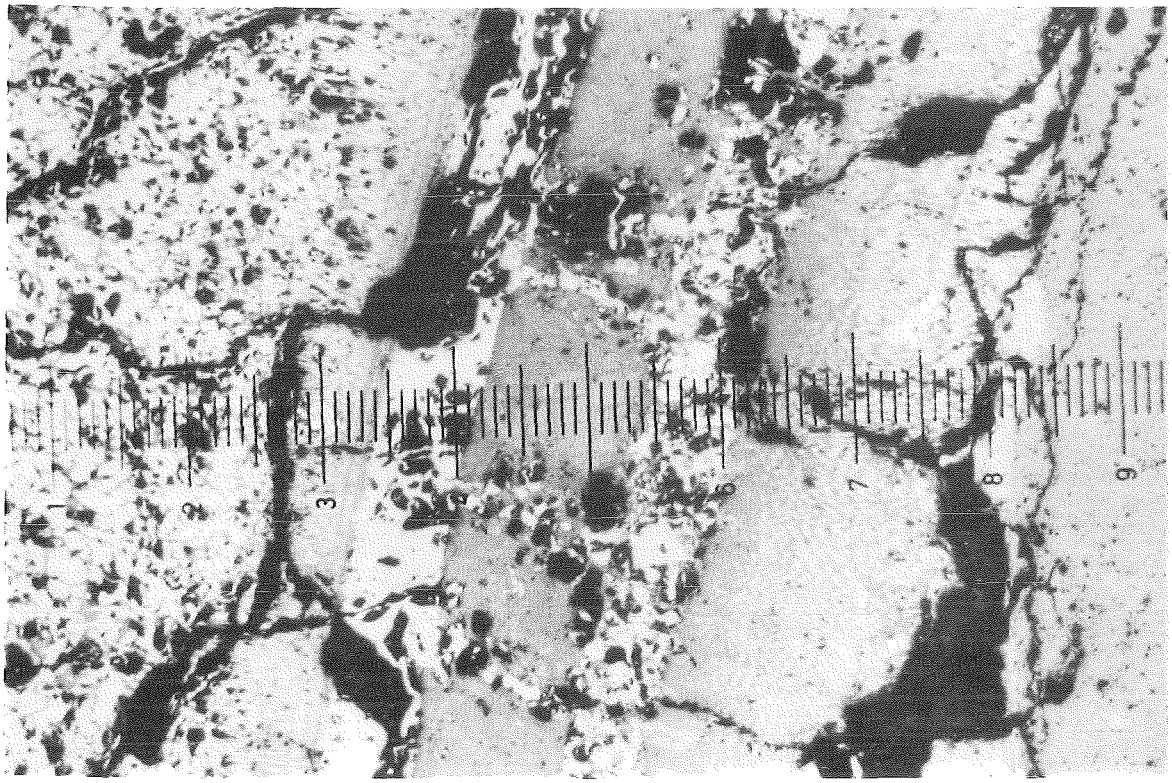

Position b

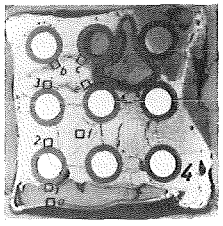

FIG. 34 DETAILS OF THE CROSS SECTION AT 106 MM AT POS. SHOWN IN THE OVERVIEW FIG. 20 (ESBU-1)

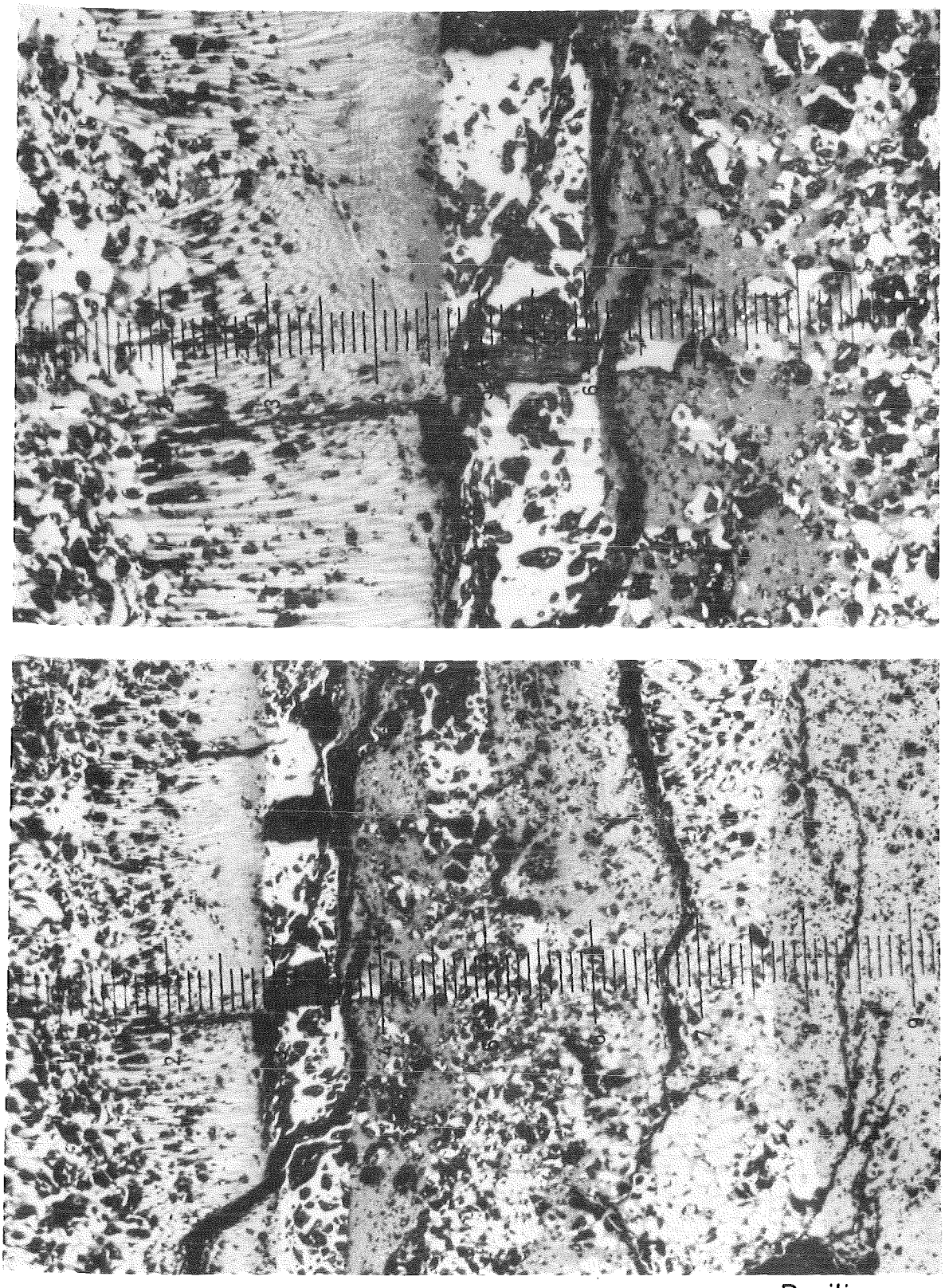

Position c

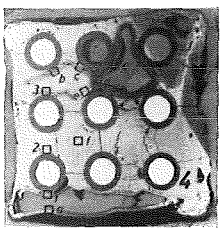

FIG. 35 DETAILS OF THE CROSS SECTION AT 106 MM AT POS. SHOWN IN THE OVERVIEW FIG. 20 (ESBU-1)

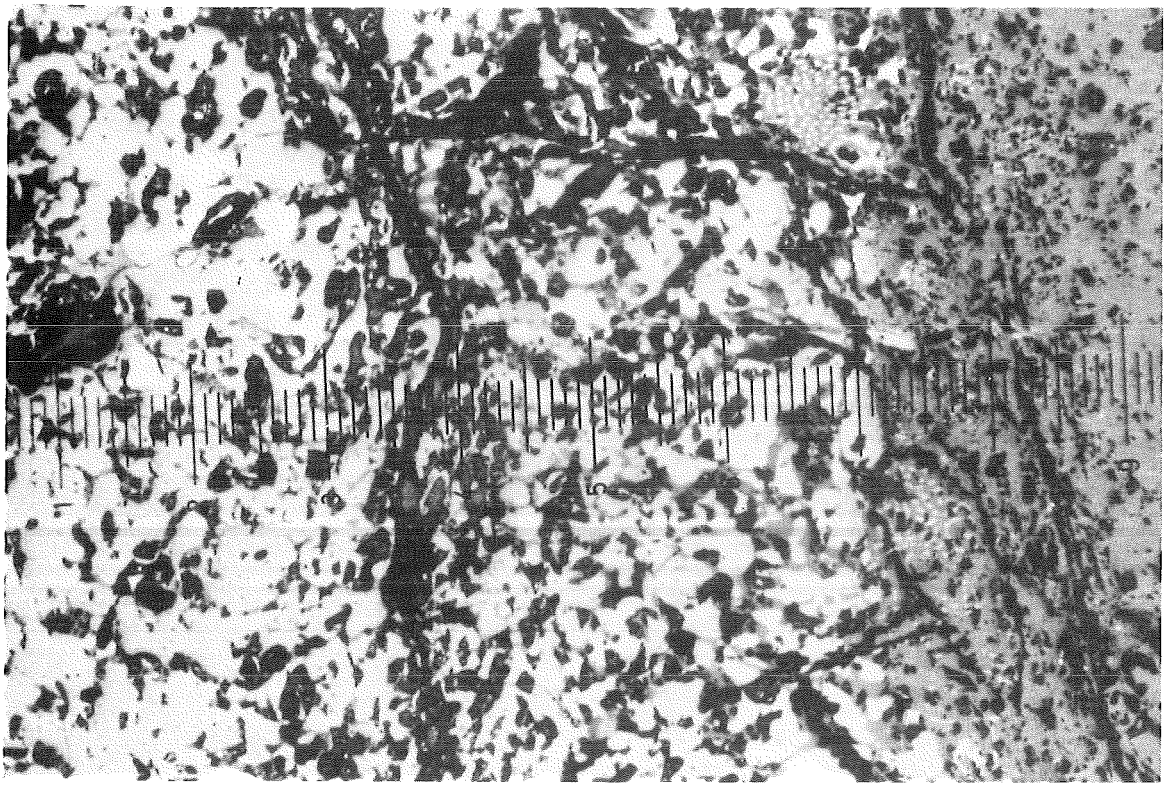

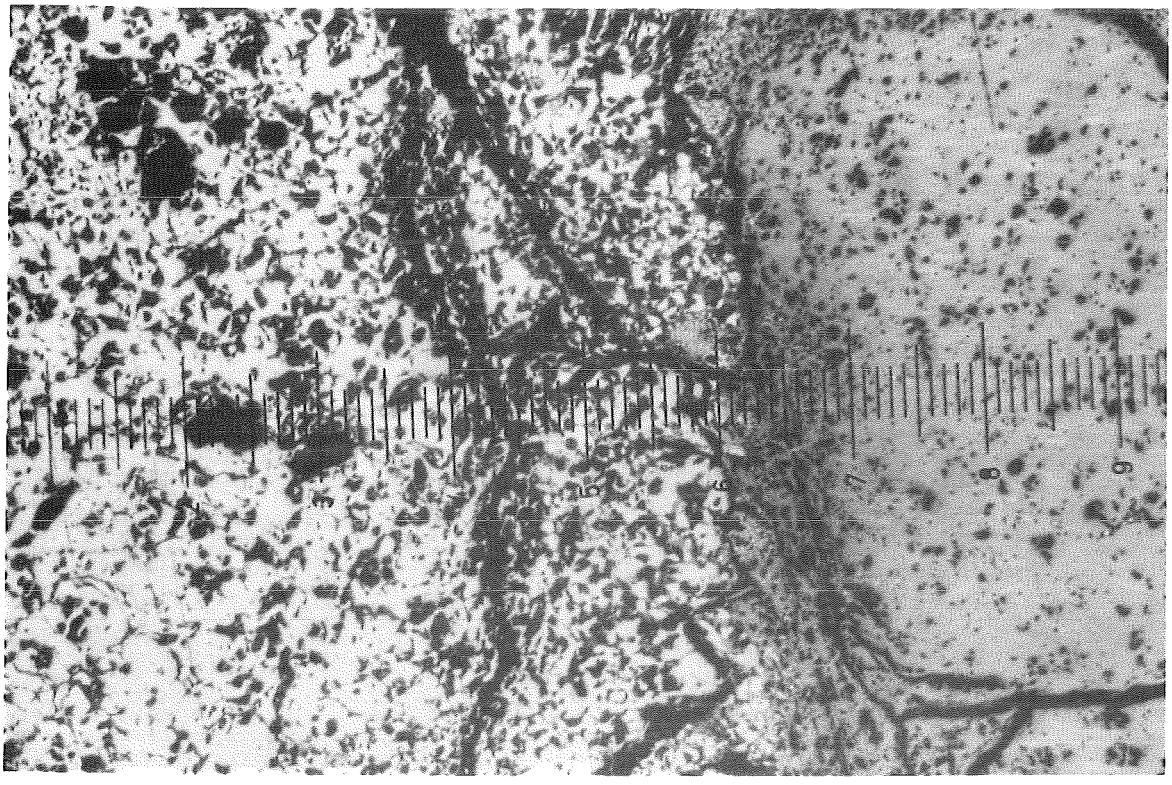

Position d

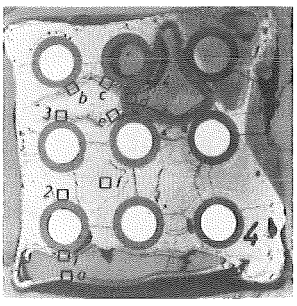

FIG.36 DETAILS OF THE CROSS SECTION AT 106 MM AT POS SHOWN IN THE OVERVIEW FIG.20 (ESBU-1)

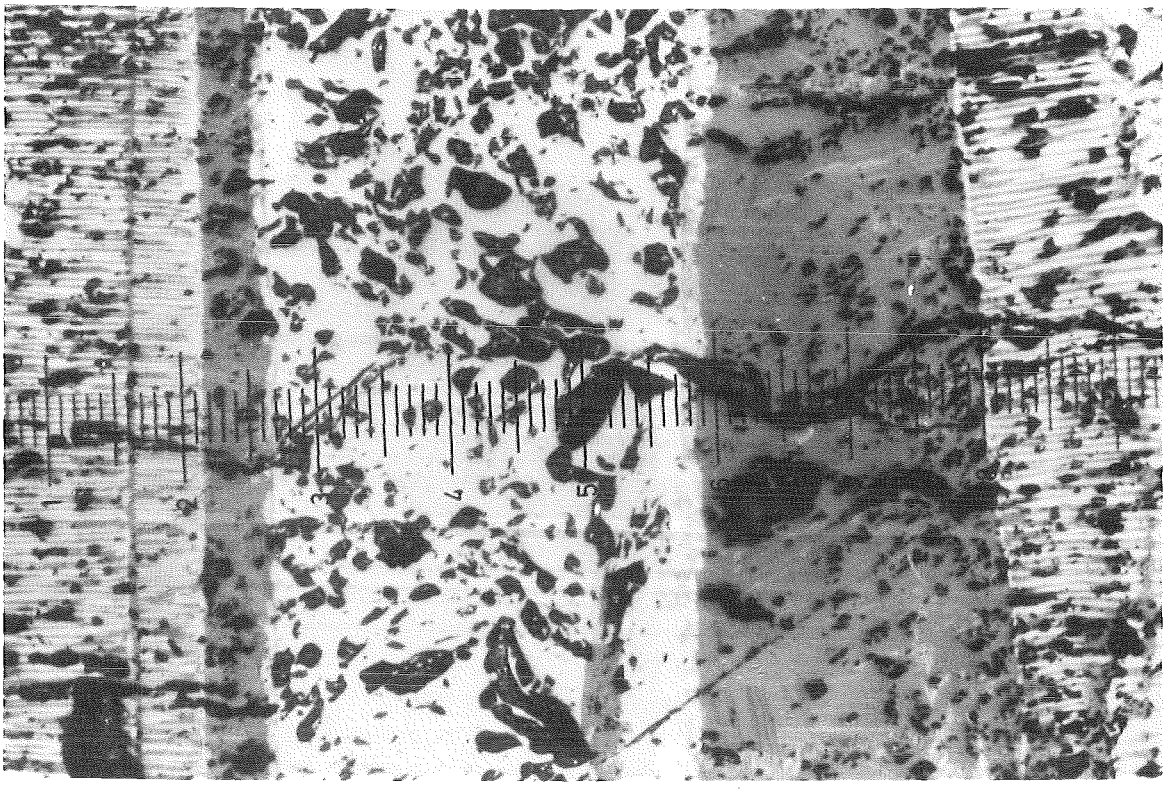

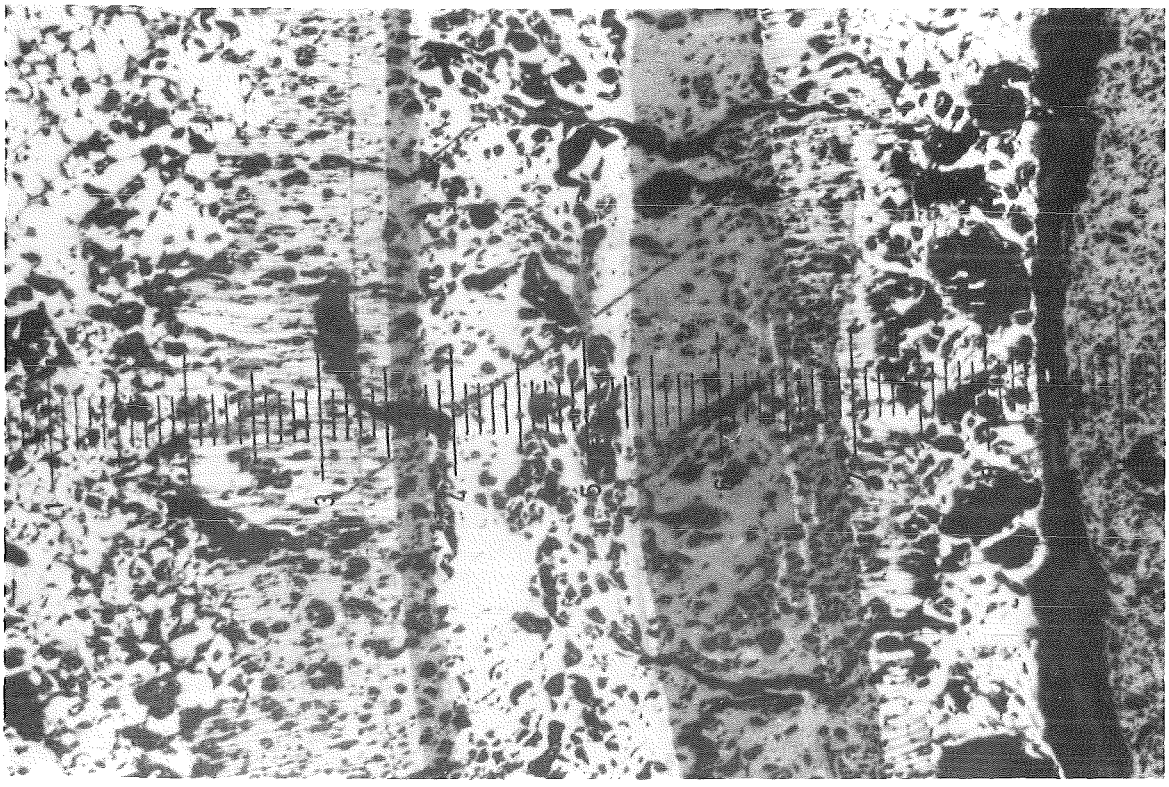

Position e

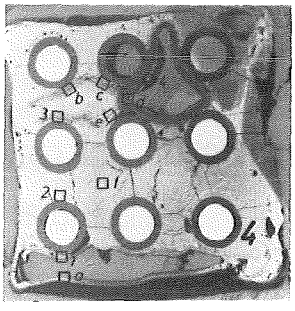

FIG. 37 DETAILS OF THE CROSS SECTION AT 106 MM AT POS. SHOWN IN THE OVERVIEW FIG. 20 (ESBU-1)

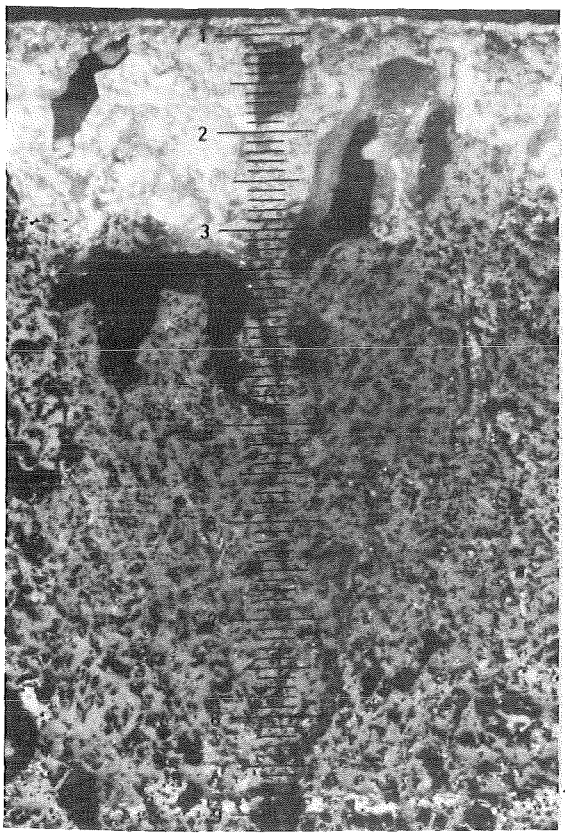

10

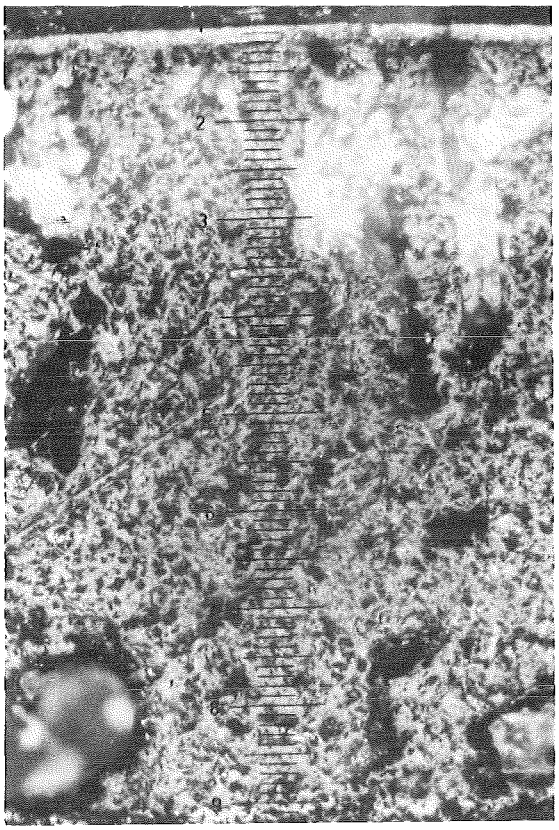

11

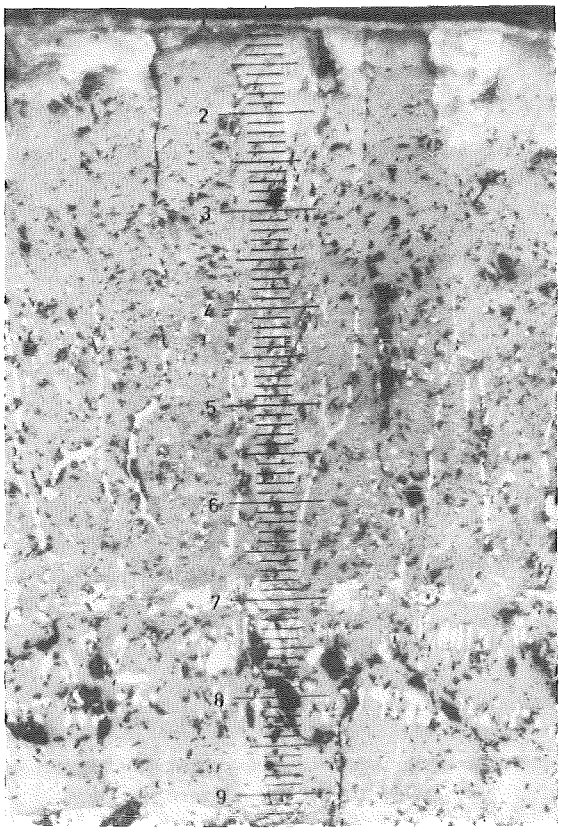

1

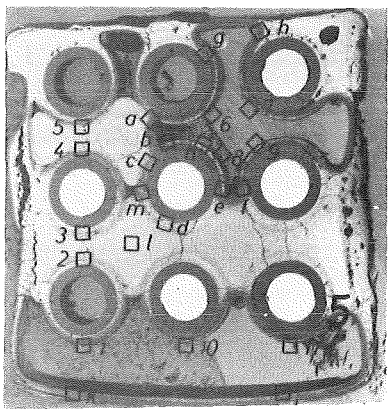

FIG. 38 DETAILS OF THE CROSS SECTION AT 96 MM AT POSITIONS SHOWN IN THE OVERVIEW FIG. 20 (ESBU-1)

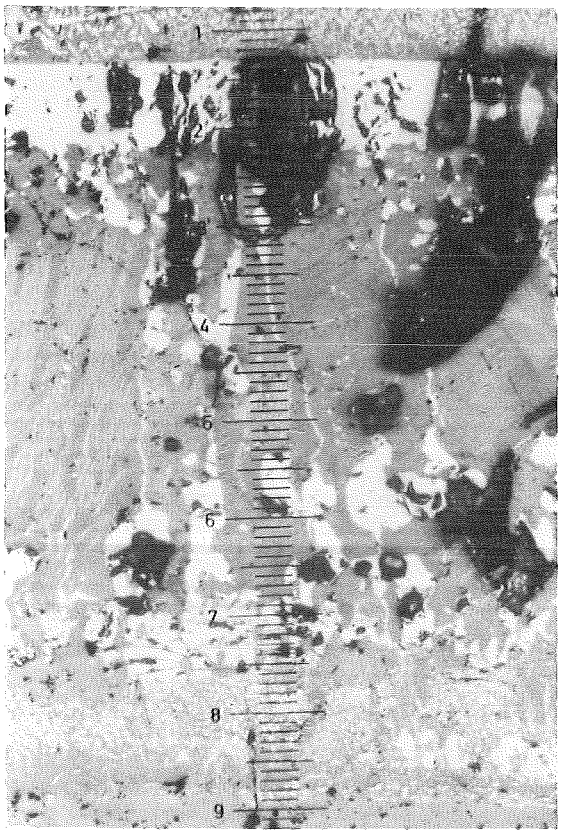

4

5

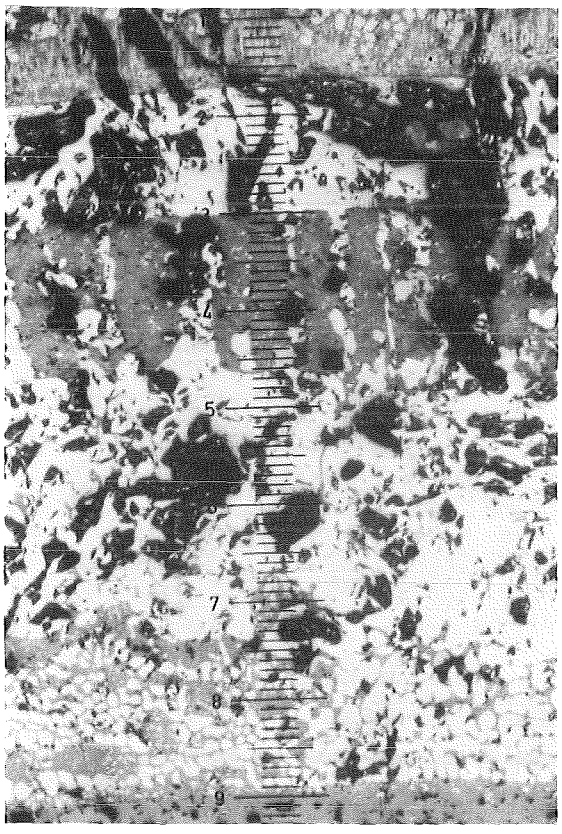

2

3

FIG. 39 DETAILS OF THE CROSS SECTION AT 96 MM AT POS. SHOWN IN THE OVERVIEW FIG. 20 (ESBU-1)

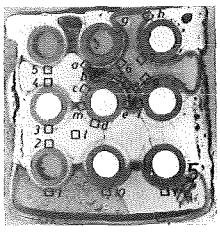

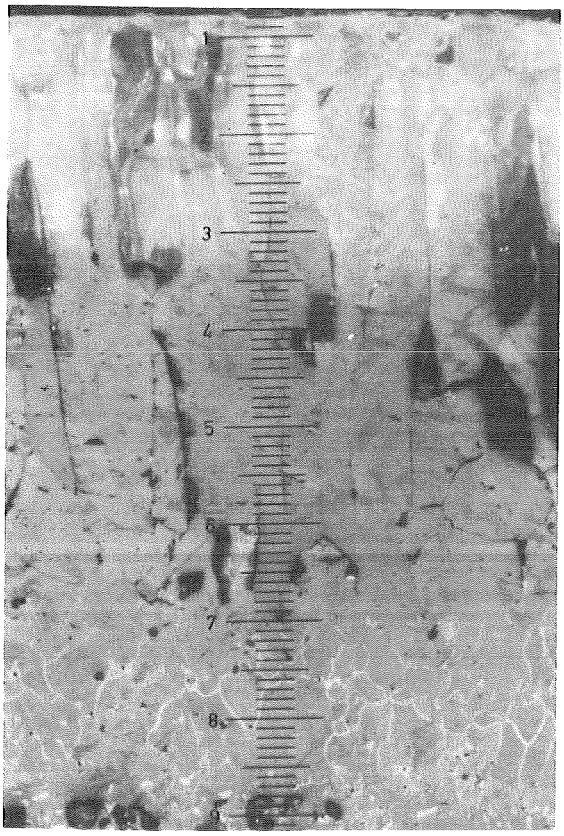

6

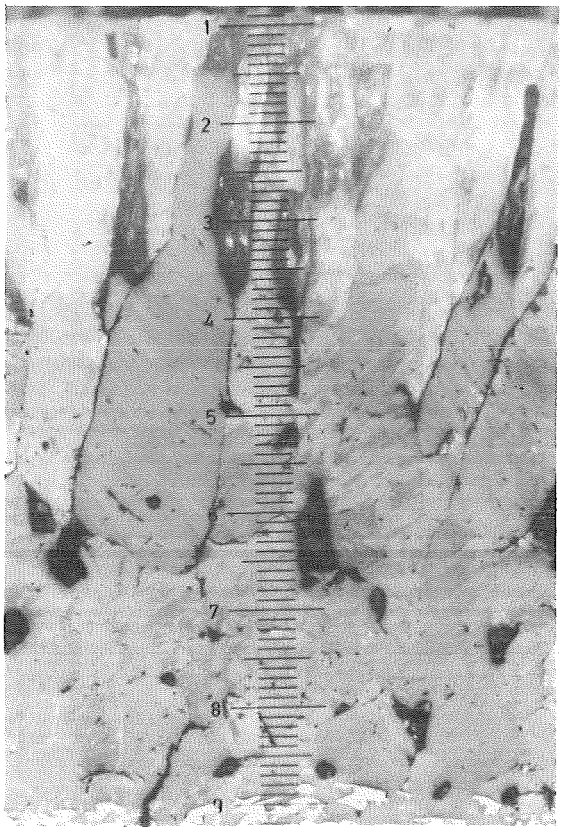

7

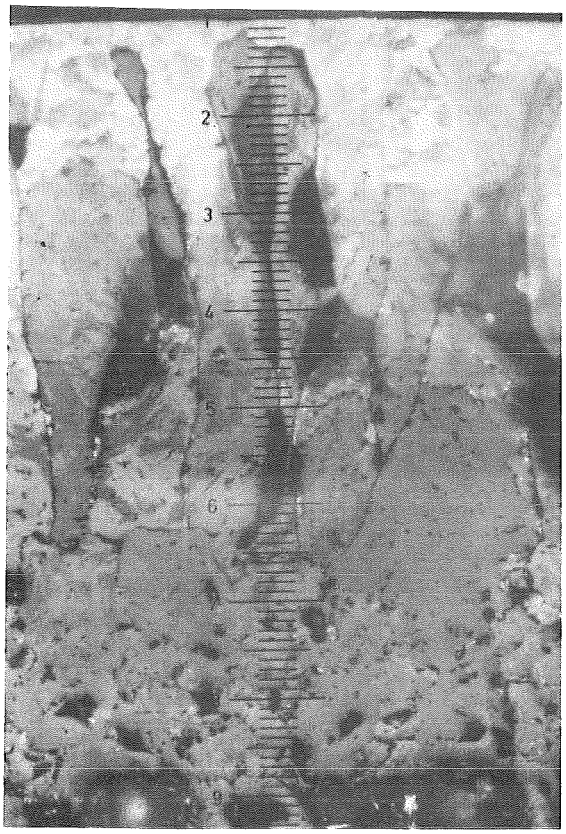

8

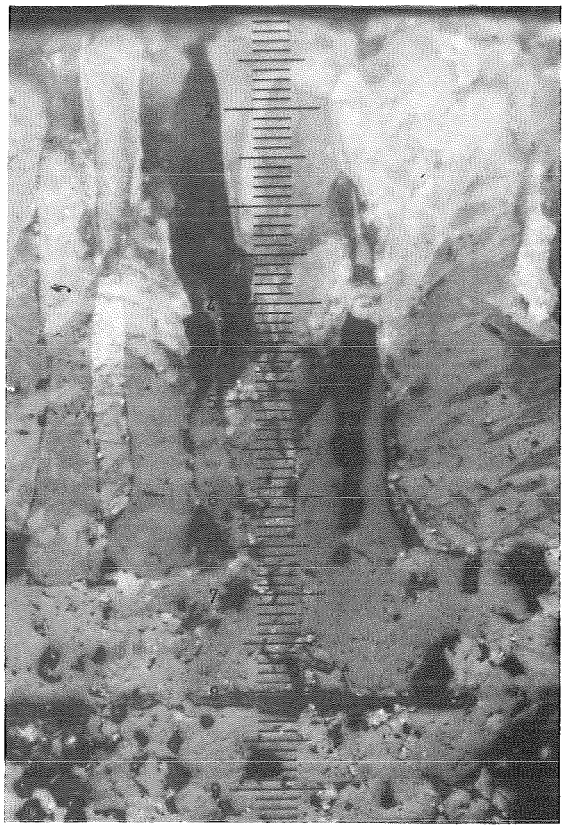

9

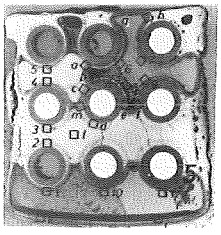

FIG. 40 DETAILS OF THE CROSS SECTION AT 96 MM AT POS SHOWN IN THE OVERVIEW FIG. 20 (ESBU-1)

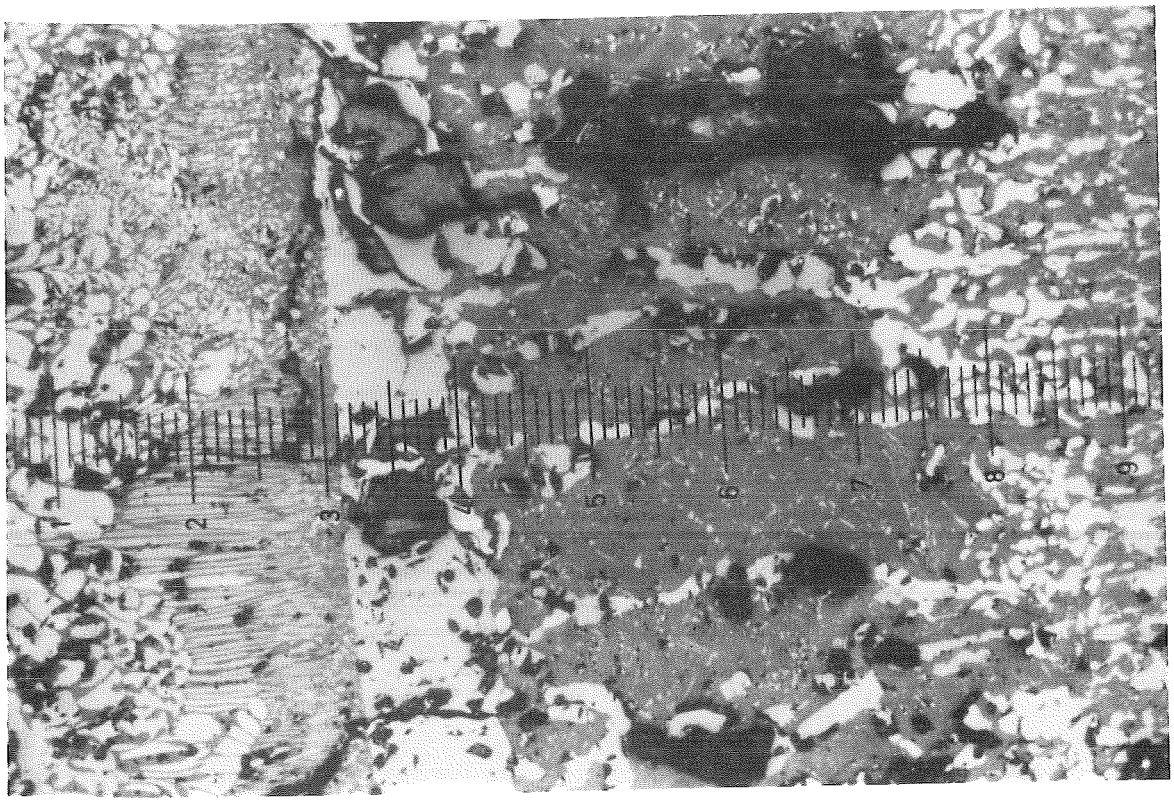

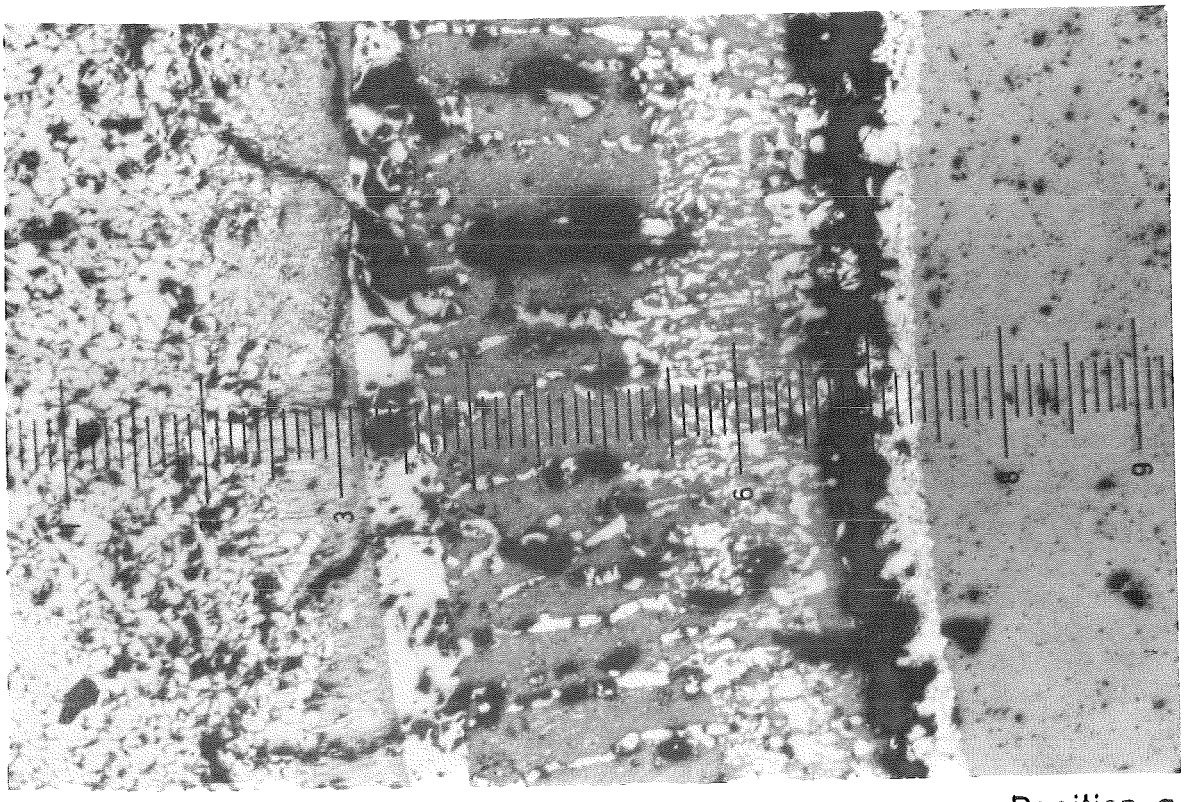

Position a

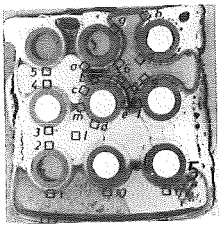

FIG. 41 DETAILS OF THE CROSS SECTION AT 96 MM AT POS. SHOWN IN THE OVERVIEW FIG.20 (ESBU-1)

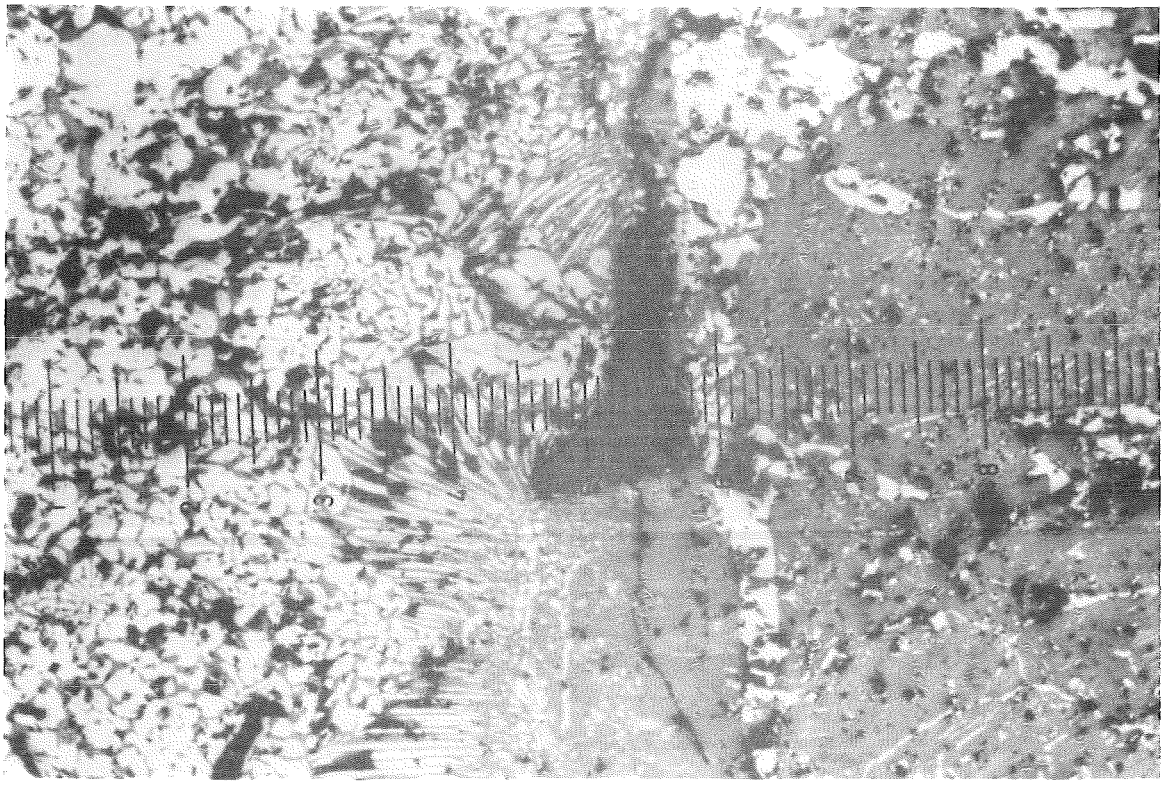

Position b

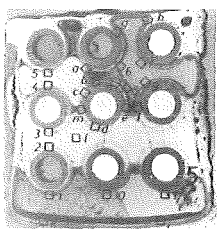

FIG.42 DETAILS OF THE CROSS SECTION AT 96 MM AT POS. SHOWN IN THE OVERVIEW FIG.20 (ESBU-1)

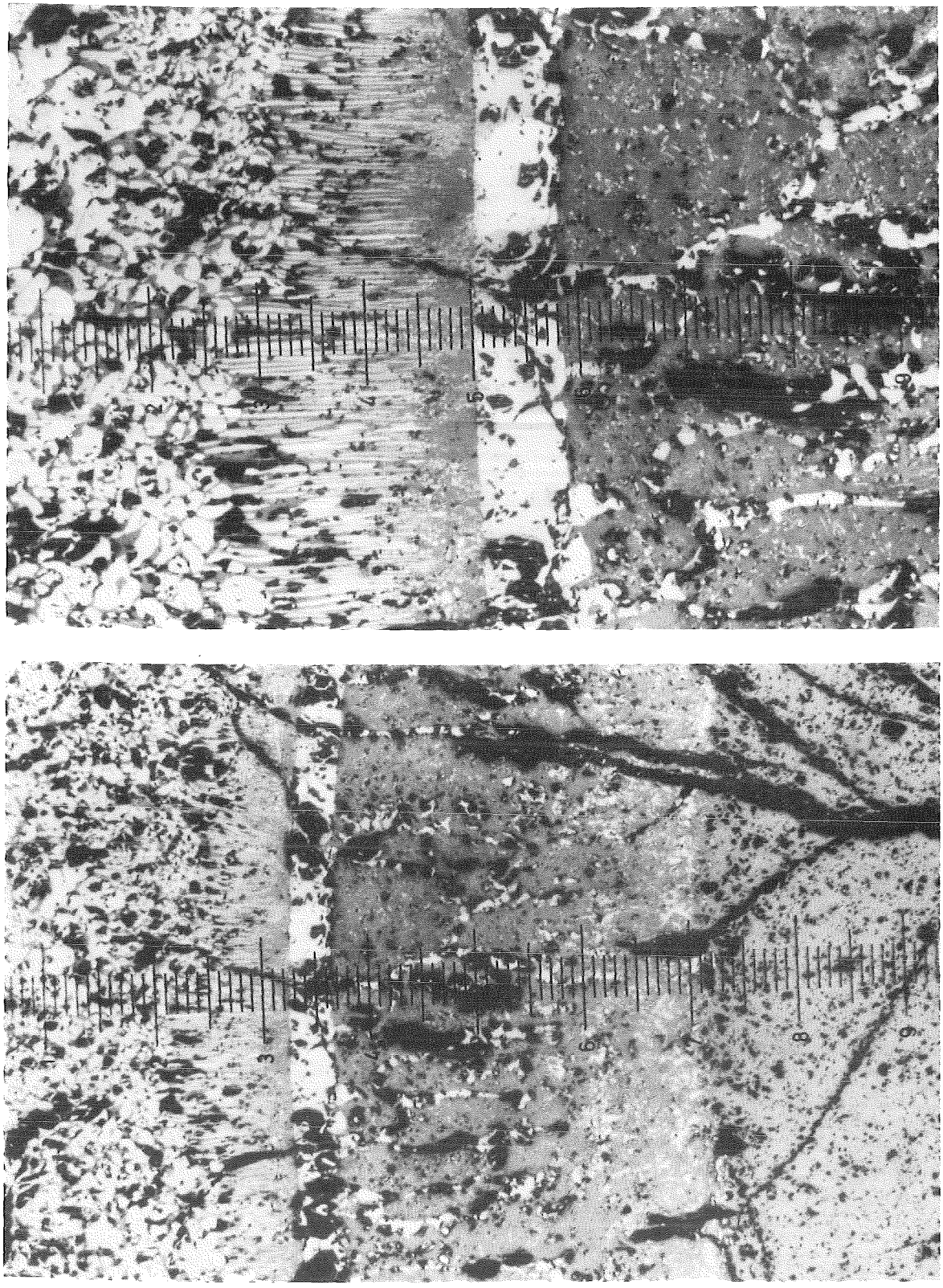

Position c

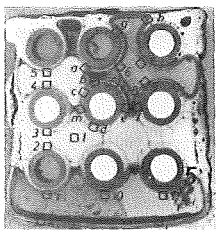

FIG. 43 DETAILS OF THE CROSS SECTION AT 96 MM AT POS. SHOWN IN THE OVERVIEW FIG. 20 (ESBU-1)

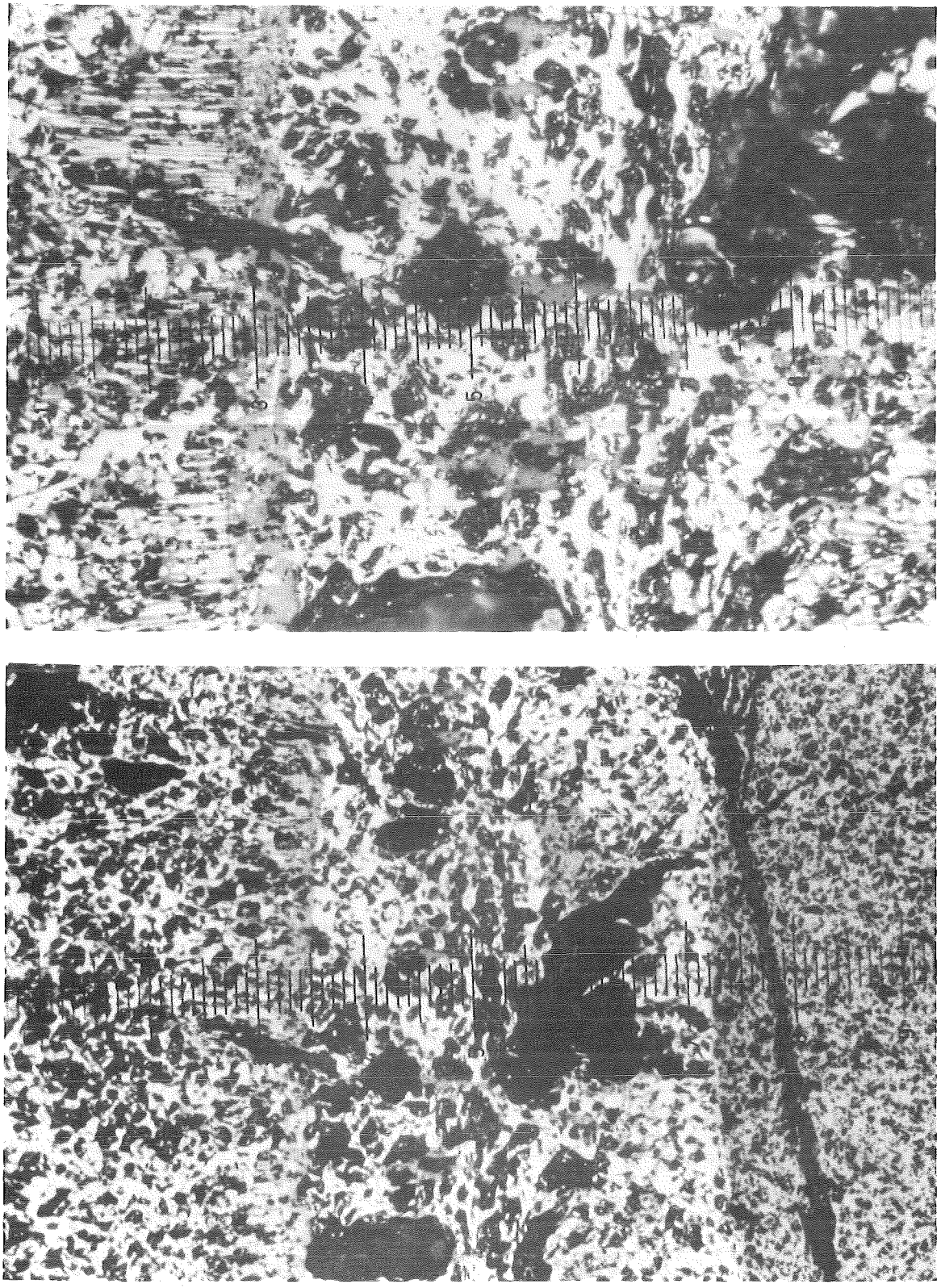

Position d

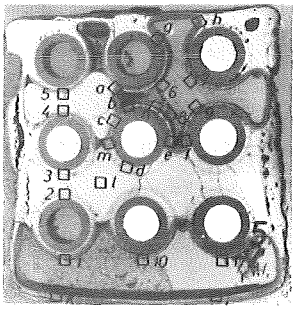

FIG. 44 DETAILS OF THE CROSS SECTION AT 96 MM AT POS. SHOWN IN THE OVERVIEW FIG. 20 (ESBU-1)

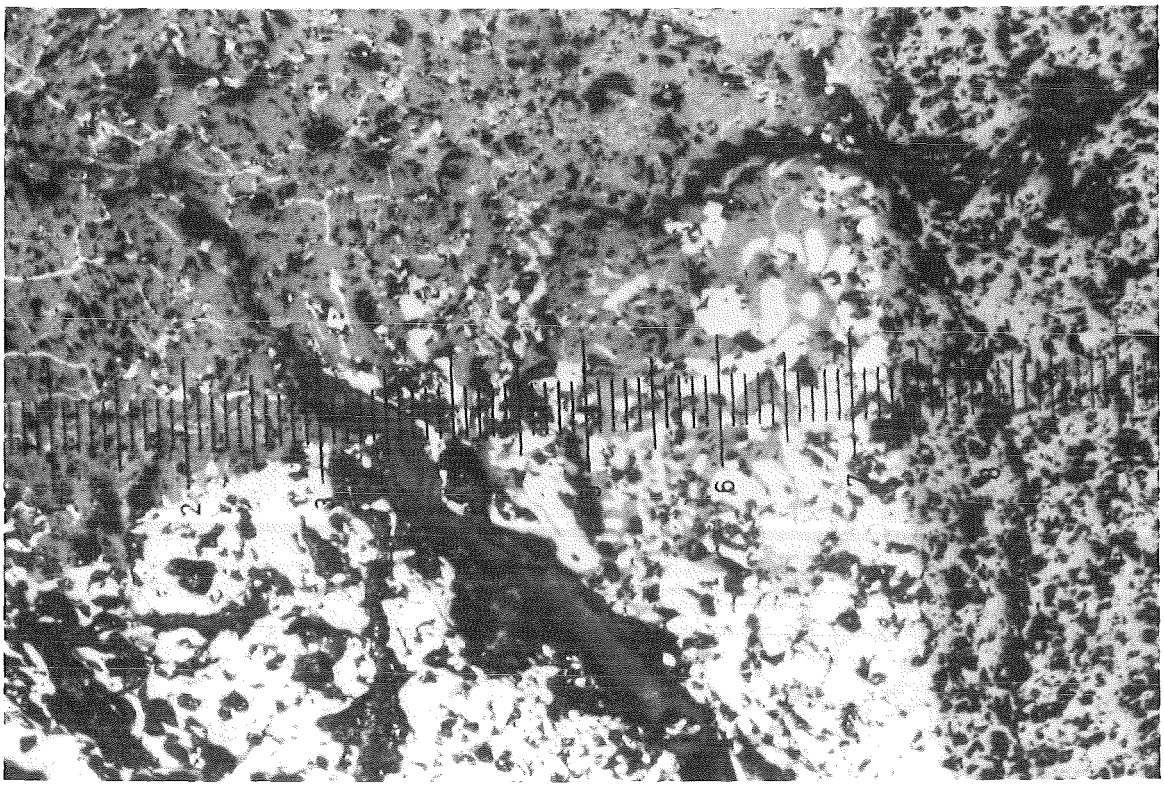

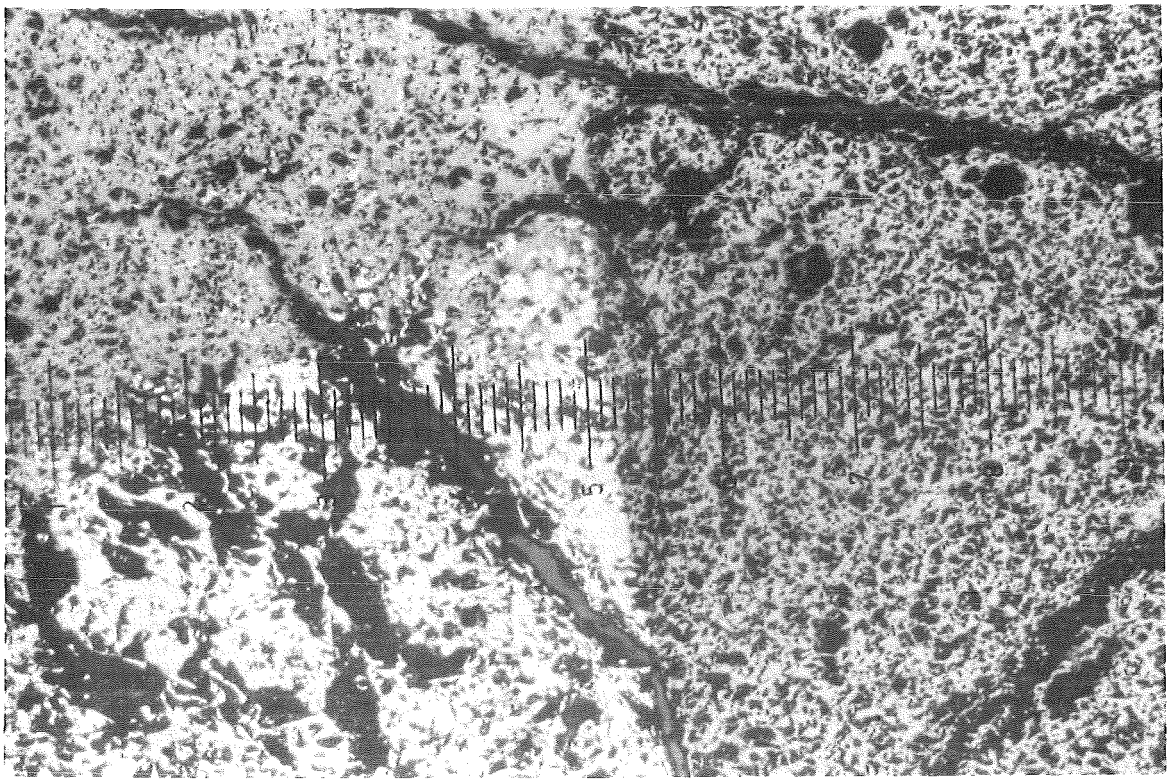

Position e

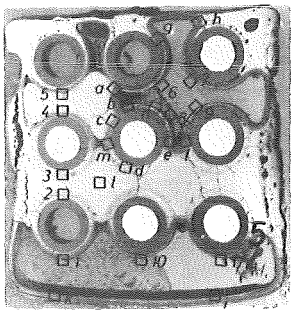

FIG. 45 DETAILS OF THE CROSS SECTION AT 96 MM AT POS. SHOWN IN THE OVERVIEW FIG. 20 (ESBU-1)

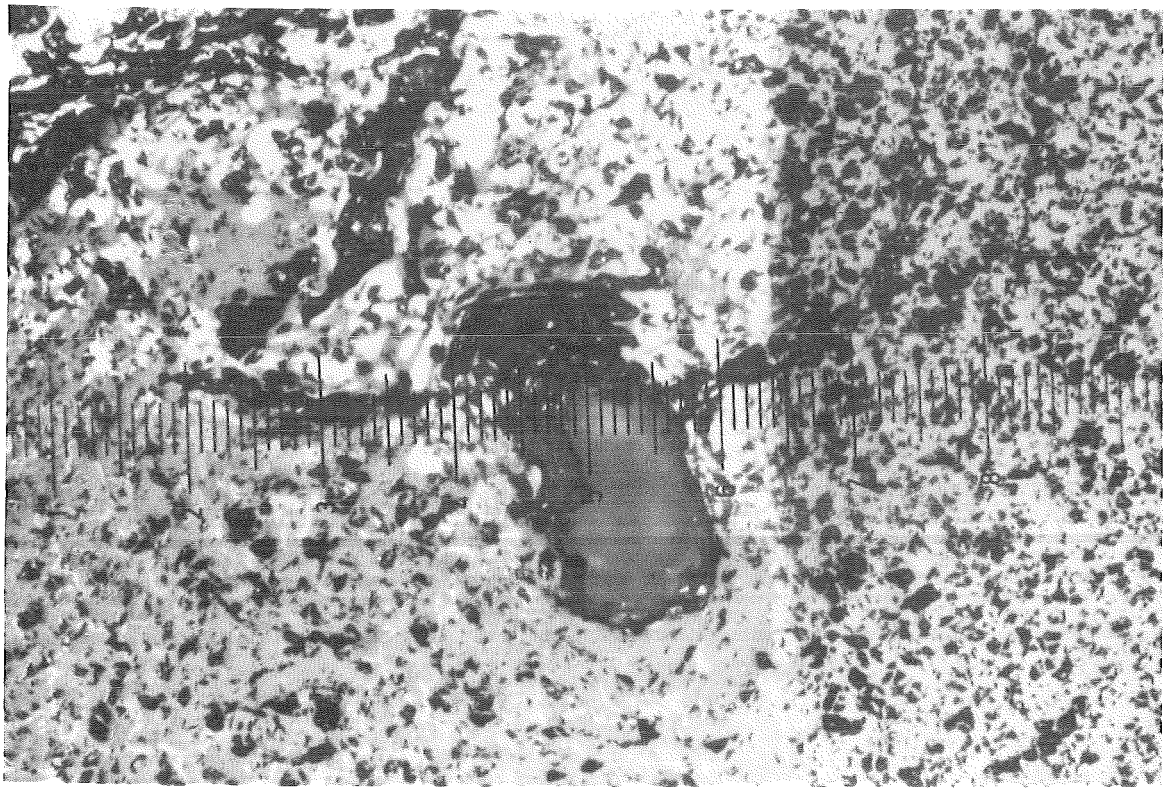

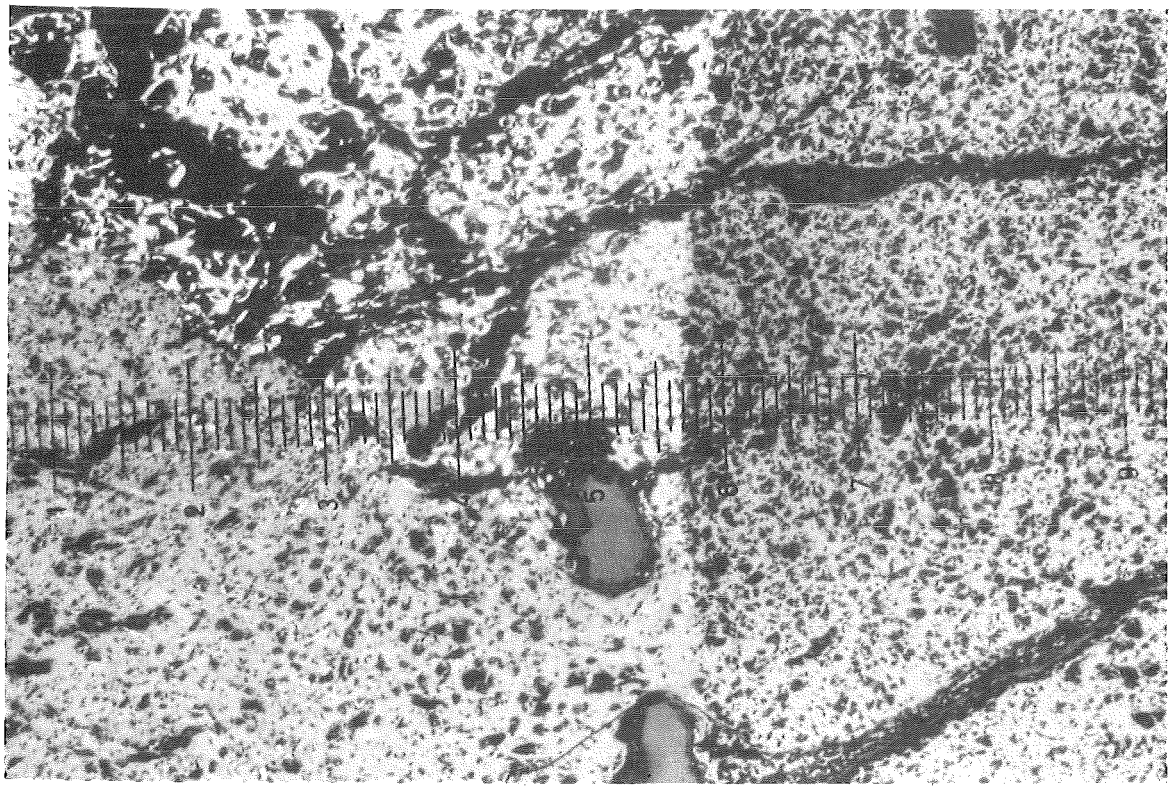

Position f

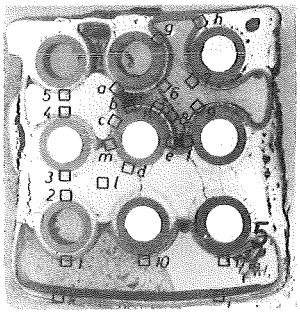

FIG. 46 DETAILS OF THE CROSS SECTION AT 96 MM AT POS. SHOWN IN THE OVERVIEW FIG. 20 (ESBU-1)

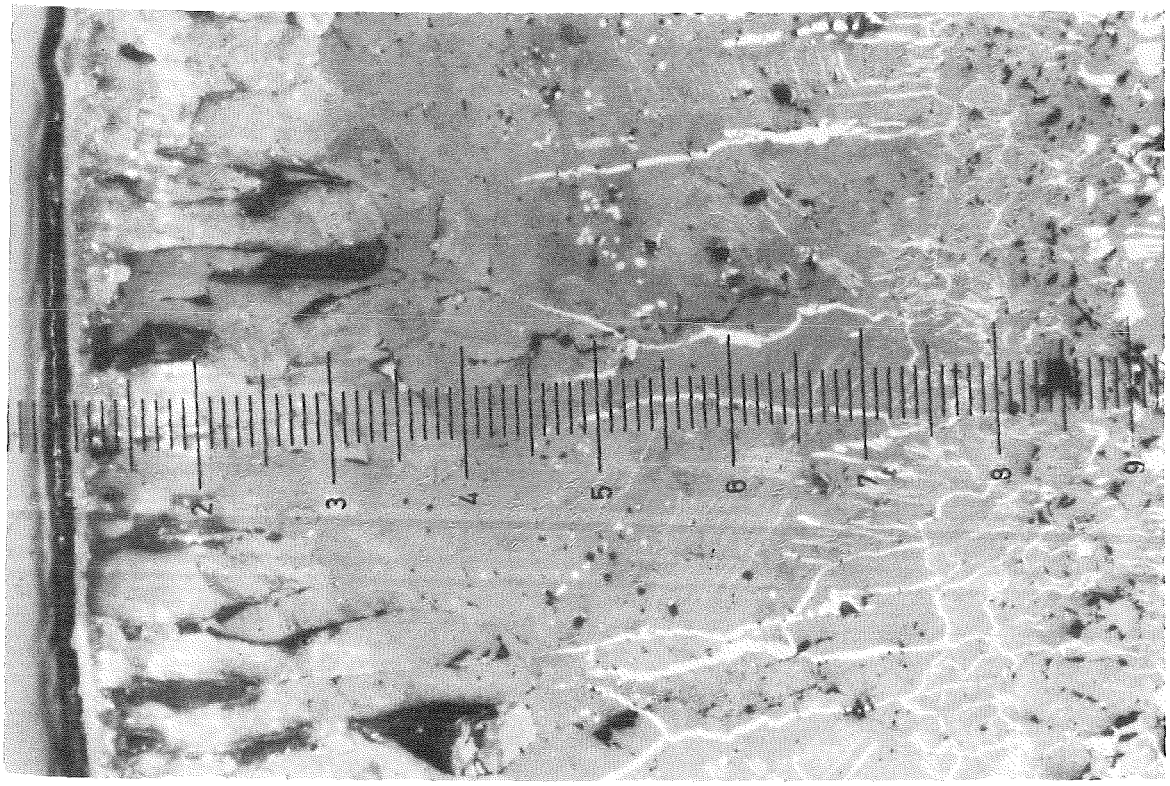

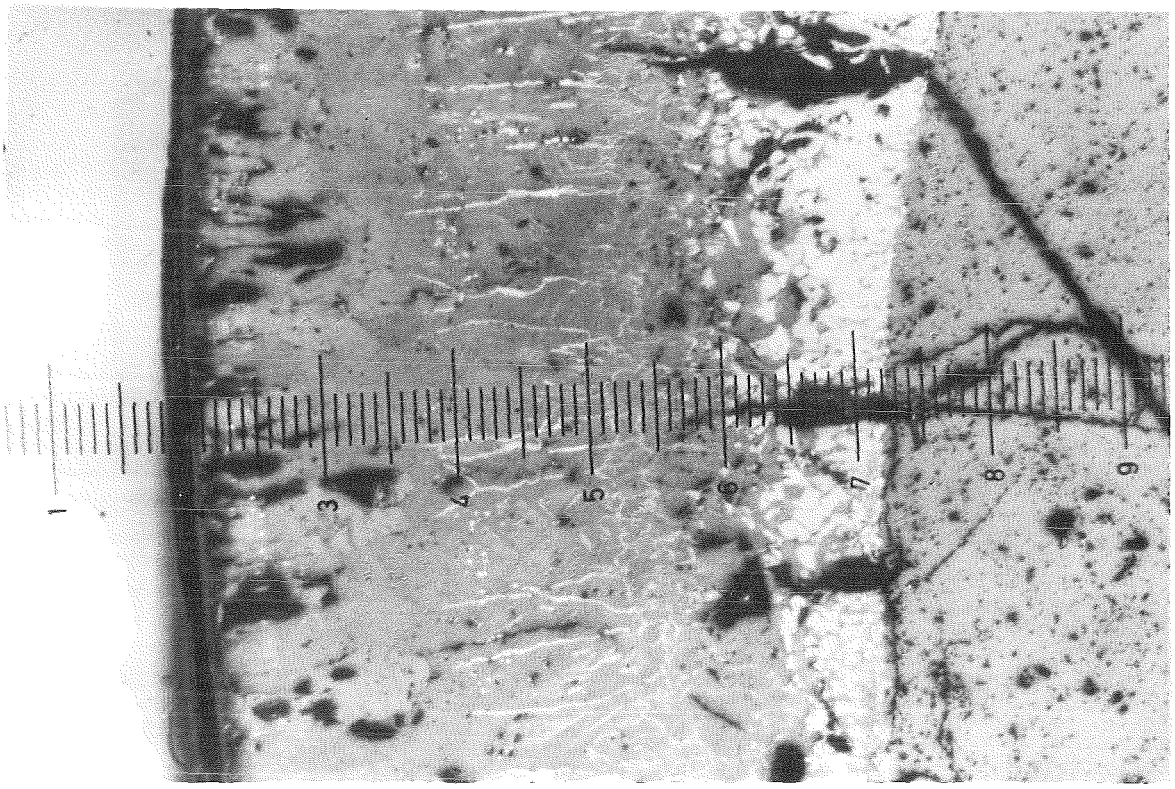

Position g

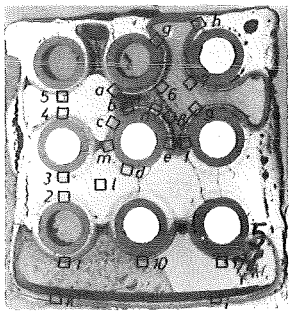

FIG. 47 DETAILS OF THE CROSS SECTION AT 96 MM AT POS. SHOWN IN THE OVERVIEW FIG. 20 (ESBU-1)

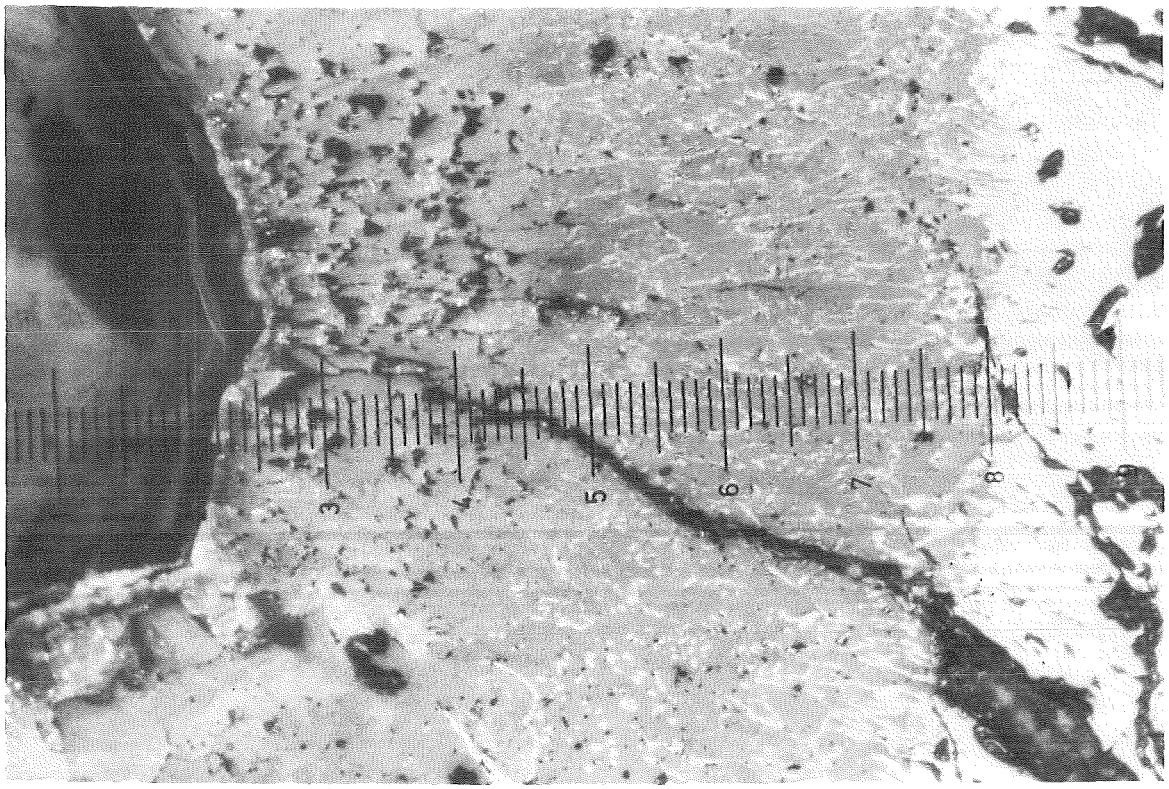

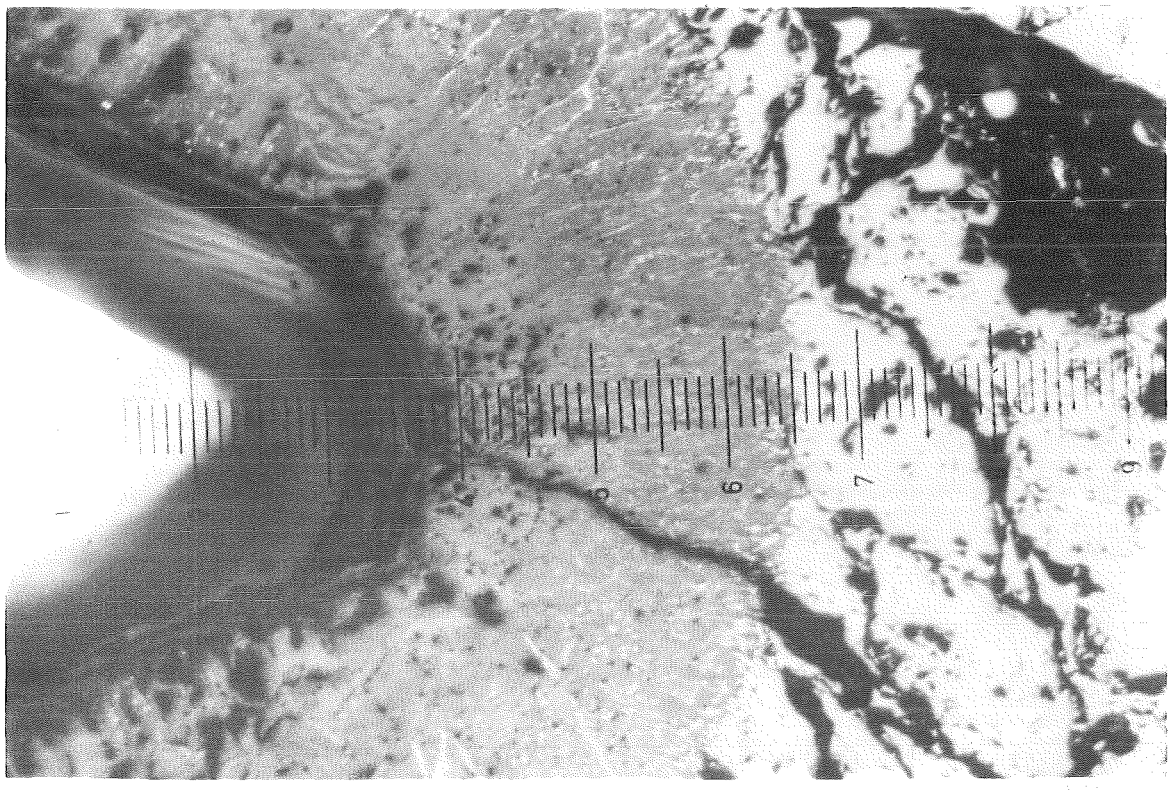

Position h

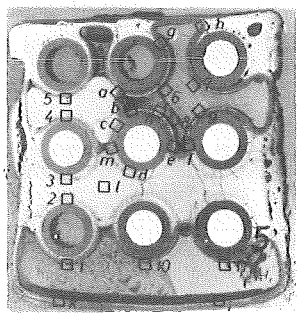

FIG. 48 DETAILS OF THE CROSS SECTION AT 96 MM AT POS. SHOWN IN THE OVERVIEW FIG. 20 (ESBU-1)

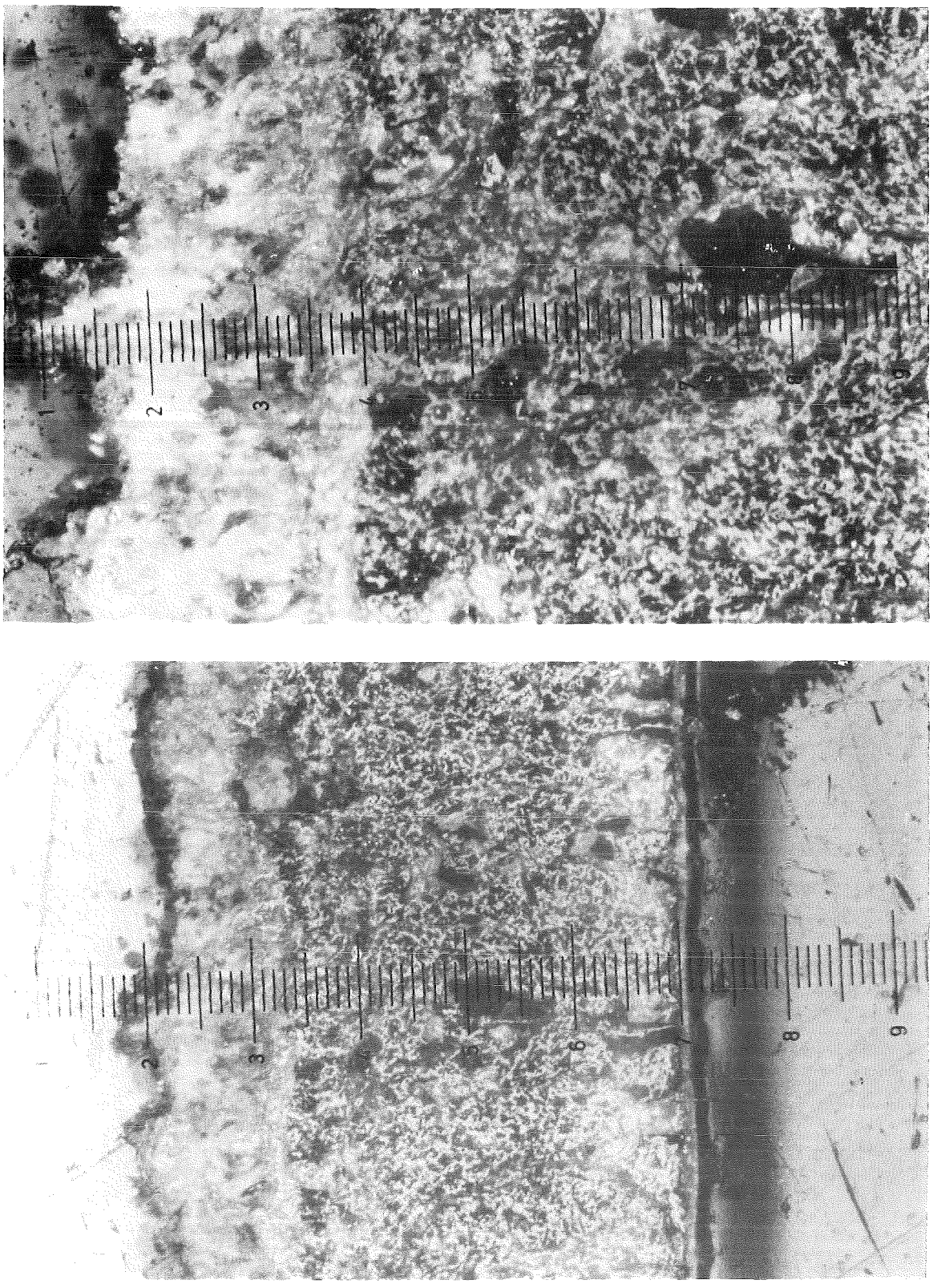

FIG. 49 DETAILS OF THE CROSS SECTION AT 96 MM AT POSITIONS SHOWN IN THE OVERVIEW FIG. 20 (ESBU-1)

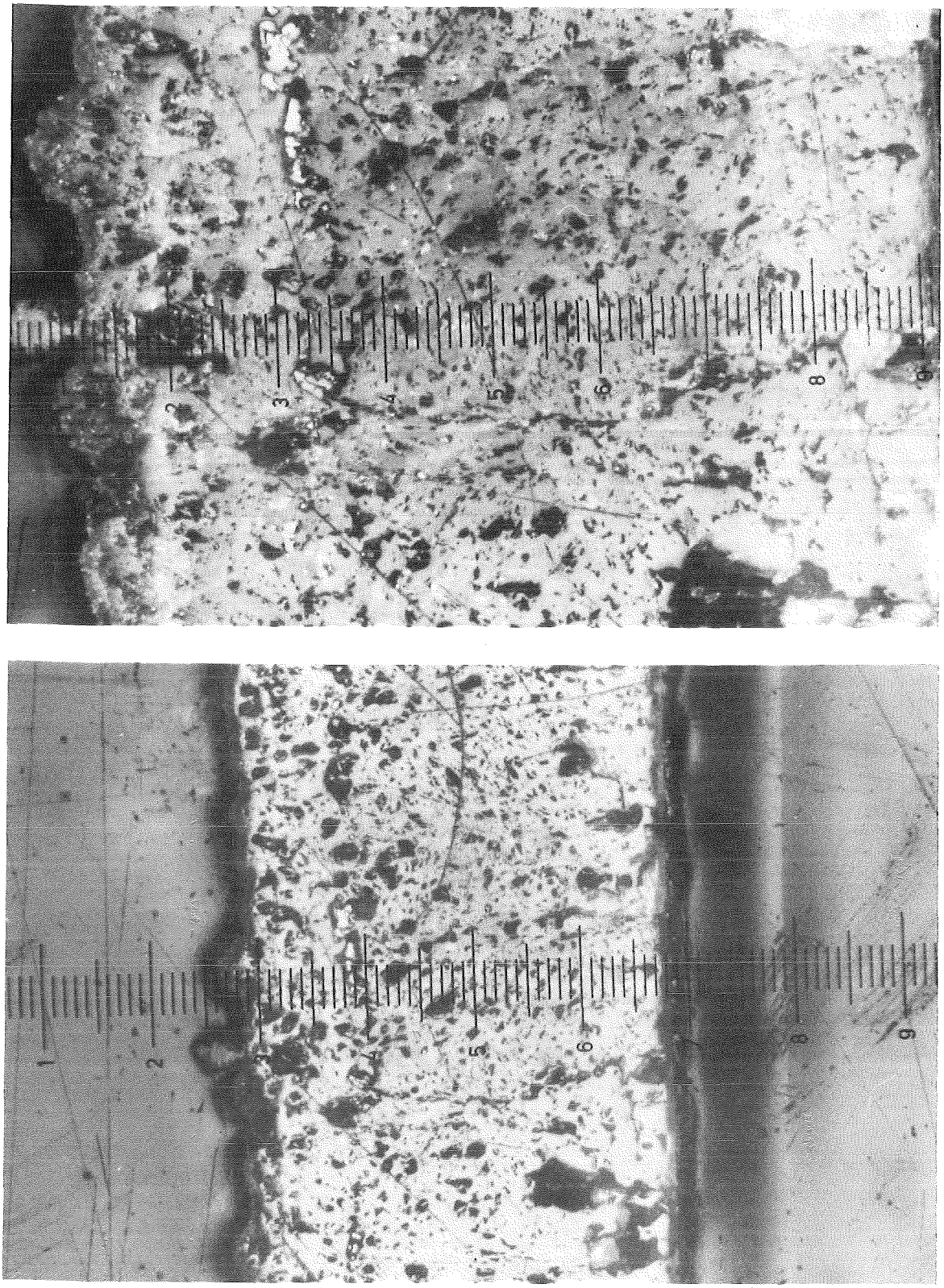

Position k

FIG. 50 DETAILS OF THE CROSS SECTION AT 96 MM AT POSITIONS SHOWN IN THE OVERVIEW FIG. 20 (ESBU-1)

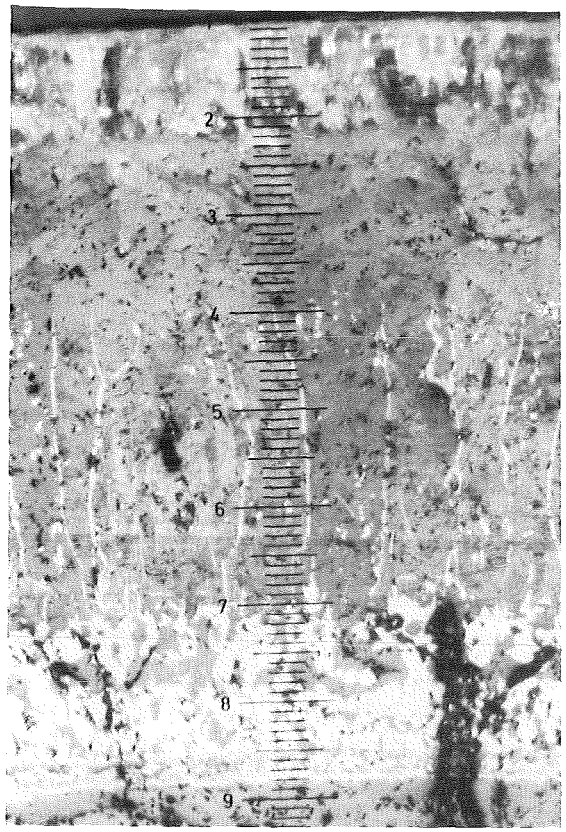

10

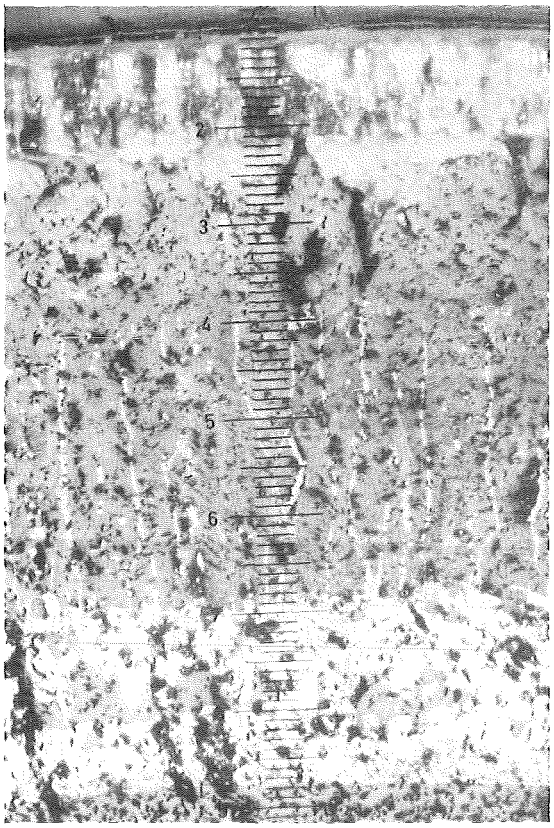

11

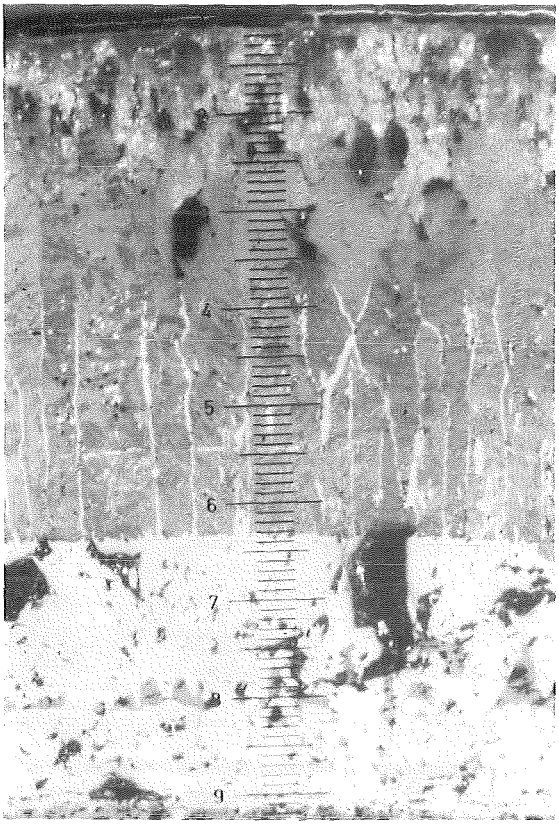

1

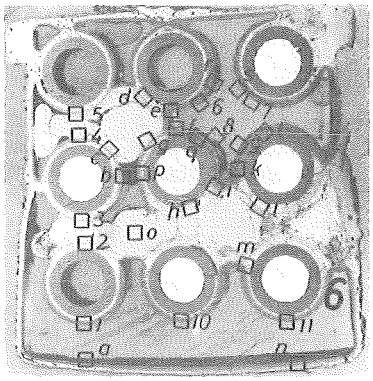

FIG. 51 DETAILS OF THE CROSS SECTION AT 86 MM AT POSITIONS SHOWN IN THE OVERVIEW FIG. 20 (ESBU-1)

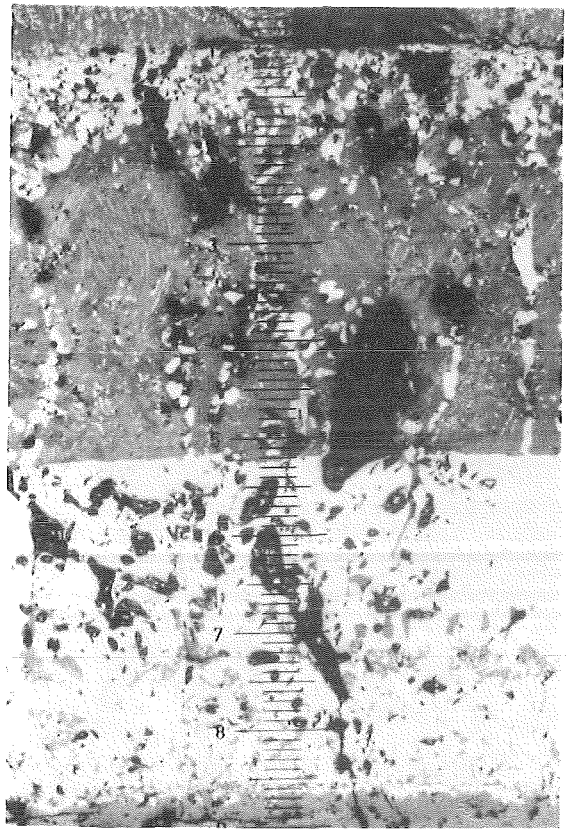

4

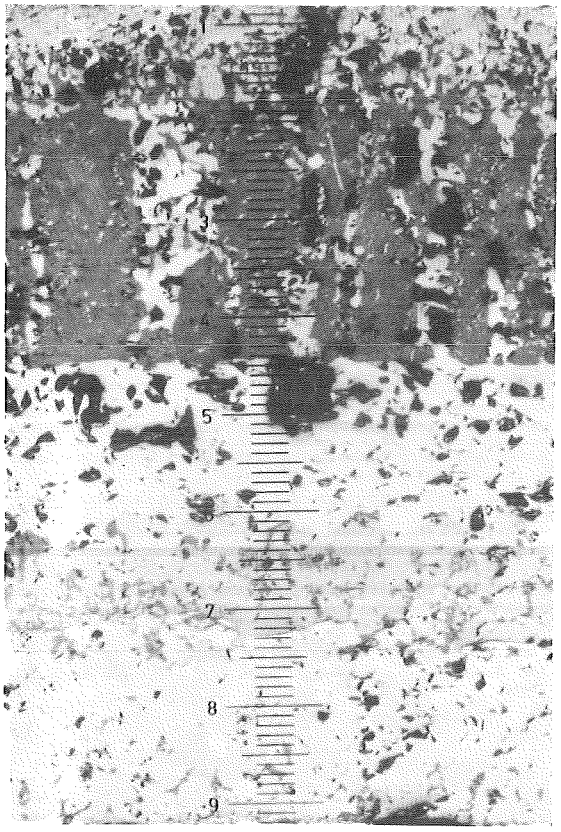

5

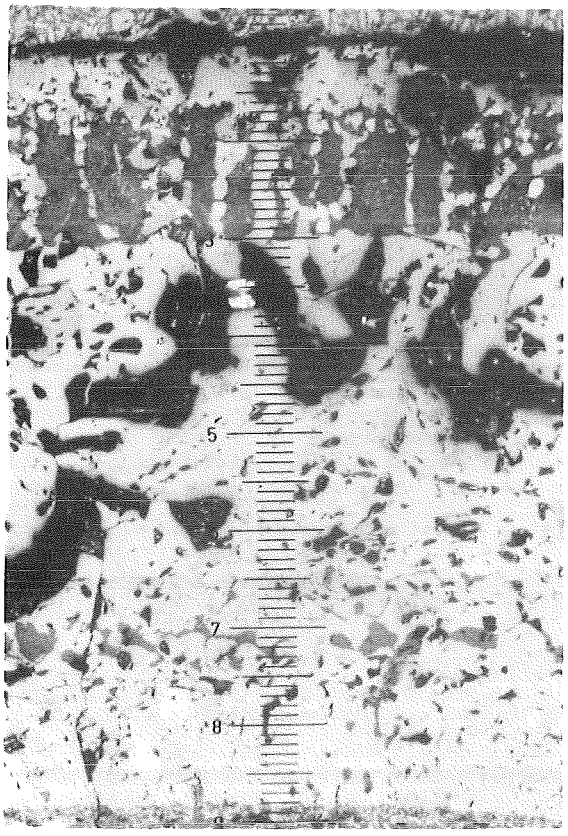

2

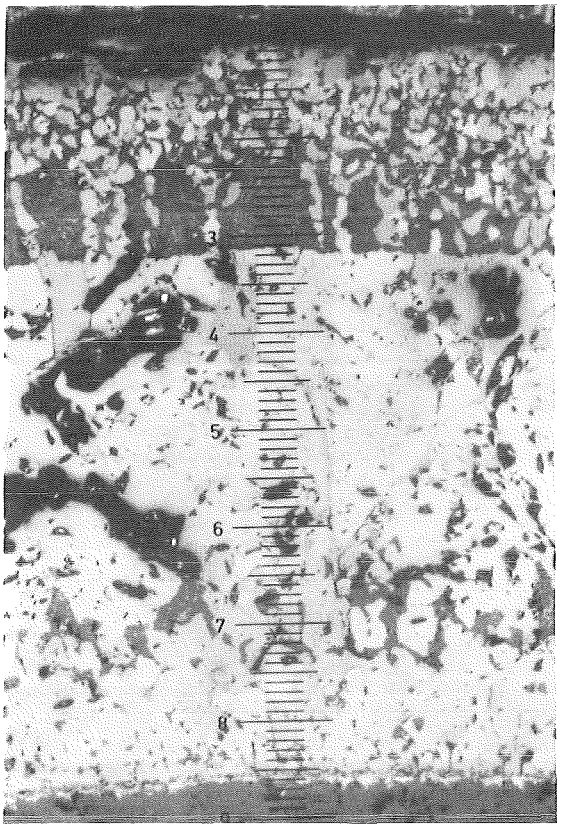

3

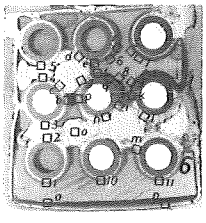

6

FIG. 52 DETAILS OF THE CROSS SECTION AT 86 MM AT POS. SHOWN IN THE OVERVIEW FIG. 20 (ESBU-1)

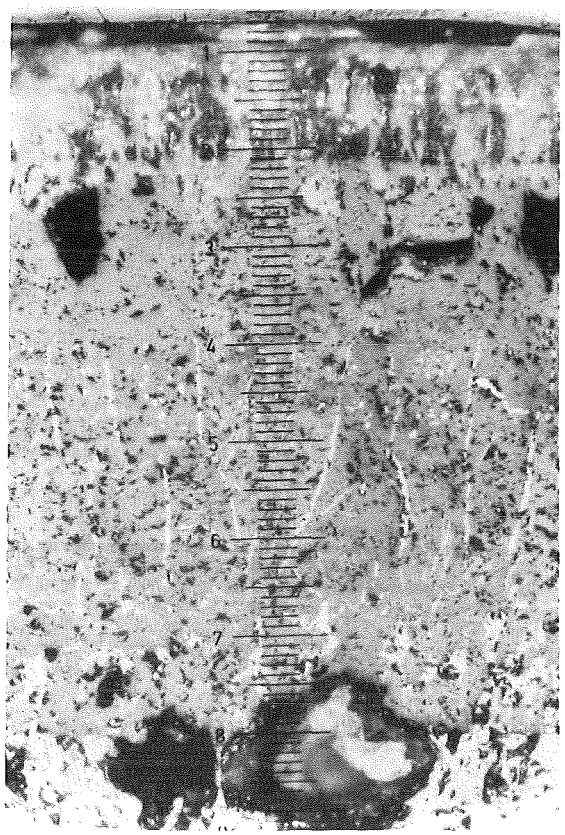

6

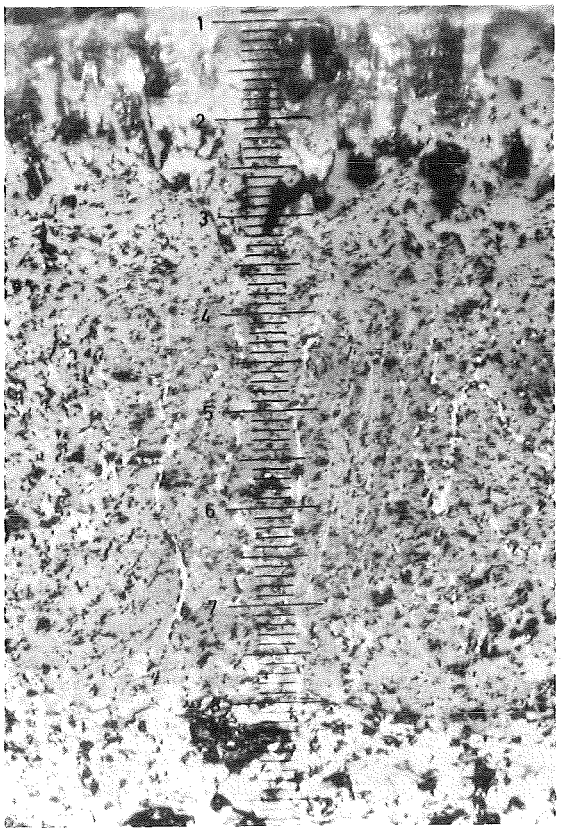

7

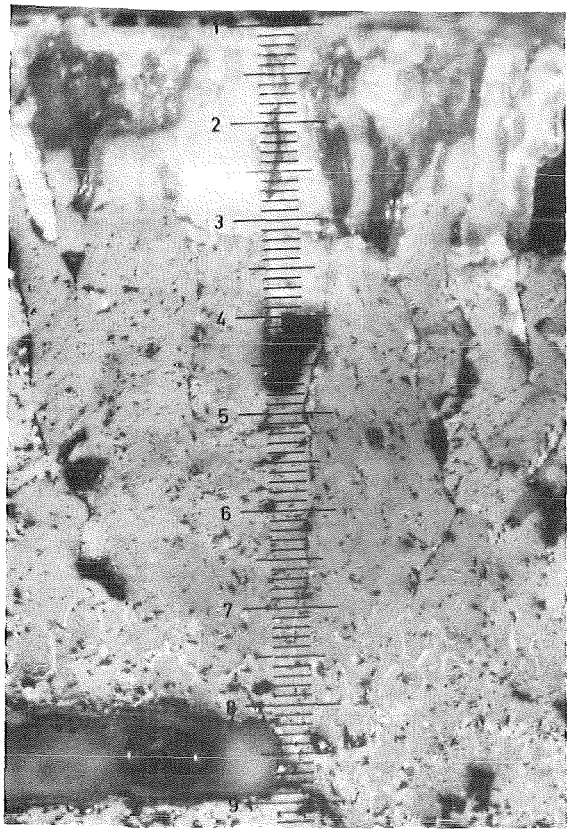

8

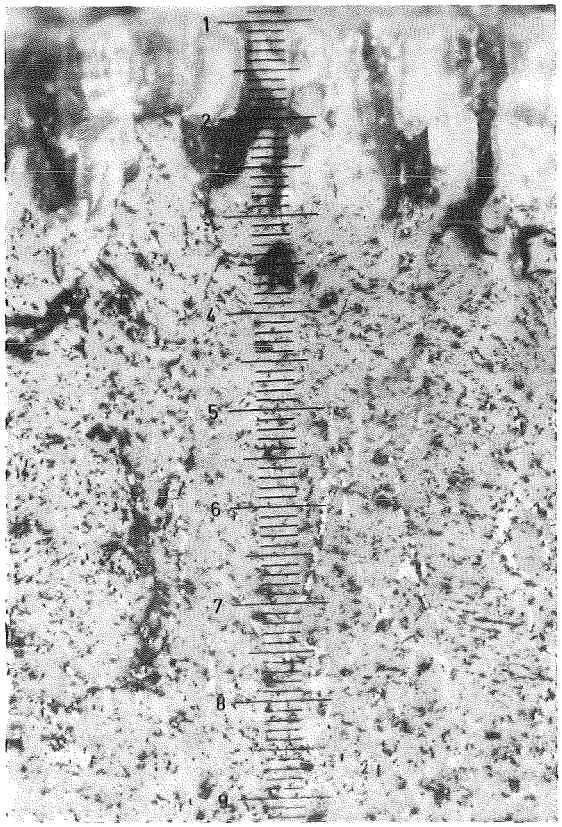

9

FIG. 53 DETAILS OF THE CROSS SECTION AT 86 MM AT POS. SHOWN IN THE OVERVIEW FIG. 20 (ESBU-1)

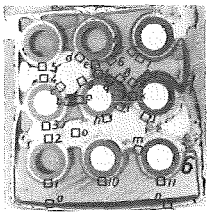

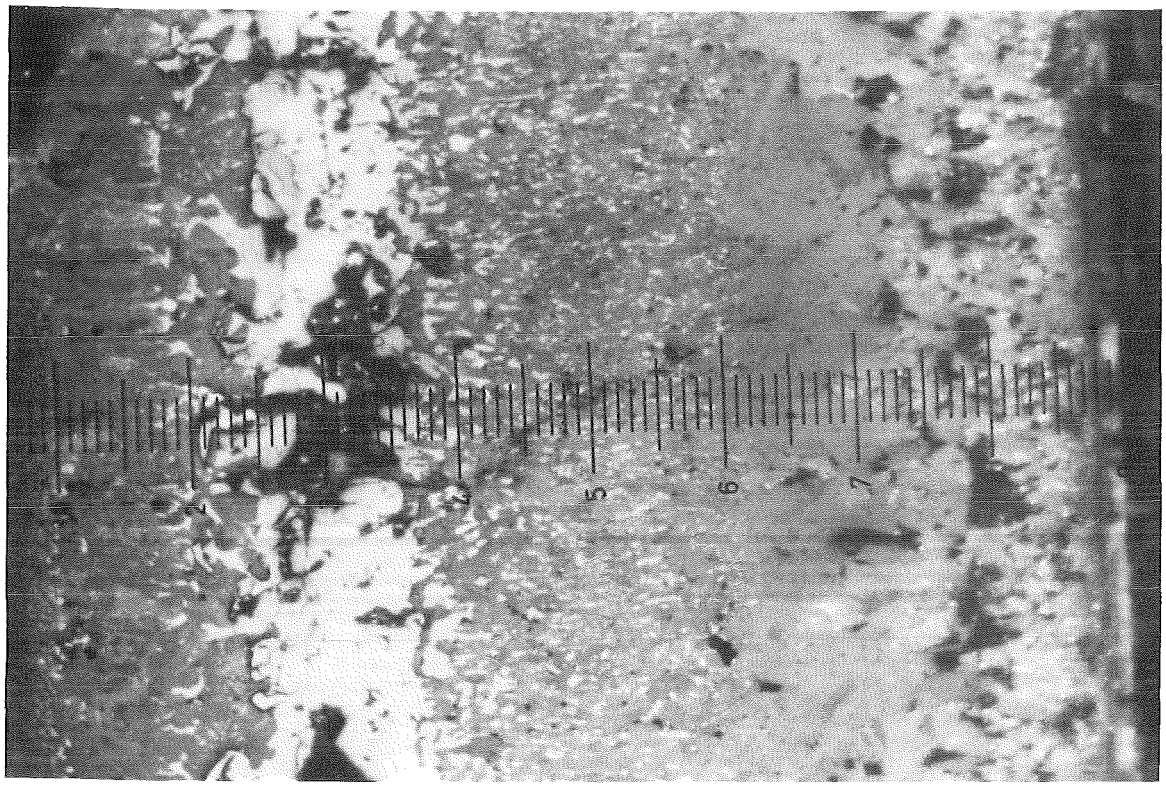

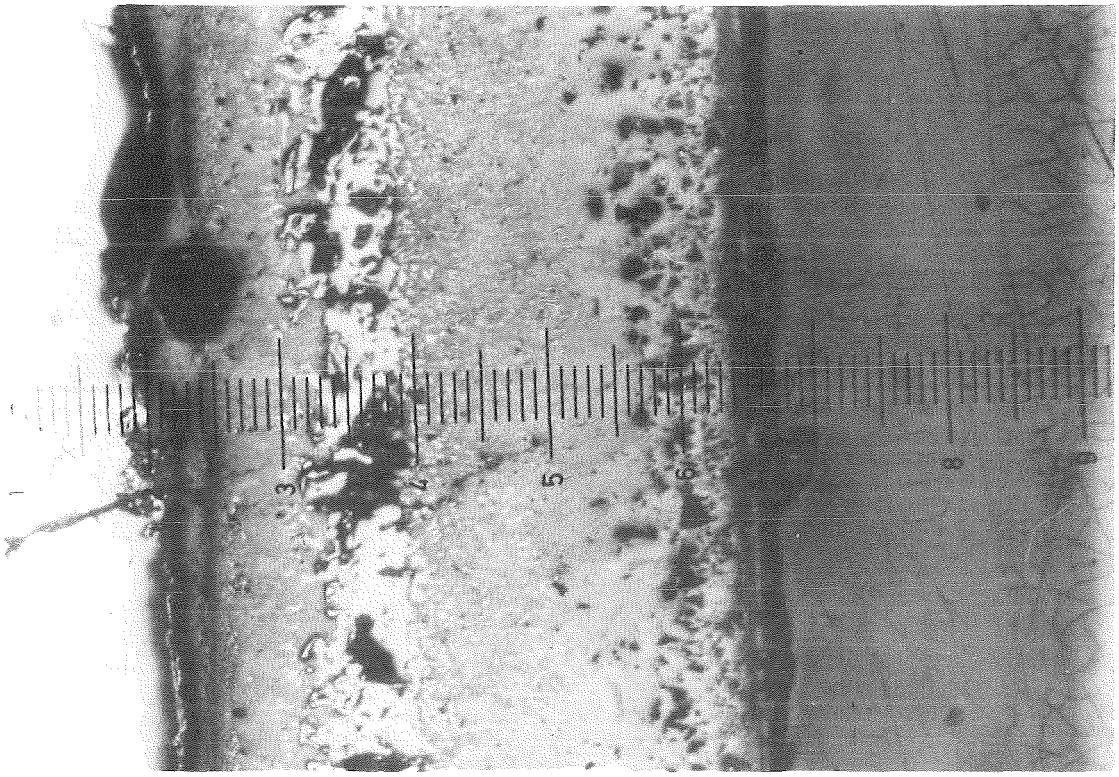

Position a

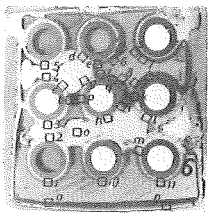

FIG. 54 DETAILS OF THE CROSS SECTION AT 86 MM AT POS. SHOWN IN THE OVERVIEW FIG. 20 (ESBU-1)

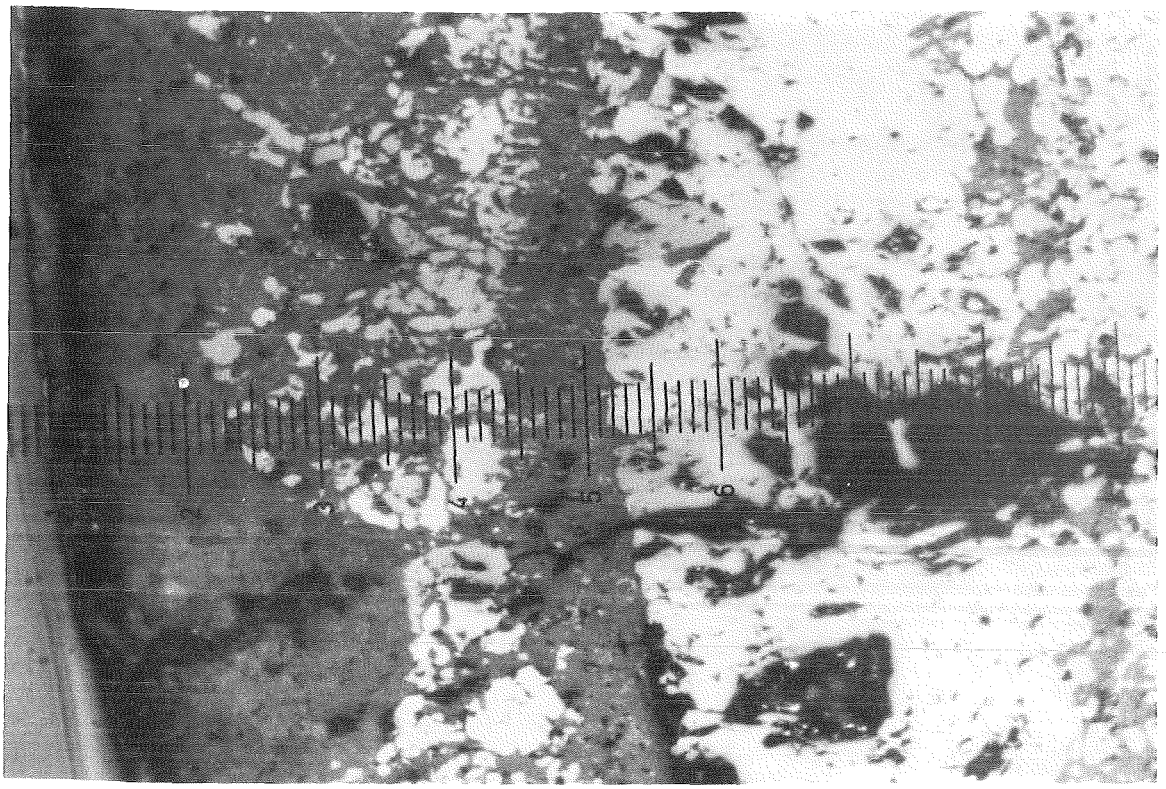

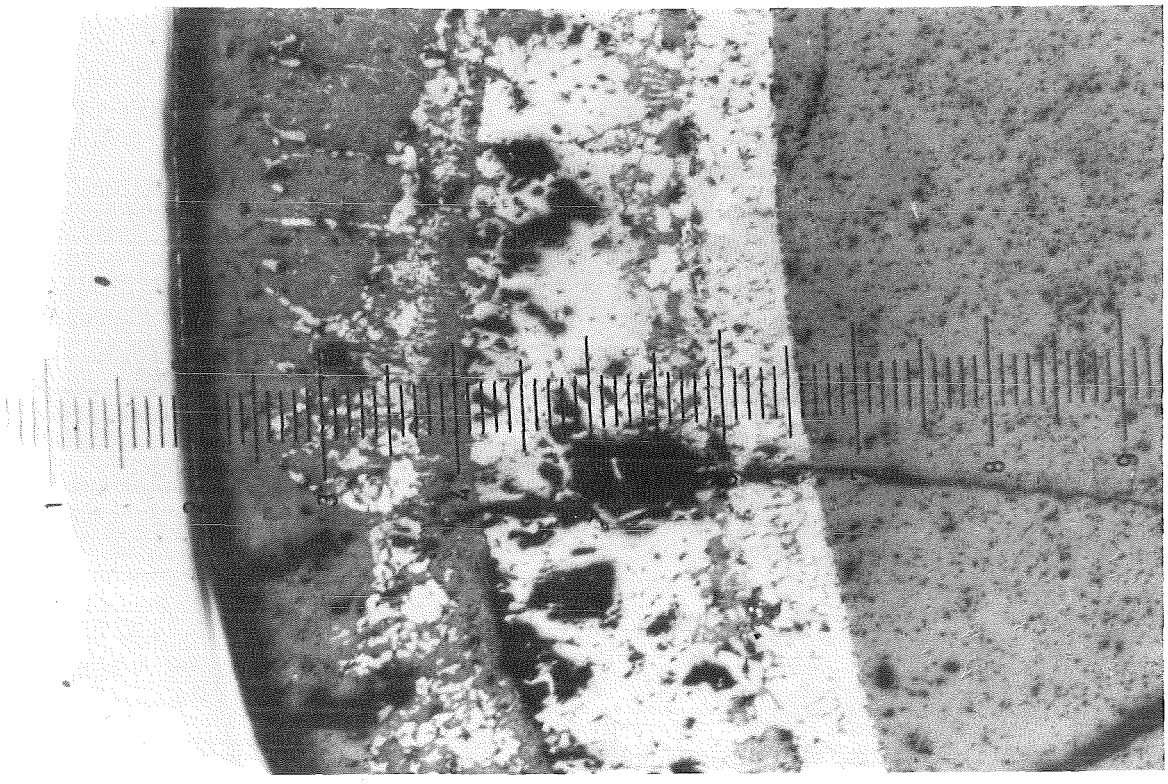

Position b

FIG. 55 DETAILS OF THE CROSS SECTION AT 86 MM AT POS. SHOWN IN THE OVERVIEW FIG. 20 (ESBU-1)

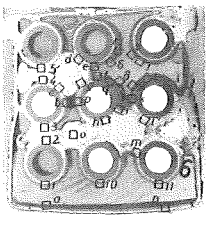

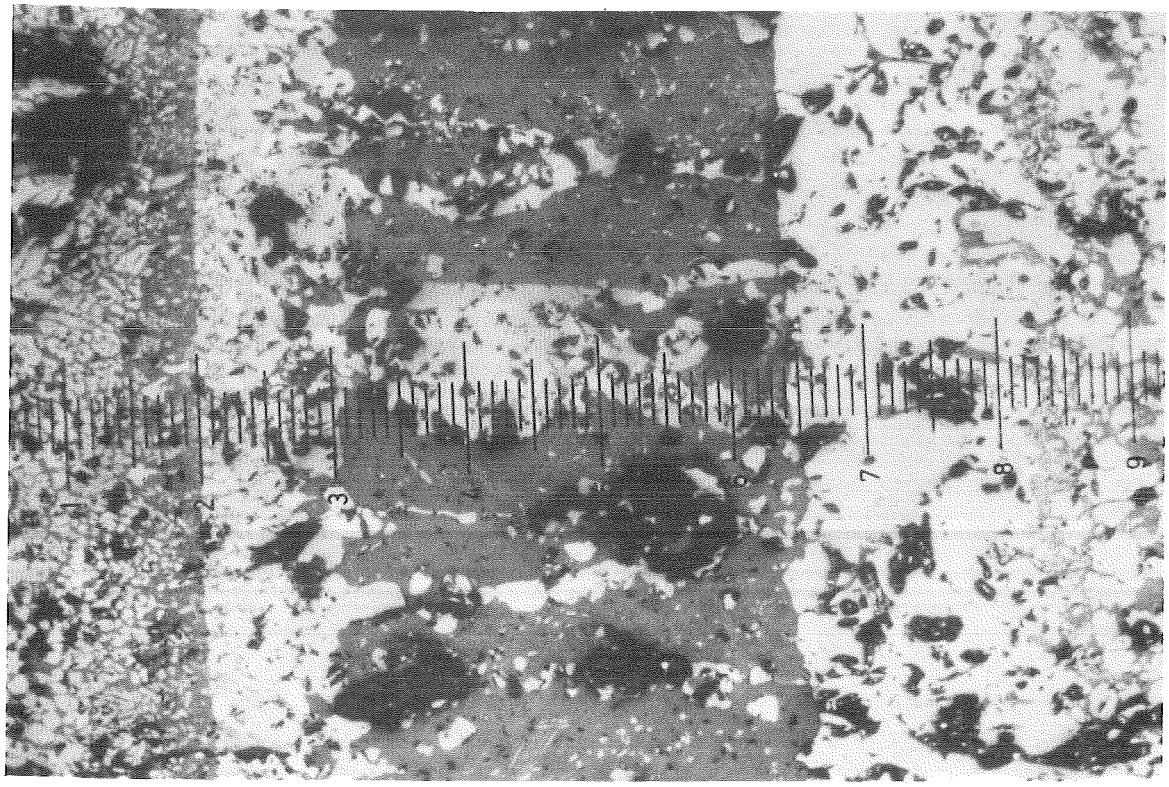

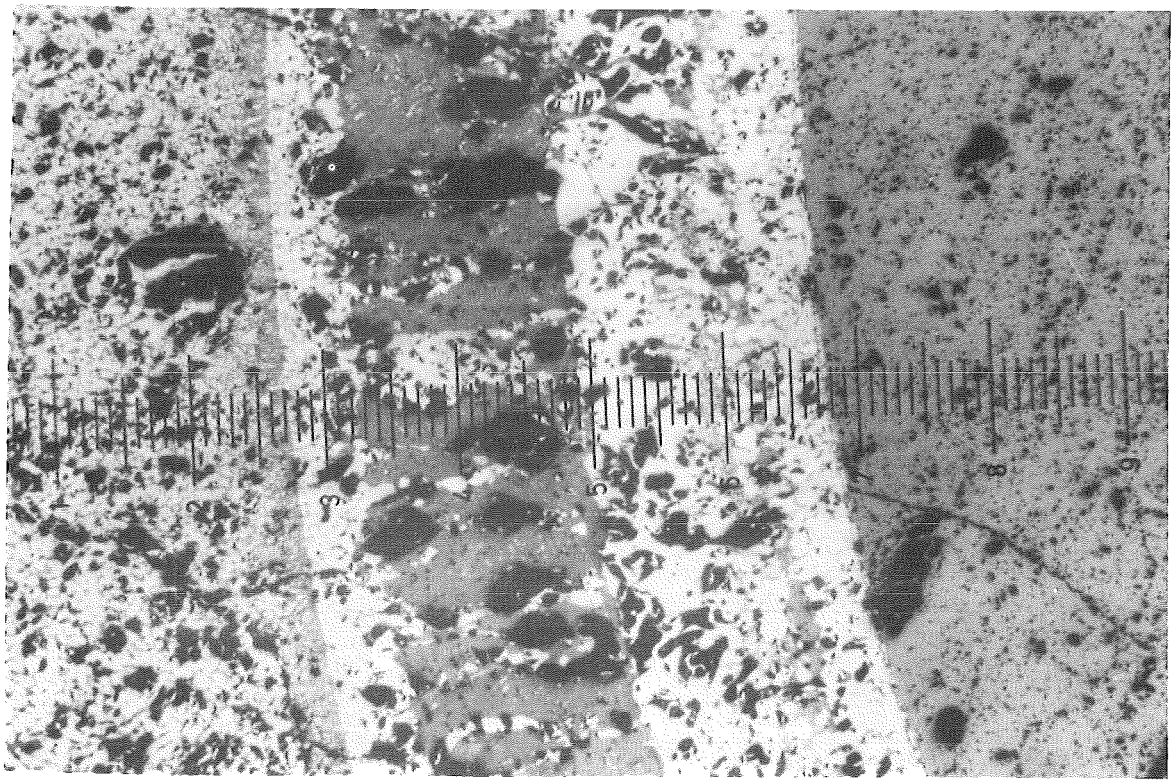

Position c

FIG. 56 DETAILS OF THE CROSS SECTION AT 86 MM AT POS. SHOWN IN THE OVERVIEW FIG. 20 (ESBU-1)

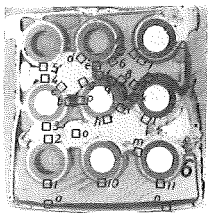

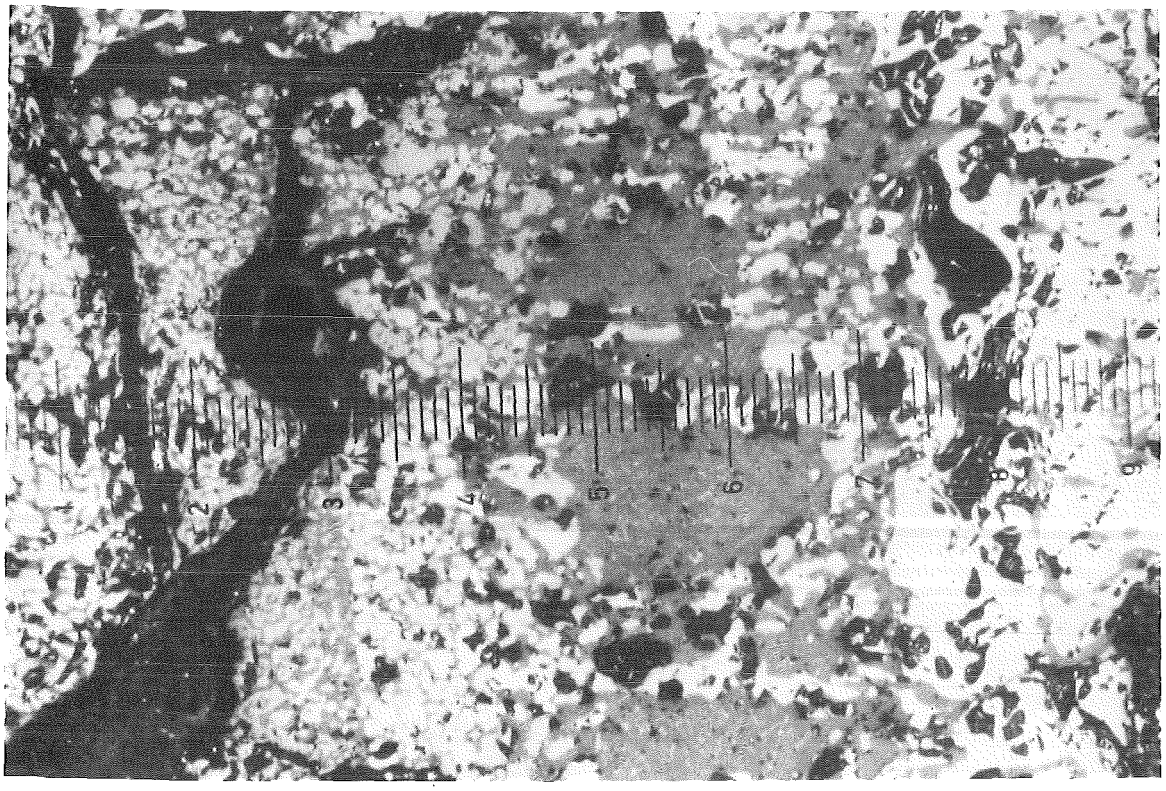

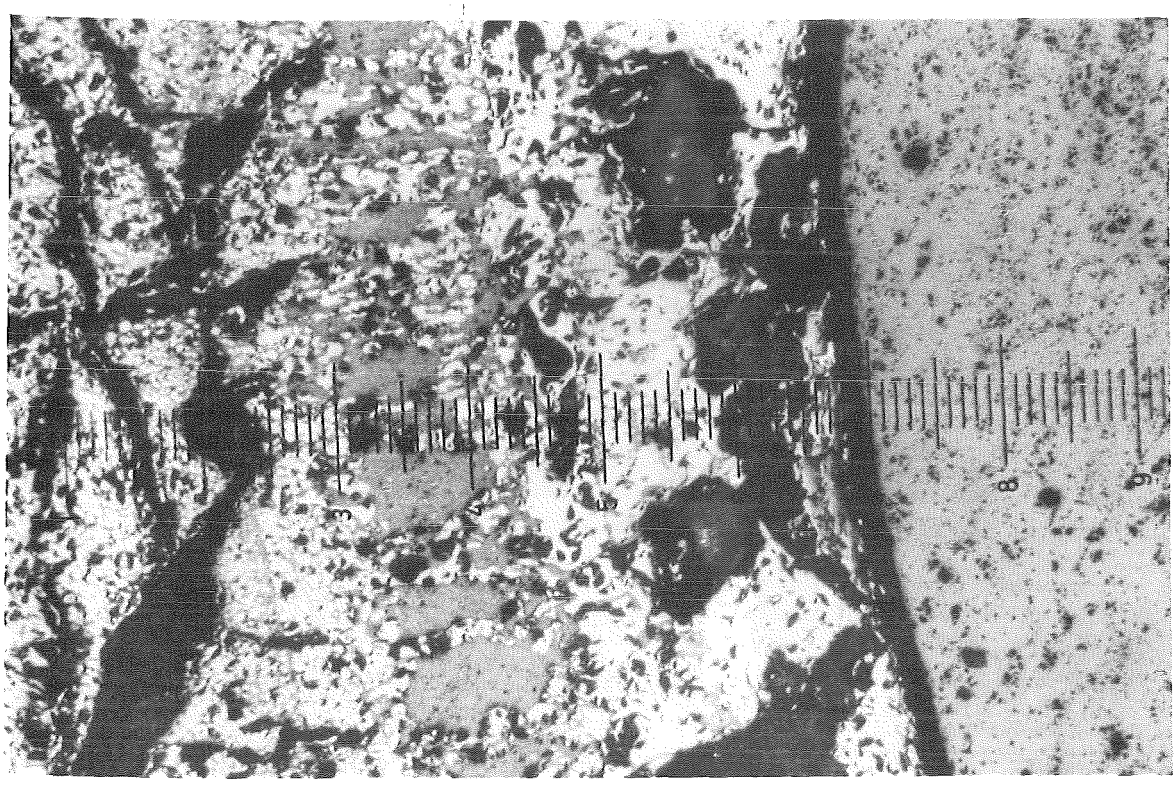

Position d

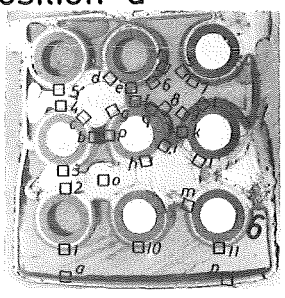

FIG.57 DETAILS OF THE CROSS SECTION AT 86 MM AT POS. SHOWN IN THE OVERVIEW FIG. 20 (ESBU-1)

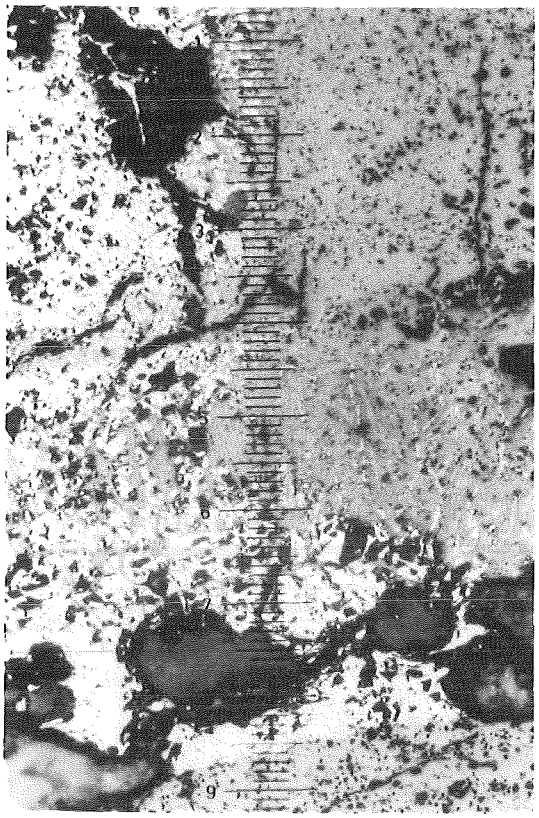

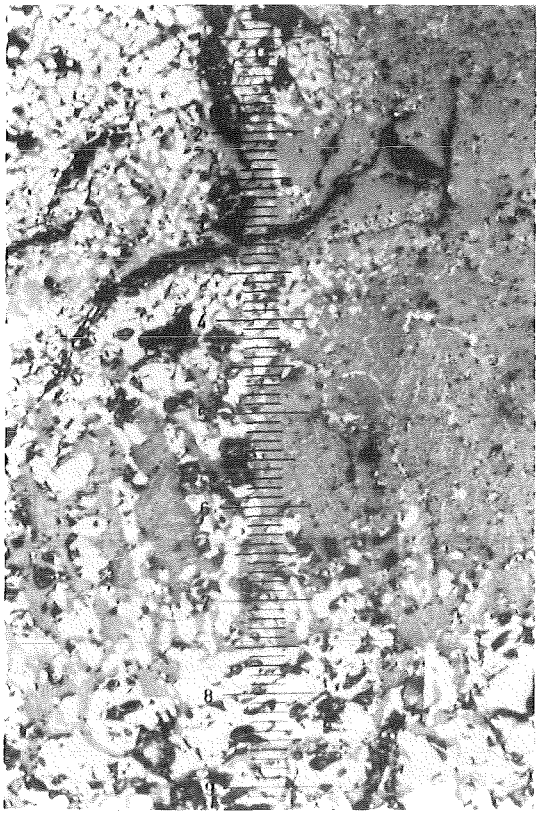

Position e

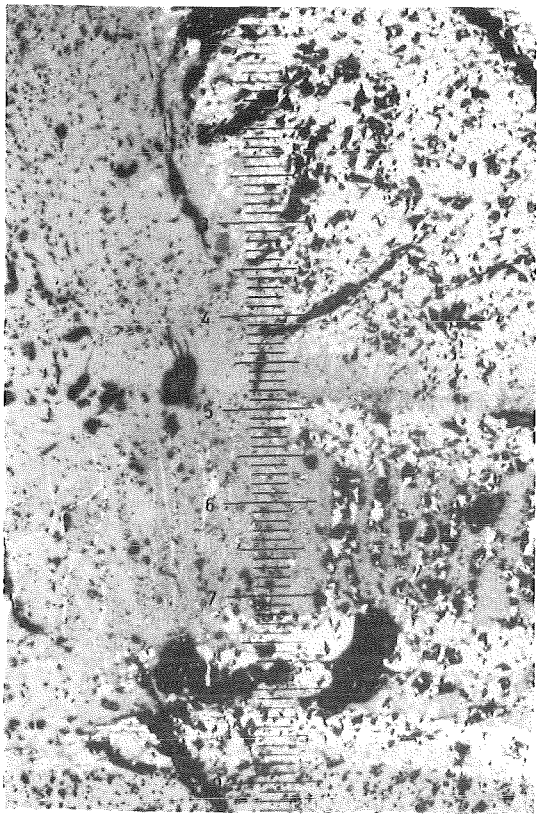

50x

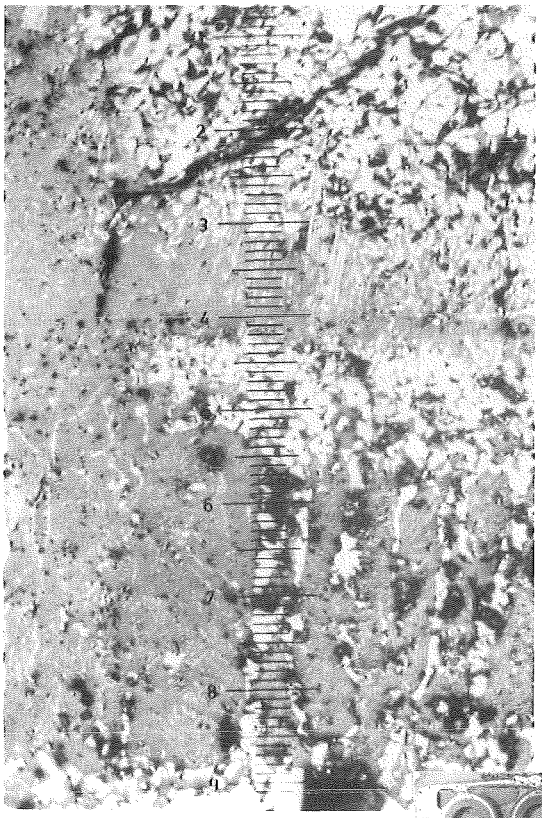

100x Position f

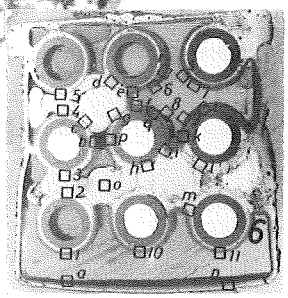

FIG. 58 DETAILS OF THE CROSS SECTION AT 86 MM AT POS. SHOWN IN THE OVERVIEW FIG. 20 (ESBU-1)

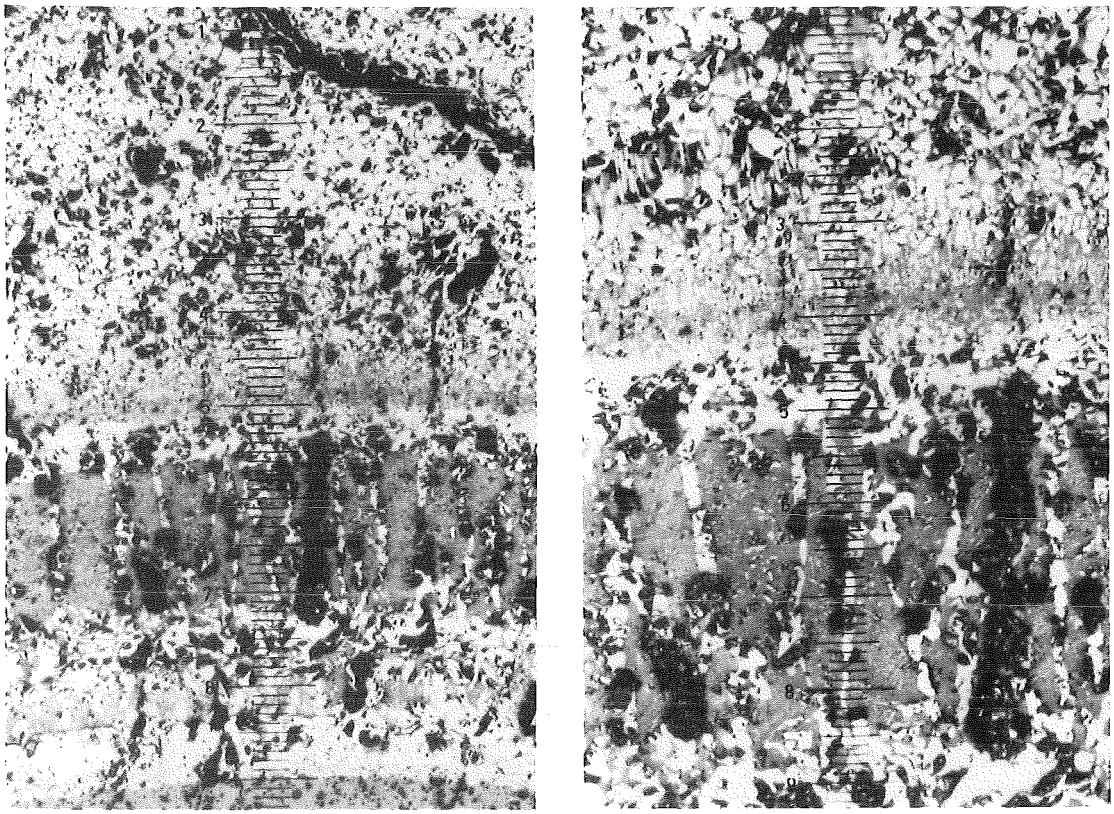

Position g

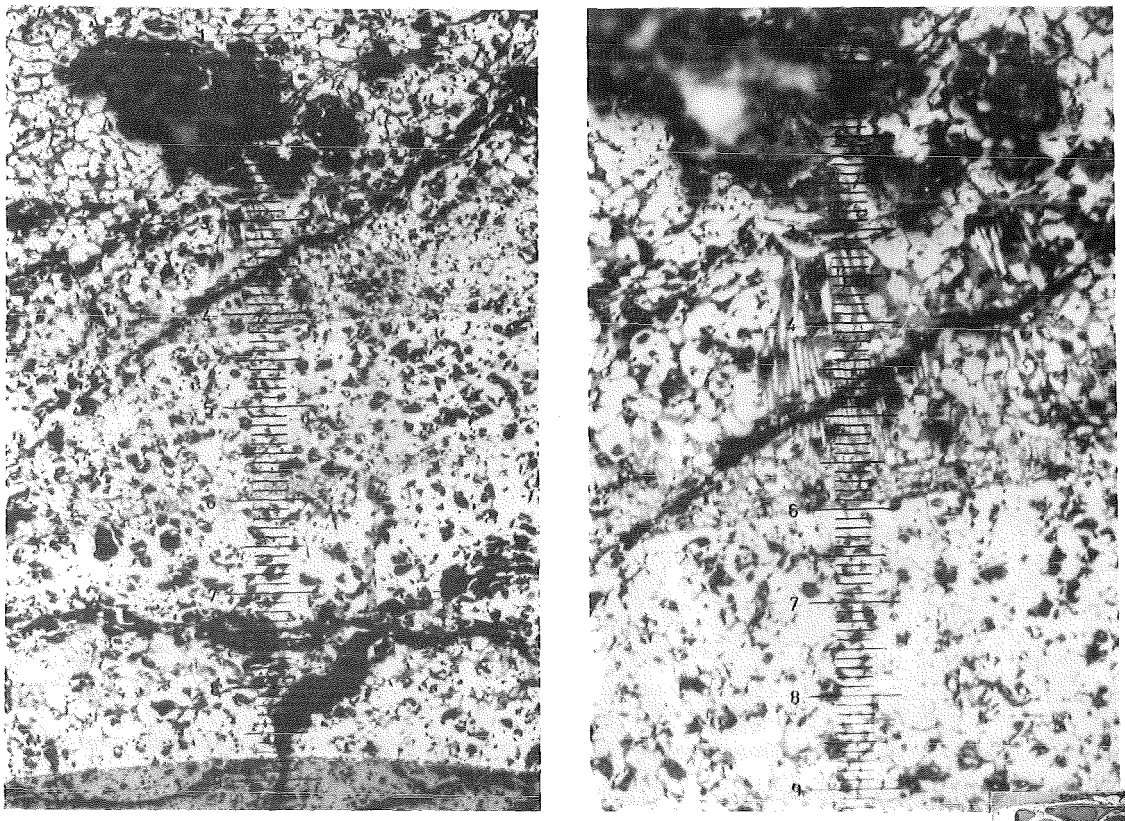

50 x

100x Position h

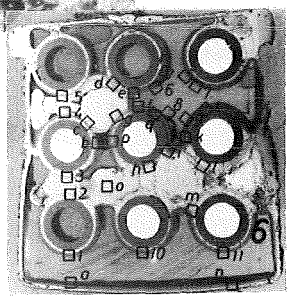

FIG. 59 DETAILS OF THE CROSS SECTION AT 86 MM AT POS. SHOWN IN THE OVERVIEW FIG. 20 (ESBU-1)

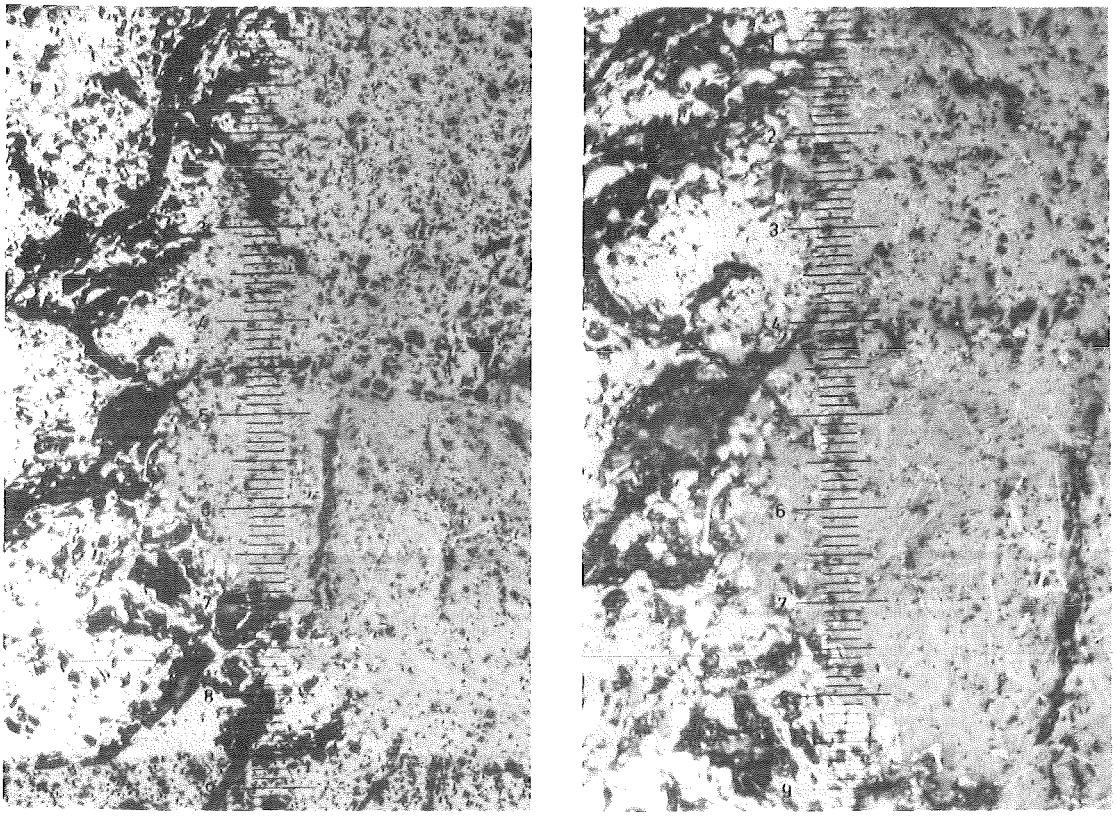

Position i

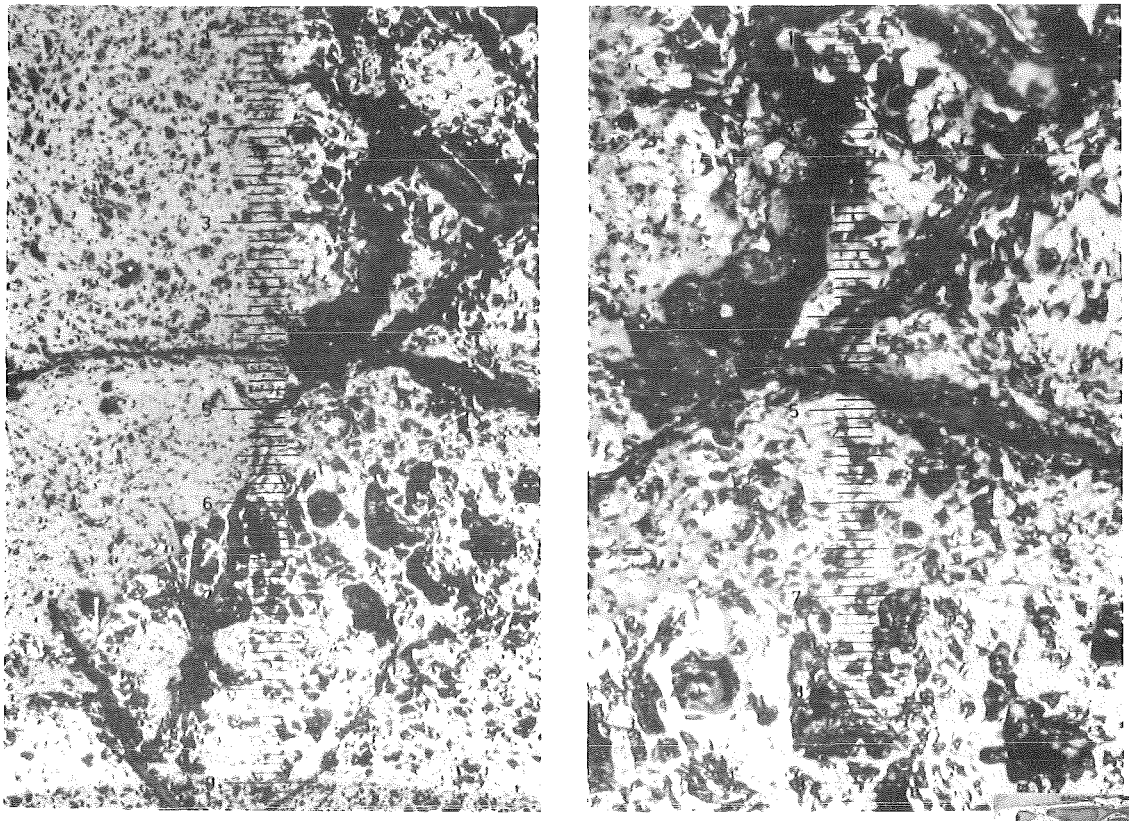

50 x

100 x Pos. k

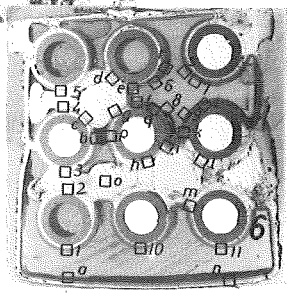

FIG. 60 DETAILS OF THE CROSS SECTION AT 86 MM AT POS. SHOWN IN THE OVERVIEW FIG. 20 (ESBU-1)

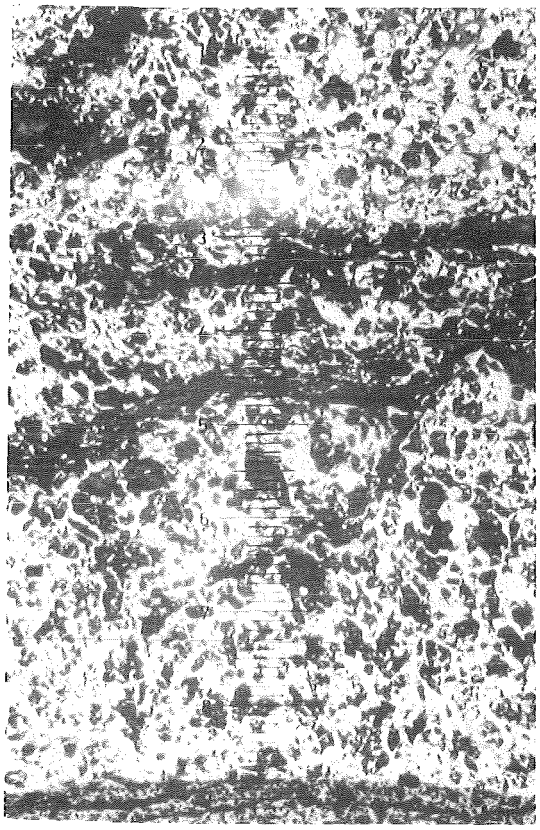

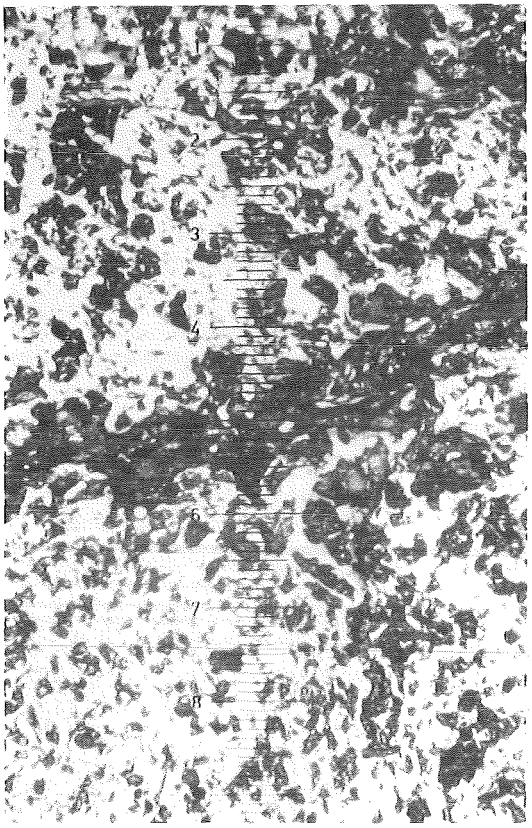

Position l

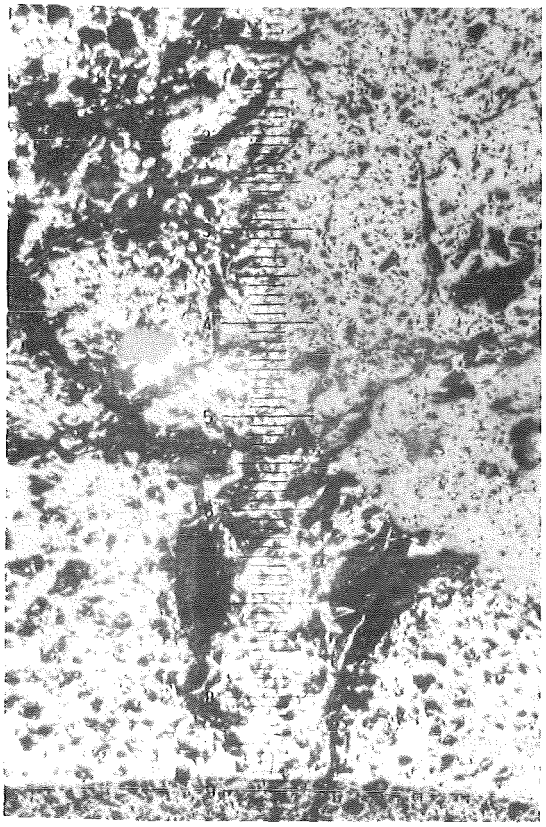

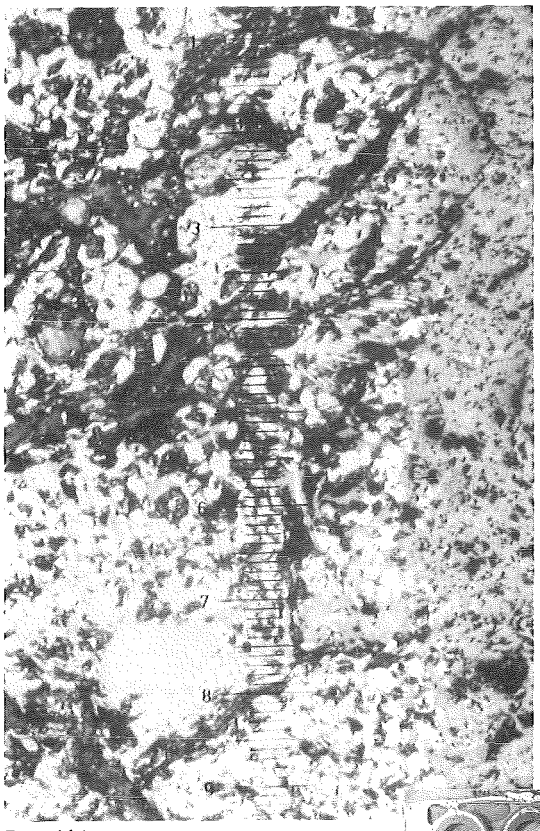

Position m

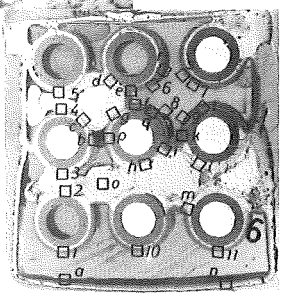

FIG. 61 DETAILS OF THE CROSS SECTION AT 86 MM AT POS. SHOWN IN THE OVERVIEW FIG. 20 (ESBU-1)

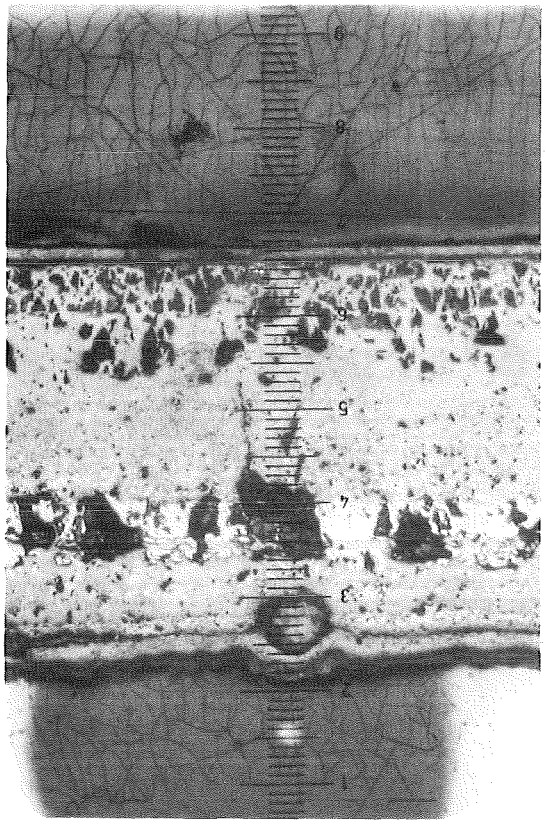

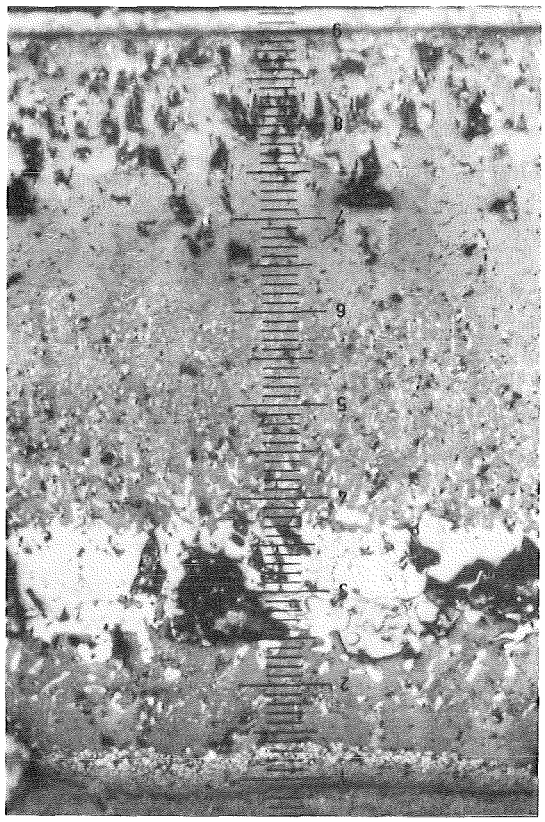

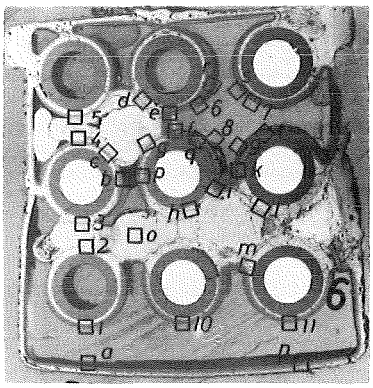

Position n

FIG.62 DETAILS OF THE CROSS SECTION AT 86 MM AT POSITIONS SHOWN IN THE OVERVIEW FIG.20 (ESBU-1)

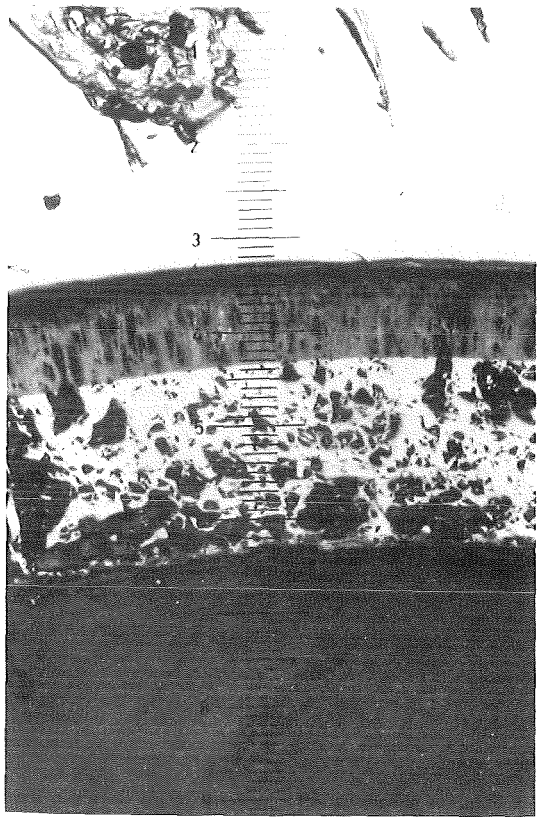

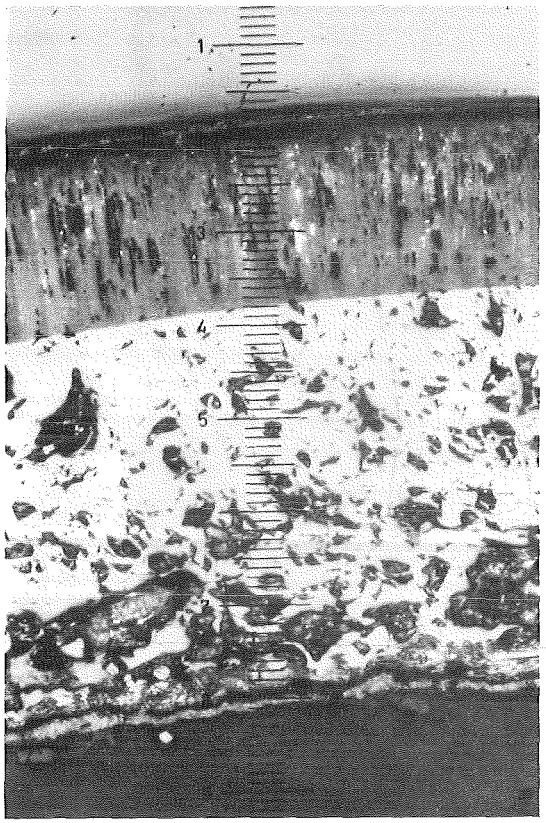

1

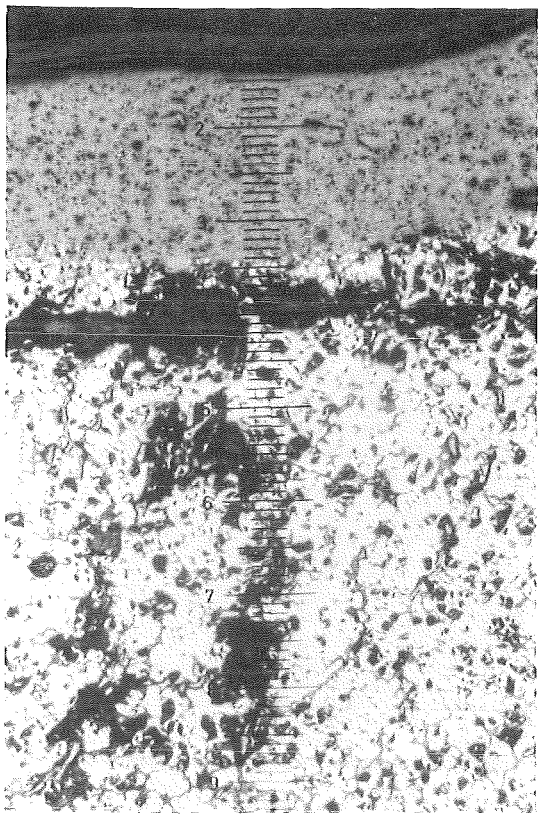

50 x

100 x

2

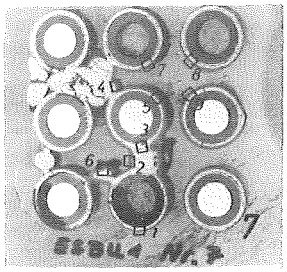

FIG.63 DETAILS OF THE CROSS SECTION AT 76 MM AT POS. SHOWN IN THE OVERVIEW FIG.20 (ESBU-1)

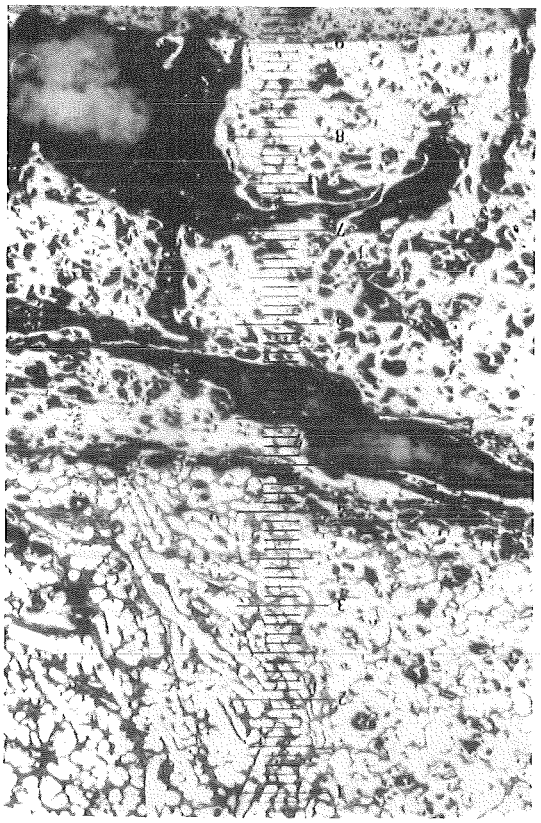

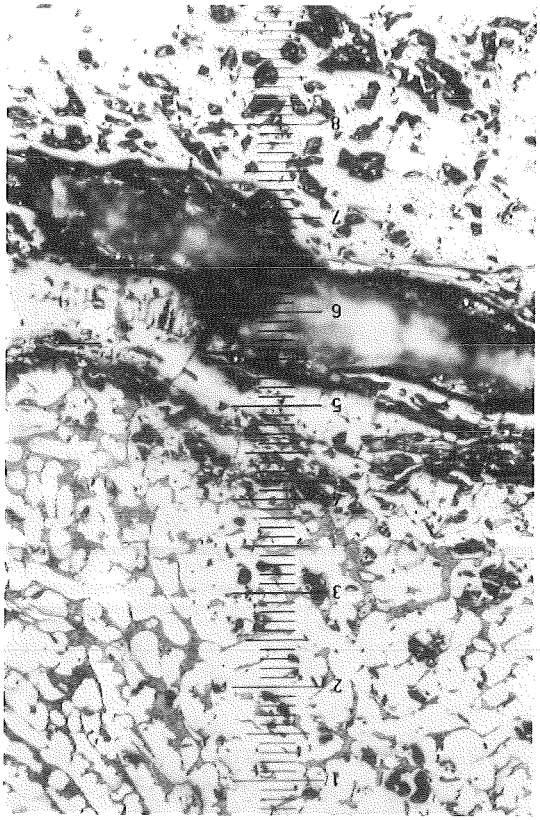

3

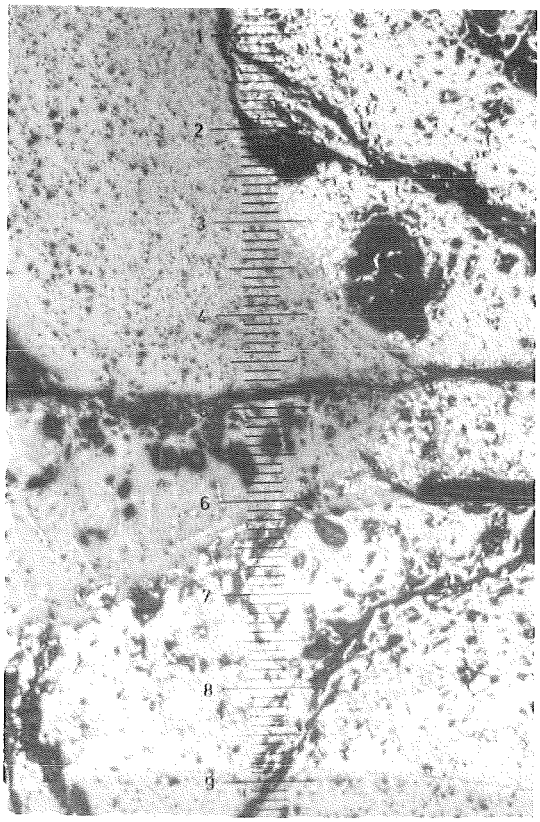

4

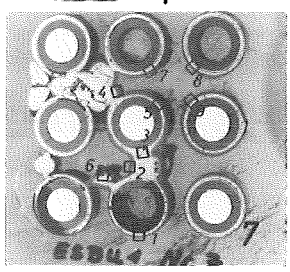

FIG. 64 DETAILS OF THE CROSS SECTION AT 76 MM AT POS. SHOWN IN THE OVERVIEW FIG. 20 (ESBU-1)

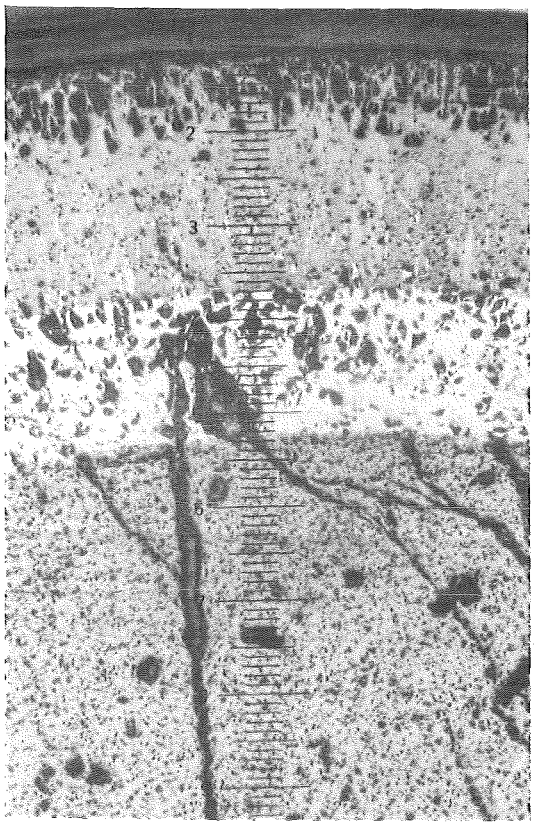

5

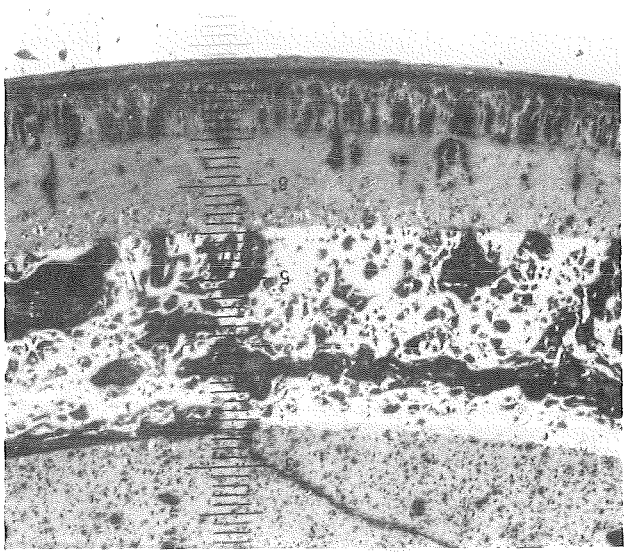

7

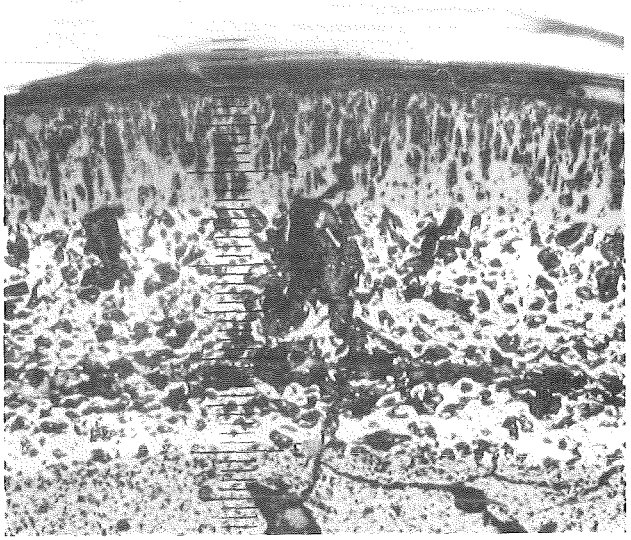

8

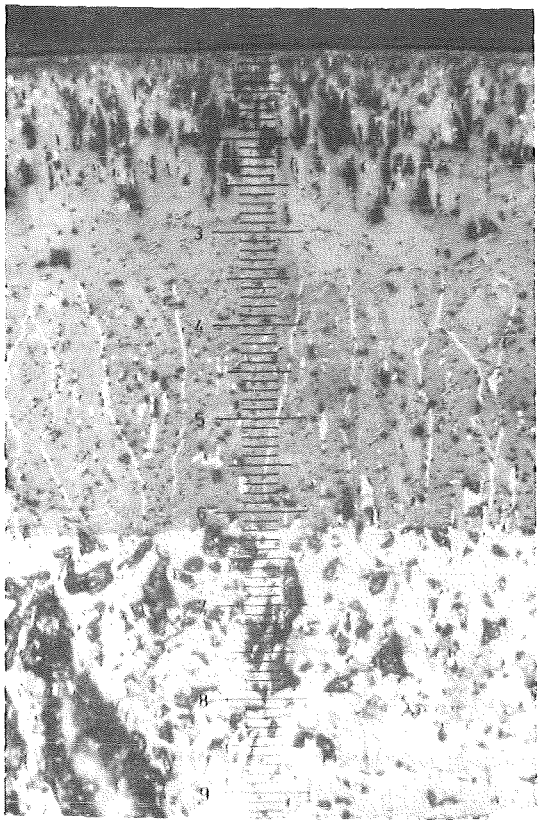

5

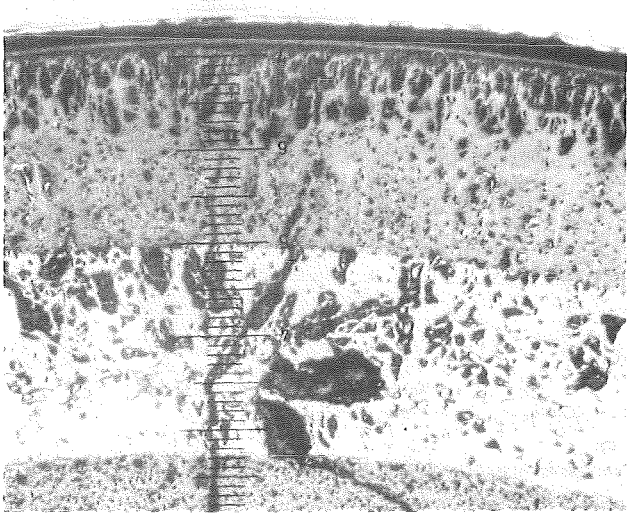

9

FIG. 65 DETAILS OF THE CROSS SECTION AT 76 MM AT POS. SHOWN IN THE OVERVIEW FIG. 20 (ESBU-1)

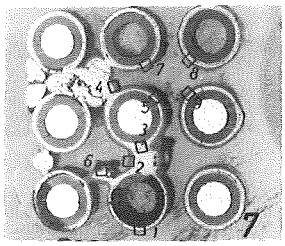

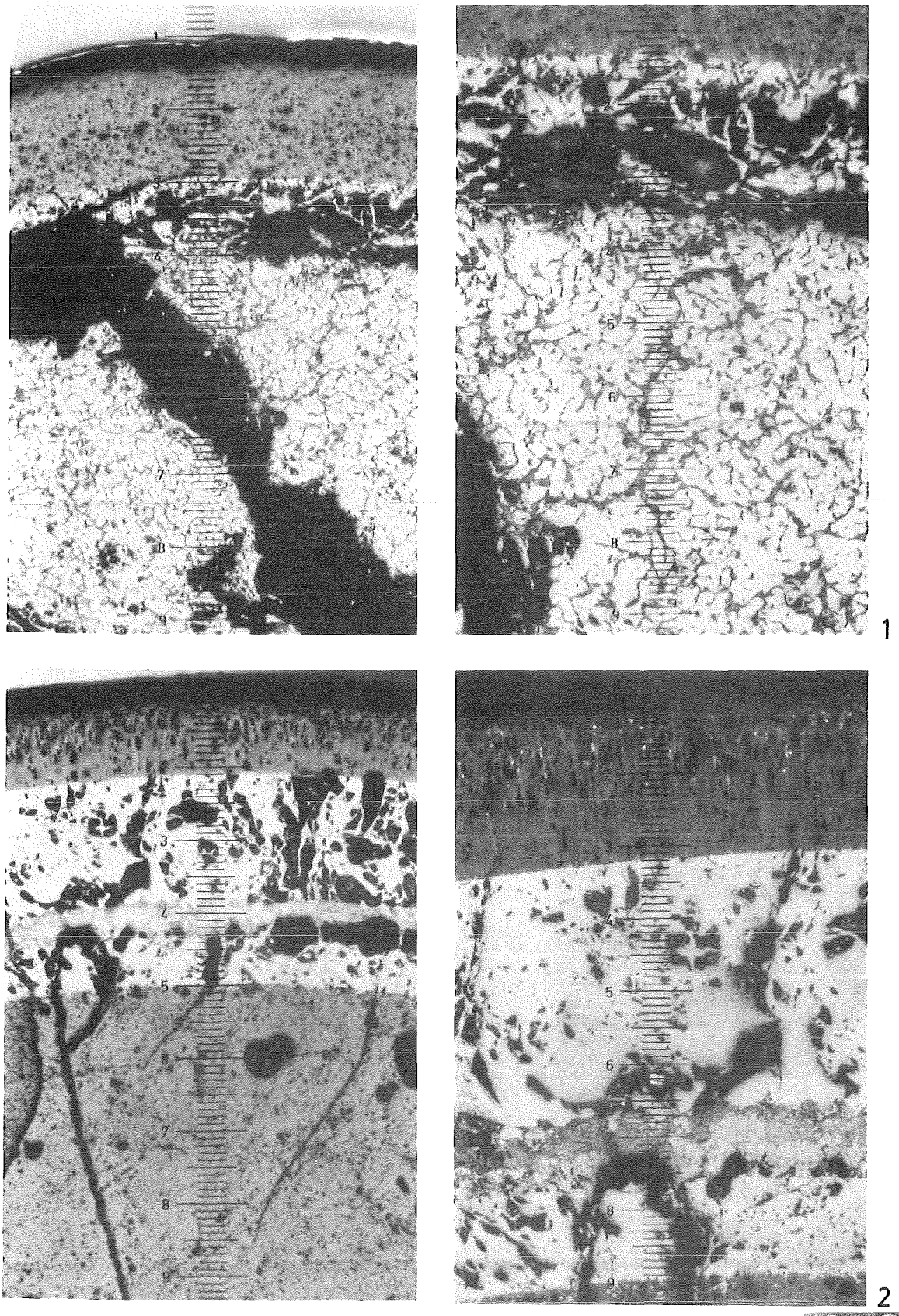

FIG. 66 DETAILS OF THE CROSS SECTION AT 66 MM AT POS. SHOWN IN THE OVERVIEW FIG. 20 (ESBU-1)

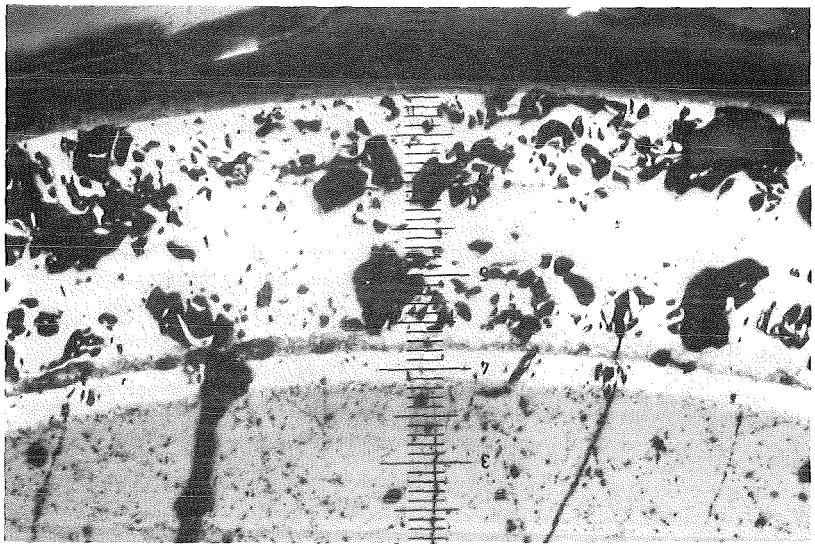

4

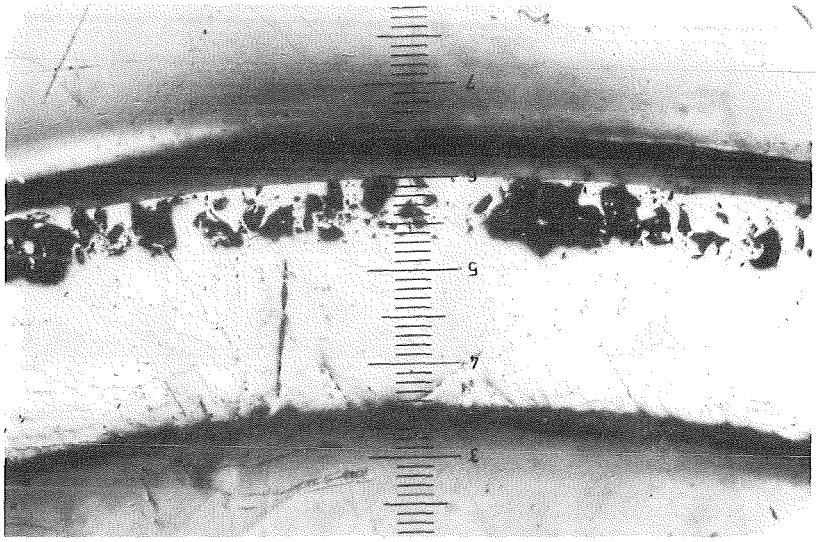

5

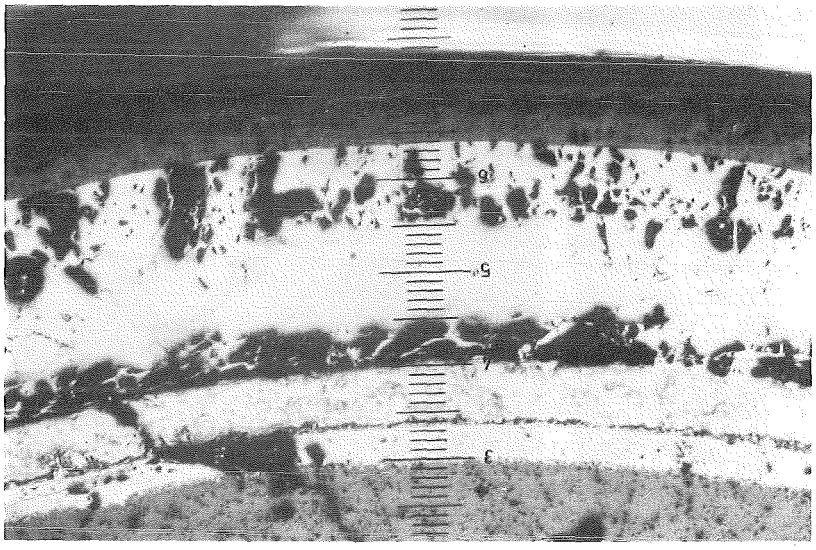

6

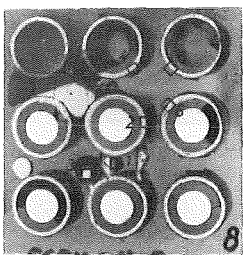

8

FIG.67 DETAILS OF THE CROSS SECTION AT 66 MM AT POS. SHOWN IN THE OVERVIEW FIG.20 (ESBU-1)

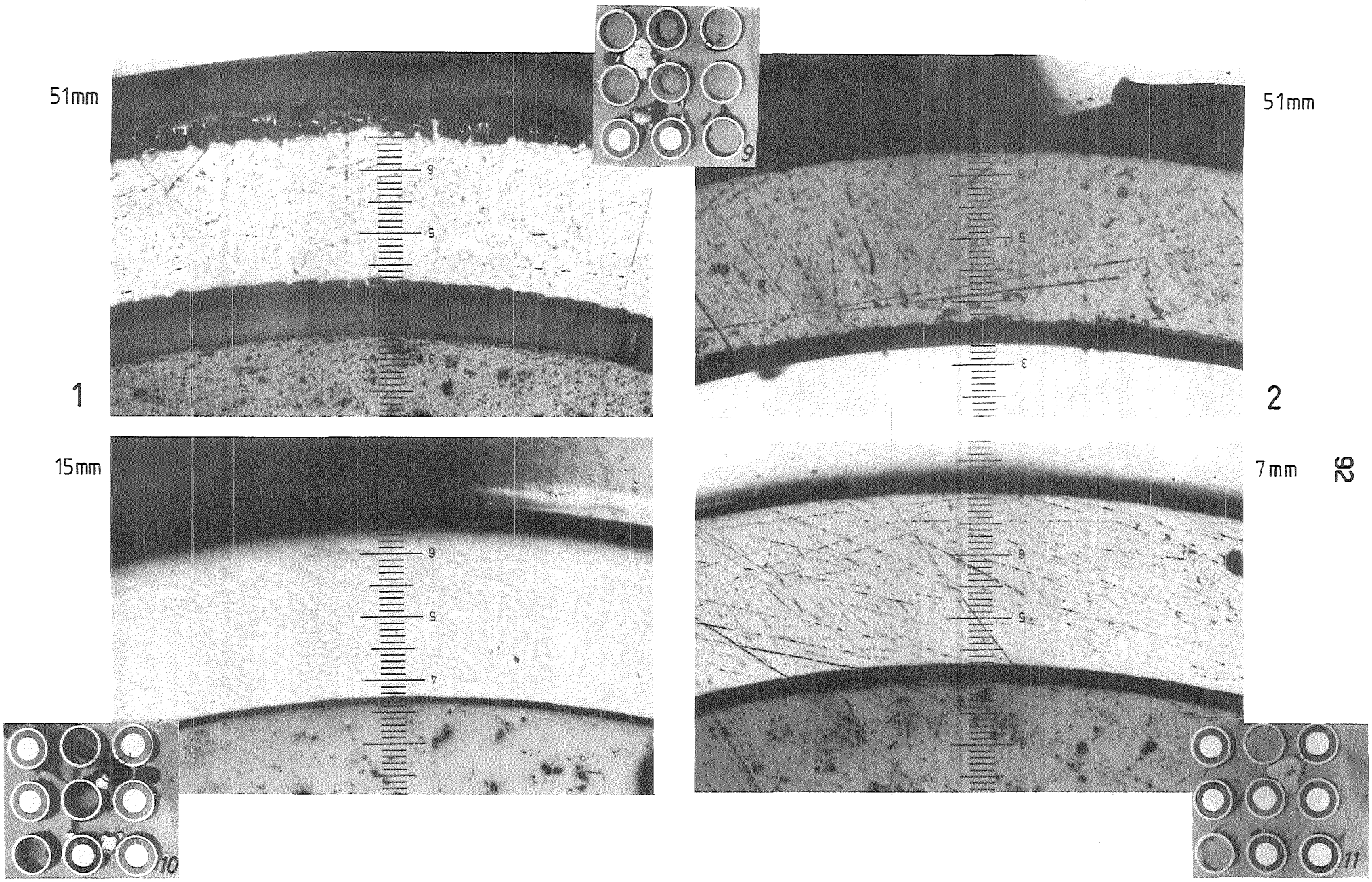

FIG. 68 : DETAILS OF CROSS SECTIONS AT 51, 15 AND 7 MM AT THE POSITIONS SHOWN.

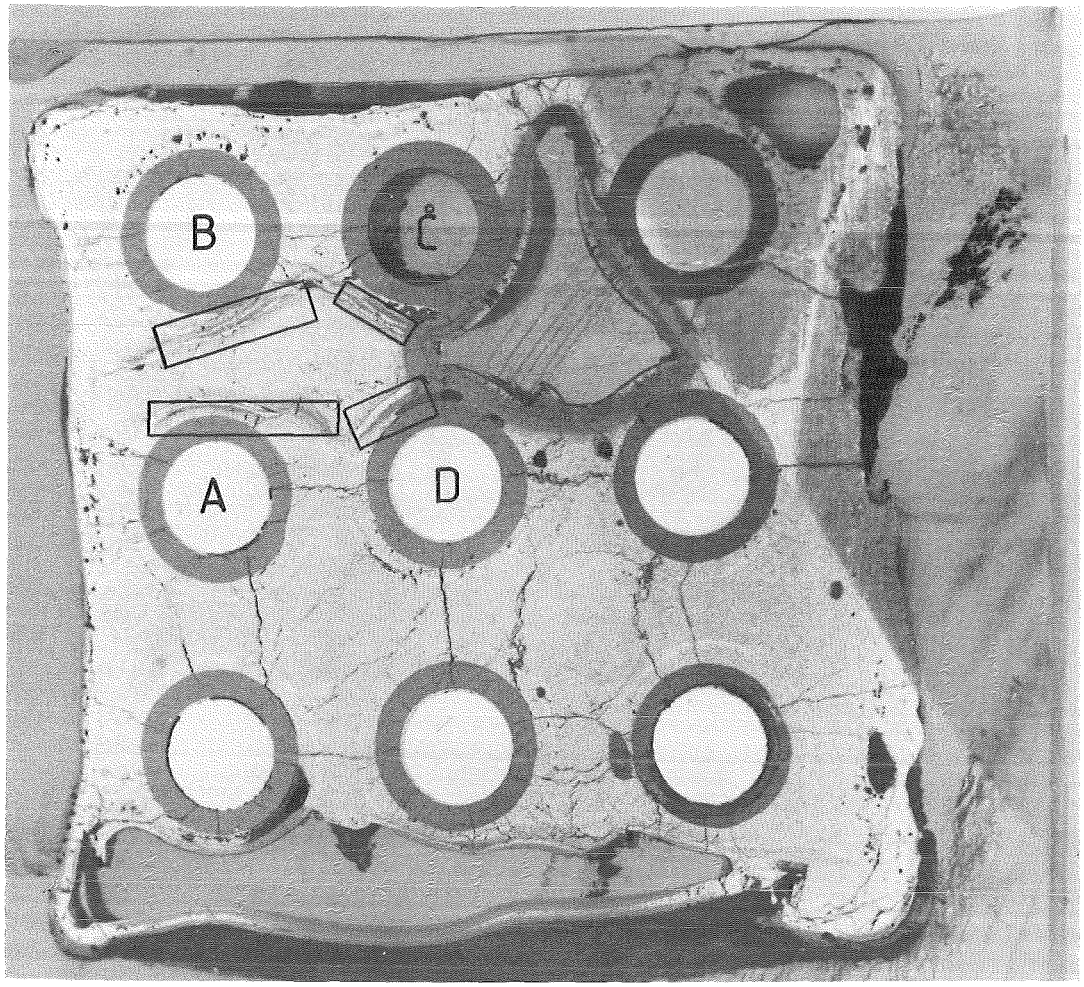

FIG.69 : POSITIONS OF ENLARGED VIEWS OF THE CROSS SECTION AT AT 106 MM GIVEN IN THE FOLLOWING FIGURES. ESBU-1

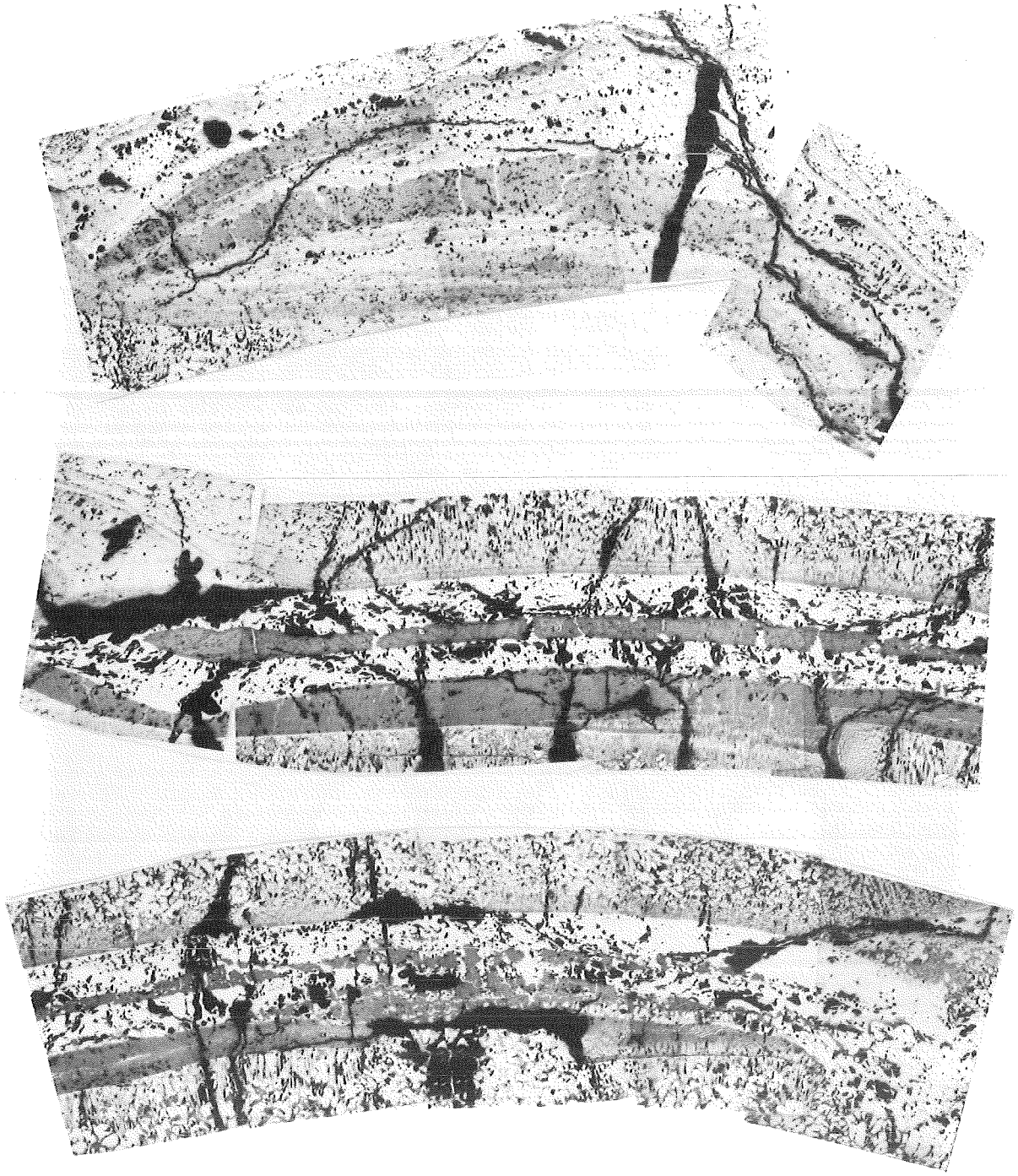

Fig.70 Enlarged View of former cladding region A of the cross section at 106mm above the bottom of the bundle. (ESBU-1)

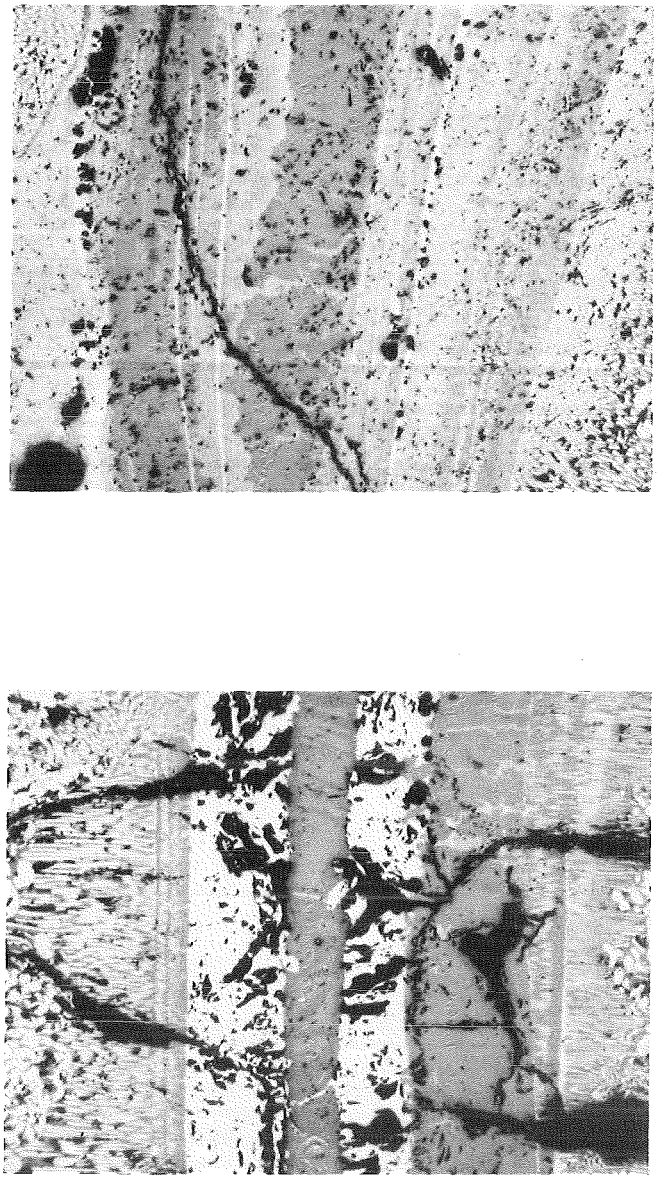

Fig.70a Details of former cladding region A in the cross section at 106mm elavation. (ESBU-1)

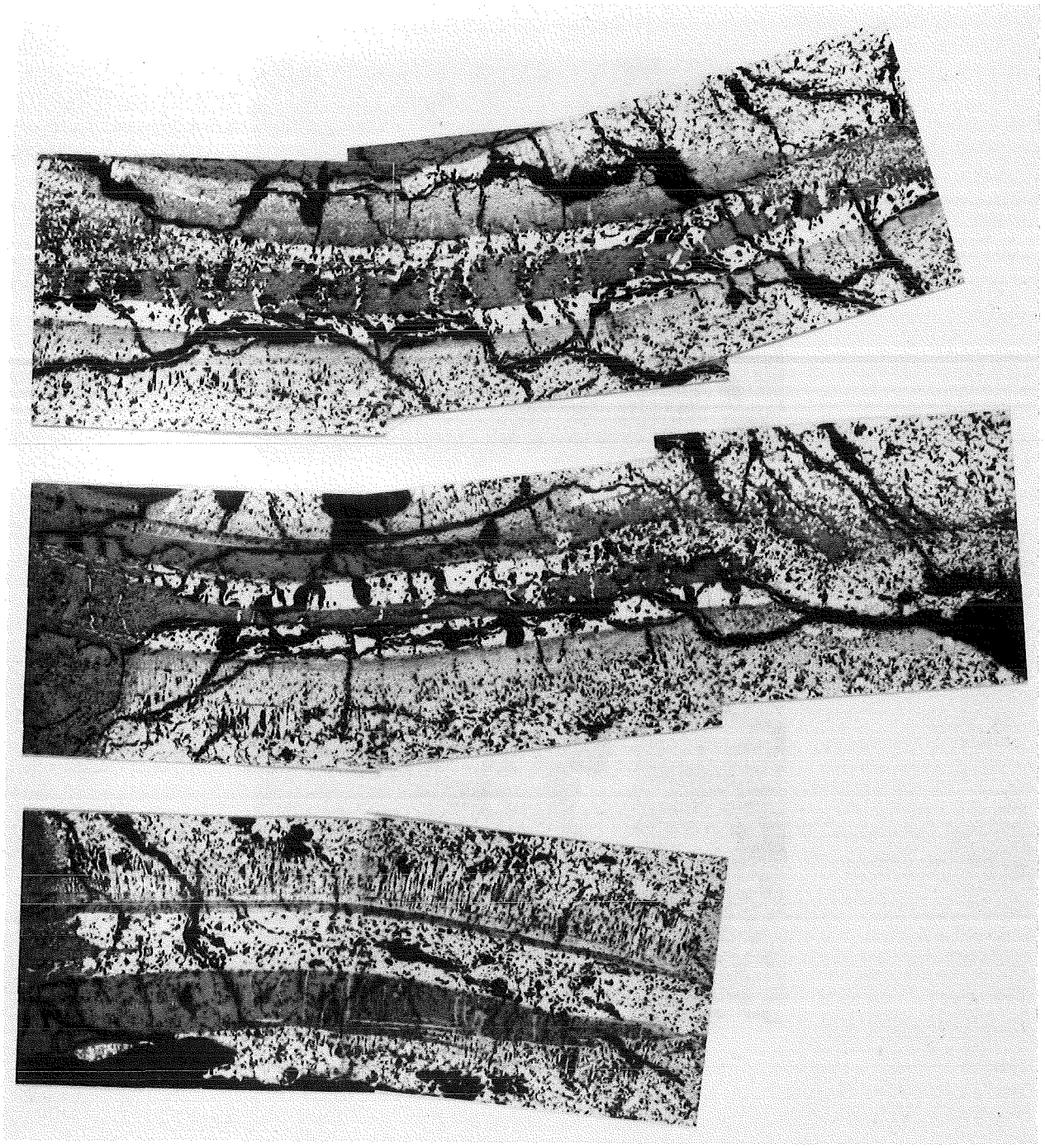

Fig.71 Enlarged Views of former cladding regions B, C, D of the cross section at 106mm above the bottom of the bundle (ESBU-1)

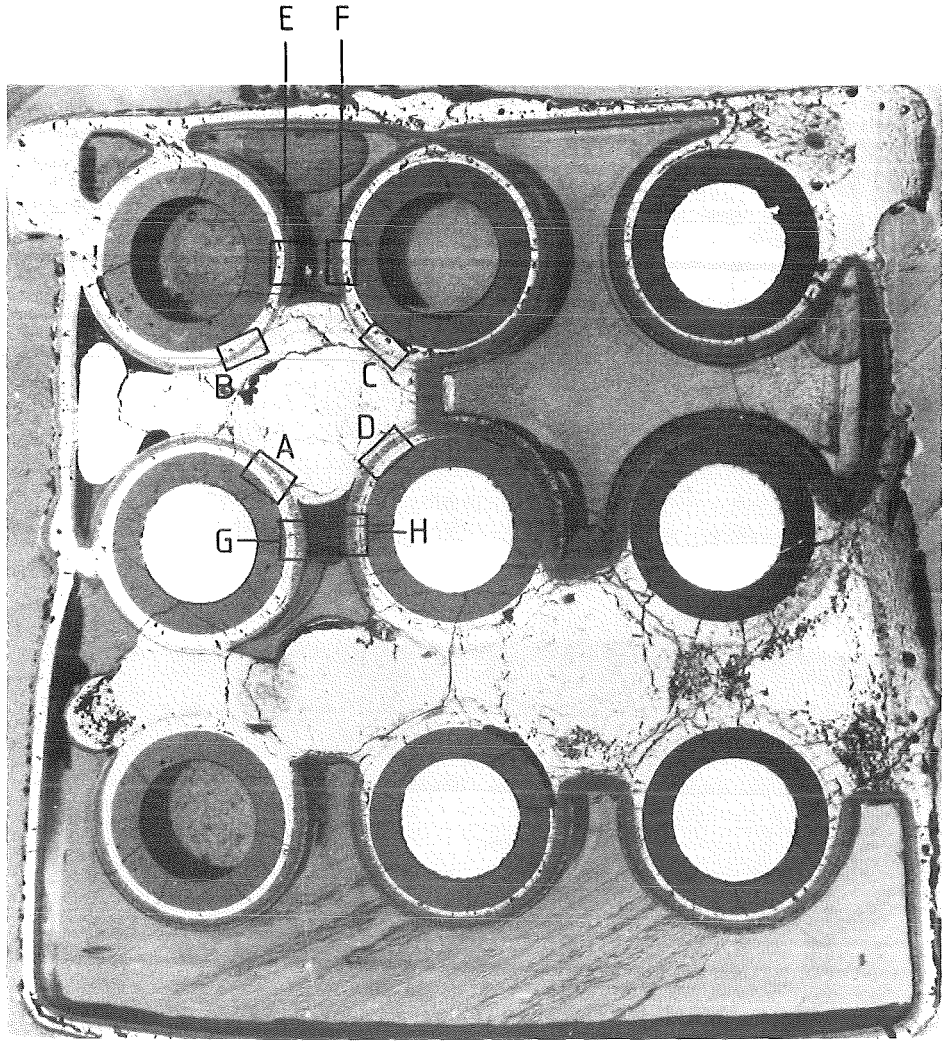

FIG. 72 : POSITIONS OF ENLARGED VIEWS OF THE CROSS SECTION AT 86 MM FOR THE COMPARISON OF SURFACE REGIONS COVERED AND UNCOVERED WITH MELT. (ESBU-1)

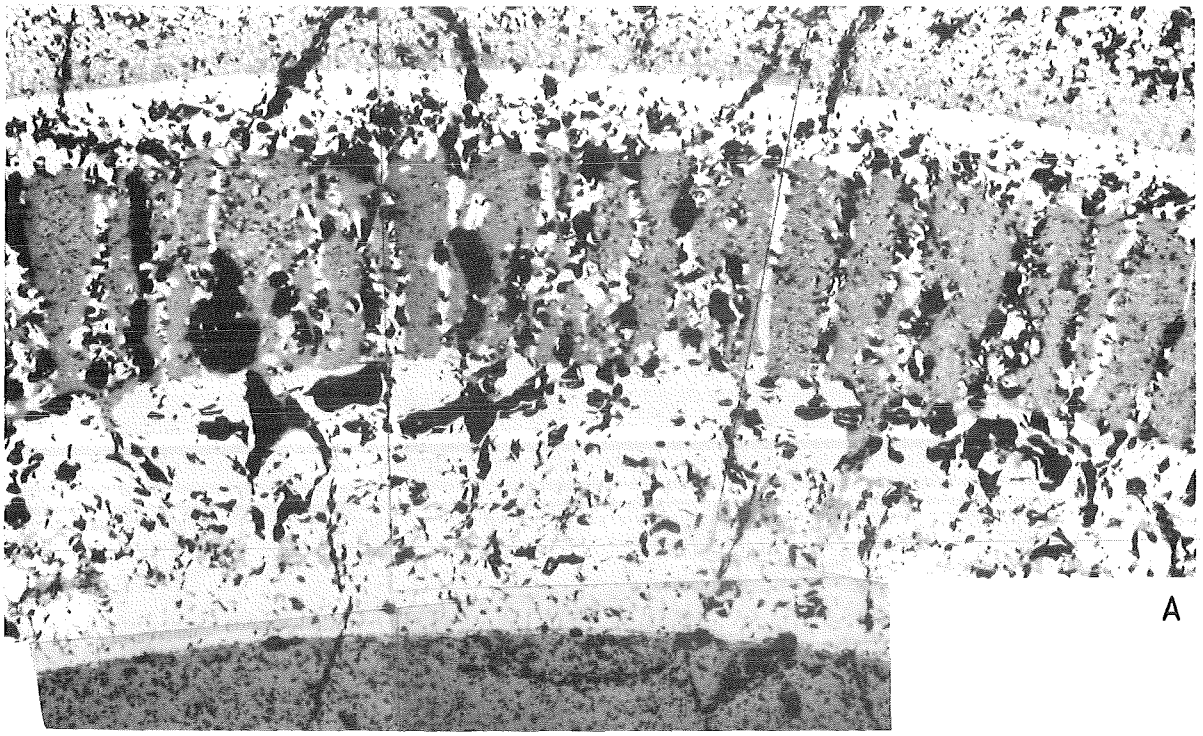

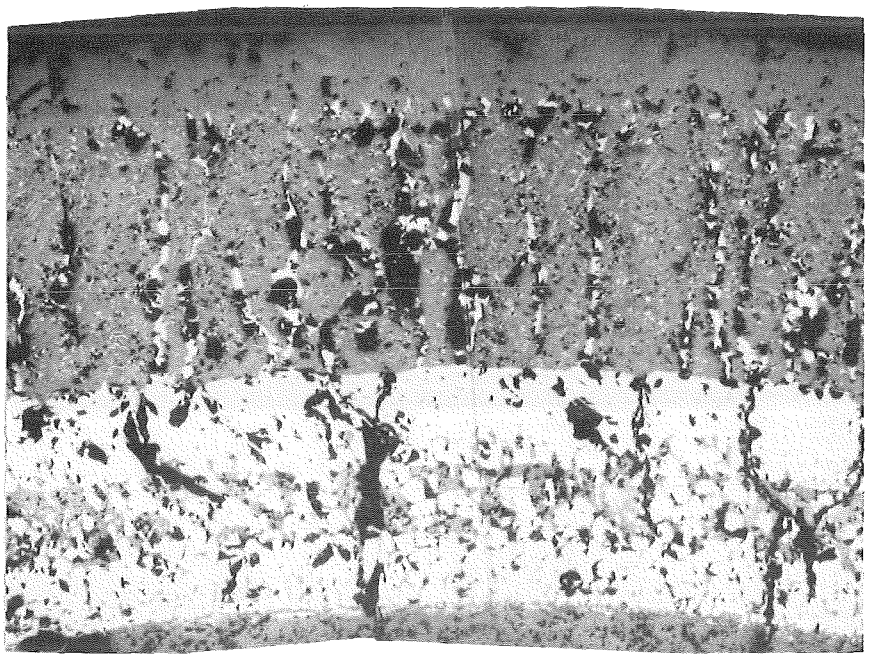

FIG. 73 : COMPARISON OF OXIDIZED PARTS OF CLADDING FROM SAME ROD. MELT COVERED REGIONS (A) AND UNCOVERED REGIONS (G) SHOWN FROM CROSS SECTION AT 86 MM ESBU-1. FIG.

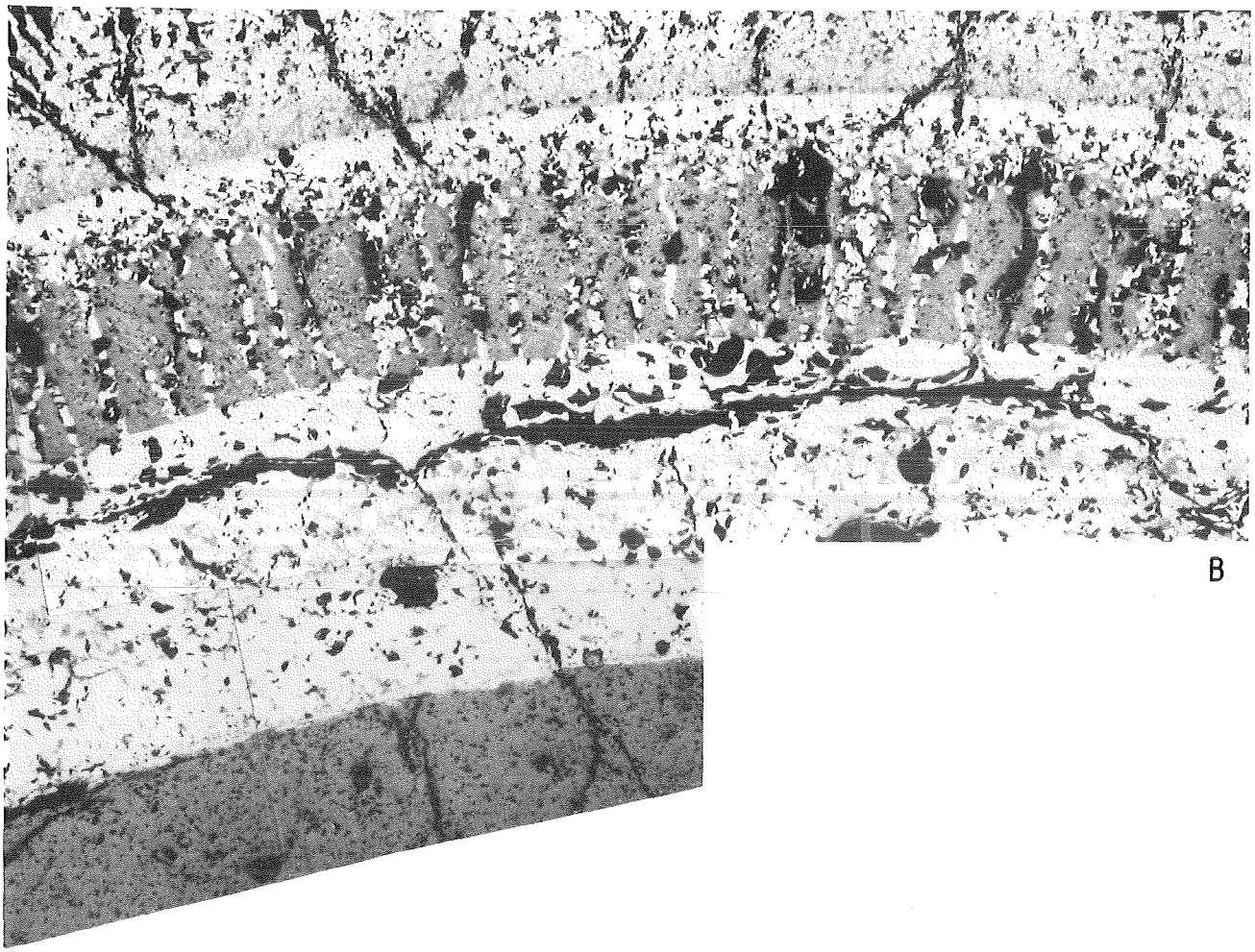

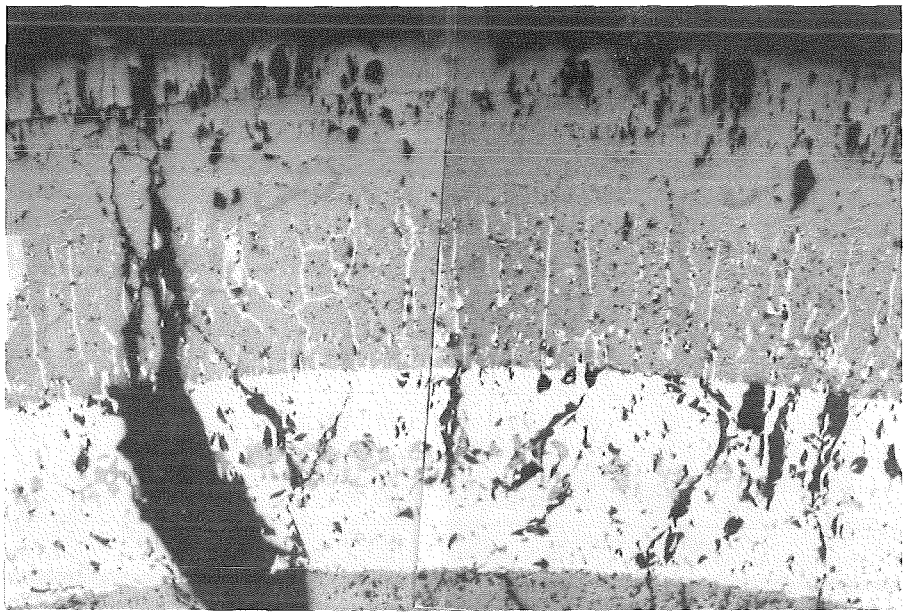

FIG. 74 : COMPARISON OF OXIDIZED PARTS OF CLADDING FROM SAME ROD. MELT COVERED REGIONS (B) AND UNCOVERED REGIONS (E) SHOWN FROM CROSS SECTION AT 96 MM ESBU-1. FIG.

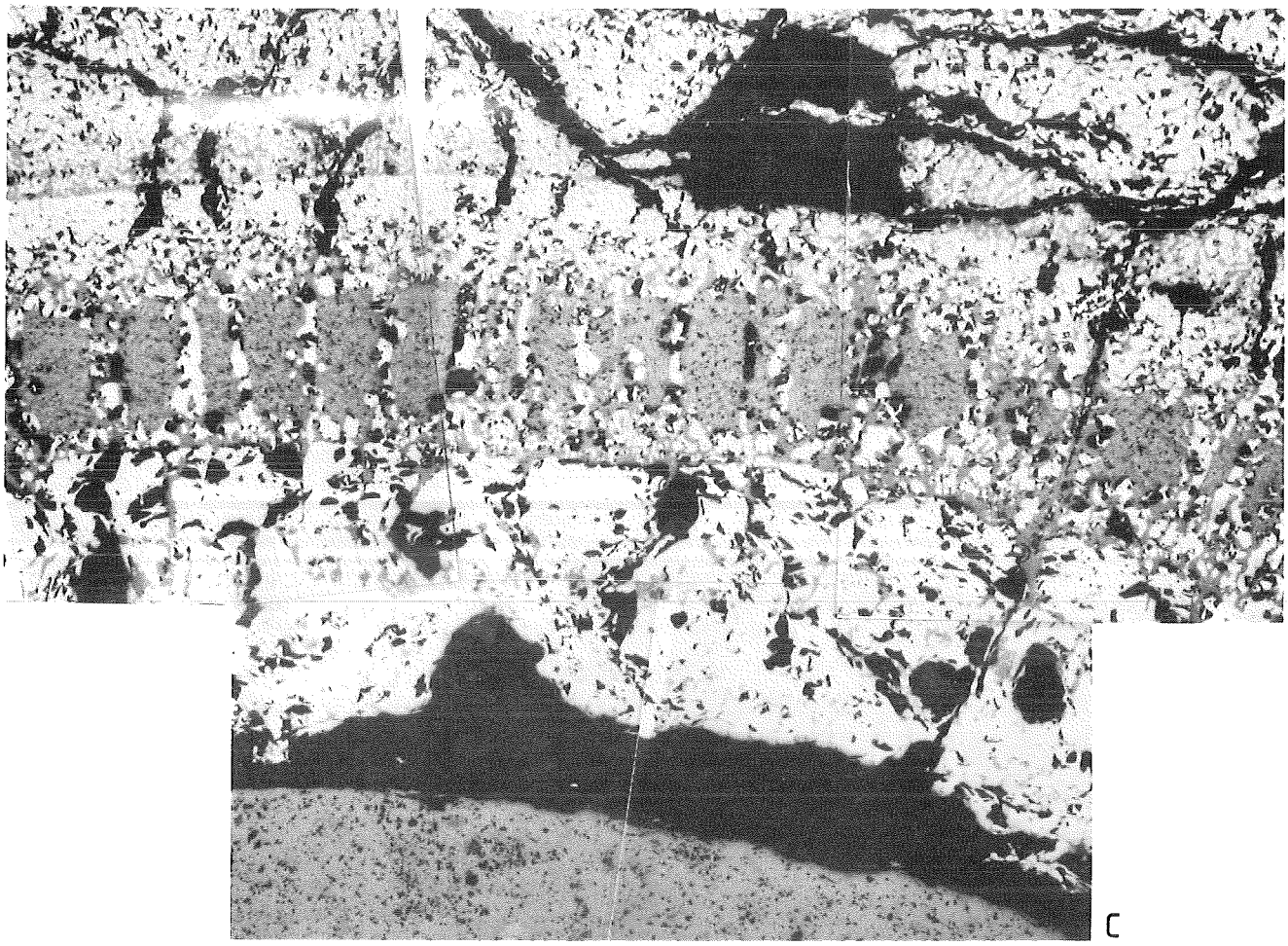

C

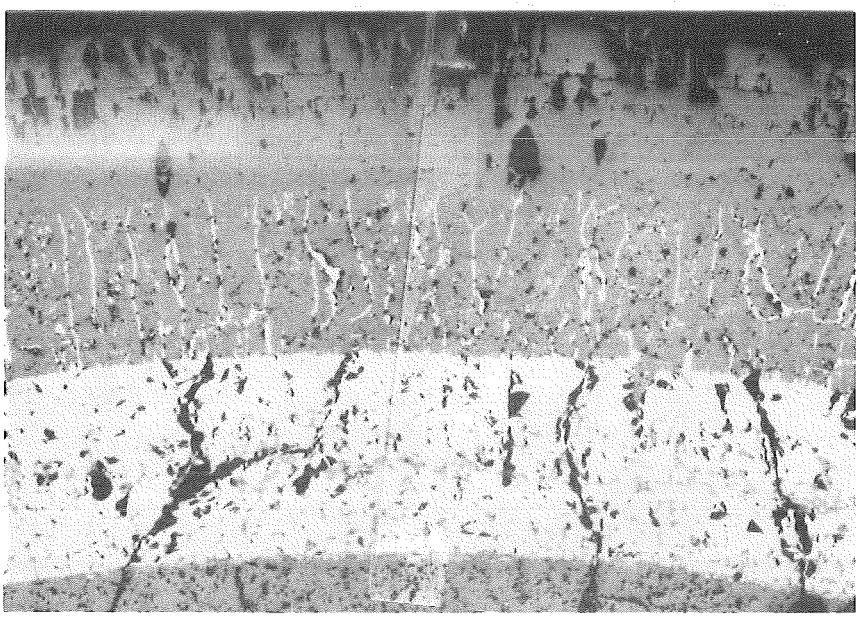

F

FIG. 75 : COMPARISON OF OXIDIZED PARTS OF CLADDING FROM SAME ROD. MELT COVERED REGIONS (C) AND UNCOVERED REGIONS (F) SHOWN FROM CROSS SECTION AT 86 MM ESBU-1, FIG.

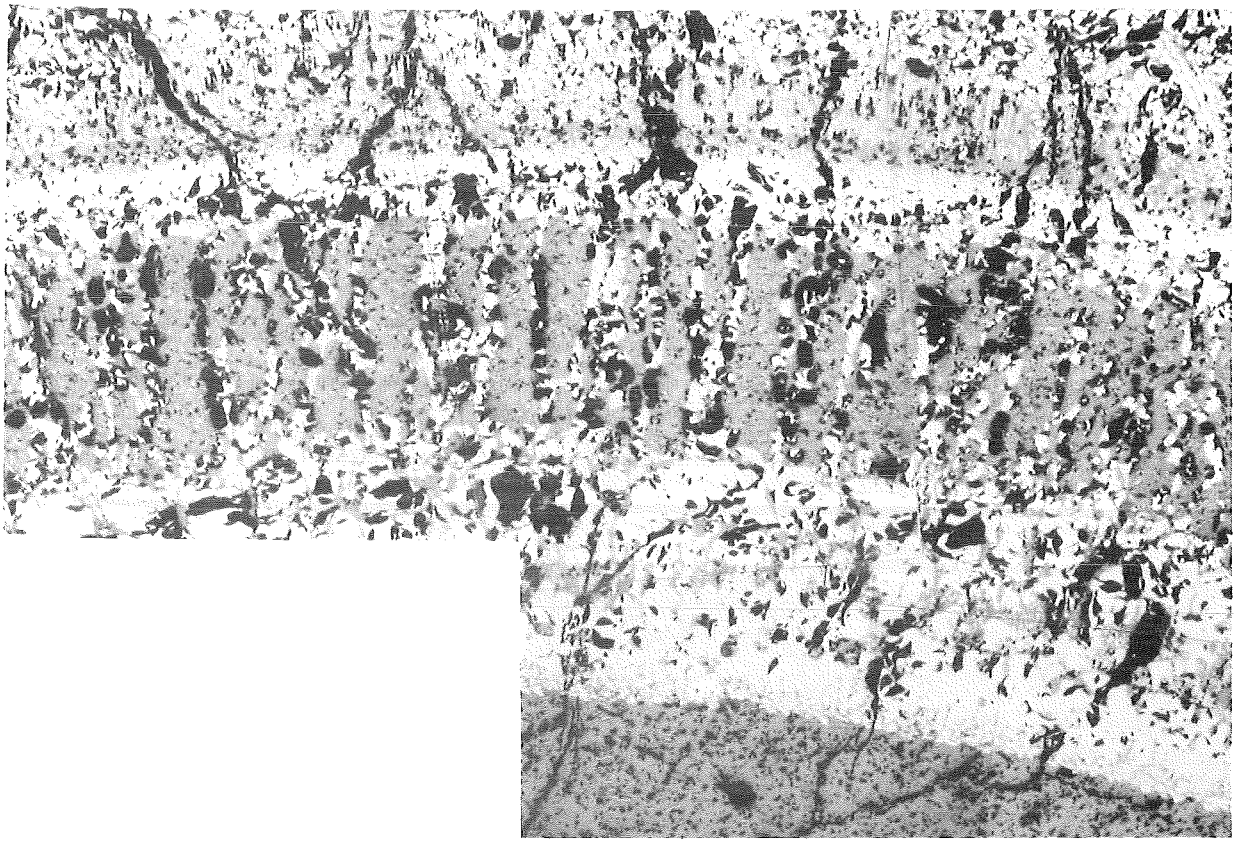

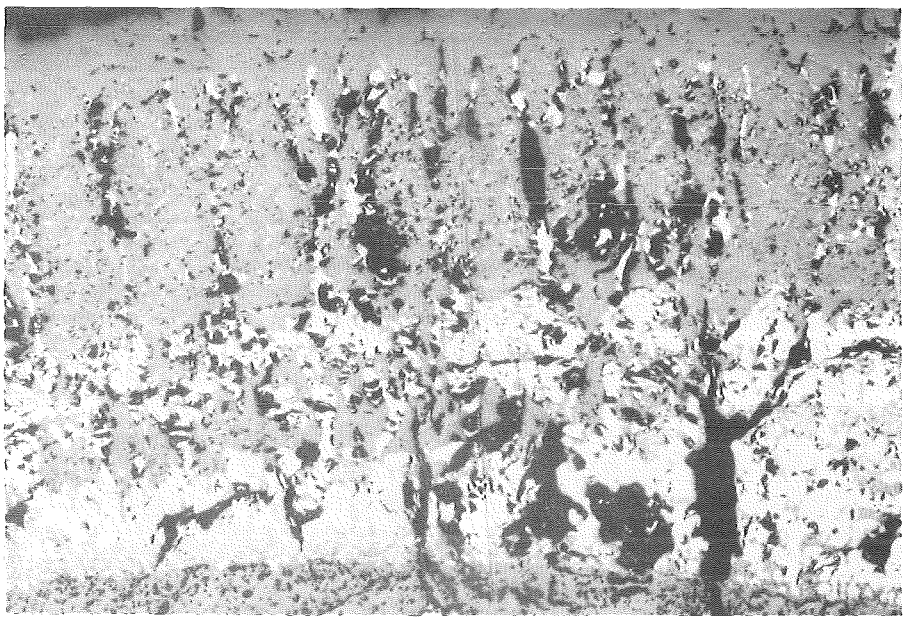

FIG. 76 : COMPARISON OF OXIDIZED PARTS OF CLADDING FROM SAME ROD. MELT COVERED REGIONS (D) AND UNCOVERED REGIONS (H) SHOWN FROM CROSS SECTION AT 86 MM ESBU-1. FIG.

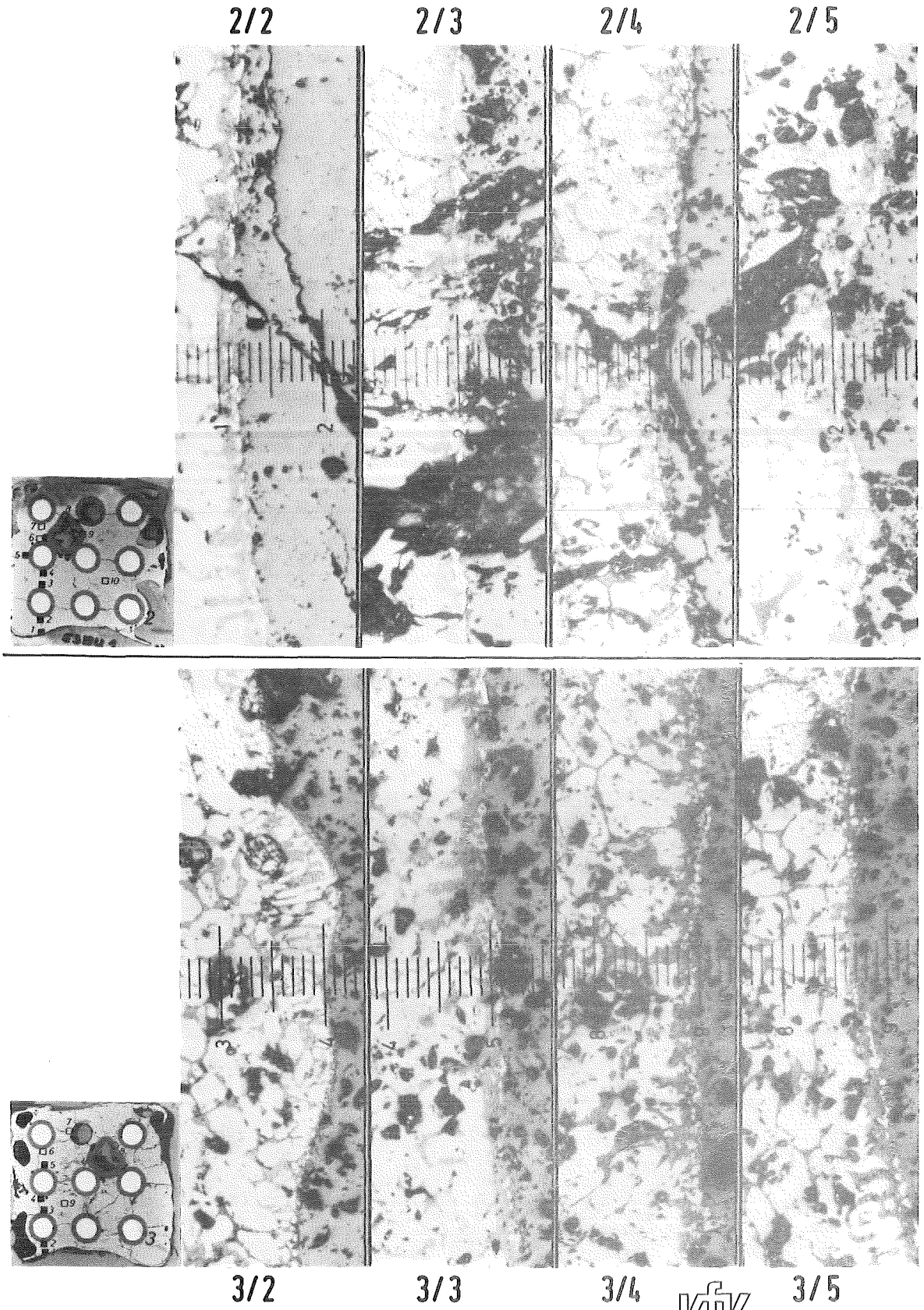

Fig.77 Dissolution of UO_2 by molten Zry for different positions of cross sections 2 (119mm) and 3 (109mm). (ESBU-1)

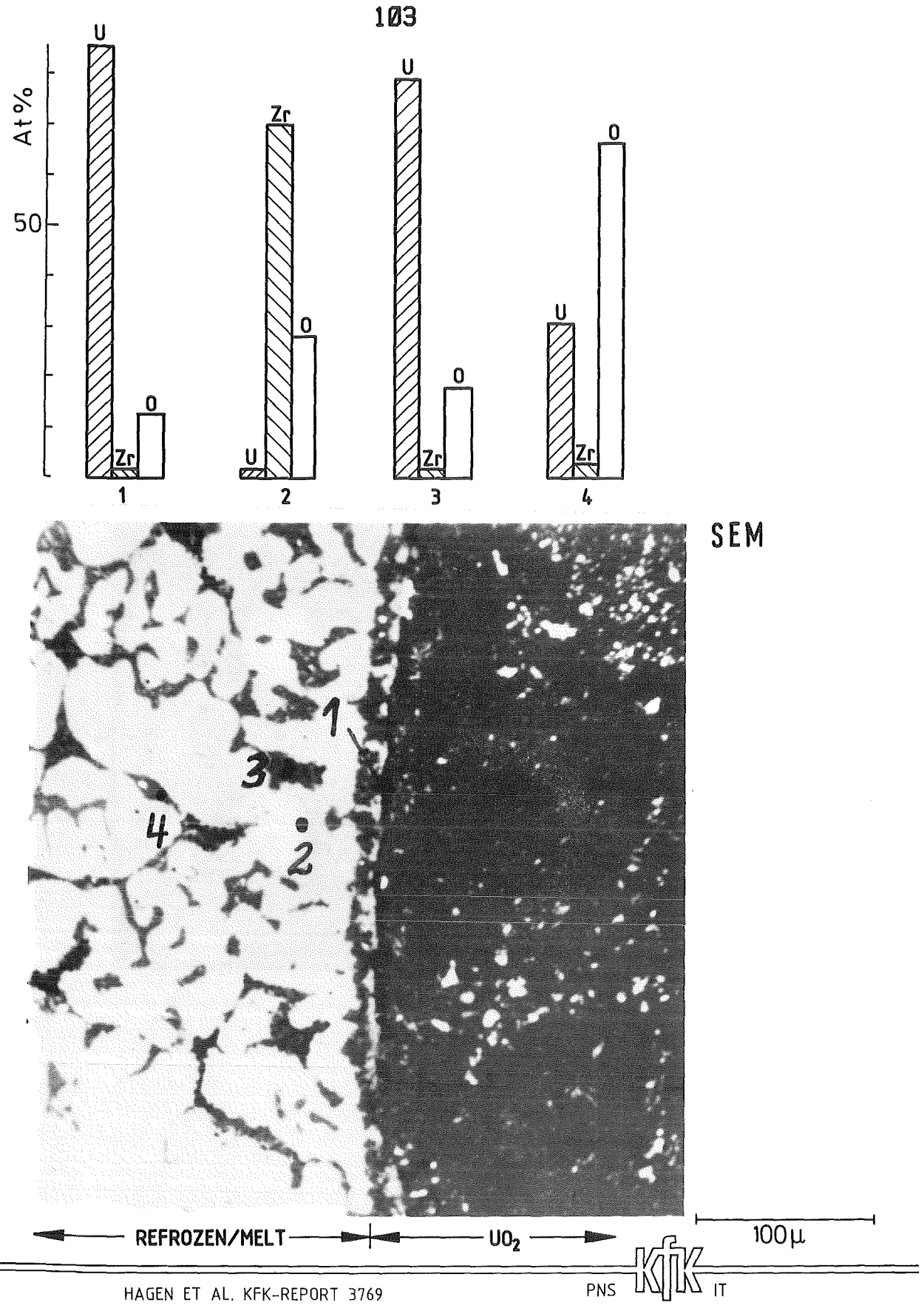

Fig.78 Microprobe results of the phases in the refrozen melt at position 2 in the cross section at 106mm, uncorrected O-values (ESBU-1)

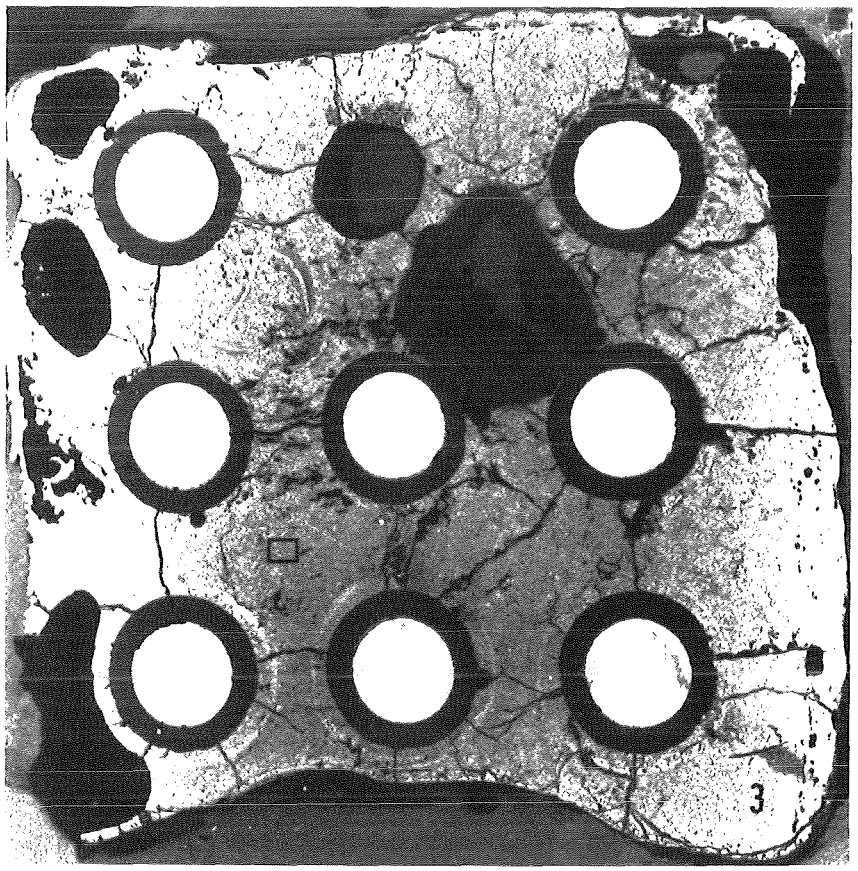

Fig.79 Positions of the microprobe analysis of the 3 phases in the refrozen melt for fig.80

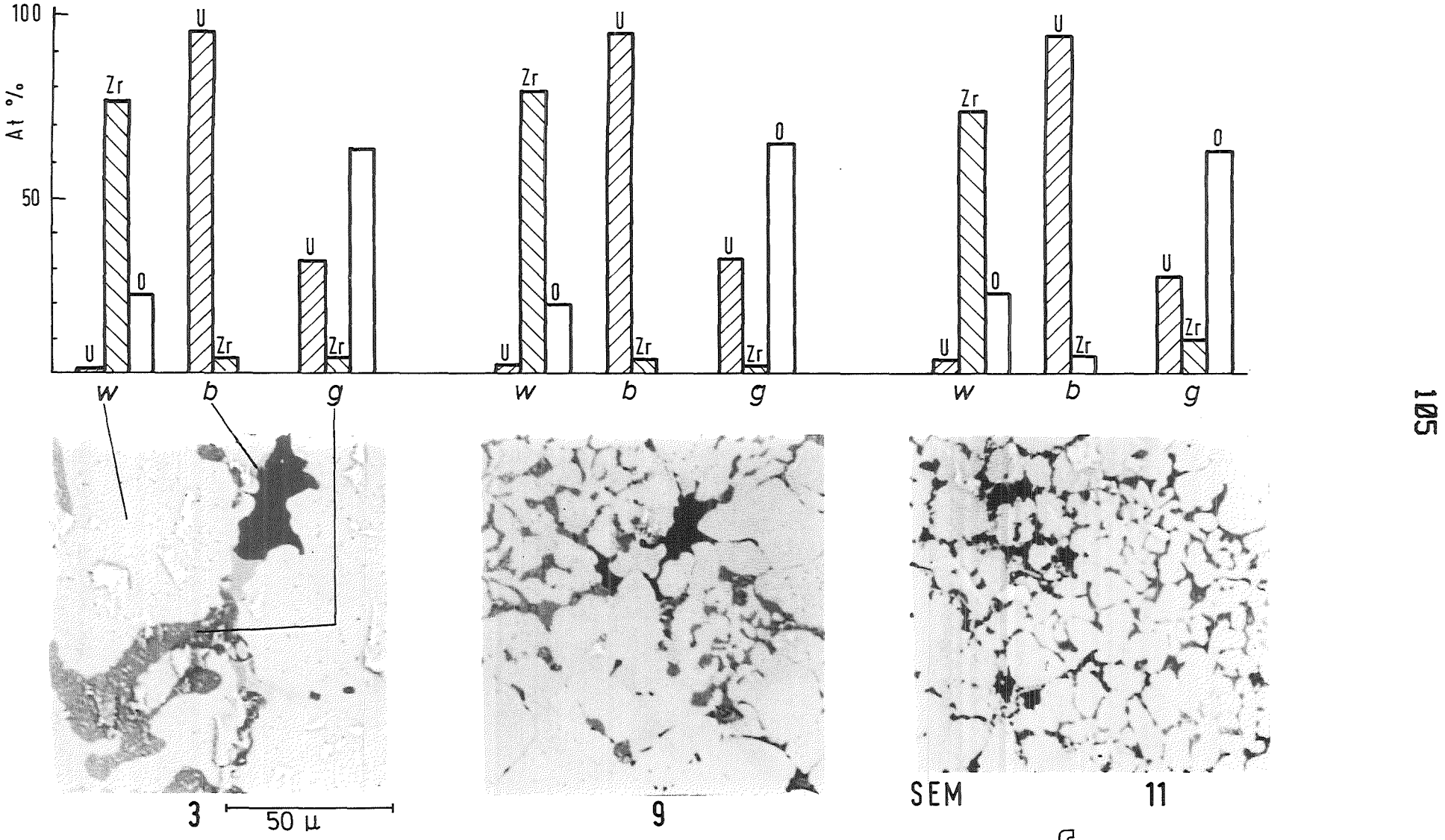

Fig.80 Microprobe analysis of the 3 phases in the refrozen melt for the elavations 3 (116mm), 9 (51mm) and 11 (7mm above bundle bottom) at the position given in fig.79.

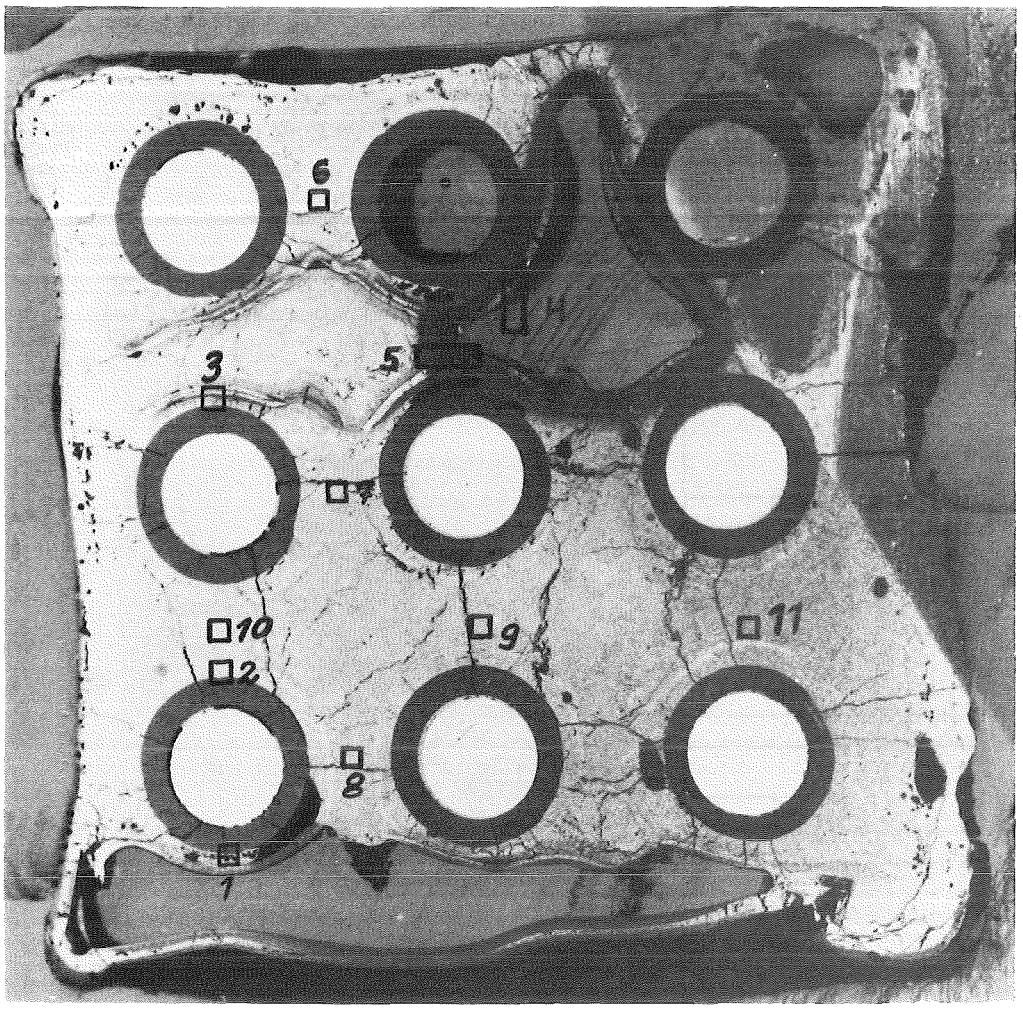

Fig.81 Locations of microprobe investigations from cross section 4 (106mm) of ESBU-1.

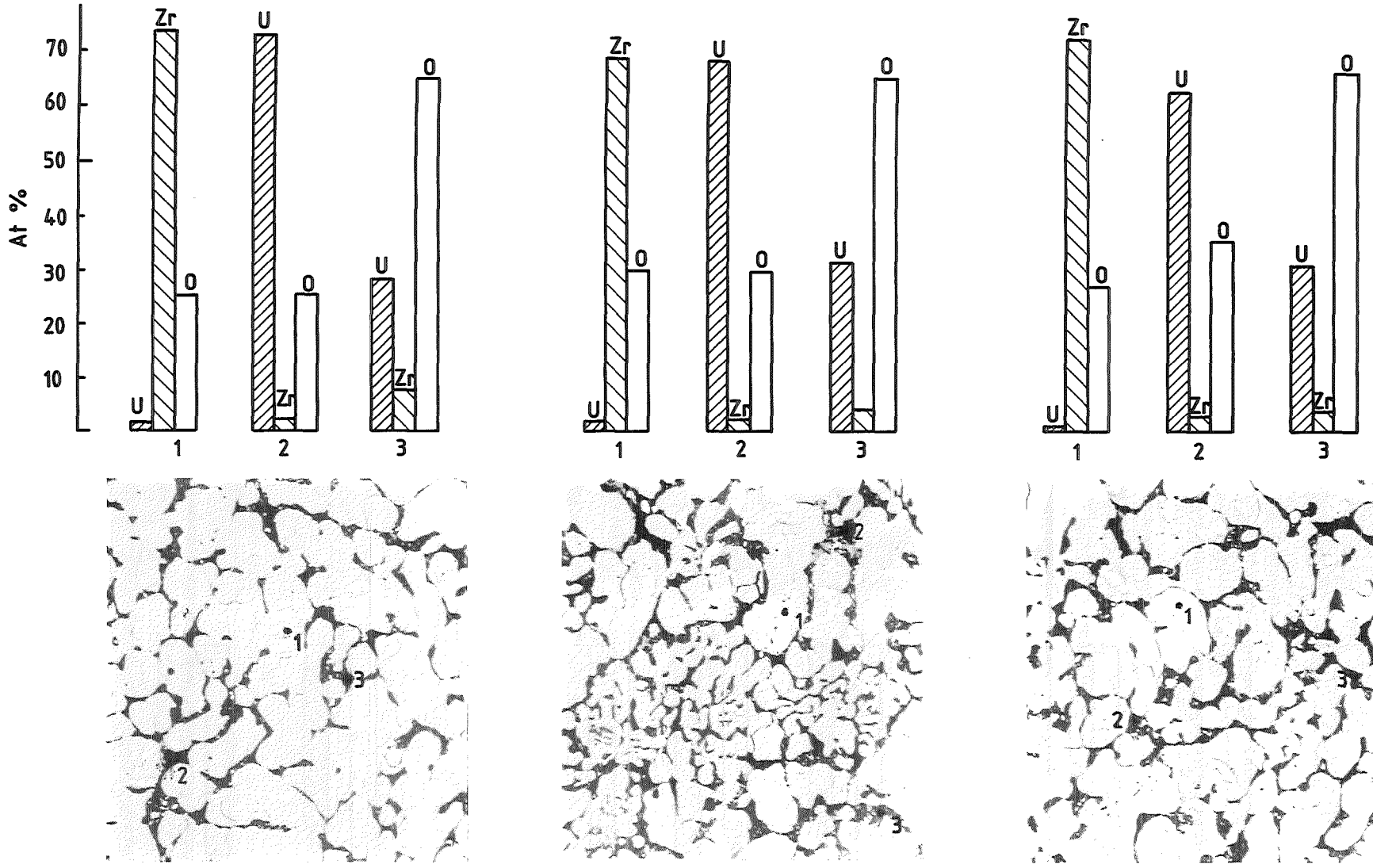

FIG. 82:
MICROPROBE ANALYSIS OF THE 3 PHASES IN THE REFROZEN MELT
ESBU-1: CROSS SECTION 4(106MM ABOVE BOTTOM) LOCATIONS SEE PHOTO; SEE FIG. 81

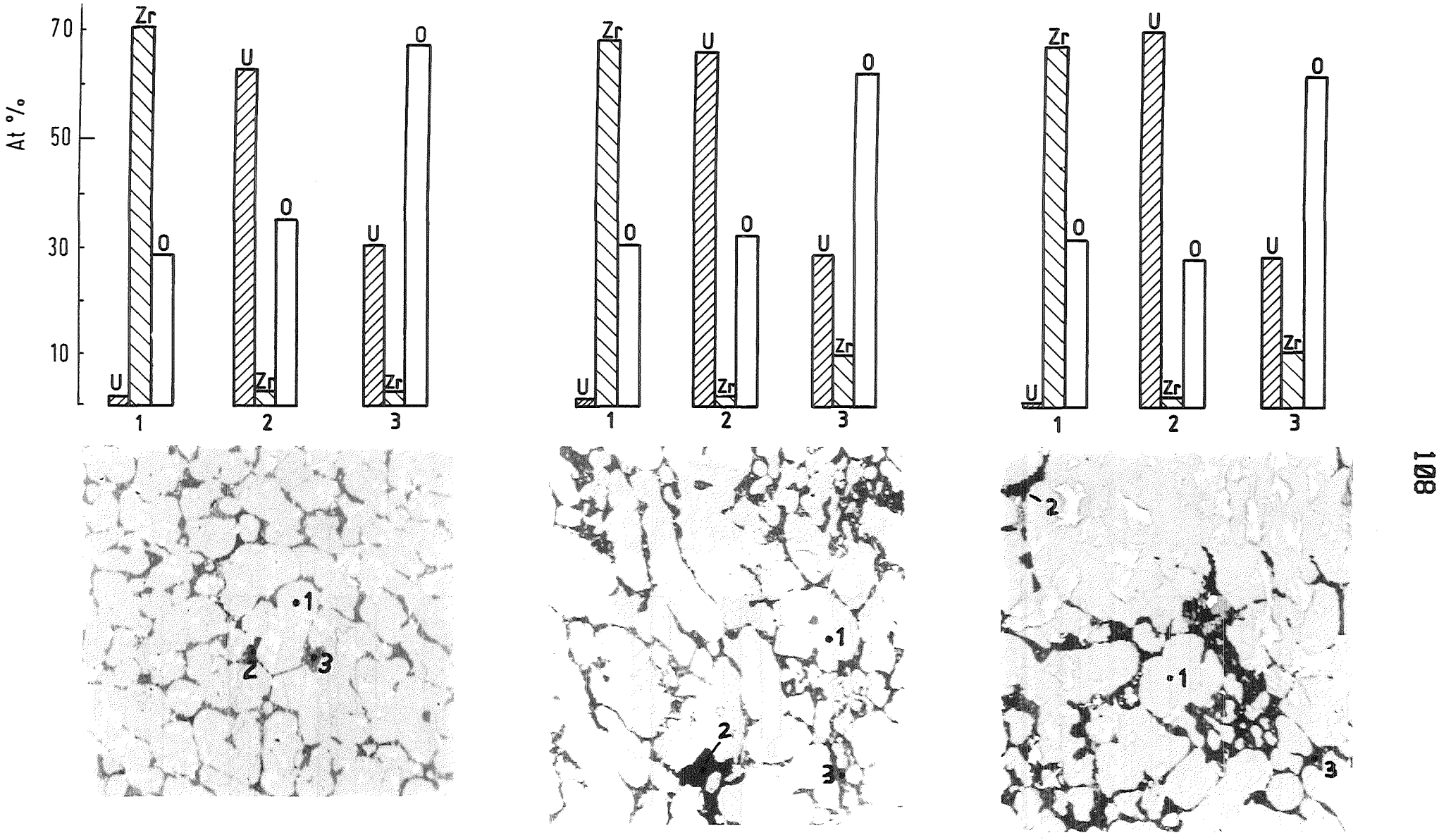

FIG. 83: MICROPROBE ANALYSIS OF THE 3 PHASES IN THE REFROZEN MELT

ESBU-1: CROSS SECTION 4 (106 mm ABOVE BOTTOM) LOCATIONS SEE PHOTO; SEE FIG. 81

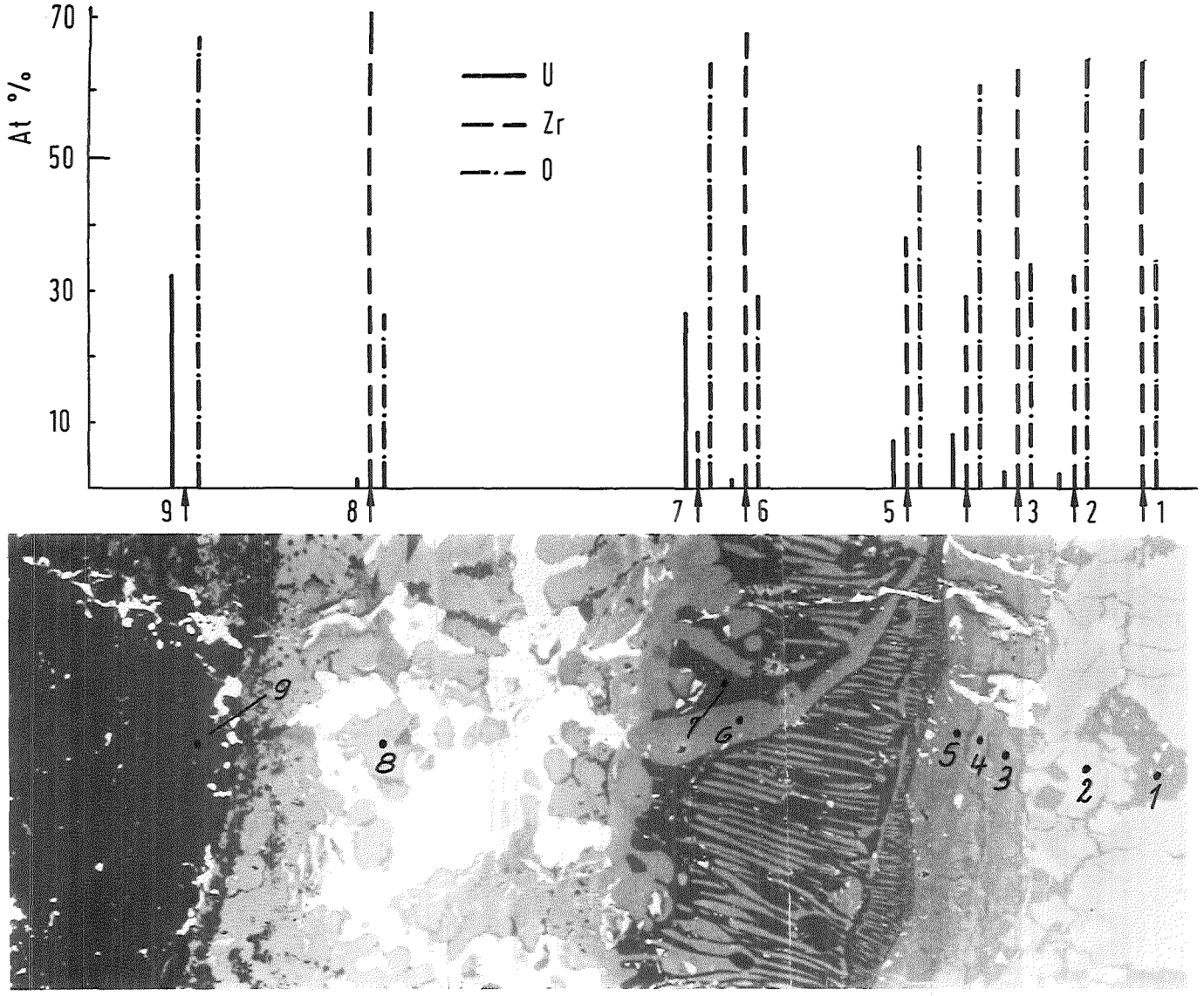

FIG. 84 : OXIDATION IN STAGNANT STEAM

ESBU-1: LOCATION 1 OF CROSS SECTION 4 (106 mm) UNCORRECTED O-VALUES; SEE FIG. 81

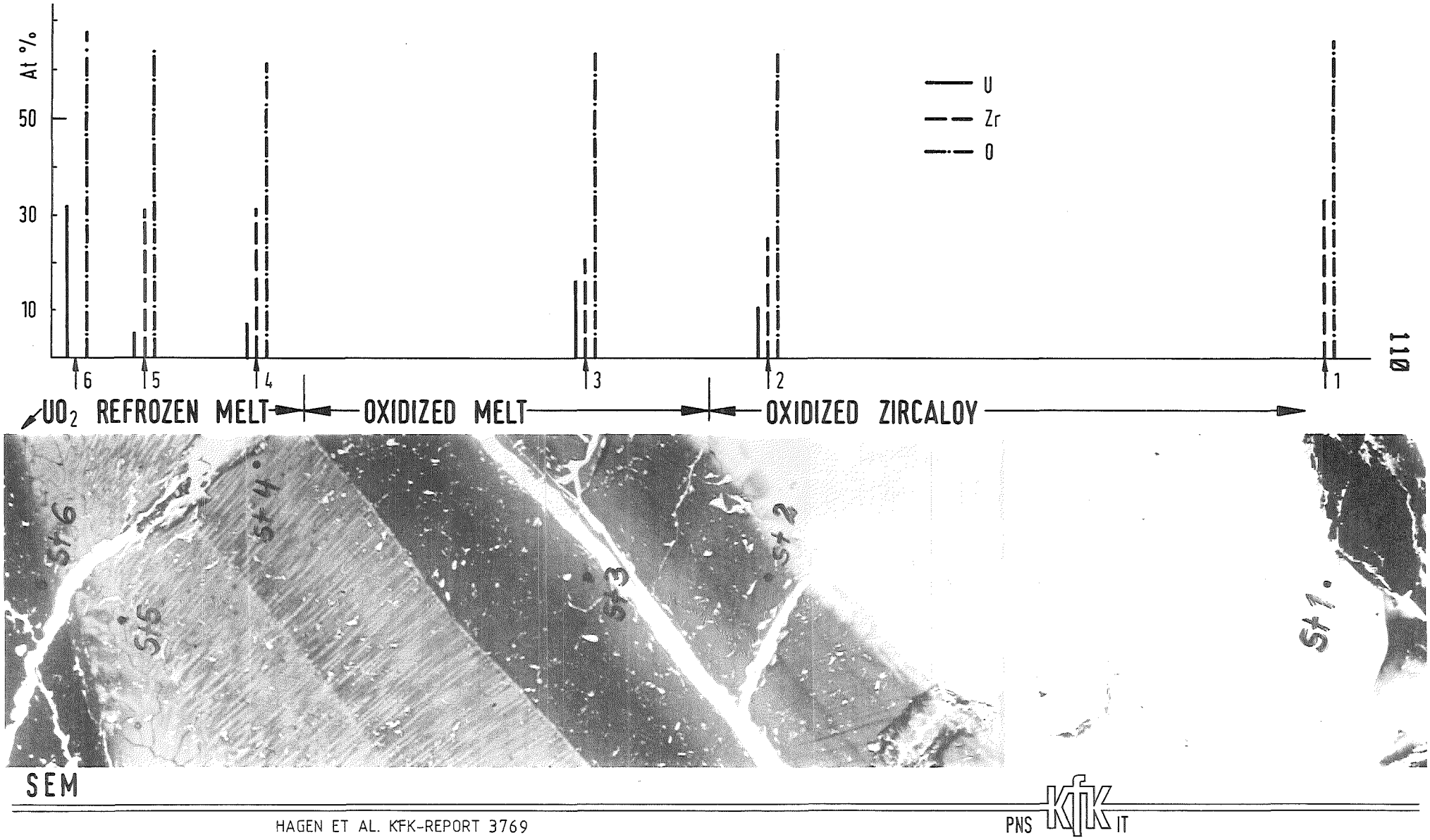

HAGEN ET AL. KFK-REPORT 3769

PNS KfK IT

FIG. 85: OXIDATION OF CLADDING IN CONTINUOUS STEAM FLOW

ESBU-1: LOCATION 4 OF CROSS SECTION 4 (106mm); SEE FIG. 81

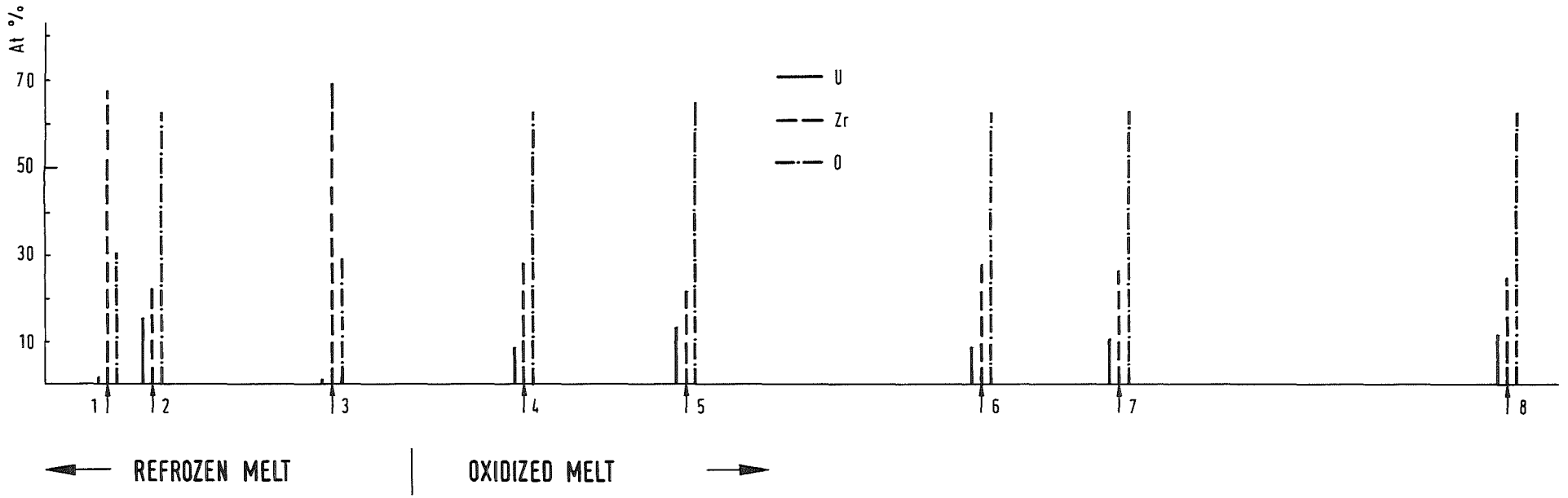

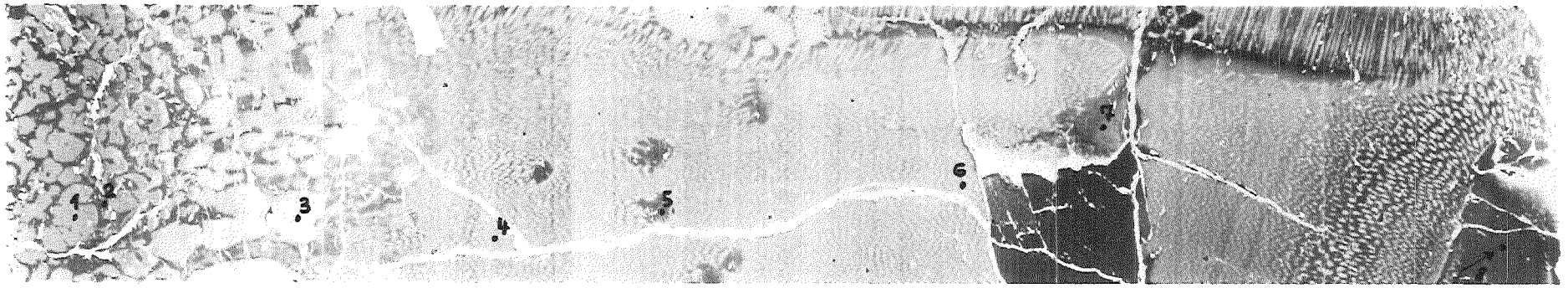

Fig.86 Oxidation of melt in direct contact with steam

ESBU-1: Location 5 of cross section 4 (106mm) ; see Fig.81

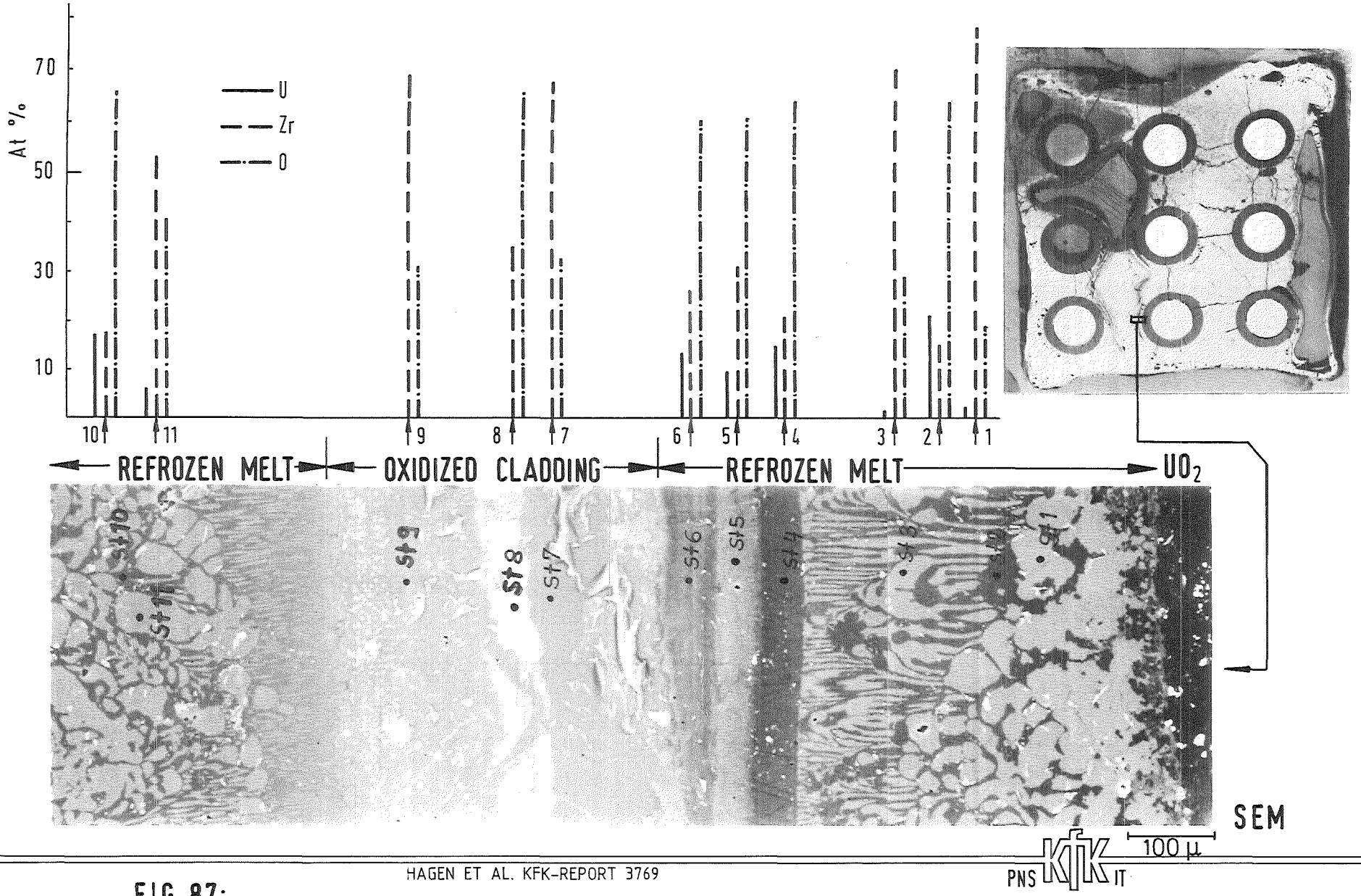

HAGEN ET AL. KFK-REPORT 3769

FIG. 87:

MICROPROBE ANALYSIS OF REMAINING OXIDIZED CLADDING IN CONTACT WITH REFROZEN MELT

ESBU-1: LOCATION 3 OF CROSS SECTION 4 (106 mm ABOVE BOTTOM); UNCORRECTED O-VALUES

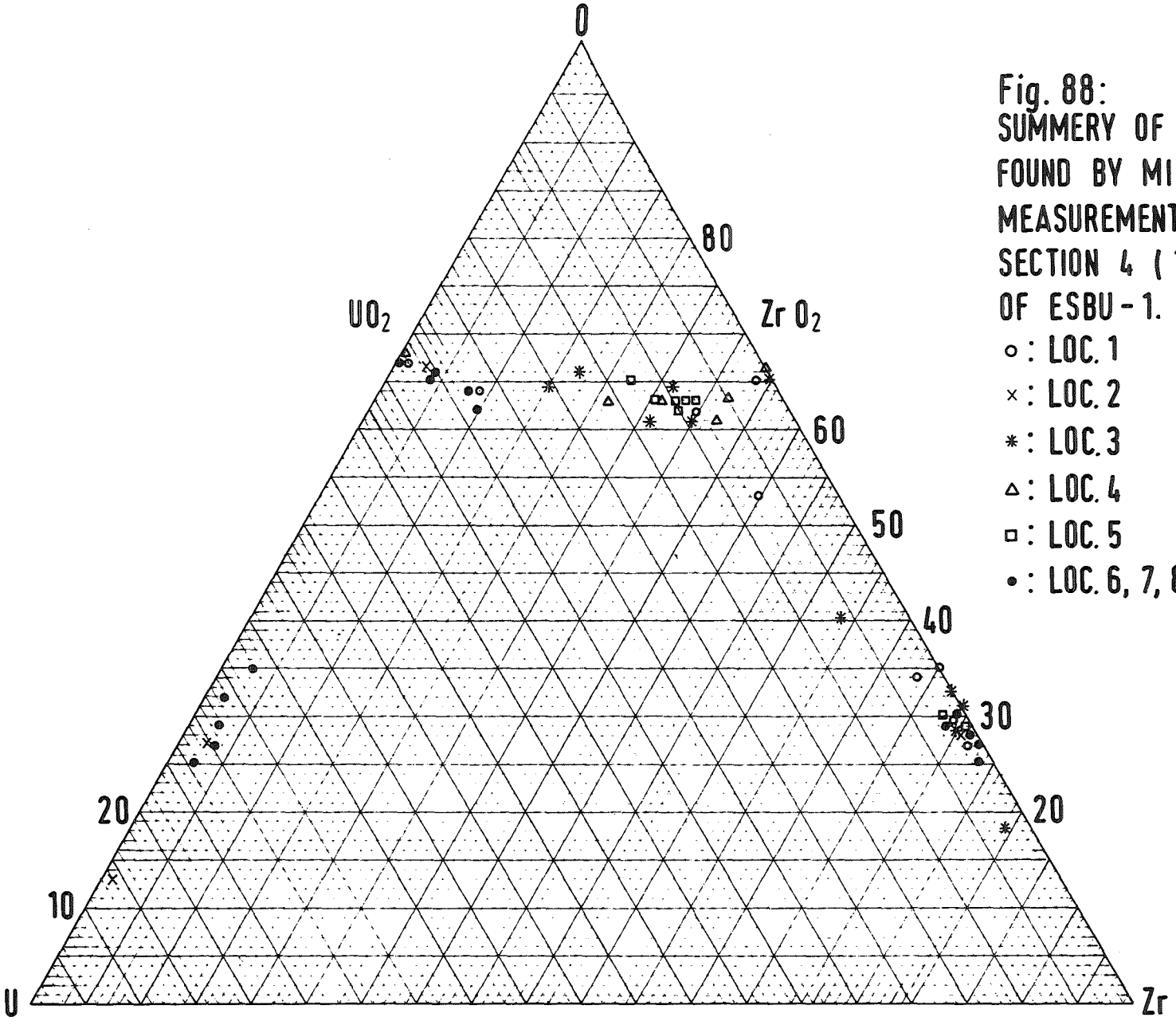

Fig. 88:
SUMMERY OF COMPOSITIONS FOUND BY MICROPROBE MEASUREMENTS AT CROSS SECTION 4 (160 MM) OF ESBU - 1.

- ○ : LOC. 1
- × : LOC. 2
- ✱ : LOC. 3
- △ : LOC. 4
- □ : LOC. 5
- ● : LOC. 6, 7, 8, 9, 10 u. 11

Fig.89: Position of microscop pictures in the following figures 90-93

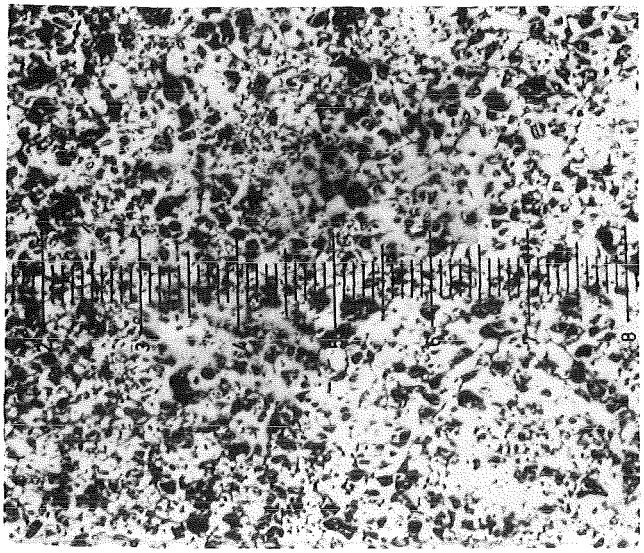

116mm

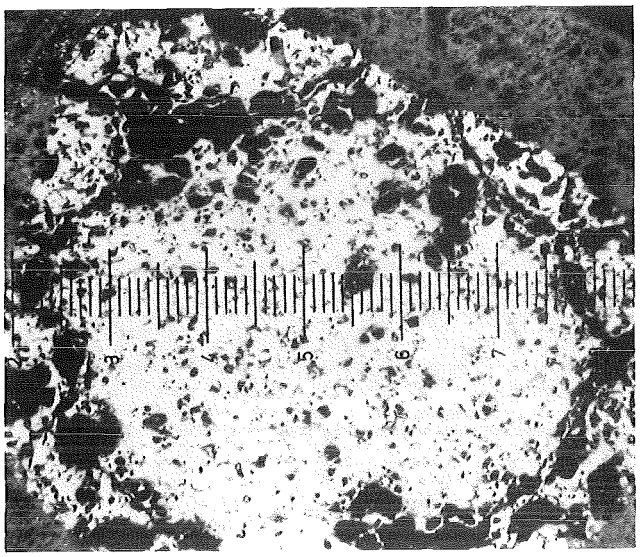

66mm

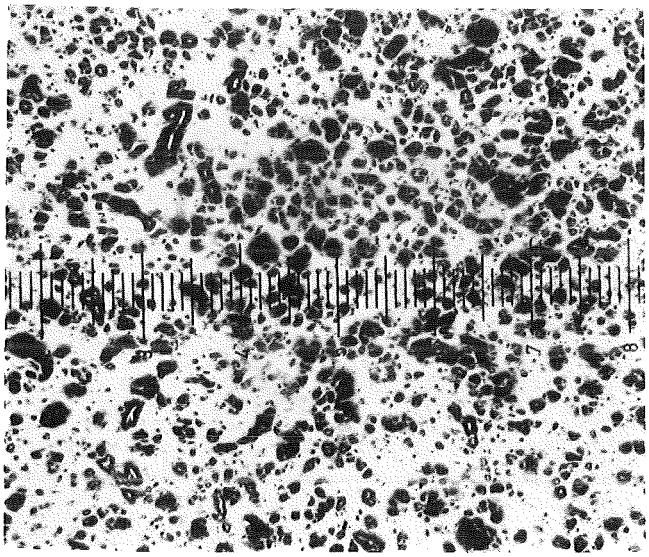

86mm

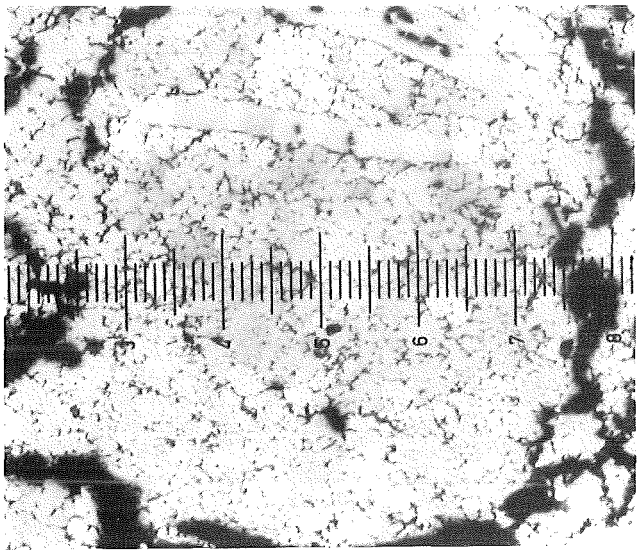

51mm

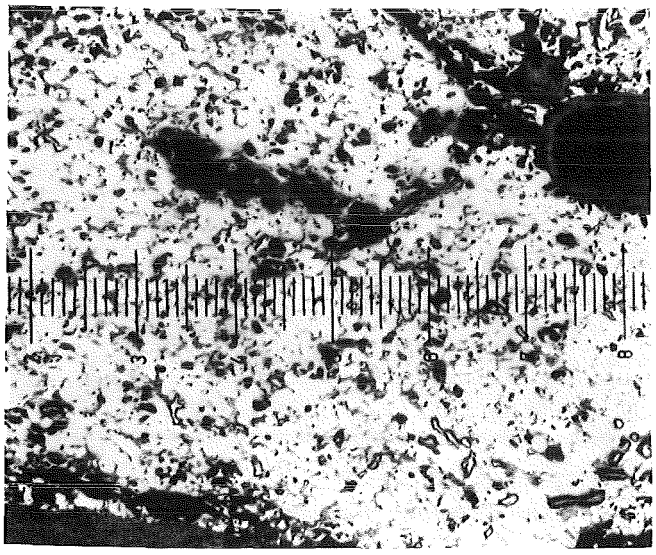

76mm

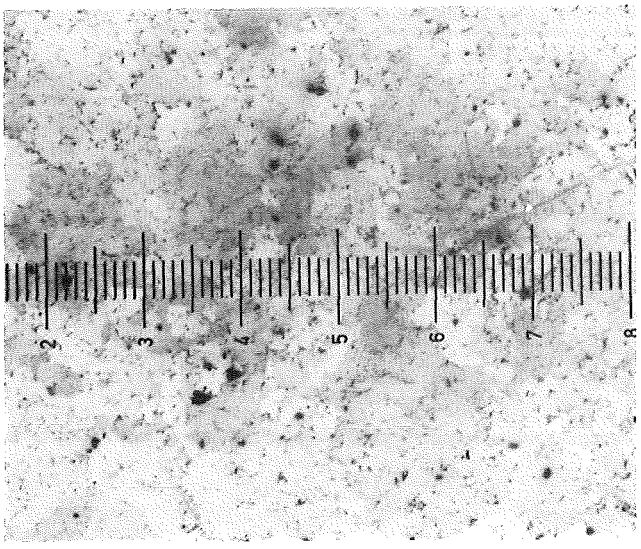

15mm

Fig.90: Structure of the refrozen melt for different elevations at the position given in Fig.89 with a magnification 50x (ESBU-1)

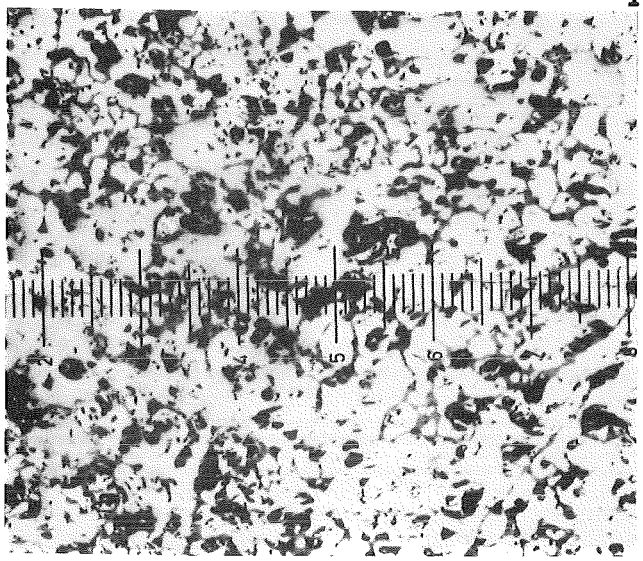

116mm

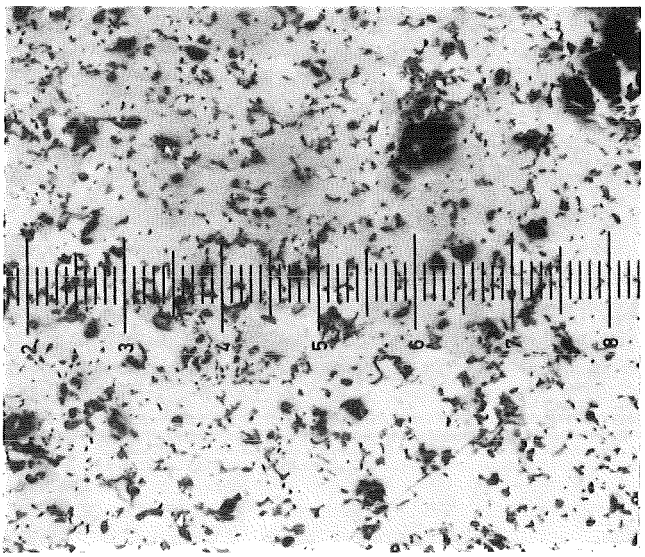

66mm

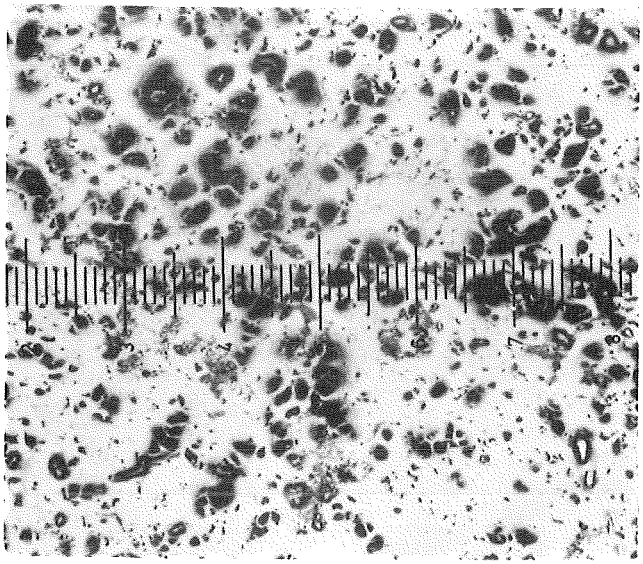

86mm

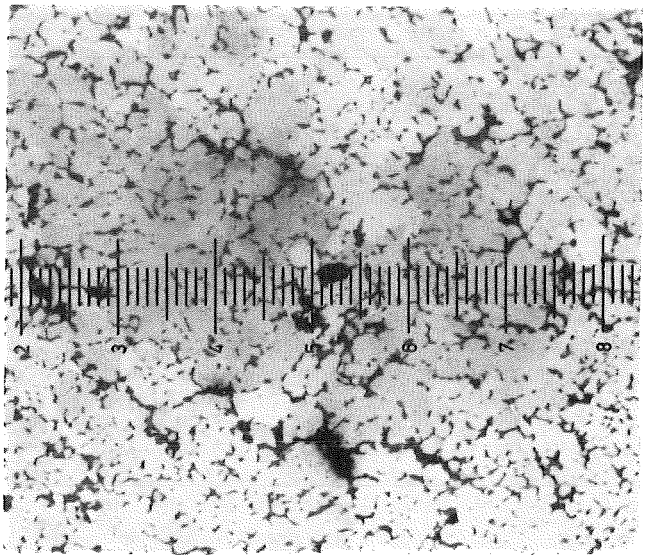

51mm

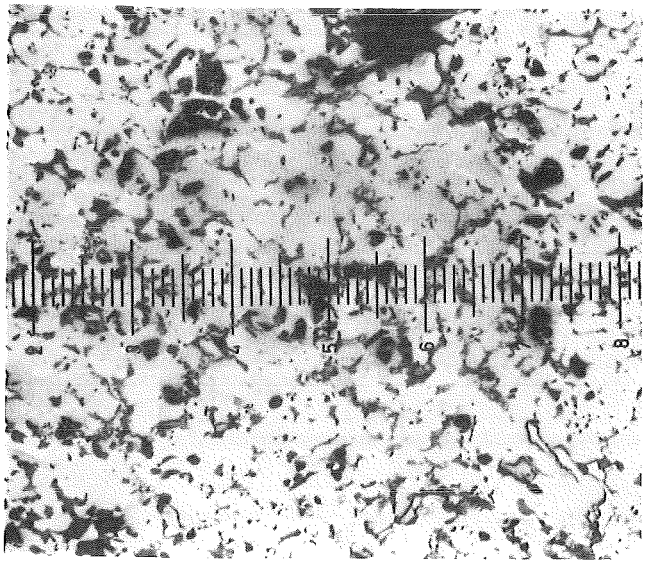

76mm

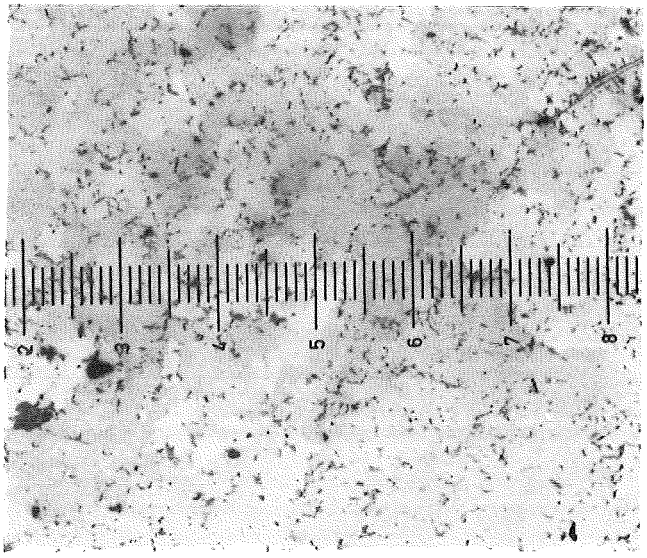

15mm

Fig.91: Structure of the refrozen melt for different elevations at the position given in Fig.89 with a magnification 100x (ESBU-1)

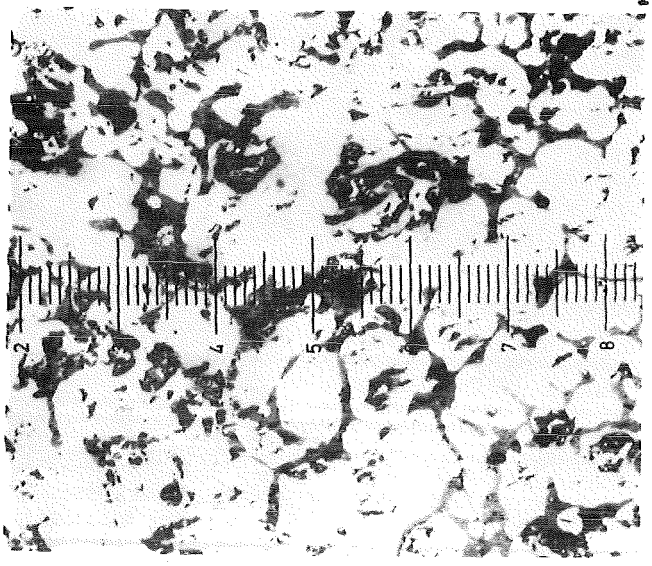

116mm

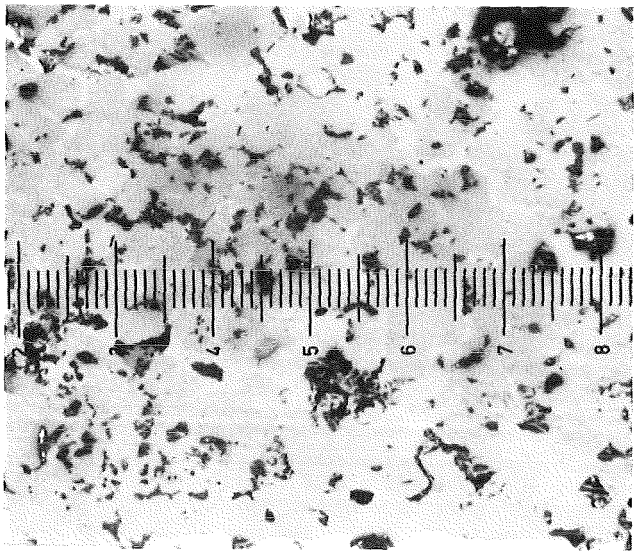

66mm

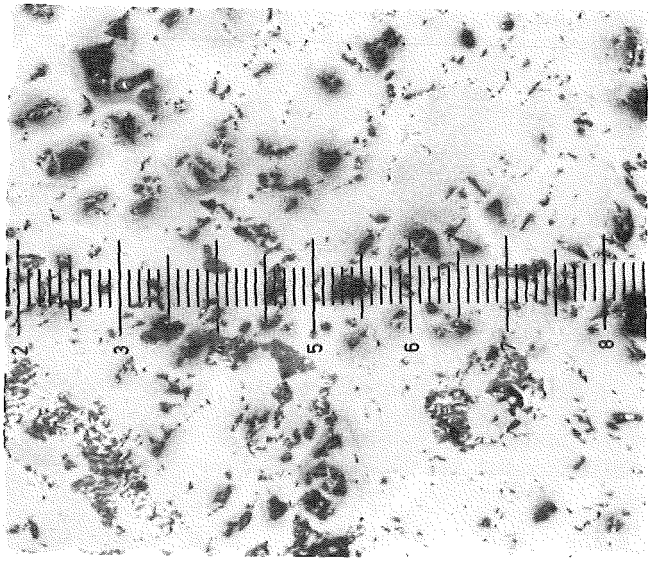

86mm

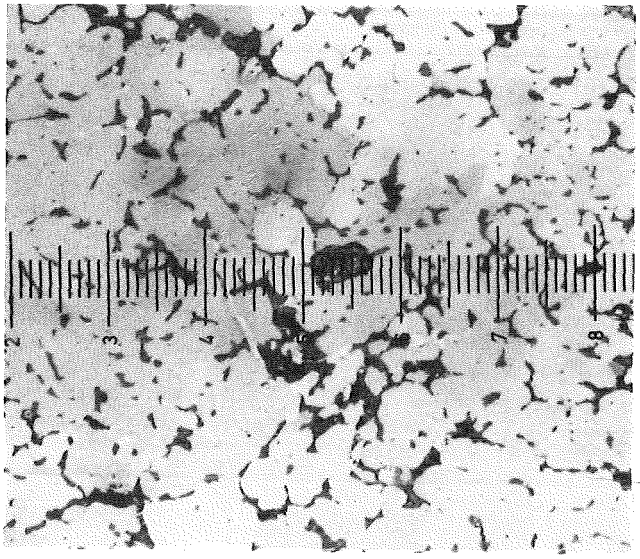

51mm

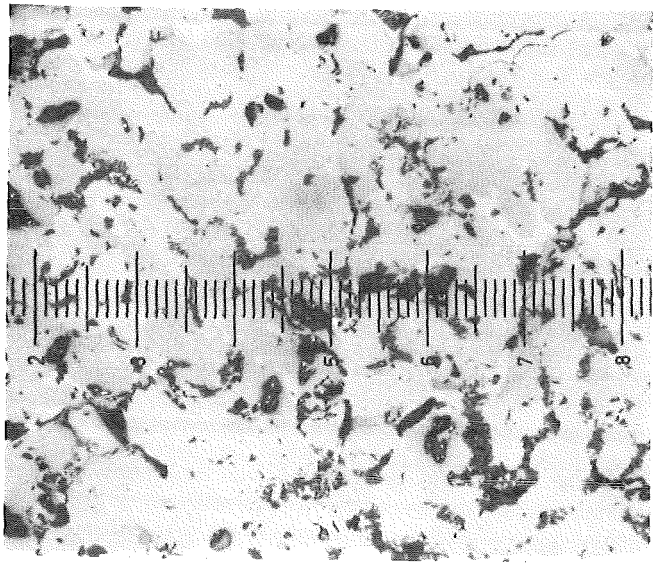

76mm

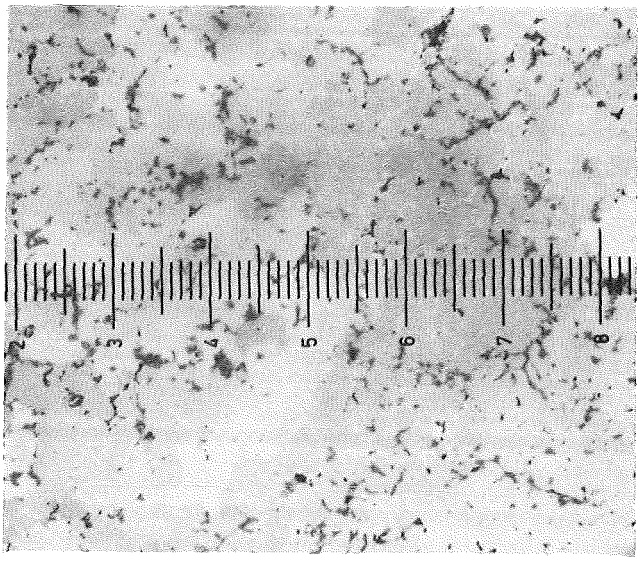

15mm

Fig.92: Structure of the refrozen melt for different elevations at the position given in Fig.89 with a magnification 200x (ESBU-1)

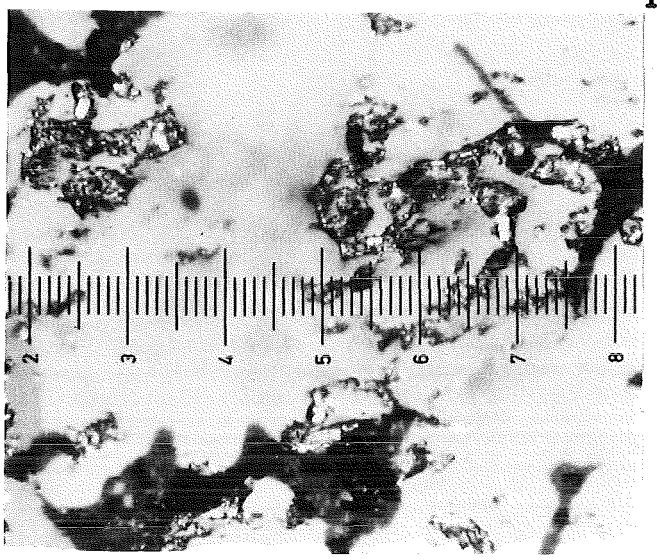

116mm

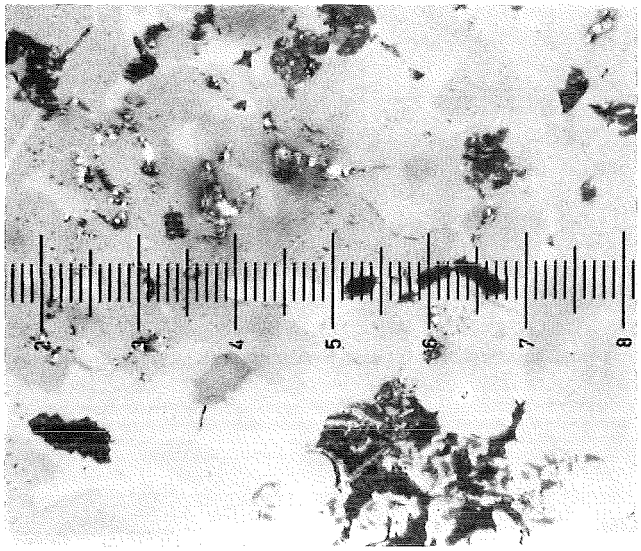

66mm

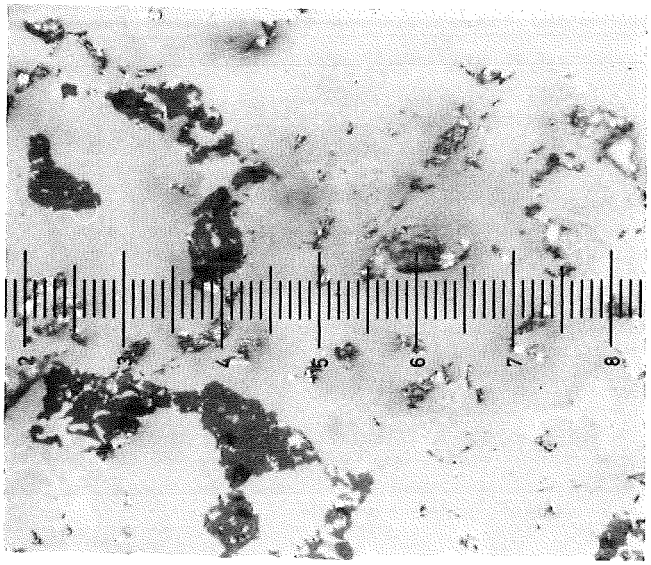

86mm

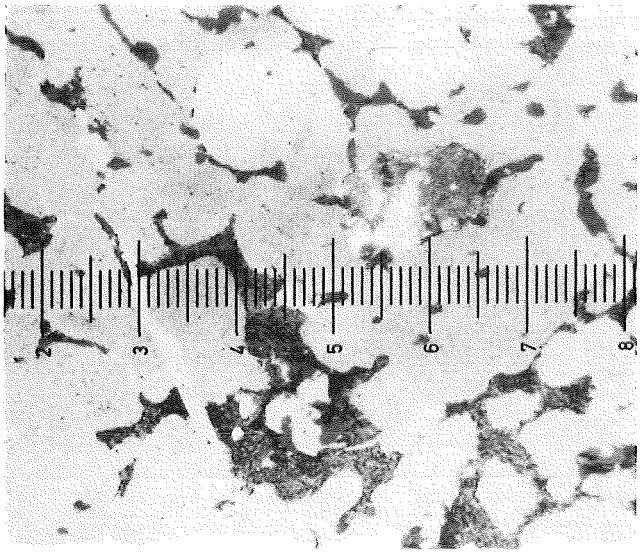

51mm

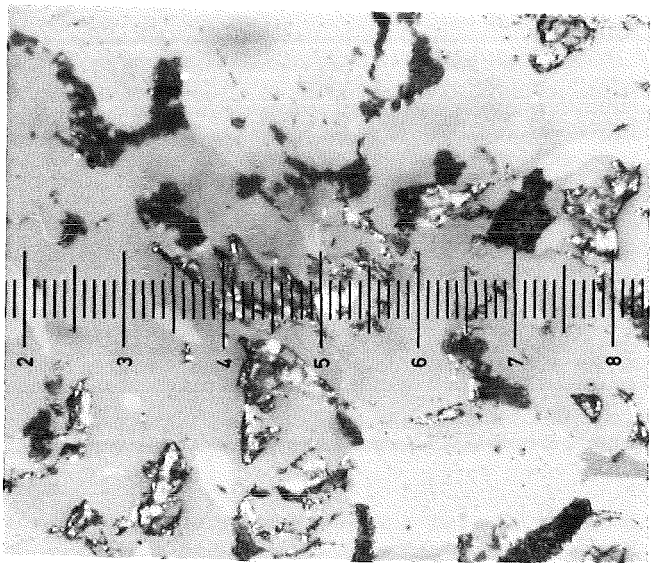

76mm

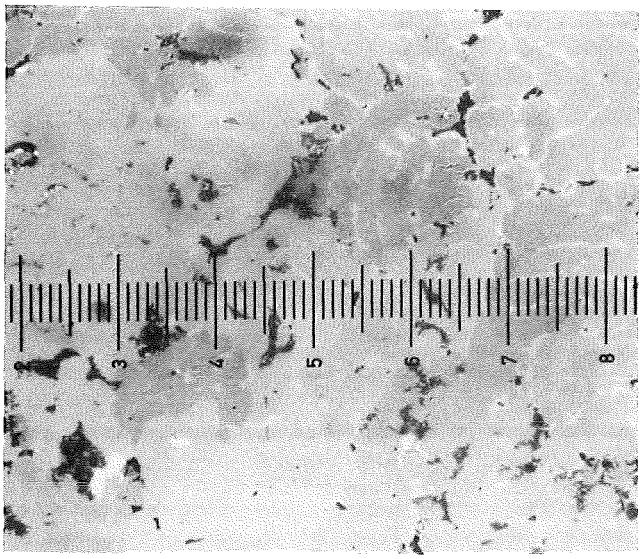

15mm

Fig.93: Structure of the refrozen melt for different elevations at the position given in Fig.89 with a magnification 500x (ESBU-1)